UNIVERSITÀ DEGLI STUDI DI MILANO

Scuola di Dottorato in Fisica, Astrofisica e Fisica Applicata
Dipartimento di Fisica

Corso di Dottorato in Fisica, Astrofisica e Fisica Applicata
Ciclo XXXI

QUPLAS: towards antimatter interferometry

Settore Scientifico Disciplinare FIS/01

Tutor: Dr. Marco GIAMMARCHI

Co-tutor: Dr. Stefano OLIVARES

Coordinatore: Prof. Francesco RAGUSA

Tesi di Dottorato di:
Simone SALA

Anno Accademico 2017-2018

External Referees:

Dr. Anna SOTER

Prof. Germano BONOMI

Final examination:

31 October 2018
Università degli Studi di Milano, Dipartimento di Fisica, Milano, Italy

Final examination Committee:

Prof. Matteo PARIS

Prof. Giovanni CONSOLATI

Dr. Ciro PISTILLO

Cover illustration:

Artist’s impression of the positron beam spot on the emulsion detector.

Design:

Simone Sala

MIUR subjects:

FIS/01

PACS:

03.75.-b, 14.60.Cd, 03.75.Dg

Contents

List of Figures **vii**

List of Tables **xi**

List of Publications **xiii**

Thesis overview **xv**
- Preface xv
- Organizational note xvii

I Introduction to the QUPLAS project 1

1 Matter-wave interference **3**
- 1.1 Interference: basic principle 3
- 1.2 Mirrors and beamsplitters 4
- 1.3 Inertial sensing and interactions with external fields 10

2 Motivation **17**
- 2.1 The three phases of QUPLAS 17
- 2.2 Testing the Weak Equivalence Principle on antimatter 17
- 2.3 Developing new techniques in matter wave-interferometry 21

3 Towards positronium interferometry **25**

II QUPLAS-0: Theoretical modelling 33

4 Asymmetric Talbot-Lau interferometry **35**
- 4.1 General description of a Talbot-Lau interferometer 36
- 4.2 Inertial sensitivity and applications 45
- 4.3 Numerical analysis 49

5 Talbot-Lau interferometry with partially coherent beams **55**
- 5.1 Analytical expression for the intensity 57
- 5.2 Measuring the input parameters 59

6 Modelling QUPLAS-0 on the L-NESS beam 63
6.1 The reference QUPLAS-0 interferometer 63
6.2 Alignment requirements 64
6.3 Beam coherence and collimation slits 70

III QUPLAS-0: experimental results 73

7 An optical asymmetric Talbot-Lau interferometer 75

8 The QUPLAS-0 interferometer and grating alignment 79
8.1 Design and specifications of the apparatus 79
8.2 Longitudinal alignment 81
8.3 Rotational alignment 86

9 Beam preparation and characterization 95
9.1 Beam alignment and collimation 95
9.2 Beam spot size and beam focusing 98
9.3 Beam coherence and interferometric visibility 101

10 Emulsion detectors 109
10.1 The QUPLAS-0 emulsion detector 109
10.2 Emulsion efficiency studies 110
10.3 Detection of micrometric fringe patterns with nuclear emulsion 112

11 Positron interferometry: preliminary measurements 127
11.1 Planned measurement campaign and goals 127
11.2 Background noise estimation 129
11.3 Interferometric measurement 133

12 First evidence of a periodic pattern 139
12.1 Measurement summary 139

13 Conclusion and future directions 149

Appendices 152

A Positronium in external fields 155
A.1 Theoretical background 155
A.2 Homogeneous magnetic field 158
A.3 Stark effect and motion in electric field gradients 165

B Full expression and implementation of equation (5.11) **173**

Bibliography 175

Acknowledgments 183

List of Figures

1.1 Sketch of a Michelson interferometer. 3
1.2 Sketch of a "Young experiment" with matter waves. 5
1.3 Double-slit experiments with electrons. 5
1.4 Buildup of the interference pattern in a double-slit setup. 8
1.5 Two-grating interferometer configurations. 9
1.6 Talbot carpet from a single grating. 10
1.7 Grating interactions with material gratings. 11
1.8 Sketch of the interfering trajectories in the COW experiment. 12
1.9 The Kasevich-Chu interferometer. 14

3.1 The L-NESS positron beam facility. 25
3.2 Sketch of the foreseen QUPLAS-II setup. 26
3.3 Ps formation and decay mechanisms in mesoporous materials. 27
3.4 Laser excitation of Positronium. 27
3.5 Stark deceleration of positronium. 28
3.6 Proposed ionization-emulsion detector for Rydberg positronium. 29
3.7 Proposed mask-mased detection methods for positronium interference. 30

4.1 Scheme of a general Talbot-Lau interferometer. 37
4.2 Talbot Coefficients for an asymmetric Talbot-Lau interferometer. 42
4.3 Intensity carpet in an asymmetric Talbot-Lau interferometer. 44
4.4 Visibility in an asymmetric Talbot-Lau interferometer. 44
4.5 Comparison of asymmetric and standard Talbot-Lau interferometers. 47
4.6 Calculated inertial displacement for a possible Positronium interferometer. 50
4.7 Visibility with a non-monochromatic beam (I). 52
4.8 Visibility with a non-monochromatic beam (II). 52
4.9 Relative inertial displacement in Talbot-Lau interferometers. 52
4.10 Inertial sensitivity of Talbot-Lau interferometers. 54

5.1 Replication of the results of the GSM model. 58
5.2 Free evolution of the parameters of a Gaussian model beam. 60
5.3 Sketch of the propagation of a partially coherent beam. 61

6.1 Reference QUPLAS-0 configuration and nominal parameters. 63
6.2 Calculated QUPLAS-0 interference pattern in ideal conditions. 65

6.3 Contrast vs. total length. 65
6.4 Contrast vs. L_1 and L_2. 66
6.5 Sketch of a moving detector plane setup. 66
6.6 Alignment requirements and beam coherence. 67
6.7 Contrast vs. L_2. 67
6.8 Drop in contrast due to rotational misalignments. 69
6.9 Beam collimation with mechanical slits. 71

7.1 Picutres of the gratings used for optical tests. 75
7.2 Sketch of the setup used for optical tests. 76
7.3 Asymmetric Talbot-Lau pattern in the optical domain. 77

8.1 Picture of the L-NESS beam and experimental chamber. 79
8.2 Drawing of the interferometer structure. 80
8.3 Picture of the interferometer components. 81
8.4 Longitudinal alignment errros. 83
8.5 Longitudinal alignment system. 85
8.6 Far field diffraction pattern of the micrometric gratings. 86
8.7 Sketch of the rotational alignment technique (I). 87
8.8 Sketch of the rotational alignment technique (II). 88
8.9 Effect of grating tilt on the rotational alignment. 89
8.10 Effects of camera tilt on grating alignment. 90
8.11 Real-time analysis software for rotational alignment. 91
8.12 Protocol to ensure parallelism of the diffraction gratings. 92

9.1 Scheme of the beam chamber with collimation slits. 95
9.2 Measurement of the beam width and position. 96
9.3 Sketch of the L-NESS beam electrostatic optics configuration. 98
9.4 Spot size as a function of focusing voltage V_F. 99
9.5 Total beam intensity as a function of V_F for different energies. 100
9.6 Evaluation of the spot density as a function of V_F. 101
9.7 Evolution of the collimated beam in "focused mode" operation. 102
9.8 Evolution of the collimated beam in "unfocused mode" operation. 102
9.9 Alignment tolerances vs. spot size for collimated beam. 104
9.10 Effect of the finite size of the gratings on beam parameters. 105
9.11 Estimated intensity transmission of the gratings. 106
9.12 Change in the density parameters due to finite-size gratings. 107
9.13 Density parameter vs. V_F with finite-size gratings. 107

10.1 Picture of the glass-supported emulsion films. 110
10.2 Plot of the results of Table 10.1. 111
10.3 SEM images of the diffraction gratings. 112
10.4 Grating membranes in *contact* with the emulsion detector. 113
10.5 Emulsion analysis example. 114
10.6 Optical aberrations correction. 115
10.7 Contrast loss with finite resolution. 117
10.8 Fit of the detected periodic signal on the emulsion. 118
10.9 Monte Carlo simulation of positron transport: stopping profiles. 119
10.10 Monte Carlo simulation of positron transport: energy and angle. 119
10.11 Beam spots of the test emulsion exposures. 120

10.12 Contrast and optimal angle maps for the test periodic patterns. 121
10.13 Scatter plots of the optimal period and measured effective resolution for the test periodic patterns. 122
10.14 Rayleigh test example. 123
10.15 Summary of the results of Grating B exposures. 124
10.16 Results of a long exposure in High Vacuum. 125

11.1 Contrast vs. positron energy. 128
11.2 C_{11}/C_{14} vs. ϕ and L_2. 128
11.3 Energy and angle distribution of $14\,\mathrm{keV}$ positrons transmitted by the grating membrane. 129
11.4 Transmission probability through the grating membranes. 130
11.5 Signal-to-noise ratio vs. energy. 131
11.6 Beam spot on the emulsion, without diffraction gratings. 132
11.7 Beam spot of the interferometric measurement (I). 133
11.8 Rayleigh test result for Monte Carlo signal with 20% contrast. 134
11.9 Rayleigh test vs. contrast. 135
11.10 Comparison of Rayleigh test searches. 136
11.11 Distribution of the Rayleigh test variable R_T. 137
11.12 Optimal parameters for real and Monte Carlo simulated views. 137
11.13 Tilted emulsion holder. 138

12.1 Rayleigh test results $E = 14\,\mathrm{keV}$, exposure A. 140
12.2 Beam spot and contrast map at $E = 14\,\mathrm{keV}$ with tilted emulsion, exposure A. 141
12.3 Two-parameter Rayleigh test search and folding histogram for best views at $E = 14\,\mathrm{keV}$, exposure A. 142
12.4 Rayleigh test results $E = 14\,\mathrm{keV}$, exposure B. 143
12.5 Beam spot and contrast map at $E = 14\,\mathrm{keV}$ with tilted emulsion, exposure B. 144
12.6 Contrast profile, $E = 14\,\mathrm{keV}$, tilted emulsion, exposure B. 145
12.7 Rayleigh test distribution, $E = 14\,\mathrm{keV}$, tilted emulsion, exposure B. 146
12.8 Analysis of a single view, $E = 14\,\mathrm{keV}$, tilted emulsion, exposure B. 146
12.9 Two-parameter Rayleigh test search and folding histogram for best views at $E = 14\,\mathrm{keV}$, exposure A. 147

13.1 Contrast vs. positron energy. 150
13.2 Contrast vs. L_2 for the classical and quantum case. 150

A.1 Kepler orbit of the relative coordinate $\mathbf{r}$. 157
A.2 Reproducing known results for Ps motion. 158
A.3 Reference frame for Ps gravity measurement. 159
A.4 Laws of motion for positronium in an homogeneous field. 160
A.5 Deviation of Ps trajectories in homogeneous fields (I). 162
A.6 Deviation of Ps trajectories in homogeneous fields (II). 163
A.7 Deviation of Ps trajectories in homogeneous fields (III). 166
A.8 Positronium ionization lifetime in an external electric field. 168
A.9 Adiabatic switch-on of external electric field. 169
A.10 Acceleration in a uniform field gradient. 172

List of Tables

2.1 Comparison of experimental WEP tests. 20

4.1 Comparison between symmetric and asymmetric Talbot-Lau setups. 45

8.1 Optimal geometrical parameters of the positron interferometer. 82

9.1 Comparison of the reference collimated and uncollimated beam configurations. 103

10.1 Summary of the experimental results on emulsion efficiency. 111
10.2 Best estimates of the measured parameters of Grating A. 122
10.3 Best estimates of the relevant parameters measured for Grating B. 124

List of Publications

As of 6 Sep 2018

Refereed publications

- [1]S. Sala, F. Castelli, M. Giammarchi, S. Siccardi, and S. Olivares.
  Matter-wave interferometry: towards antimatter interferometers.
  J. Phys. B: At. Mol. Opt. Phys., 48:195002, 2015.
- S. Aghion, A. Ariga, T. Ariga, M. Bollani, E. Dei Cas, A. Ereditato, C. Evans, R. Ferragut, M. Giammarchi, C. Pistillo, M. Romé, S. Sala, and P. Scampoli.
  Detection of low energy antimatter with emulsions.
  Journal of Instrumentation, 11(06):P06017, 2016.
- S. Sala, M. Giammarchi, and S. Olivares.
  Asymmetric Talbot-Lau interferometry for inertial sensing.
  Phys. Rev. A, 94:033625, Sep 2016.
- S. Aghion, A. Ariga, M. Bollani, A. Ereditato, R. Ferragut, M. Giammarchi, M. Lodari, C. Pistillo, S. Sala, P. Scampoli, and M. Vladymyrov.
  Nuclear emulsions for the detection of micrometric-scale fringe patterns: an application to positron interferometry.
  Journal of Instrumentation, 13(05):P05013, 2018.

Publications under review

- [2]A. Ariga, A. Ereditato, R. Ferragut, M. Giammarchi, M. Leone, C. Pistillo, S. Sala and P. Scampoli.
  First observation of antimatter wave interference.
  arXiv:1808.08901, 2018

---

[1] This paper was published before the beginning of my PhD, however it is strictly connected to the research reported in this thesis.

[2] This publication contains the final result of the QUPLAS-0 measurement campaign, which provided evidence for the quantum mechanical origin of the periodic patterns observed in the interferometer (chapter 12). Although I was fully involved in the activities, these results are not included in the final version of this thesis. The experiment took place after the thesis draft was submitted for external review. The same analysis and measurement principles described in this thesis were applied.

Thesis overview

Preface

In my Master's thesis, titled *"Antimatter wave interferometry with e^+, positronium and $\overline{p}$"*, I studied the possibility of testing aspects of fundamental quantum mechanics on antimatter systems, using grating-based matter wave interferometry as a tool [1, 2]. We also investigated the use of nuclear emulsion detectors for this application. Our group has access to this technology thanks to a collaboration with the Laboratory for High Energy Physics at the University of Bern [3].

By the time I started my PhD program, these ideas had evolved into the experimental project that we refer to as **QUPLAS**: **QU**antum interferometry and gravity with **P**ositronium and **LAS**ers. The proposed activities are based on the positron beam facility of the L-NESS laboratory in Como [4].

QUPLAS has the ambitious long-term goal of measuring the gravitational acceleration of positronium (Ps): a matter-antimatter symmetric, purely leptonic exotic atom, discovered in 1951 by Martin Deutsch [5]. Positronium has two spin states, the spin zero state (para-positronium) has a very short radiative lifetime of $125\,\mathrm{ps}$ and decays in two $511\,\mathrm{keV}$ gamma rays, while the spin triplet state (ortho-positronium) decays in three gammas with a lifetime of $\tau = 142\,\mathrm{ns}$ [3].

The topic of gravitational interactions of antimatter at low energy has attracted a large interest in the scientific community, as evidenced by the combined effort of the experiments currently ongoing at CERN (AEgIS[6], ALPHA[7], GBAR[8]), targeting antihydrogen gravity with various techniques. The proposed positronium measurement would be complementary to these studies on antihydrogen.

The short term goal of QUPLAS, on the other hand is the observation of matter-wave interference of positrons; this is instrumental in paving the way for future measurements on positronium by establishing the basic techniques, and would be an original result on its own. We refer to this initial phase of the project as QUPLAS-0. At the time when the QUPLAS collaboration started, matter wave phenomena had been demonstrated on a large class of objects: electrons [9, 10], neutrons [11], even larger objects like C_{60} fullerene [12], but not yet on elementary antimatter.

During the first year as a PhD student, I took part to the preliminary design of all the phases of QUPLAS. The main body of work was constituted by the theoretical modelling of the QUPLAS-0 positron interferometry experiment, which required to find the most suitable interferometric configuration to carry out the measurement, given the constraints of our experimental setup. As a result of this study, a paper was published [13], where the use of a novel *asymmetric* Talbot-Lau interferometer is suggested. This design is based on unequal grating periodicities and produces period-magnifying effects, which could also improve inertial sensitivity in future applications to positronium gravimetry.

---

[3] In this thesis the prefix "ortho-" will often be suppressed. The name positronium or the symbol Ps *always* refers to the longer lived state, unless otherwise stated.

At the same time, I was also involved in the data taking and analysis for a test exposure of nuclear emulsion detectors. The results were then published in a paper [14] where the capability to detect low energy positrons with high efficiency is assessed.

Since the beginning of my second year I have been more deeply involved in the experimental implementation of QUPLAS-0: a first interferometric test was performed. I was responsible for the rotational alignment of the diffraction gratings, and helped the L-NESS team in the preparation of the beam and installation of the interferometer in the weeks before the experiment. The analysis of the measurement protocols prompted an in-depth investigation of the interplay between beam coherence and interferometer alignment from a theoretical point of view. Coupling well-known analytical models with a detailed description of the specific features of our beam I was able to determine the alignment requirements on the interferometer components, thus the necessary technical improvements needed. To open up the possibility of interferometric studies on a more intense and coherent beam, I started (in collaboration with the Plasma Physics group of the University of Milan) the implementation of a test electron beam with suitable features. I was also co-supervisor of a Bachelor's Degree thesis connected with this activity. Meanwhile, I also developed the data analysis software needed to reconstruct the interference fringes from the raw data digitized from the emulsion film at the Bern microscope scanning facility. In the framework of this collaboration with the Bern group, an experiment was devised to assess the performance and spatial resolution of emulsion detectors for the specific purpose of positron interferometry. I participated to the data taking at L-NESS, as well as to the emulsion development and scanning phase in Bern. A paper [15] was published in which $6\,\mu\mathrm{m}$ fringe patterns were successfully detected. This is approximately the expected periodicity of the quantum interference pattern produced by the QUPLAS-0 interferometer.

This test allowed me to refine and validate the data analysis software in view of the interferometric tests. During my third year I started to work routinely at the L-NESS laboratory in preparation for the positron interferometry runs. In particular I took part in the preliminary beam characterization and collimation phases, and was responsible for the longitudinal and rotational alignment of the diffraction gratings. Specifically, I developed a reliable laser-based protocol for rotational alignment with $\approx 10\,\mu\mathrm{rad}$ accuracy. The apparatus has been able to run reliably for the long exposure times required (of the order of a week), and a few attempts to the interferometric measurement have been made in different experimental conditions.

First evidence of a periodic pattern produced at the positron energy of $14\,\mathrm{keV}$, consistent with the theoretical expectations was eventually found. This result proves that the QUPLAS-0 system, designed and commissioned in the framework of this thesis, fulfils the requirements in terms of beam quality, alignment accuracy and detector performance to perform matter-wave interference experiments. This preliminary results constitutes the foundation of a measurement campaign at different energies that established the quantum-mechanical origin of the observed phenomenon by excluding geometrical shadow (moiré) effects.

Organizational note

The structure of this Thesis follows the summary of activities outlined above. The work is therefore divided in three main parts:

> **Part I - Introduction to the QUPLAS project**. An overview of QUPLAS is presented: focus is on the physics goals and their theoretical motivation. A preliminary design of the planned future stages is also illustrated; additional details on a study of Ps motion in external fields are reported in **Appendix A**.
>
> **Part II - QUPLAS-0: theoretical modelling**. A realistic model of matter-wave interference experiments, suitable for our setup, is described. Attention is given to the Talbot-Lau regime that has been employed in all the phases of the experiment. In particular the interplay of beam coherence and interferometer alignment requirements is studied.
>
> **Part III - QUPLAS-0: experimental results**. The main items connected to the experimental implementation of QUPLAS-0 are discussed: interferometer alignment techniques, beam preparation and characterization, the use of nuclear emulsions for the detection of micrometric-scale fringe patterns. Finally, results of the measurement runs with the QUPLAS-0 interferometer are reported.

Part I

Introduction to the QUPLAS project

CHAPTER 1

Matter-wave interference

Since matter-wave interference is the main ingredient behind QUPLAS, this chapter aims to provide a concise introduction to the underlying physics. A more advanced treatment is discussed in Part II.

1.1 Interference: basic principle

Generally speaking, the term *interference* in physics refers to a class of phenomena were two suitably correlated (coherent) *waves* are superimposed to form a resulting wave of different amplitude, dependent on their relative phase and frequency. This phenomenon is observed, for instance, for the whole electromagnetic spectrum, for acoustic waves and for surface waves on water. All these examples of wave-like propagation have different physical origin, yet all of them obey the *superposition principle*. Together with phase coherence this is the requirement for the manifestation of interference. The superposition principle is one of the main postulates of quantum mechanics, therefore it is apparent that in suitable circumstances, *interference* effects that share common traits with their classical counterparts are possible. *Interferometry* labels a range of techniques where waves are made to interfere in a controlled manner, in order to extract measurable information on their properties. The apparatus to perform this measurement is aptly named an *interferometer*, the most familiar among them is probably the Michelson interferometer. It is useful to recall a few points to stress differences and similarities with

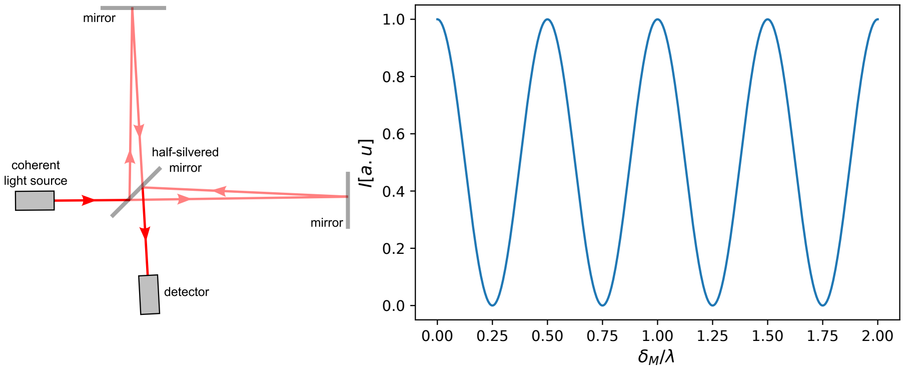

Figure 1.1. Left: scheme of the traditional optical Michelson interferometer. Right: Interference *fringes* in the intensity at a fixed observation point, swept by moving one of the two mirrors by δ_M, as a function of the ratio δ_M/λ. The parameter λ is the wavelength of the interfering light.

the quantum matter-wave experiments we will describe later. A scheme of the Michelson apparatus is shown in Fig. 1.1: a coherent light source such as a laser beam, is *split* by a beam splitter, the two wavefronts are made to propagate along two different paths by means of *mirrors* and finally detected after they overlap again in space.

Mirrors and *beamsplitters* are two key building blocks of the Michelson interferometer. In the following discussion, it will be apparent that all the of interferometers we will mention, also for matter waves, ultimately make use of different mechanisms to implement the action of mirrors and beam splitters: material diffraction gratings, crystalline solids, excitation laser pulses...

In a minimal description of the physics, we can assume the output of the Michelson interferometer is the superposition of two plane waves of equal amplitude and frequency,

$$x(t) = A\cos(\omega t - kz) + A\cos(\omega t - kz')$$

where z and z' represent the optical path length traveled by the two waves. Summing the terms and taking the square, the intensity at a fixed observation point is proportional to:

$$I \propto \cos^2\left[\frac{k(z-z')}{2}\right] = \cos^2(k\delta_M).$$

Here an optical path length difference $z-z'$ is generated by moving one of the mirrors by $\delta_M = (z-z')/2$, therefore the interference is constructive and yields maximum intensity for displacements which are integer multiples of $\lambda/2$, as shown in Fig. 1.1. In practice it is not required to move the mirror to see interference fringes, as they naturally appear if the interferometer output is observed on a screen. This fact is due to the finite size of the wavefronts. However we wanted to emphasize the idea that the experimenter can sweep a fringe pattern by varying a parameter. This helps to understand the working principle of atom gravimeters based on quantum interference that we are going to describe shortly.

1.2 Mirrors and beamsplitters

As mentioned before, exploiting the analogy with the working principle of the Michelson interferometer most (if not all) kinds of *interferometers for matter waves* rely on the use of appropriate mirrors and beam splitters. We will now present an introductory description of the most common examples, to set the stage for the theoretical motivation of the relevance of QUPLAS discussed in the following chapter.

1.2.1 Matter-wave interference with diffraction gratings

The previous example was related to the interferometry of classical electromagnetic radiation. We now introduce the idea of *matter-wave interference* with quantum mechanical objects, starting from a simple ideal experiment.

Consider a single point-like particle with speed v and mass m that travels towards a screen with two apertures, and assume a position-sensitive detector is located a distance L downstream the slits (see Fig. 1.2). This is the quantum-mechanical analogue of the Young double slit interference experiment and can be generalized to more complicated diffraction gratings; it is therefore useful as the main building block for two (or more) grating interferometers. What is the expected position distribution of the particles on the screen? Two famous experiments answered this question a few decades ago and their results are reproduced in Fig. 1.3. In 1974 the team of Pier Giorgio Merli, Gian Franco Missiroli and Giulio Pozzi at the University of Bologna observed for the first time

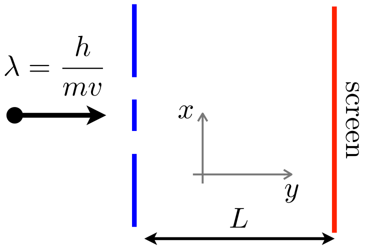

Figure 1.2. Schematic representation of a Young like experiment with a particle of mass m and speed v.

electron interference from a double slit [10] or, more precisely, from an *electron biprism* acting as a double slit [16]. The effect of interference is the appearance of a fringe pattern in the position distribution of electrons on the detector. The result was later confirmed independently in 1989 by Akira Tonomura et al. [9] with a very low intensity beam (electrons passing one by one through the slits), proving that a true quantum interference effect was being observed without any influence of electron-electron interactions. This single-electron double-slit experiment, originally proposed as a thought experiment by Richard Feynman [17], was voted *"The most beautiful experiment in physics"* by *Physics World* readers [18] in 2002.

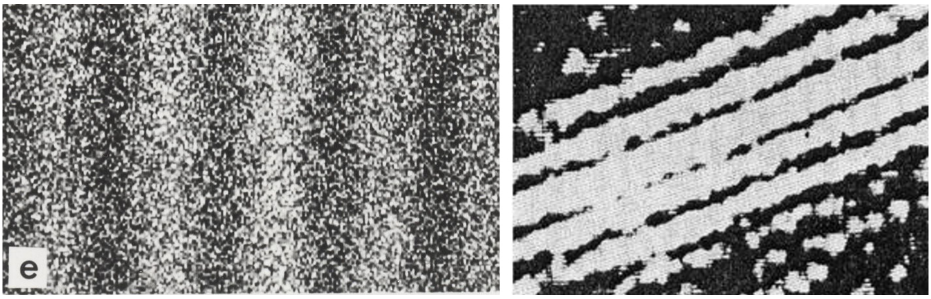

Figure 1.3. On the left, the distribution of electrons in the famous Tonomura experiment [9]. On the right, a similar result from the Merli, Missiroli, Pozzi experiment performed in 1974 [18]. (Both images available for reproduction under the Creative Commons license).

The theoretical explanation for this observation is the heart of quantum matter-wave interference. In 1924 L. de Broglie proposed in his PhD thesis [19] that under appropriate circumstances massive particles can show a wave-like behavior with a wavelength inversely proportional to their momentum $p = mv$

$$\lambda_{dB} = \frac{h}{p}$$

The so called *de Broglie hypothesis*, revolutionary at the time of its proposal, is now well established and experimentally confirmed, not only on point-like particles like electrons or neutrons [11], but also on extended objects with a complex internal structure like C_{60} and C_{70} fullerene molecules. These mesoscopic particles produce interference patterns dependent on the deBroglie wavelength associated with their center-of-mass motion [12, 20].

One could invoke the deBroglie hypothesis to conclude that the observed pattern is no different to the one produced with radiation of wavelength $\lambda = \lambda_{dB}$ on the same grating.

Although this is essentially correct, the analogy between classical optics and quantum mechanics can be established more carefully.

Let us go back to our (nonrelativistic) particle of momentum $p = \sqrt{2mE}$ impinging on a set of slits (see Fig. 1.2). Under the assumption that the particle energy E is weakly perturbed during its propagation, the relevant equation to describe its motion is the spatial part of the Schrödinger equation for the wave function $\psi(\mathbf{x})$:

$$\nabla^2\psi(\mathbf{x}) + k_{dB}^2 \underbrace{[1 - V(\mathbf{x})/E]}_{n_q^2(\mathbf{x})} \psi(\mathbf{x}) = 0. \tag{1.1}$$

We defined the de Broglie wave number as $k_{dB} = 2\pi/\lambda_{dB}$ and assumed that an interaction potential $V(\mathbf{x})$ acts on the particle, the coordinate $\mathbf{x}$ being the position of the center of mass. On the other hand, it is well known [21, 22] that diffraction from a system of apertures of a monochromatic scalar field, for instance, one Cartesian component of the electric vector field $\mathbf{u}(\mathbf{x})$ is well described by the Helmholtz equation:

$$\nabla^2 u(\mathbf{x}) + k^2 n^2(\mathbf{x}) u(\mathbf{x}) = 0 \tag{1.2}$$

where k is the wave number and $n(\mathbf{x})$ is the refractive index, possibly position dependent. Comparing equations (1.1) and (1.2), it is clear that u and ψ satisfy the same equation, where the potential term $n_q^2(\mathbf{x}) = [1 - V(\mathbf{x})/E]$ plays the role of a *refractive index* for the quantum mechanical object. Finally, the measured quantity is in the classical case the intensity distribution of the diffracted light, and is in the quantum case the position distribution of the particles; both quantities, are proportional to the square modulus of u and ψ respectively:

$$\begin{aligned} I_{\text{class.}}(x) &\propto |u(x)|^2 \\ I_{\text{quant.}}(x) &\propto |\psi(x)|^2 \end{aligned}$$

This completes the formal analogy, which allows us to adopt classical optics to model quantum interference, although the different physical meaning of the quantities involved should always be kept in mind. For the sake of simplicity, in this work the term *intensity* will be used loosely, to indicate the expected spatial distribution particles in a quantum interference experiment, whether it was derived with a classical optics analogy or a quantum mechanical treatment. Moreover, we will drop the subscript dB to identify the de Broglie wavelength, and simply use the symbol λ throughout all this thesis.

If the potential is negligible with respect to the particle energy, then $n_q^2 \approx 1$, therefore the wave function obeys the same equation of classical light diffracted in vacuum. In this simplified case, we will now sketch how the intensity pattern behind a system of slits is linked to the evolution of the initial wavefunction. This discussion follows the paper *"Matter-wave interferometry: towards antimatter interferometers"* published on Journal of Physics B: Atomic, Molecular and Optical Physics and based on results from my Master's thesis [1].

If the slits are sufficiently wide along the z-axis (see Fig. (1.2)) diffraction is negligible in that direction. Therefore we can represent the state just after the grating at time $t = 0$ and $y = 0$ as the following superposition state [23, 24]:

$$\psi^{(N)}(x, t = 0) \propto \sum_{n=1}^{N} \psi_n(x, t = 0), \tag{1.3}$$

where $\psi_n(x,t=0)$, with $n=1,\dots,N$, is the wave function describing the particle passed through the n-th slit. Note that we identified $t=y/v$; this corresponds to the assumption of classical unperturbed motion along the y-axis. For a system of identical slits with period D, we can write $\psi_n(x,0)=\psi_0(x-nD)$. As the grating prepares the system in the state of equation (1.3), we can assume that the motion along the x-axis is governed by the free Hamiltonian:

$$H_{\text{eff}}=\frac{p_x^2}{2m}. \tag{1.4}$$

Therefore, the evolved state $\psi(x,t)$ is obtained by solving the Schrödinger equation with the Hamiltonian (1.4). In particular, the probability density distribution along the x-axis on the screen at position $y=L$ (i.e. the interference pattern), is given by $I(x)=|\psi^{(N)}(x,t=L/v)|^2$, with:

$$\psi^{(N)}(x,t=L/v)=\frac{1}{\sqrt{i\lambda L}}\int_{-\infty}^{+\infty}\exp\left[i\frac{\pi}{\lambda L}(x-x')^2\right]\,\psi^{(N)}(x',0)\,\mathrm{d}x', \tag{1.5}$$

which is formally identical to the Fresnel integral of classical optics [22], as expected from the formal analogy we established. Following a common assumption adopted in the literature [23, 24, 25], it is convenient to assume a Gaussian form for the initial single slit wavefunction, namely (dropping the overall normalization constants):

$$\psi_n(x,0)=\exp\left[-\frac{(x-nD)^2}{4\sigma^2}\right], \tag{1.6}$$

where the parameter σ is usually set to $\sigma=a/(2\sqrt{2\pi})$. This choice allows to compute equation (1.5) analytically, in particular the solution for a double slit ($N=2$) is compactly expressed as

$$\psi_2(\hat{x},\hat{L})=\sum_{n=1,2}\exp\left[-\frac{(\hat{x}-\hat{x}_n)^2}{4\left(1+\hat{L}^2\right)}\left(1-i\hat{L}\right)\right]$$

Where we introduced the adimensional variables:

$$\hat{x}=\frac{x}{\sigma},\quad \hat{D}=\frac{D}{\sigma},\quad \text{and}\quad \hat{L}=\frac{\hbar t}{2m\sigma^2}=\frac{L\lambda}{4\pi\sigma^2}, \tag{1.7}$$

in particular, $\hat{x}_1=-\hat{D}/2$ and $\hat{x}_2=+\hat{D}/2$. The generalization for a set of N equally separated slits is straightforward. After simple algebraic manipulations, defining

$$F_\pm=\exp\left[-\frac{(\hat{x}\pm\hat{D}/2)^2}{2(1+\hat{L}^2)}\right]$$

the intensity reads

$$I(\hat{x},\hat{L})=F_+ + F_- + 2\sqrt{F_+F_-}\cos\left[\frac{\hat{L}\hat{x}\hat{D}}{2(1+\hat{L}^2)}\right], \tag{1.8}$$

which clearly shows the appearance of an interference pattern due to the oscillating term (see Fig. 1.4). It is worth noting that the condition for observing the interference maxima

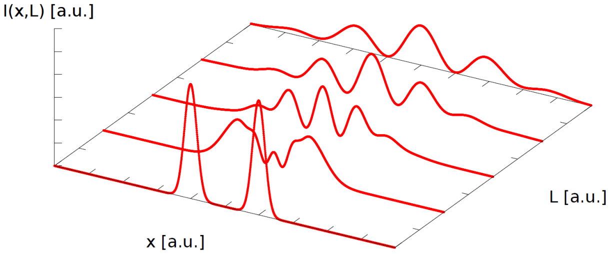

Figure 1.4. The buildup of the interference pattern (1.8) shown with its dependence on the screen distance L.

in far field turns out to be the usual relation of classical optics; in the limit $\hat{L} \gg 1$, the condition for observing a maximum reduces to

$$\frac{\hat{x}\hat{D}}{2\hat{L}} = 2n\pi \rightarrow \frac{xD\pi}{L\lambda} = n\pi$$

which is indeed the expected classical relation. The formal analogy with classical optics also ensures that the choice of the initial single slit profile impacts only the envelope of the intensity pattern and not its oscillatory behaviour. The classical Fraunhofer field outgoing a double slit setup reads

$$I_{\text{class}}(x, L) \propto \text{sinc}^2\left(\pi a \frac{xL}{\lambda}\right)\left[1 + \cos\left(2\pi D \frac{xL}{\lambda}\right)\right]$$

while starting from (1.8) it easy to recover a Fraunhofer-like expression by taking the far field limit in the form $\hat{L} \gg 1$ and $\hat{x} \gg \hat{D}$, so that

$$F_+ = F_- \simeq \exp\left(-\frac{\hat{x}^2}{2\hat{L}^2}\right).$$

Finally, in order to highlight the similarity with the classical expression in the Fraunhofer limit, we use equations (1.7) and (1.8) to obtain:

$$I(x, L) = 2\exp\left[-2\left(2\pi\,\sigma\frac{x}{\lambda L}\right)^2\right]\left[1 + \cos\left(2\pi D \frac{xL}{\lambda}\right)\right]. \tag{1.9}$$

So, much alike the classical case, in a quantum treatment based on the free evolution of single-slit wave functions, the latter factorizes and determines the envelope of the pattern. This *Young-like* experiment is the main building block of grating-based matter-wave interference experiments. Now we can more accurately define the term *matter-wave interference*: the quantity that manifests wave-like interference phenomena is the wavefunction ψ describing the translational motion of the center of mass of the particle. Therefore, by shining a low intensity beam towards, for instance, a single diffraction grating and gradually accumulating the impact point on a position-sensitive detector, one can sample the underlying probability distribution, proportional to $|\psi|^2$. This is the matter wave counterpart to a traditional Fraunhofer diffraction experiment performed in classical optics and described by scalar diffraction theory.

With this tool in our hands, gratings can be combined to arrange a proper *interferometer* in several different schemes. The most interesting setups require two gratings

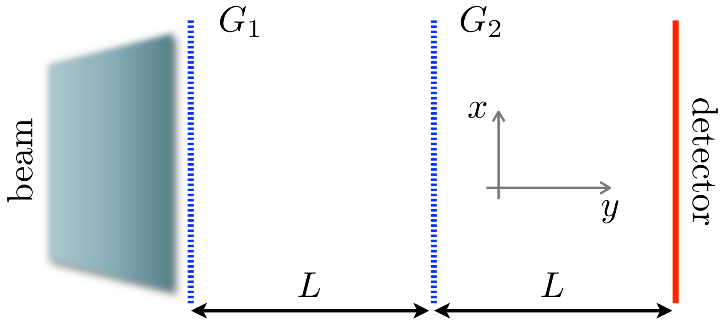

Figure 1.5. Scheme of a general two grating based interferometer. The goal is to form interference fringes at a certain plane where a suitable detector is placed. The two gratings G_1 and G_2 are commonly chosen with the same period d. In Part II we will discuss the advantages of using different periods in a two grating interferometer.

to produce high-contrast interference patterns. A sketch of the geometry is drawn in Fig. 1.5. This two grating setup can operate in different regimes, as in classical optics, and the boundary between these working conditions is set by the same rules of classical diffraction. Introducing the *Fresnel number* [21] as

$$F = \frac{d^2}{L\lambda},$$

then if the second grating is located in the *far field* of the first, namely $F \ll 1$ (and the same holds for the detector plane and the second grating, due to the symmetry of the configuration) a *Mach-Zehnder* type interferometer is realized [26]. We have sketched before that in the far field of a diffraction grating, distinct peaks form as the wave function propagates. So we can say that qualitatively in the Mach-Zehnder regime the particle is split into distinct wave packets that travel different trajectories in space and are then recombined to interfere at the detector. The gratings are truly acting as mirrors and beam splitters for the wave function of the particle. As it is well known from the classical theory *coherent* light is needed to observe far field diffraction. The same then holds for a matter wave Mach-Zehnder setup, where the role of *coherence* is inherited essentially by the width of the transverse (along the x-axis in Fig. 1.5) momentum distribution of the particle beam (see Part II for a detailed discussion).

It is not straightforward to have arbitrarily well collimated, hence *coherent*, beams especially when low intensity antimatter sources are used. For this reason, QUPLAS is based on the Talbot-Lau interferometer [26, 27, 28], which is obtained when the gratings operate in the *near field* of each other.

The physics arises from the interplay of two effects: in the near field ($F \gtrsim 1$) of a coherently illuminated diffraction grating (for example point source or plane wave illumination [2]), high contrast interference fringes appear, with a peculiar longitudinal structure known as the *talbot carpet* (see Fig. 1.6). In particular if the observation distance L satisfies

$$L = \frac{d^2}{\lambda} = L_T \tag{1.10}$$

the detected fringes are *self-images* of the grating transmission function. This is known as the *Talbot effect* [22] and the distance defined in Eq. (1.10) is labelled the *Talbot Length*[1].

---

[1] Actually self-images at even and odd multiples of L_T are shifted by half periods, as evident in Fig. 1.6.

In 1948 it was discovered [30] that if two identical gratings are arranged in the symmetric configuration of Fig. 1.5 and $L = L_T$, high contrast fringes are observed even with incoherent illumination. This phenomenon is known as the *Lau effect* and can be understood by considering the slits of the first grating as an array of point sources [31]. A displaced point source will produce a displaced *talbot carpet* [2, 31]. Since the Talbot images are periodic, it is possible for an ensemble of laterally displaced and mutually independent point sources to produce fringes that overlap "constructively". This occurs if the elementary displacement on the detector plane produced in moving between adjacent sources equals the period of the Talbot image (or an arbitrary integer multiple). This is realized when the resonance conditions $L = L_T$ are met. With more sophisticated tools the same principle is described in terms of the first grating producing light with a d-periodic *mutual intensity function* [32], thus able to coherently illuminate the second grating and produce a Talbot-like effect.

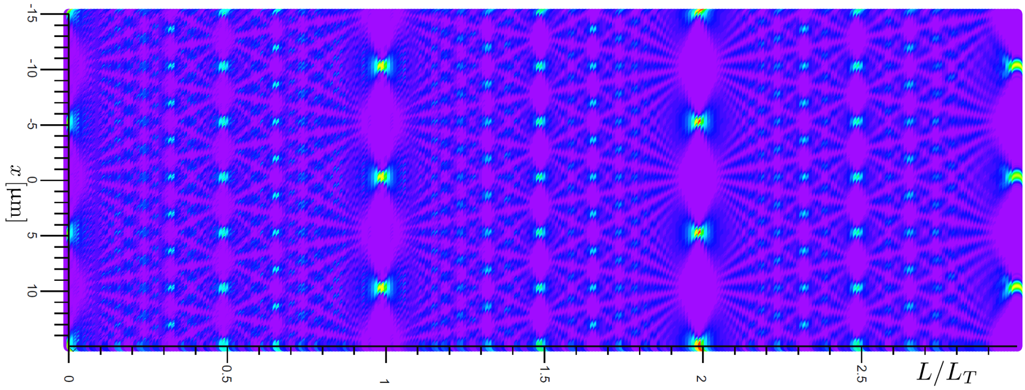

Figure 1.6. Example of a Talbot carpet from plane wave illumination of a single grating, calculated in Kirchhoff diffraction theory [2]. The longitudinal scale is in units of the Talbot length, and the grating period is $d = 10\,\mu\mathrm{m}$. Intensity is represented by the color scale. Fractional period self images can be seen at the expected distances, in addition to the main d-periodic Talbot revival at $L = L_T$. Similar carpets have been observed experimentally in both classical and atom optics experiments [29]

In more practical terms, this means that a Talbot-Lau setup in matter wave interferometer will produce high contrast fringes even when illuminated by a poorly collimated beam. This is in principle correct, however, as the beam gets increasingly less coherent the region along the longitudinal axis where fringes are visible becomes narrower. This in turn requires to know the grating periods with a very high degree of accuracy. The issue is discussed in details in Part II and represents one of the main experimental challenges for QUPLAS.

1.3 Inertial sensing and interactions with external fields

A Talbot-Lau interferometer is also an inertial sensing device: an external constant force acting on the particles in the transverse direction produces a rigid displacement of the

---

For this reason in the literature the Talbot length is sometimes defined as $\frac{2d^2}{\lambda}$. In this thesis we adopt instead the convention of equation (1.10).

interference fringes [13, 33]. For instance, if we consider the force due to the gravitational field of the Earth $F = mg$, then this displacement is given by :

$$\Delta x \propto gT^2 \tag{1.11}$$

where T is the time of flight between the two gratings, and the exact proportionality constant depends on the geometry of the apparatus (see Part II). Effective techniques have been demonstrated[2] to measure fringe shifts down to the level of $10\,\mu\mathrm{m}$ [34], which allow to perform gravimetry on slow atomic beams.

So far we have relied on the full analogy between equations (1.1) and (1.2), so it is worth concluding this overview with the key difference that prevents the correspondence to be completely trivial, namely the potential term $n_q^2(\mathbf{x}) = [1 - V(\mathbf{x})/E]$. In this context we neglected any interaction of the interfering particle with the environment. This is usually physically reasonable in vacuum, save for peculiar cases, where the whole issue of *decoherence* comes into play [25, 35, 36, 37]. However, when transmitted by material gratings the particles are forced to pass at very short distances from the walls of the gratings (membranes with a slit width as small as $45\,\mathrm{nm}$ have been used for electron experiments [38]). This inevitably gives rise to an interaction mediated by a potential $V(\mathbf{x})$. Since the thickness of the gratings δ (see Fig. 1.7) is much smaller than the free propagation distance, it is convenient to drop the potential term from the equations of motion. The effect of the grating is rather incorporated into a *transmission function* $T(\mathbf{x})$ that acts as a multiplicative factor on the incoming wavefunction $\psi(\mathbf{x})$. This usually has a periodic real part accounting for the spatial intensity modulation, and a phase factor acting on each period, as sketched in Fig. 1.7. For neutral atoms and molecules, the dominant contribution is the van der Waals atom-surface interaction [39] defined as $V(r) = -C_3 r^{-3}$, where r is the distance from the slit walls and the C_3 coefficient was first introduced by Lifshitz [40]. A more general form of the interaction that includes retardation effects is the so called Casimir-Polder potential [41, 42] which scales as r^{-4}. Charged particles will interact via the Coulomb force, which in this scenario is typically modelled with an image-charge model that depends on the dielectric constant of the

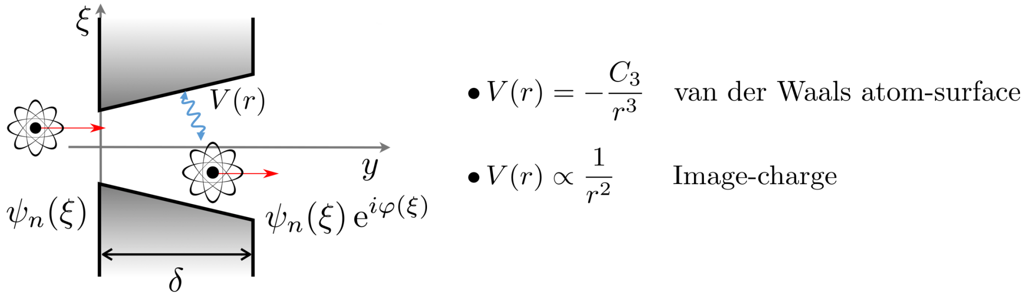
ξ
$V(r)$
y
$\psi_n(\xi)$
$\psi_n(\xi)\,\mathrm{e}^{i\varphi(\xi)}$
δ
• $V(r) = -\frac{C_3}{r^3}$ van der Waals atom-surface
• $V(r) \propto \frac{1}{r^2}$ Image-charge

Figure 1.7. Sketch of the interfering particles interacting with the walls of a grating slit. The effect of interactions is typically embedded in a transmission function of the form $e^{i\phi(\xi)}$, where ξ labels the transverse coordinate. More details can be found in [1] and references therein.

---

[2] To avoid confusion, I remark that the work cited employs a *moiré* deflectometer. It is essentially the very same two grating setup outlined above, but operating in the *classical* regime, where quantum diffraction is negligible and particles behave as ballistic projectiles. This condition is realized if the gratings operate at distances much smaller than the Talbot Length. Nevertheless, the inertial sensitivity properties are analogous (see Part II).

material gratings [1]. For weak potentials, the standard approach [38, 39, 43] is to determine the phase shift $\varphi(\xi)$ via the semiclassical eikonal approximation. Denoting with v the particle speed:

$$\varphi(\xi) = -\frac{1}{\hbar v} \int V(\xi, y)\, \mathrm{d}y. \tag{1.12}$$

The potential must be specified on the (ξ, y) plane, and complicated geometries as shown in Fig. 1.7 can be considered. It can be shown [1] that as a first approximation the effect of a potential is to reduce the effective slit width; this feature has been observed in various situations [39], a notable example being the C_{60} experiments [12].

We now describe two notable examples of matter-wave interferometers related to the field of gravitational measurements applied to elementary particles and atoms.

1.3.1 The COW experiment

The so-called COW experiment (from the initials of its authors Colella, Overhauser and Werner) was conducted in 1957, and observed interference effects do to the quantum-mechanical phase shift caused by interaction with the gravitational field in a neutron interferometer. Their 1975 paper titled *"Observation of Gravitationally Induced Quantum Interference"* [44] is well known as one of the first works investigating the interface between gravity and quantum mechanics.

The geometry of the apparatus is sketched (simplified to rectangular shape) in Fig. 1.8: a beam of neutrons with a de Broglie wavelength of $\lambda = 1.445$ Å was split (point z_1) in two separate trajectories and then recombined (at point z_3) by means of three thin silicon slabs (yet another different way to realize mirrors and beam splitters). This device was derived from the so-called Bonse-Hart interferometer [45], and could rotate by an angle θ in such a way that the horizontal branches of each trajectory were separated by a gravitational potential difference $\Delta U = m_g^n \Delta z g \sin\theta$, where m_g^n is the neutron gravitational mass. The difference in neutron intensities $\Delta I(\theta)$ at the two output detectors of the interferometer displayed interference fringes as a function of θ [44]. This is an effect of the phase shift $\Delta\phi$ induced by the potential difference. To derive its dependence (for

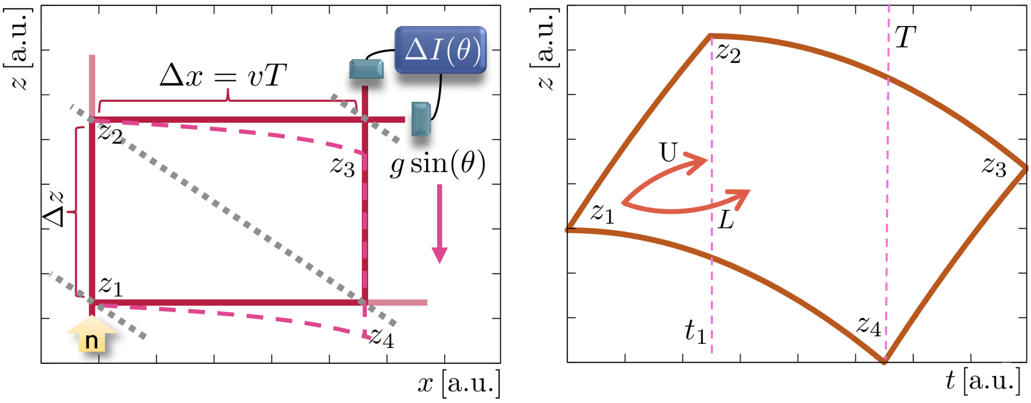

Figure 1.8. Left: sketch of the geometry of the COW experiment[44] in real space. The gray dotted lines represent the silicon crystals, which are acting as beam splitters and mirrors for the neutrons. Right: parabolic motion in the two arms of the interferometer which is used to calculate the phase shift in the presence of gravity. The transit times t_1 and T defined in the picture are relevant for equation (1.14).

our simplified geometry) it is useful to introduce a path integral description [46], which relates the phase shift between two trajectories to the difference of the classical action evaluated along the paths, namely $\hbar\Delta\phi = S^L_{\rm cl} - S^U_{\rm cl}$. The U/L labels refer to the upper and lower trajectories in the $z-t$ diagram of the simplified COW interferometer shown in Fig. 1.8. For a particle in a gravitational potential, the classical action between the points (z_a, t_a) and (z_b, t_b) has the following analytical expression [46]:

$$S_{\rm cl}(z_b, t_b; z_a, t_a) = \frac{m_g}{2}\frac{(z_b - z_a)^2}{t_b - t_a} - \frac{g m_g}{2}(z_b - z_a)(t_b - t_a) - \frac{g^2 m_g}{24}(t_b - t_a)^3. \qquad (1.13)$$

Taking into account that $z_2 - z_1 = z_3 - z_4 = \Delta z$ (see Fig. 1.8) and making the substitution $g \to g\sin\theta$, the final result for the phase shift is:

$$\Delta\phi = \frac{m_g g \sin\theta}{\hbar}\left(\Delta z T + t_1(z_1 - z_4)\right) \approx \frac{m_g g\sin\theta\Delta z T}{\hbar}, \qquad (1.14)$$

where the approximation[3] is justified by $T \gg t_1$ and $\Delta z \gg (z_1 - z_4)$. Manipulating the expression further in terms of the de Broglie wavelength, one obtains:

$$\Delta\phi = \frac{2\pi m_I m_g g\sin\theta\lambda\Delta x\Delta z}{h^2}, \qquad (1.15)$$

which, apart from a difference in numerical factors due to the simplified geometry, captures all the physics of the COW experiment. We remark that the calculated phase shift of quantum-mechanical origin arises from the free propagation of the two trajectories which are subjected to different gravitational potentials. This simple final expression containing both Planck's constant and Newton's constant (through g), indeed places this experiment at the interface between gravity and quantum mechanics.

1.3.2 The Kasevich-Chu interferometer

The so called Kasevich-Chu interferometer, proposed in [47], uses stimulated Raman transitions to manipulate atoms. It is this interaction to play the role of the mirror and beam splitter that we need to build an interferometer.

The working principle of this device can be summarized as follows: alkali atoms are cooled in a magneto-optical trap down to $\approx$ µK temperatures or even lower (in the most recent experiments, Bose Einstein condensates are even used [48]). The atom cloud is then launched upwards in an atomic fountain and *interrogated* with a series of laser pulses, separated by a fairly large time interval (even up to T $\approx$ 1 s). The probability to find the atom in a chosen (e.g. excited) state is then measured by fluorescence. We will sketch a derivation of the dependence of this probability on the phase shift ϕ accumulated during propagation and interaction with the lasers. In particular, in contrast with the COW experiment, in this setup the contribution due to propagation alone cancels out to first order (i.e. if gravity gradients are neglected). The laser-dependent part instead is controlled by the experimenter (in analogy with the movable mirror in a Michelson interferometer), so the experiment can be repeated multiple times and the probability measured to sweep a fringe pattern (see Fig. 1.9). We can derive the phase shift due to the laser within a simple toy model that contains the basic physics. Consider an ideal two-level atom (basis $|g\rangle, |e\rangle$), interacting with an external electric field

---

[3] Note that the same result could also be obtained with a straightforward calculation of the quantum-mechanical phase shift between two free particles (plane waves) propagating for a time T, subjected to a potential difference $\Delta U = m_g g\sin\theta\Delta z$. In the eikonal approximation this reads: $\Delta\phi = \frac{\Delta U T}{\hbar}$.

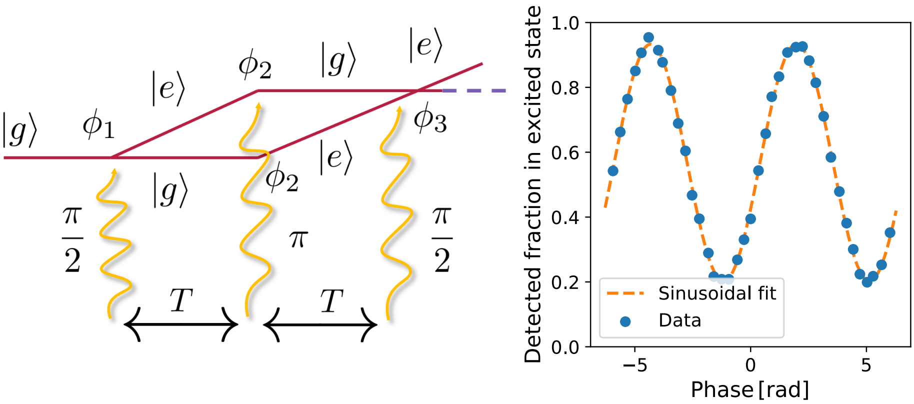

Figure 1.9. Left: sketch of the sequence of laser pulses with their phases ϕ_1, ϕ_2, ϕ_3 in a Kasevich-Chu interferometer. Right: typical fringe pattern as a function of a reference laser phase (see text). The data shown (from [49]) were taken in one minute with pulses separated by $T = 160\,\mathrm{ms}$ and a least squares fit determines g with an uncertainty of $3 \times 10^{-9} g$.

of the form $\mathbf{E} = \mathbf{E_0} \cos(\omega t + \phi)$ representing an excitation laser. Then the interaction Hamiltonian $\hat{H}_I = -\mathbf{d} \cdot \mathbf{E}$ gives rise to the well known phenomenology of Rabi oscillations [50]. Defining the Rabi frequency as $\Omega_r = \mathbf{d} \cdot \mathbf{E}_0 / \hbar$ and the interaction time τ, then two meaningful combinations can be realized:

- $\Omega_r \tau = \pi/2$, usually called a $\pi/2$-*pulse*, the action on the ground state is [49]:

  $$\hat{U}^{\frac{\pi}{2}} |g\rangle \propto |g\rangle - ie^{-i\phi} |e, \hbar k_L\rangle \,.$$

  This is a superposition state, where due to conservation of momentum, the excited state also undergoes a momentum kick $\hbar k_L$ depending on the laser wave number k_L. Therefore the two parts of the wave packet propagate trough different paths in space. For this reason, this is also aptly named a *beam splitter pulse*.

- $\Omega_r \tau = \pi$, usually called a π-*pulse*, acting on the ground state as [49]:

  $$\hat{U}^{\pi} |g\rangle \propto -ie^{-i\phi} |e, \hbar k_L\rangle \,.$$

  The result is a population reversal, with the same momentum kick and, as before, the laser phase is imprinted on the wave function of the state. This is usually called the *mirror pulse*.

In the Kasevich-Chu interferometer, three of such pulses separated by a time interval T are combined in the so called "$\pi/2 - \pi - \pi/2$" sequence, which acts on the ground state as follows:

$$|g\rangle \to \hat{U}^{\frac{\pi}{2}} \hat{U}^{\pi} \hat{U}^{\frac{\pi}{2}} |g\rangle = -\frac{i}{2} \left(e^{-i\phi_2} + e^{i(\phi_2 - \phi_1 - \phi_3)} \right) |e\rangle + (\cdots) |g\rangle$$

where the phase of the tree laser pulses are labelled as $\phi_{1,2,3}$. The probability of finding the atom in the excited state is easily obtained

$$P_e = \frac{1}{2} \left[1 - \cos(\Delta\phi) \right]$$

with $\Delta\phi \equiv \phi_1 + 2\phi_2 + \phi_3$. The pulse sequence suggests a schematic representation as shown in Fig. 1.9 on the left hand side. The phase shift $\Delta\phi$ can be controlled (all the experimental details are outside the scope of this work), producing the *fringe* pattern in probability shown in Fig. 1.9 as predicted by the equation above. If one compares Fig. 1.9 with Fig. 1.1, the conceptual analogy is pretty striking.

One of the most important applications of this interferometer is as a *gravimeter*. Our sketchy derivation can be made more precise by accounting for the presence of gravity, which determines the exact trajectory of the atoms, therefore the position at which they interact with the laser pulse, and in turn the correct value of the overall phases $\phi_{1,2,3}$. The resulting phase shift in the presence of constant and uniform gravity is [49]:

$$\Delta\phi = \Delta\phi_{\text{las}} + \cancel{\Delta\phi_{\text{prop}}} = k_L g T^2 + \phi_1^0 - 2\phi_2^0 + \phi_3^0 \tag{1.16}$$

The parameters ϕ_i^0 are constant phase factors that can be controlled experimentally. Without going into the details, we want to stress that the total phase shift expressed in equation (1.16) has in principle two contributions: the laser phase shift $\Delta\phi_{\text{las}}$ which gains the additional $k_L g T^2$ term, and the phase shift due to propagation $\Delta\phi_{\text{prop}}$. The latter can be evaluated in a path integral approach as outlined for the COW experiment [46], but is exactly zero for this "atomic fountain" configuration. A nonzero contribution emerges when gravity gradients are accounted for (which is necessary for very precise measurements). This point highlights the different physical origin of the interference effects with respect to the COW experiment. In the Kasevich-Chu interferometer the position of atoms as they fall is imprinted into the phases of their wave functions by the laser interactions; the sequence of pulses is constructed so that a measurement of these phase differences yields experimental access to g [49]. In a certain sense it is reminiscent of how a classical "falling corner cube" gravimeter [51] measures the position of an object as it falls at three instants of time separated by an interval T to obtain a measurement of g.

There are several techniques to exploit the phase shift dependence on g to realize an absolute gravimeter[49]. The sensitivity scales quadratically with the time interval. To this date, atom interferometers are the benchmark for absolute gravimetry of atoms, reaching a level of precision better than $\sigma_g/g = 10^{-9}$ on Cs atoms [52], with proposed experiments set to reach the 10^{-15} level [53, 54]. This capability can be useful both for applied physics (geodesy, for instance [55]) and fundamental research. Two different atomic species can be run trough the same atomic fountain at the same time, to perform a differential g mesurement. This is a test of the weak equivalence principle of General Relativity. The relevance of such measurements from a theoretical point of view will be discussed in the next chapter.

To conclude this section we stress that, although this technique is the current benchmark for accuracy on absolute and differential g measurements, it is not easily adapted to exotic systems such as positronium, nor it is particularly advantageous; mainly because the g-dependent sensitivity scales as the square of the "interaction time" just like the Talbot-Lau interferometer, so the extremely short lifetime of positronium ($\tau_{\text{Ps}} = 142\,\text{ns}$ for the longest lived spin triplet ground state) remains the main limit for the measurement precision. Furthermore, the Kasevich-Chu interferometer is so accurate as a consequence of the high degree of control that current technology can provide on alkali atoms. It is not yet feasible, to the best of our knowledge, to produce an ultra cold (sub-µK) cloud of positronium, neither it is easy to perform coherent and carefully controlled laser excitation to long-live states with properties comparable to the ones of alkali atoms.

CHAPTER 2

Motivation

This chapter illustrates the motivation for pursuing the goals set forth in the QUPLAS project, and discusses their relevance in the present state of the art.

2.1 The three phases of QUPLAS

As mentioned in the introduction, QUPLAS foresees three consecutive stages of increasing sophistication, each one targeting an intermediate goal which is instrumental for the completion of the subsequent step.

1. **QUPLAS-0**: observation of matter wave interference of positrons (e^+) in a Talbot-Lau interferometer. The result can be compared with an electron beam in the same apparatus with almost identical experimental conditions. Direct detection of the interference pattern will be carried out with high-resolution nuclear emulsions.

2. **QUPLAS-I**: observation of matter wave interference of positronium (Ps), again in a Talbot-Lau configuration. This can give experimental access to several properties of this peculiar system.

3. **QUPLAS-II**: measurement of the gravitational acceleration g_{Ps} of Rydberg excited (high principal quantun number n) Ps atoms, using inertial sensing techniques based on Talbot-Lau interferometry.

The three main goals are a concise description of *what* QUPLAS aims to achieve. The following sections aim to explain *why* these goals are relevant and interesting to pursue.

2.2 Testing the Weak Equivalence Principle on antimatter

We start this discussion from the final and most ambitious phase of QUPLAS, which fits into the wide field of research that probes our current understanding of gravitation, namely General Relativity, in a low energy regime. Low energy means targeting systems on a small (non cosmological) scale such as atoms, in the gravitational field of the Earth. We will focus on the general theoretical framework that is the motivation for this research and thus for the QUPLAS project.

2.2.1 General relativity and the Einstein Equivalence Principle (EEP)

General relativity (GR) is commonly accepted as the current description of gravitation in modern physics. It is based on a consistent mathematical formalism and provides a satisfactory description of most of the observed phenomenology: from the so called *classical tests of general relativity*[1], proposed by Einstein [58] in 1916, to the recent direct detection of gravitational waves [59].

Nevertheless, there are still sufficiently strong reasons to question the validity of GR as the most fundamental theory of gravity, and to motivate the search for hints of physics beyond GR:

- General relativity is a classical (as in *non quantum*) theory, difficult to reconcile with quantum field theory.
- Dark energy and dark matter.

These are widely believed to be among the most pressing "unsolved problems" in modern physics. According to the currently accepted ΛCDM cosmological model and the most recent experimental data [60], the Universe contains only 4.9% baryonic matter, while the bulk is 26.8% dark matter, 68.3% dark energy and a small amount of neutrinos and photons. Although the model gives an accurate account of many observed properties of the cosmos, such as the features of the cosmic microwave background radiation, the data we mentioned suggest that some modifications or extensions are needed, either in the standard model of particle physics, or in our understanding of gravity.

Atom interferometry is a useful (and very precise) tool to search for deviations from the predictions of GR. In particular we focus on tests for violations of the so-called weak equivalence principle, which will be formally defined shortly.

General Relativity belongs to the class of *metric theories* of gravitation. Following Will [61], these theories are characterized by the following defining features:

i Spacetime is endowed with a metric tensor $g_{\mu\nu}$

ii The world lines of test bodies are geodesics of the metric

iii In local freely falling frames the laws of physics are those of special relativity

Loosely speaking, these features correspond to a description of gravity as a *geometrical* phenomenon: knowledge of spacetime geometry allows to predict the motion of all bodies. Gravity is in this sense *universal*: in the language of field theories it couples with the same strength to all forms of matter, there is no such thing as a *gravitational charge*. Different theories can be constructed starting from these principles, for example by postulating different equations of motion for the metric. The Einstein equations [62] $G_{\mu\nu} = 8\pi T_{\mu\nu}$, are a particular choice giving rise to general relativity, but other theories also exist (such as the so called Brans-Dicke theory [63]).

---

[1] The precession of the perihelion in Mercury's orbit, the deflection of light by the sun, and the gravitational redshift of light. Only the anomaly in the speed of Mercury's precession was known at the time, and GR theory correctly justifies it. The latter two were predictions, whose experimental confirmation [56, 57] contributed to establish GR as the mainstream theory of gravitation.

It can be proven that metric theories of gravity satisfy the **Einstein Equivalence Principle** [61] (**EEP**), which can be stated in terms of these three sub-principles:

- **Weak equivalence principle (WEP) or Universality of free Fall (UFF)**: if an uncharged test body is placed at a given point in spacetime, and given an initial velocity there, its trajectory will be independent of its internal structure and composition.
- **Local position invariance (LPI)**: the outcome of any local non-gravitational experiment is independent of the location in space-time where it is performed.
- **Local lorentz invariance (LLI)**: the outcome of any local non-gravitational experiment is independent of the velocity of the (freely falling) apparatus.

The so called *Shiff's conjecture* [61] states that a violation of any one of the three sub-principles implies a violation of the other two. This has not been proven with mathematical rigour, but several arguments can be made in favour of this hypothesis. The main point is that the validity of all three principles holds in any metric theory of gravity (according to the above definition), including general relativity. Therefore, irrespective of the validity of Shiff's conjecture, a violation of the WEP undermines the very foundation of General relativity as a geometrical theory of gravity, implying that the correct description cannot be in the form of a metric theory. In this sense we can say that testing the WEP is more fundamental than testing the phenomenology that is predicted by the Einstein equations. A modification of the Einstein equations within the same framework would not be sufficient to produce a WEP violating theory of gravity. The same reasoning applies to the other sub-principles, which motivates for instance the search of Lorentz invariance violations in ultra-high-energy cosmic rays [64, 65].

Although there are theories which predict a violation of the WEP in certain systems[2], it is generally impossible to produce a quantitative estimate of the level at which the violation should occur. Therefore the current approach guiding the experiments is to search for violations on a large class of systems (recall that WEP states the *universality* of free fall), and to use the results to put increasingly strict bounds on WEP violating parameters. As an example, a simple parametrization used in the literature [61, 67] assumes that the motion of a test body in a gravitational field $U(x)$ (we can assume one dimensional motion for simplicity) is governed by the following *non-newtonian* Lagrangian[3]:

$$\mathcal{L} = -m_0 c^2 + \frac{1}{2} m_0 v^2 - (m_0 + \delta m_p^U) U(x),$$

where m_0 is the total mass including binding energy for composite objects. The parameter δm_p^U is called *passive anomalous gravitational mass*, and arises from an hypothetical anomalous coupling between the test body and the source of the gravitational field. Therefore it depends on both the nature of the body (if composite, from the interactions contributing to its binding energy) and from the source of the gravitational field. The superscript U is added to remind this dependence. Different combinations of sources and test bodies thus put constraints on independent parameters. The equations of motion following from $\mathcal{L}$ read:

$$\frac{d^2 x}{dt^2} = \left(1 + \frac{\delta m_p^U}{m_0}\right) \frac{dU(x)}{dx},$$

---

[2] For a recent overview of this topic, see [66].

[3] We consider a minimal toy model starting from the general formulation [61], sufficient to capture the meaning of the WEP violating parameters.

defining $\beta^U = \frac{\delta m_p^U}{m_0}$, and assuming the source to be the approximate gravitational field on the surface of the Earth (the potential is of the form $U(x) = g_0 x$), then

$$\frac{d^2x}{dt^2} = \left(1 + \beta^{\text{Earth}}\right) g_0.$$

This is clearly a WEP violating result, since different bodies having a different β parameter fall at a different rate. Differential acceleration measurements between two objects labelled X and Y can then be performed to put bounds on the combination

$$\eta_{X,Y}^{\text{Earth}} = 2\frac{\beta_X^{\text{Earth}} - \beta_Y^{\text{Earth}}}{\beta_X^{\text{Earth}} + \beta_Y^{\text{Earth}}}$$

which is essentially the so-called Eötvös parameter. In Table 2.1, we summarize some of the current experimental bounds on the violation of the WEP, with different techniques. The first two experiments, employing macroscopic test masses, are still the most precise. In the future dual species atom interferometers are expected to surpass them and reach the level of 10^{-15} [54]. However, in light of our discussion it is not particularly meaningful to compare these results in terms of accuracy, since they are actually measuring different parameters by testing different species. Objects to be compared are therefore usually chosen following some rationale, for example the dual species test on ^{88}Sr/^{87}Sr atoms aims to constrain possible anomalous coupling of gravity with spin, by comparing isotopes of different total spin (spin-zero boson vs. fermion).

Technique	**Species compared**	**Result or goal for** $\eta_{X,Y}$
Torsion balance [68]	Be/Ti test masses	$(0.3 \pm 1.8) \times 10^{-13}$
Lunar laser ranging [69]	Earth/Moon in the field of the Sun	$(-0.8 \pm 1.8) \times 10^{-13}$
Atom interferometry (AI) [70]	Cs atoms/falling Corner Cube (CC)	$(7 \pm 7) \times 10^{-9}$
Dual species AI [71]	^{88}Sr/^{87}Sr atoms (boson vs. fermion)	$(0.2 \pm 1.6) \times 10^{-7}$
Moiré deflectometer [6, 72] (AEGIS)	Antihydrogen ($\overline{H}$)/CC	10^{-2} (goal)
Talbot-Lau interferometer (QUPLAS)	Positronium/CC	10^{-1}-10^{-2} (goal)

Table 2.1. Comparison of selected (proposed and already performed) experimental tests of the WEP. The techniques mentioned are all ground based, with several space-based atom interferometry experiments to be launched in the near future [73, 74]. In terms of our parametrization, all experiments measure $\eta_{X,Y}^{\text{Earth}}$, except the Lunar laser ranging experiment. The latter is a measurement of the differential acceleration of the Earth and the Moon freely falling in the field of the Sun (measuring $\eta_{\text{Moon,Earth}}^{\text{Sun}}$). The *falling Corner Cube* refers to the moving mirror freely falling in a classical gravimeter such as the FG5-x [51]. The last two experiments, including the present project are proposed tests on antimatter.

WEP tests on antimatter

The AEGIS experiment mentioned in Table 2.1 was designed to search for WEP violations on antihydrogen atoms at the level of 10^{-2} [6, 72] using beam based techniques (a moiré deflectometer). There is a striking difference of 7 orders of magnitudes with respect to the most precise test performed to date on individual Caesium atoms [70]. As we mentioned in concluding section 1.3.2, the precise techniques of atom interferometry cannot be applied on systems like $\overline{H}$ and positronium, although advancements in this directions have been made[4]. The unique experimental challenges posed by exotic atoms will be apparent in the following chapters, and suggest a distinction between two different philosophies: on the one hand one can rely on objects that can be controlled very well and reach ever increasing accuracy; on the other hand one can probe exotic systems where there are stronger reasons to believe that unusual physics might be at play.

Are there reasons to believe that antimatter might violate the WEP? The issue is controversial. For an historical overview summarizing the main arguments against "antigravity", the idea that matter and antimatter could have a repulsive gravitational interaction, see [77]. A more recent paper [78] argued that antigravity follows naturally when the CPT theorem is applied to general relativity. This conclusion has later been challenged on theoretical grounds [79]. A suggestive cosmological model, known as *Dirac-Milne* cosmology [80], by assuming antigravity as a postulate, gives an elegant solution to two well known problems of the ΛCDM cosmological model (known as the *horizon problem* and the *cosmic age problem*).

In summary, the debate cannot be settled until sufficient experimental evidence has been collected. Currently the most stringent bound comes from the ALPHA Antihydrogen experiment [7], that loosely constrains the gravitational to inertial mass ratio for $\overline{H}$ to the range $-65 < m_g/m_i < 110$. This result still does not rule out antigravity, and would be substantially bettered by the foreseen 10^{-2} level measurements.

The search for WEP violations in positronium has already been proposed in the past [81, 82]. This section should have clarified the importance of testing the WEP on a variety of systems, and the main reasons why the proposed Ps measurement well complements the ongoing efforts on $\overline{H}$ are:

- It would still be able to rule out "antigravity", by measuring $g_{\mathrm{Ps}} \neq 0$.
- It can put constraints on WEP violation parameters (δm_p) on a purely leptonic system, bound by the electromagnetic interaction only.

2.3 Developing new techniques in matter wave-interferometry

We recall that matter-wave interference (in any shape or form) has been observed on a broad range of objects, initially elementary particles [9, 10, 11], and recently on composite objects up to the size of large molecules [83] which require a variety of different techniques. It will become clear in the next chapter that tackling the measurement of g_{Ps} requires improvements in several technical items which are at the forefront of current research. Therefore, the first two phases of QUPLAS are instrumental in developing such techniques, contributing with new solutions to an already rich state of the art.

Several interesting studies of fundamental interest could also be carried out on exotic antimatter systems like Ps. We summarize schematically the main points of interest, beyond the gravitational measurement, that motivate the efforts on Ps interferometry experiments.

---

[4] For example, the Alpha collaboration at CERN succeeded in trapping $\overline{H}$ for the first time [75] and recently paved the way for precision spectroscopy of antihydrogen [76].

2.3.1 QUPLAS-0 and positron interferometry

- Matter wave interference on elementary antimatter has not been observed yet, and in our apparatus we have the possibility to compare in the same conditions positrons with electrons. The CPT theorem [84] establishes the equality of the e^+/e^- masses, which has been tested to very high precision (10^{-8} level [85]) in Ps spectroscopy experiments. However, recalling the de Broglie relation $\lambda = \frac{h}{mv}$ the question if $\lambda = \overline{\lambda}$, while not competitive as a test of the equality of the masses can still be interesting to answer; at least interpreted as the search for any possible difference between e^+/e^- interferometric patterns.

- A potential source of discrepancies could arise from the interaction with the gratings. Interaction with material gratings for electrons has been a subject of several studies [38] and could be further investigated for positrons.

- The theory of matter-wave interference experiments is grounded in non-relativistic quantum mechanics, and most experimental work involved low energy electrons (up to $5\,\mathrm{keV}$ [27]) or atomic beams travelling at an even lower speed. At $20\,\mathrm{keV}$ relativistic effects start to be non-negligible. The minimal modification required is a correction to the de Broglie wavelength to account for the relativistic momentum. In terms of the kinetic energy it reads:

  $$\lambda_{\mathrm{rel}} = \frac{h}{\sqrt{2mE_k}} \left[1 + \frac{E_k}{2mc^2}\right]^{-\frac{1}{2}} . \tag{2.1}$$

  It is worthy of investigation whether this correction to the wavelength is sufficient to describe the observed patterns with the usual theoretical models, which are based on the non-relativistic Schrödinger equation, or if more profound changes are required.

- We propose a novel asymmetric Talbot-Lau configuration (Part II), and the use of nuclear emulsion detectors (Part III). By virtue of its unmatched position resolution this detector allows direct detection of micrometric fringe patterns. The synergy of high position resolution and a careful theoretical modeling of the beam could prove useful to extract more detailed information from the detected pattern in comparison to detectors based on moving grating masks [86].

2.3.2 QUPLAS-I and positronium interferometry

- Positronium interference has never been observed so far, and grating-based interferometers can be useful to investigate several properties of this exotic system.

- For instance, with the possibility to excite Rydberg states, studies on the transmission of such states by mechanical apertures [87] could be improved. The impact of finite "classical" size of the Rydberg atoms on the interference pattern could be studied.

- Atomic properties can be measured accurately in grating interferometers. The most precise determination of the ground-state polarizability of caesium and rubidium was recently performed with a three-nanograting Mach-Zehnder interferometer [88].

- Being very light, positronium could be an interesting probe for the physics of decoherence (for instance by experimentally controlling the vacuum pressure to tune the coupling strength with the environment [89]).

Positronium interferometry requires the development of several techniques, which could also be useful for other applications and experiments. An overview of the required advancements is discussed in the next chapter.

CHAPTER 3

Towards positronium interferometry

This chapter contains an overview of the main ideas behind the QUPLAS-I and QUPLAS-II phases of the experiment. I was involved in the development of these ideas, and also performed a preliminary study on the motion of positronium in magnetic and electric fields. This is of interest for several stages of the experiment. The main focus of this thesis is on QUPLAS-0, therefore these results are postponed to appendix A to keep the presentation more compact. Furthermore, we stress that this chapter does not aim to provide a quantitative feasibility study of the advanced QUPLAS phases, but rather to introduce the reader to the main challenges involved and discuss possible solutions.

The L-NESS positron beam

The positron beam operating at the L-NESS laboratory [4], shown in Fig. 3.1, is the main building block of all QUPLAS phases. It exploits a ^{22}Na source (activity at the time of writing is approximately $5\,\mathrm{mCi}$). High-energy positrons from β decay (end-point energy is approximately $540\,\mathrm{keV}$) are moderated by a monocrystalline tungsten film, from which thermalized positrons are emitted with a small energy ($\approx 3\,\mathrm{eV}$) related to the work function of the material. Moderated e^+ are then electrostatically accelerated and guided trough a $90°$ bend which filters out the unwanted residual high-energy component (the purpose of the bend is also to allow more effective shielding against the γ background from the source). Positron energy can be tuned in the $0.1 - 20\,\mathrm{keV}$ range and the beam

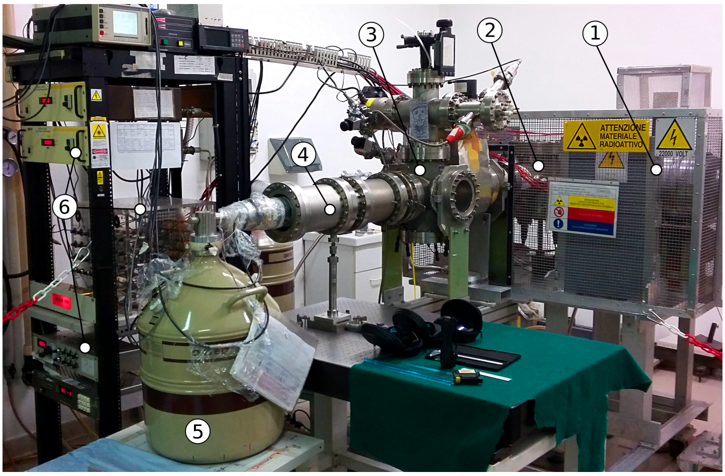

Figure 3.1. Positron beam facility at the L-NESS laboratory [4]. Labelled parts are: 1. ^{22}Na radioactive source and moderator inside lead shielding; 2. Electrostatic optics and 90° bend; 3. Main experimental chamber; 4. Extended chamber with mu metal shielding, housing the interferometer; 5. High purity germanium detector (HpGe); 6. Power supply and beam control electronics.

is highly monochromatic ($\sigma_E/E \ll 1\%$, limited mainly by the stability of the associated electronics). The typical positron flux is at the level of 10^3 to $10^4\,\mathrm{s}^{-1}$.

The L-NESS beam is a low intensity continuous beam, thus well suited to perform true single-particle matter-wave interference experiments. The electrostatic optics also ensures the required stability for fairly long measurements (on the time scale of one week), which are routinely performed at L-NESS [4].

Main challenges in positronium interferometry

A sketch of the foreseen QUPLAS-I/II setup is shown in Fig. 3.2 for positronium interferometry and, possibly, gravity measurements. In the following the main steps involved are described:

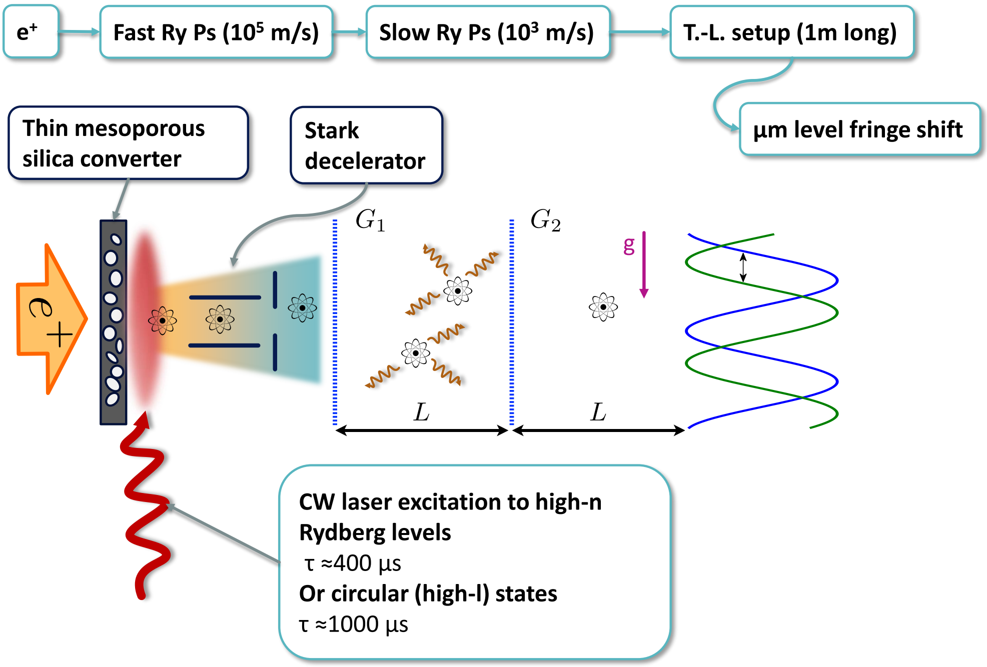
e⁺
Fast Ry Ps (10^5 m/s)
Slow Ry Ps (10^3 m/s)
T.-L. setup (1m long)
µm level fringe shift
Thin mesoporous silica converter
Stark decelerator
G_1
G_2
g
e^+
L
L
CW laser excitation to high-n Rydberg levels
τ ≈400 µs
Or circular (high-l) states
τ ≈1000 µs

Figure 3.2. Sketch of the foreseen setup to perform positronium interferometry (QUPLAS-I) and possibly gravity measurements (QUPLAS-II). Details are discussed in the text.

Positronium production is achieved by implanting positrons in a suitable *converter* material, typically made of porous materials such as silica, with a variety of different structures [90, 91, 92]. For interferometry a beam of particles with a well defined direction is needed, and many efforts are ongoing in the community to reach this goal. A relevant step in this direction could be the development of transmission-mode conversion targets [93]: samples sufficiently thin to allow the escape of positronium atoms in the downstream direction, possibly with smaller angular spread compared to typical reflection-mode targets. Recent advances have been made [91, 92]: in particular conversion effi-

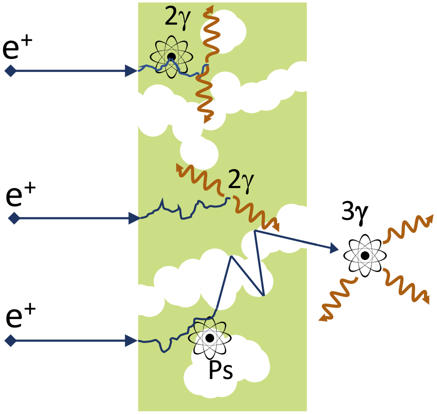

Figure 3.3. Scketch of the process of positronium formation and emission in vacuum in mesoporous materials. The implanted positrons can form positronium after stripping an electron from the material as they scatter inside it. If a long lived ortho-Ps state is formed, it can escape in vacuum through the open pore network. Pores have a typical average diameter of several nanometres. Annihilation of the positron to 2γ can also occur with an electron from the material either before of after Ps formation. The latter process is called pick-off annihilation.

ciencies of the order of 10% for atoms forward-emitted with an angle smaller than $50°$ has been demonstrated [91]. Promising transmission targets (called ”3D silica”) have also been realized in the framework of our collaboration [94]. Ps atoms are typically emitted from mesoporous targets with a high average velocity of the order of 10^4 to 10^5 m/s and a broad Maxwell-Boltzmann type distribution.

Laser excitation of Ps atoms to Rydberg levels might also be required to extend the lifetime of positronium to match the intended time-of-flight through the interferometer [95, 96]. The lifetime of Rydberg states scales with the principal and orbital quantum numbers approximately as n^3l^2 [97]. For reference an $n = 65, l = 2$ state has a lifetime of $\tau \approx 290\,\mu\text{s}$ (see Fig. 3.4). A viable continuous-wave laser system consists of two tunable Ti:Sa units, both pumped by the 2nd harmonic of a $1064\,\text{nm}$ Nd:YAG. A first $1.5\,\text{W}$ Ti:Sa system will operate at $972\,\text{nm}$, to generate, upon quadruplication, approximately $300\,\mu\text{W}$ of $243\,\text{nm}$ radiation driving the $1 \to 2$ transition. The second Ti:Sa laser will generate up to approximately $4\,\text{W}$ of $\approx 730\,\text{nm}$ light, to excite the transition to Rydberg states, up to $n = 70 - 90$.

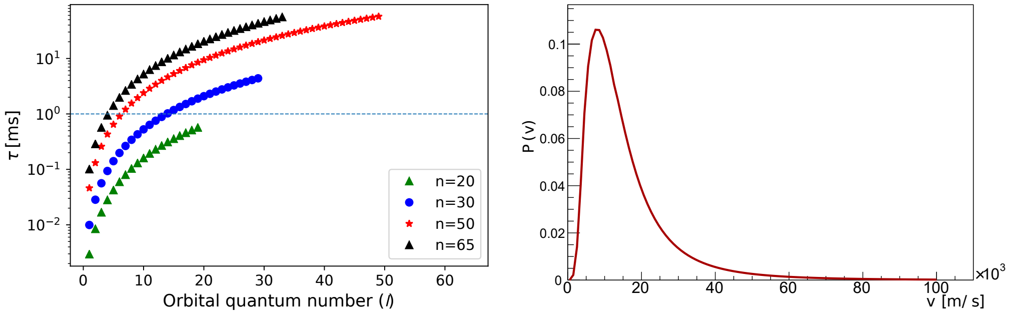

Figure 3.4. Left: lifetime of Rydberg levels as a function of l for representative choices of the principal quantum number n; the dotted line at $\tau = 1\,\text{ms}$ is added to guide the eye and represents the ideal goal for gravity measurements. Right: preliminary simulation of the expected excitation probability as a function of Ps velocity with realistic laser parameters.

This excitation scheme, applied to a continuous Ps beam, can also provide velocity selection: the distance of the laser spot from the Ps production target can be tuned so that a sizeable fraction of atoms (below a certain speed threshold) decays before reaching the excitation region. On the other hand, laser intensity can be selected so that fast atoms will have an interaction time too short for efficient excitation. I performed a proof-of-concept simulation of this principle, using a Bloch equations approach with realistic spectral features, adapting a model of laser phase noise from [98]. An example of the velocity-dependent excitation probability is shown in Fig. 3.4. In particular the $n = 20$ case is reported, with an elliptical Gaussian laser spot of $200\,\mu\mathrm{m} \times 20\,\mu\mathrm{m}$ located $1\,\mathrm{mm}$ after the converter; the applied power was set to $360\,\mu\mathrm{W}$ and $270\,\mathrm{mW}$ for the $1 \rightarrow 2$ and $2 \rightarrow n$ transitions respectively. Very high-n states are very fragile and sensitive to stray fields (consider that the polarizability scales as n^7 [97]). This drives the ongoing effort towards the development of techniques for the excitation of the so called *circular states* (high-l) states. This likely requires the addition of a microwave excitation system, as demonstrated experimentally on Na atoms [99] and Hydrogen atoms [100]. To the best of our knowledge, the technique has not yet been implemented on positronium.

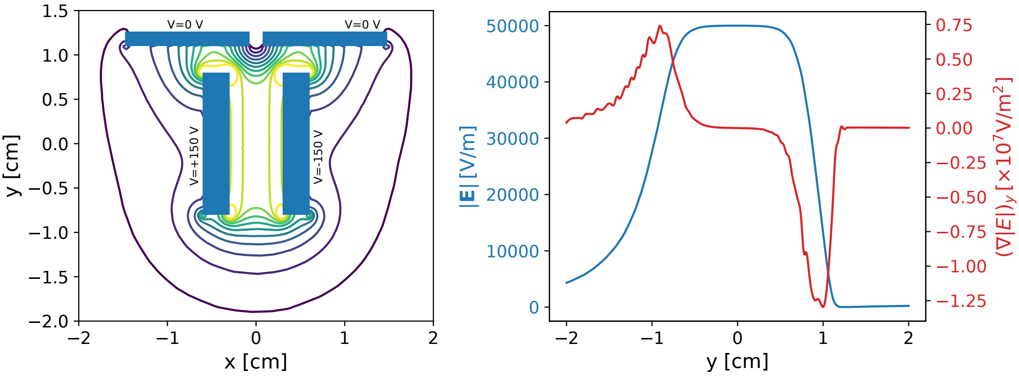

Figure 3.5. Left: stark decelerator suitable for Ps, with the same geometry proposed in [101] (the numerical simulation was performed independently using the *maxFEM* software [102]); contour lines for $|\mathbf{E}|$ are shown. Right: plot of $|\mathbf{E}|$ and of the y-component of $\nabla|\mathbf{E}| \propto \mathbf{F}$ along the y-axis. Rydberg-Stark states should be produced inside the decelerator (in the constant field region) and decelerated by the strong gradient near the gap between the two top electrodes.

A cold positronium beam, with an average speed down to approximately $10^3\ \mathrm{m/s}$ could be required for the gravity measurement, in order to maximize the transit time T for a given interferometer length (we recall that in Talbot-Lau based gravimeters, the fringe displacement due to gravity is proportional to gT^2). Rydberg atoms have high polarizability and can be manipulated by means of the Stark effect. An inhomogeneous electric field $\mathbf{E}$ will exert a force on the atom $\mathbf{F} \propto \nabla|\mathbf{E}|$. Stark decelerators based on time-indepentend electric fields (thus suited for continuous beams) have been demonstrated for hydrogen atoms [101] and are capable of accelerations of the order of $10^8\mathrm{m\,s^{-2}}$. Lighter positronium atoms are even easier to accelerate; preliminary simulations suggest that it is possible to decelerate $10^4\ \mathrm{m/s}$ Ps down to $10^3\ \mathrm{m/s}$ in a few centimetres long setup like the one shown in Fig. 3.5. The implementation of such a device is correlated with the laser excitation. The landscape of accessible states is changed in an external field (to the so called Rydberg-Stark states [103]). States with a well-defined combination of quantum numbers have to be selectively excited so that they can be coherently

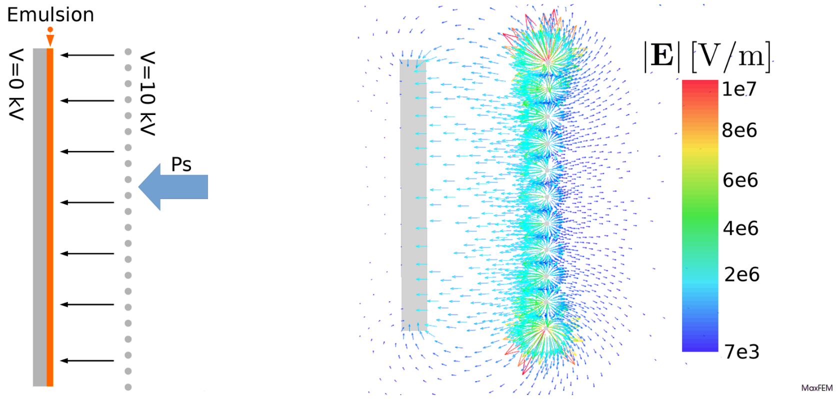

Figure 3.6. On the left, sketch of the geometry of a wire-based ionization detector coupled with emulsion films. On the right, a proof-of-concept simulation of the electric field in such a configuration. Wires $0.1\,\mathrm{mm}$ in diameter are separated by $1\,\mathrm{mm}$ and located at a distance of $5\,\mathrm{mm}$ from the planar electrode. The potential difference is set to $10\,\mathrm{kV}$.

decelerated [104]. More details on the motion of Rydberg states in field gradients are reported in Appendix A, for an extensive review of Stark deceleration techniques see [103].

A suitable Talbot-Lau setup has to be devised for the intended application. At a speed of $10^5\,\mathrm{m/s}$ ground state ortho-Ps ($\tau \approx 142\,\mathrm{ns}$) can survive a few centimetres, and its de Broglie wavelength is approximately $\lambda = 3.6\,\mathrm{nm}$. A short Talbot-Lau setup can therefore be built using $d \approx 10\,\mathrm{\mu m}$ material gratings (Talbot length $\approx 2.7\,\mathrm{cm}$). This could constitute a viable QUPLAS-I setup to perform the range of studies suggested in 2.3.2. For the proposed QUPLAS-II gravity measurements, the inertial sensitivity of a candidate $1\,\mathrm{m}$ long Talbot-Lau setup will be thoroughly discussed in section 4.2. This order of magnitude in total length is arguably the best compromise between a sizeable fringe displacement in the $\mathrm{\mu m}$ range (scaling quadratically with the time of flight) and the loss of intensity suffered by a slow Rydberg Ps beam ($v \approx 10^3\,\mathrm{m/s}$) excited to $\tau \approx 10^2\,\mathrm{\mu s}$ lifetimes. This setup would require a grating periodicity of approximately $400\,\mathrm{\mu m}$. Depending on the Rydberg states employed (circular or very high-n), the feasibility of interferometry with material diffraction gratings has to be evaluated carefully: although the slit width will still be larger than the (classical) size Rydberg Ps, and there are models suited for strong interaction regimes[105], the C_3 coefficient of van der Waals interaction for Rydberg Ps can be several orders of magnitude higher than in the ground state. This suggests to consider laser-produced *light gratings* based on the so called Kapitza-Dirac effect [106, 107, 108], that have been developed specifically for highly-polarizable molecules [109].

Detection of the interference pattern is a challenge even if the periodicity of the interference pattern could be in the $10\,\mathrm{\mu m}$ range for QUPLAS-I and approach $10^2\,\mathrm{\mu m}$ for the gravity measurement. Being neutral objects with sub-eV kinetic energy, Ps atoms cannot be observed directly with nuclear emulsions even for $v > 10^5\,\mathrm{m/s}$. A possibility that is being investigated is to supplement the emulsion detector with an electric field that ionizes Ps and accelerates the positrons (or electrons) at a few keV towards the emulsion surface. A geometry as sketched in Fig. 3.6 could be devised, with electrode wires long enough to ensure that there is negligible field gradient in a preferred direc-

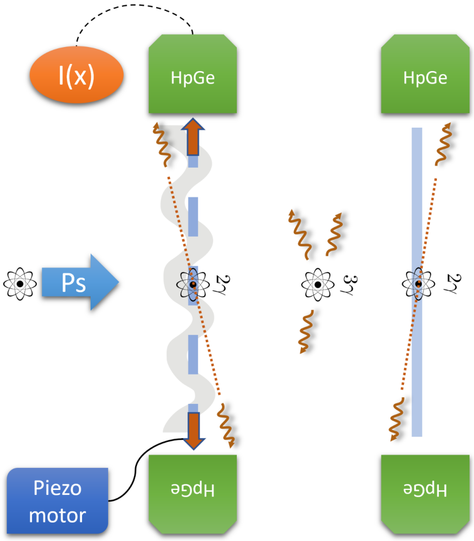

Figure 3.7. Principle of moving mask detection: a grating mask with the same periodicity is placed on the plane where interference fringes are expected. The mask must be moved with a linear piezo motor, and the intensity $I(x)$ of transmitted (or stopped) is monitored as a function of mask position x. The output of several detectors can be combined with standard time or time/energy coincidence methods to improve the signal-to-noise ratio. Annihilations to two photons on the mask or on a target placed downstream, as well as three-photon decays in flight can be exploited.

tion. The detector can then be oriented to provide the best resolution in the direction where interference effects takes place. The field gradient should be fine-tuned for the target Rydberg levels, to ensure that the majority of ionization events occur well inside the region of approximately uniform electric field. Additional details on the calculation of ionization lifetimes for high-n Rydberg states in strong electric fields are discussed in Appendix A. An alternative approach exploits the more conventional grating mask method and is sketched in Fig. 3.7. The mask allows to recover the contrast of the original fringe pattern as a modulation of the intensity of transmitted (or stopped) atoms as a function of mask position. This scheme is very flexible and allows to consider several different signals, depending on the geometry of the setup. For instance the direct annihilation on the mask can be monitored with one (or more) pairs of HpGe detectors in time coincidence for the two $511\,\mathrm{keV}$ back-to-back photons. Unless a detector with a very small opening is employed to suppress (geometrically) any signal from annihilations on the other two gratings, this configuration is better suited for Talbot-Lau layouts longer than a few cm. Annihilations on a fixed target placed at a certain distance after the mask can also be used. Detection of the three coincident photons with $E < 511\,\mathrm{keV}$ from in-flight decays (with a larger array of detectors) is also viable. Accurate simulations should be conducted, but the high energy resolution of HpGe detectors coupled with standard time coincidence methods should ensure a very high signal-to-noise ratio.

Detection of the gravity-induced fringe shift $\Delta x \propto gT^2$ requires sensitivity to relative displacements $\Delta x/d_3$ of the order of 1% or less, d_3 being the fringe period. Furthermore, how to establish the reference "$g = 0$" position is not trivial and could require a form of very precise geometrical alignment between the two gratings and the mask, or to perform a Talbot-Lau interference experiment with light on the same setup. A peculiar advantage of slow positronium is that its de Broglie wavelength is in the visible range ($\lambda = 454\,\mathrm{nm}$ at $v = 800\,\mathrm{m/s}$), therefore a reference laser could be used in the same setup.

A high intensity e^+ **beam** is needed for gravity measurements, due to the many processes with finite efficiency involved in the experimental chain, from Ps production to pattern detection. A realistic order-of-magnitude estimate can be attempted. For reference we now estimate the required positron flux to obtain a $\frac{\sigma_g}{g} = 10\%$ level measurement of g in one day of data taking. The main ingredient is the formula for the inertial sensitivity that will be derived in section 4, and reads:

$$\frac{\sigma_g}{g} = \frac{1}{\sqrt{N}} \frac{1}{2\pi C \, \Delta x / d_3},$$

where C is the contrast of the pattern and N is the integrated flux at the detector. We can define this quantity in terms of the integration time $T_{\text{meas}} = 86\,400\,\text{s}$, an initial positron flux η_0 and a total efficiency ϵ_{tot}, namely $N = \eta_0 \epsilon_{\text{TOT}} T_{\text{meas}}$. The total efficiency is the product of several factors that we estimate as follows: conversion efficiency $\epsilon_{\text{conv}} \approx 0.1$, Rydberg excitation efficiency $\epsilon_{\text{exc}} \approx 0.1$, deceleration and velocity selection $\epsilon_{\text{vel}} \approx 0.1$, geometrical losses (collimation of the formed beam) $\epsilon_{\text{coll}} \approx 0.01$, transmission of the two gratings $\epsilon_{\text{transm}} \approx 0.1$, detection efficiency $\epsilon_{\text{det}} \approx 0.1$, radiative decay in flight $\epsilon_{\text{dec}} = \exp(-2T/\tau)$. Assuming a lifetime $\tau = 500\,\mu\text{s}$, then $\epsilon_{\text{dec}} \approx 0.13$ setting $T = 500\,\mu\text{s}$ as the time of flight between the first two gratings. Putting all the information together the required positron flux is estimated as

$$\eta_0 \approx 2 \times 10^8\,\text{s}^{-1}$$

Clearly, this estimate is affected by a very large uncertainty, since several efficiency factors are poorly known at this stage, and technology is rapidly advancing for example in the field of transmission targets specialized on slow Ps production. This discussion is perhaps best seen as a way to establish realistic *requirements* that each process should reach rather than as an assessment of the feasibility with current technology.

However, this result does not exclude the feasibility of a QUPLAS-II type experiment, since very intense e^+ beams are available at user facilities such as the NEPOMUC [110] nuclear reactor based source, providing a flux of 1×10^9 moderated $1\,\text{keV}$ positrons per second. The L-NESS beam could also be upgraded with a new source and a suitable solid neon moderator could be implemented. This improvement could lead to a flux at the level of $10^5 - 10^6\text{s}^{-1}$. In a best case scenario where the required flux has been overestimated by an order of magnitude, a 10% level g measurement is within reach in tens of days of data taking with a highly upgraded L-NESS beam.

To conclude this section, we stress that all the outlined steps are highly challenging if undertaken individually, even more so if integrated together. Interesting alternative proposals of gravity measurements on purely leptonic systems, such as muonium [1] have been put forward [112], and involve unique challenges as well. The ideas proposed in the framework of this thesis and the QUPLAS project could provide interesting contributions to the field of positronium interferometry and gravity. This is a developing field, as evidenced by striking recent results such as the experimental demonstration of a focused beam of fast Rydberg positronium able to travel for $6\,\text{m}$ [113].

---

[1] The bound state of an electron and an anti-muon, which decays with a lifetime $\tau \approx 2.2\,\mu\text{s}$ [111].

Part II

QUPLAS-0: Theoretical modelling

CHAPTER 4

Asymmetric Talbot-Lau interferometry

In this chapter, we will discuss in details the properties of an interesting family of Talbot-Lau configurations. A period-magnifying Talbot-Lau setup will be exploited by the QUPLAS-0 positron interferometer to allow direct detection of the interference fringes with nuclear emulsion detectors. The theoretical model employed, based on the Wigner function formalism [114], makes the simplifying assumption of a fully incoherent incoming beam (the meaning of this statement will be clarified). A more refined model for partially coherent beams will be introduced in chapter 5, where we will also argue that the two approaches are fully consistent and formally equivalent although based on a different mathematical description. In spite of the simplified treatment of the beam, this chapter should serve as a useful introduction for the reader to the general features (resonance conditions, inertial sensitivity) of Talbot-Lau interferometers.

This study was stimulated by the need to find the interferometric scheme best suited to the peculiar features of our beam and detector. This optimization effort is made possible by the flexibility of grating-based interferometry, which offers several useful working regimes.

Considering the recent interest (as outlined in the introduction) for the topic of antimatter gravity it is also worthwhile to search for the best configuration using inertial sensitivity as a figure of merit. Given the challenges in manipulating antimatter beams, any advantage in comparison to the standard Talbot-Lau setup could be relevant for the feasibility of a certain measurement. Inertial sensors based on material diffraction gratings exist and have been studied extensively (see for example [115, 116]). Commonly, these devices are moiré deflectometers [117]: two-grating setups operating in the classical regime, with the particles following ballistic trajectories to produce geometrical shadow fringe patterns. We recall that a constant and uniform force in the transverse direction (corresponding to an acceleration a) induces a displacement $\Delta x \propto aT_1^2$ in the fringe pattern, where T_1 is the time of flight between the two gratings. It is known that the Talbot-Lau matter-wave interferometer also possesses the same inertial sensitivity [33], as we already mentioned. In this chapter we will prove these statements, then proceed to investigate the sensitivity properties of a peculiar period-magnifying [31, 118] setup that we refer to as the *asymmetric* Talbot-Lau interferometer. The following analysis shows that the absolute fringe displacement scales quadratically with the period magnification factor in asymmetric configurations. The se calculations are also useful to find the best trade-off in the design of an inertial sensor based on a Talbot-Lau interferometer, given the specific properties of the particle beam and the limitations of the detection technique. We conclude this chapter with a numerical simulation applied to the case of positronium gravity measurements; the results indicates that asymmetric configurations are useful for this purpose due to their peculiar properties.

The structure of this chapter closely follows the paper *"Asymmetric Talbot-Lau interferometry for inertial sensing"* [13], published as a result of this study.

4.1 General description of a Talbot-Lau interferometer

A satisfactory treatment of grating based matter-wave interferometers exploits the analogy with classical scalar diffraction theory [1, 31]. This is justified by the formal correspondence between the time evolution of the wave function calculated via the Schrödinger equation, and the Fresnel-Kirchhoff diffraction integral [31, 119] for a classical scalar field of wavelength $\lambda = \lambda(v) = h/(mv)$, where m and v are the mass and velocity of the particle, respectively. We recall one of the main features of the Talbot-Lau interferometer (sketched in Fig. 4.1), namely the capability to operate with weakly collimated beams. This result is known as the Lau effect [30, 120] and originates from the matching of the periodicity of the coherence function generated by the first grating, acting as a pure intensity mask, with the period of the second grating, d_2 [32]. The role of coherence in our specific asymmetric Talbot-Lau interferometer is discussed in details in chapter 5 for partially coherent beams. For the time being we assume a *fully incoherent beam*. The intensity pattern produced by such a beam can be modeled by integrating the intensity distribution of point sources placed on the plane of the first grating [1, 31, 118]. Schematically, the intensity pattern measured at the detection plane (see Fig. 4.1) is given by

$$I(x|\lambda) = \int I_{\text{Point}}(x|x_0, \lambda)|\mathcal{T}_1(x_0)|^2 \mathrm{d}x_0 \tag{4.1}$$

where $I_{\text{Point}}(x|x_0, \lambda)$ is the intensity pattern produced by a monochromatic point source of wavelength $\lambda = \lambda(v)$ illuminating the second grating from the point x_0. The function $\mathcal{T}_1(x)$ is the transmission function of the first grating [22]. In the case of non-monochromatic beams (as considered in section 4.3), the intensity pattern $I(x)$ is found by further integrating $I(x, \lambda)$ weighted by the probability distribution $p_\lambda(\lambda)$, or equivalently the speed distribution $P(v)$:

$$I(x)_{\text{NM}} = \int I_{\text{Point}}\left(x|x_0, \lambda\right) |\mathcal{T}_1(x_0)|^2 P(v) \mathrm{d}x_0 \mathrm{d}v \tag{4.2}$$

The Fresnel integral formalism cannot easily take into account the presence of an external force acting on the interfering particles. We will thus employ an equivalent description of the Talbot-Lau interferometer based on the Wigner function [114, 121]. This approach allows to incorporate a constant acceleration a in a straightforward manner [33, 121], and has been used to obtain the intensity pattern for symmetric configurations ($d_1 = d_2$ and $\eta = 1$) in the presence of a transverse acceleration [33]. The same theoretical framework has also been applied to the asymmetric setups of our interest ($d_1 \neq d_2$ and $\eta \neq 1$), but the external force was neglected [105].

A general calculation that takes both effects into account is now developed, together with an in-depth analysis of the period magnification properties of asymmetric setups. Following [33, 105], we introduce the Wigner function phase-space representation of the quantum state of the particle within the interferometer, given its density operator ρ:

$$W(x,p) = \frac{1}{2\pi\hbar} \int \mathrm{e}^{ips/\hbar} \left\langle x - s/2 \right| \rho \left| x + s/2 \right\rangle \mathrm{d}s. \tag{4.3}$$

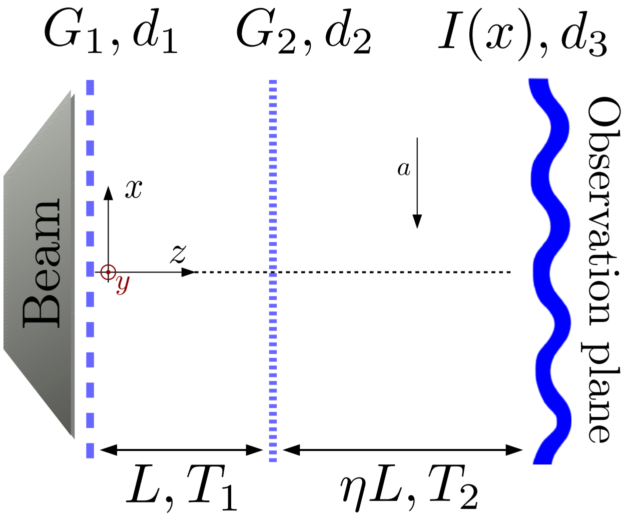

Figure 4.1. General Talbot-Lau setup in the presence of an external acceleration a acting on the particles along the x-direction. The particles travel along the z-axis with longitudinal speed v. Two diffraction gratings G_1 and G_2 of period d_1 and d_2 are located on the $z = 0$ and $z = L$ planes, respectively. The detection plane is placed at $z = (1 + \eta)L$, where an interference fringe pattern $I(x)$ with period d_3 is formed. The time of flight between the two gratings is $T_1 = L/v$ while $T_2 = \eta T_1$ is the time of flight between G_2 and the detection plane for an unperturbed longitudinal motion. Grating slits are taken to extend indefinitely in the y-direction, therefore the intensity pattern is considered to be a one dimensional function of the transverse coordinate x only.

In our analysis, the relevant degrees of freedom are the *transverse* center-of-mass position and momentum (x and p respectively), whereas the longitudinal motion (along the z-axis in Fig. 4.1) is assumed to be essentially classical. Specifically, uniform motion satisfying $t = z/v$ where v is the longitudinal speed of the particle. This relation links time to the longitudinal space evolution of the interference pattern. In the presence of a linear potential $V(x) = -x\,ma$, resulting in a constant acceleration a along the x-direction, the Wigner function evolved at time t reads [33, 105]:

$$W_t(x,p) = W_0\left(x - \frac{pt}{m} + a\frac{t^2}{2}, p - mat\right). \tag{4.4}$$

Therefore, the intensity distribution, is given by the marginal distribution

$$I_t(x) = \int W_t(x,p)\mathrm{d}p.$$

We now focus on the Talbot-Lau interferometer. The action of the grating on the incoming particle in the state $\rho = |\psi\rangle\langle\psi|$ is modelled by a transmission function $\mathcal{T}(x)$. Therefore, just after the grating, the particle wave function is $\psi'(x) = \mathcal{T}(x)\psi(x)$, where

$\psi(x) = \langle x|\psi\rangle$. The corresponding Wigner function is:

$$\begin{aligned}\widetilde{W}(x,p) &= \frac{1}{2\pi\hbar}\int \mathrm{d}s\, \mathrm{e}^{ips/\hbar}\, \mathcal{T}(x-s/2)\, \mathcal{T}^*(x+s/2) \\ &\qquad\qquad \times \langle x-s/2|\psi\rangle \, \langle\psi|x+s/2\rangle\,, \qquad (4.5) \\ &= \int \mathrm{d}x_0 \mathrm{d}p_0 K(x,x_0;p,p_0) W(x_0,p_0), \qquad (4.6)\end{aligned}$$

where [105]:

$$\begin{aligned}K(x,x_0;p,p_0) &= \frac{\delta(x-x_0)}{2\pi\hbar} \\ &\times \int \mathrm{d}s\, \mathrm{e}^{i(p-p_0)s/\hbar}\, \mathcal{T}(x-s/2)\mathcal{T}^*(x+s/2). \qquad (4.7)\end{aligned}$$

Assuming the incoming particle beam is fully incoherent, namely, $\Delta p \gg \hbar/d_1$ [105], where Δp is the standard deviation of the transverse momentum distribution[1], the Wigner function after the grating G_1, defined by its transmission function $\mathcal{T}_1(x)$, reads [105]:

$$\widetilde{W}_0(x,p) = \frac{1}{\mathcal{N}p_y}|\mathcal{T}_1(x)|^2 \mathcal{P}\left(\frac{p}{p_y}\right), \qquad (4.8)$$

where $p_y = mv$ is the longitudinal momentum, $\mathcal{P}(p/p_y)$ the transverse momentum distribution, and $\mathcal{N}$ a suitable normalization factor. The initial state (4.8), first undergoes free evolution for a time $T_1 = L/v$, governed by Eq. (4.4). The grating transformation (4.6) is then applied with the transmission function $\mathcal{T}_2$ of G_2, followed by free evolution for a time $T_2 = \eta T_1$ to obtain the Wigner function at the detection plane: $W_{T_1+T_2}(x,p) \equiv W_2(x,p)$. The calculation therefore proceeds as in the following scheme (we drop the explicit dependence on x and p):

$$\widetilde{W}_0 \xrightarrow[T_1]{G_1 \to G_2} W_1 \xrightarrow[\mathcal{T}_2(x)]{G_2} \widetilde{W}_1 \xrightarrow[T_2]{G_2 \to \text{Screen}} W_2$$

where we have introduced the Wigner functions immediately before and after the second grating, $W_1(x,p)$ and $\widetilde{W}_1(x,p)$ respectively, and the final state $W_2(x,p)$ from which the intensity distribution at the detection plane is recovered.

We now develop explicitly the steps needed to evolve the initial state (4.8) to the observation plane. First of all we note that assuming the second grating has a periodic transmission function $\mathcal{T}_2(x)$, it can be expanded in a Fourier series. Inserting the Fourier decomposition $\mathcal{T}_2(x) = \sum_n b_n^{(2)} e^{i\frac{2\pi}{d}nx}$ into equation (4.7) yields the following form for the needed grating transformation:

$$\begin{aligned}K_2(x,x_0;p,p_0) &= \delta(x-x_0)\sum_{k,n} \mathrm{e}^{i2\pi x(n-k)/d_2} \\ &\times b_n^{(2)} \left[b_k^{(2)}\right]^* \delta\left[p - p_0 - \frac{\pi\hbar}{d}(n+k)\right]. \qquad (4.9)\end{aligned}$$

---

[1] The link between beam coherence and the transverse momentum distribution will be established more carefully in chapter 5 with the aid of a more realistic model of the beam.

Applying the evolution equation (4.4) and the grating transformation (4.6) with the form (4.9) for the grating convolution function, we get the following expressions:

$$W_1(x,p) = \widetilde{W}_0\left(x - \frac{pT_1}{m} + a\frac{T_1^2}{2}, p - maT_1\right)$$

and

$$\widetilde{W}_1(x,p) = \int dx_0 dp_0\, K_2(x,p;x_0,p_0)\widetilde{W}_0\left(x_0 - \frac{p_0T_1}{m} + a\frac{T_1^2}{2}, p_0 - maT_1\right)$$

and finally the state $W_2(x,p)$ after a final free evolution step for a time T_2:

$$\begin{aligned} W_2(x,p) = \int dx_0 dp_0\, \mathcal{P}\left(\frac{p_0 - maT_1}{p_y}\right)\frac{1}{\mathcal{N}p_y}\left|\mathcal{T}_1(x_0 - \frac{p_0T_1}{m} + a\frac{T_1^2}{2})\right|^2 \times \\ \times K_2\left(x - \frac{pT_2}{m} + a\frac{T_2^2}{2}, p - maT_2; x_0, p_0\right). \end{aligned}$$

We now first apply the following change of variables in the integral (the Jacobian determinant is equal to 1)

$$\begin{cases} p_0' = p_0 - maT_1 \\ x_0' = x_0 - p_0T_1/m + aT_1^2/2 \end{cases}$$

then insert the explicit expression (4.9) for the convolution factor K_2, and integrate over p to get the final position distribution $I(x) = \int W_2(x,p)dp$:

$$\begin{aligned} I(x) = \sum_{n,k}\frac{b_n b_k^*}{Gp_y}\int dx_0' dp_0' dp\, |\mathcal{T}_1(x_0')|^2 \mathcal{P}\left(\frac{p_0'}{p_y}\right)\exp\left\{i\frac{2\pi(x - pT_2/m + aT_2^2/2)}{d_2}(n-k)\right\} \times \\ \times\, \delta\left[p - maT_2 - p_0' - maT_1 - \frac{\pi\hbar}{d_2}(n+k)\right]\delta\left(x - \frac{pT_2}{m} + a\frac{T_2^2}{2} - x_0' - \frac{p_0'T_1}{m} - a\frac{T_1^2}{2}\right). \end{aligned} \tag{4.10}$$

After performing the integration over p and x_0', shifting the k summation index as $k' = n - k$, and also introducing the Fourier series expansion of $|\mathcal{T}_1(x)|^2 = \sum_l A_l \mathrm{e}^{i2\pi xl/d_1}$, one obtains:

$$\begin{aligned} I(x) = \sum_{n,k,l}\int \frac{dp_0'}{\mathcal{N}p_y}\mathcal{P}\left(\frac{p_0'}{p_y}\right) A_l b_n b_{n-k}^* \exp\left\{i\,2\pi^2\frac{(k-2n)\hbar T_2}{m}\left(\frac{k}{d_2^2} + \frac{l}{d_1d_2}\right)\right\} \times \\ \times \exp\left\{i\,2\pi\frac{k}{d_2}\left(x - \frac{T_2p_0'}{m} - a\frac{T_2^2}{2} - aT_1T_2\right)\right\} \\ \times \exp\left\{i\,2\pi\frac{l}{d_1}\left[x - \frac{p_0'}{m}(T_1+T_2) - \frac{a}{2}(T_1+T_2)^2\right]\right\}. \end{aligned} \tag{4.11}$$

We now introduce the so-called *Talbot coefficients* [33]:

$$B_k(\xi) = \sum_{n=-\infty}^{\infty} b_n b_{n-k}^* e^{i\pi\xi(k-2n)} \tag{4.12}$$

and the scaled Fourier transform of the initial momentum distribution

$$\int \frac{dp}{p_y}\mathcal{P}\left(\frac{p}{p_y}\right)\mathrm{e}^{-ipq} \equiv \tilde{\mathcal{P}}(q). \tag{4.13}$$

The expressions (4.12) and (4.13), with the definition

$$\xi = 2\pi\frac{\hbar T_2}{m}\left(\frac{k}{d_2^2}+\frac{l}{d_1 d_2}\right),$$

can be substituted in (4.11) to obtain

$$I(x) = \frac{1}{\mathcal{N}}\sum_{k,l} A_l B_k(\xi)\tilde{\mathcal{P}}\left(\frac{2\pi}{m}\left[\frac{l}{d_1}(T_1+T_2)+k\frac{T_2}{d_2}\right]\right)\exp\left\{i\frac{2\pi}{d_2}\left[x\left(k+l\frac{d_2}{d_1}\right)\right]\right\}\times$$
$$\times\exp\left\{-i\frac{2\pi}{d_2}\left[a\left(kT_1T_2+k\frac{T_2^2}{2}+\frac{ld_2}{2d_1}(T_1+T_2)^2\right)\right]\right\}. \tag{4.14}$$

Upon assuming that the momentum distribution is broad enough that $\tilde{\mathcal{P}}(q) \approx \delta(q)$ and substituting $T_2 = \eta T_1$, the final expression for the intensity distribution $I(x) \equiv \int W_2(x,p)\mathrm{d}p$ reads:

$$I(x) = \frac{1}{\mathcal{N}}\sum_{l=-\infty}^{\infty} A_l^* B_{l\cdot q}(\alpha_l)\exp\left\{\frac{2i\pi l}{\eta d_1}\left[x-\Delta x\right]\right\}. \tag{4.15}$$

We have introduced the following expression for the Talbot coefficients:

$$B_{l\cdot q}(\alpha_l) = \sum_{n=-\infty}^{\infty} b_n^{(2)}(b_{n-l\cdot q}^{(2)})^*\,\mathrm{e}^{i\pi\alpha_l(l\cdot q-2n)}, \tag{4.16}$$

where:

$$\alpha_l = \frac{L}{L_T}\frac{d_2}{d_1}l. \tag{4.17}$$

The parameter α_l contains the usual definition of the Talbot length $L_T = d_2^2/\lambda$ [28, 31], and the parameter q reads:

$$q = \frac{d_2}{d_1}\frac{(1+\eta)}{\eta}. \tag{4.18}$$

In general, q can be a rational number, however in the following we focus on the special case of integer q, as this choice corresponds to the highest visibility resonances [105]. Finally, it is apparent that the effect of a nonzero acceleration a is to rigidly displace the fringe pattern by the following quantity:

$$\Delta x = a\frac{T_1^2}{2}\eta(\eta+1), \tag{4.19}$$

which is proportional to aT_1^2 as anticipated. The inertial displacement is discussed in section 4.2. We remark that the use of Fourier series expansion to define the coefficients (4.16) and A_l is appropriate because the functions $\mathcal{T}_i(x)$ are periodic. To obtain our final result, equation (4.15) it is also assumed that the gratings extend indefinitely in space. This is a reasonable requirement, as long as the number of periods N illuminated by the particle beam is large $N \gtrsim 10^2$.

Being based on the transmission function formalism, this model is very general and can be applied to a wide range of particles and diffraction gratings at G_2, pure intensity masks as well as phase gratings that alter the phase of the incoming wavefunction.

Furthermore, this treatment can also account for a broad range of particle-gratings interactions; examples include the van der Waals atom-surface interaction [1, 39, 122] or electrostatic forces for charged particles [1, 38]. Sufficiently weak interactions, in particular, result in a reduced *effective* slit width [1, 39], that has also been observed experimentally [12]. For stronger interactions, a more general approach beyond the Eikonal approximation [105] can still make use of this formalism. The properties of the general equation (4.15) are now discussed in detail for the cases of our interest.

4.1.1 Features of the interference pattern and resonance conditions

First of all we note that equation (4.15), describing the statistical interference fringe pattern in a Talbot-Lau interferometer, is a Fourier series expansion with a magnified period $d_3 \equiv \eta d_1$. The dependence on the length L only enters through the dimensionless ratio L/L_T. The factor η can also be less than unity, however we are particularly interested in the case $\eta > 1$, therefore, from now on we will refer to η as the *magnification factor*. As we mentioned, the properties of the gratings are encoded in the coefficients $B_{l\cdot q}(\alpha_l)$ and A_l. For the sake of clarity, we now specialise our analysis to gratings described by the following (single period) transmission function:

$$\mathcal{T}(x|w,z,f,d) = \begin{cases} w & \text{if} \quad x \in [0, fd] \\ z & \text{if} \quad x \in [fd, d], \end{cases}$$

where d and f are the period and the *open fraction* of the grating, respectively, and $w, z \in \mathbb{C}$. This form is particularly convenient since, upon writing the Fourier expansion $\mathcal{T}(x,|w,z,f,d) = \sum_n b_n(w,z,f) \exp\{i2\pi x/d\}$, we have the following analytical expression for the Fourier coefficients:

$$b_n(w,z,f) = f\,\mathrm{sinc}(\pi n f)\left(z\,\mathrm{e}^{-i\pi n f} + w\,\mathrm{e}^{i\pi n f}\right). \tag{4.20}$$

Partial transparency of the grating substrate together with a possible (constant) phase added could be accounted for by a suitable choice of w and z. However, in the present calculation we set $w = 1$ and $z = 0$, to describe material gratings realised as open slits in a substrate [12, 123]. The open fraction then corresponds to the ratio between the slit width and the grating period. Furthermore, in the following we drop the explicit dependence of the Fourier coefficients (4.20) on the parameters (w, z, f) as the two gratings G_1 and G_2 are assumed to have the same open fraction and transmission properties. We now look for the resonance conditions of equation (4.15), i.e., the set of parameters η, d_1, d_2, and L/L_T that maximises the visibility of the pattern. Note that while η, d_1, and d_2 characterize the gratings, L/L_T depends on the De Broglie wavelength (see Fig. 4.1) through the definition of T_L. We recall that the visibility or contrast C of the fringe pattern $I(x)$ is defined as

$$C = \frac{I_{\max} - I_{\min}}{I_{\max} + I_{\min}}. \tag{4.21}$$

Since the function $I(x)$ is a Fourier series, one can truncate the summation to the lowest orders, and consider the visibility of the resulting sinusoidal function as a good approximation of the actual visibility. This parameter is called the *sinusoidal visibility* [12, 20], and for equation (4.15) it reads:

$$C_{\sin}(\alpha_1, q) = 2\frac{|A_0 B_q(\alpha_1)|}{|A_0|^2} = 2\frac{|B_q(\alpha_1)|}{|A_0|}. \tag{4.22}$$

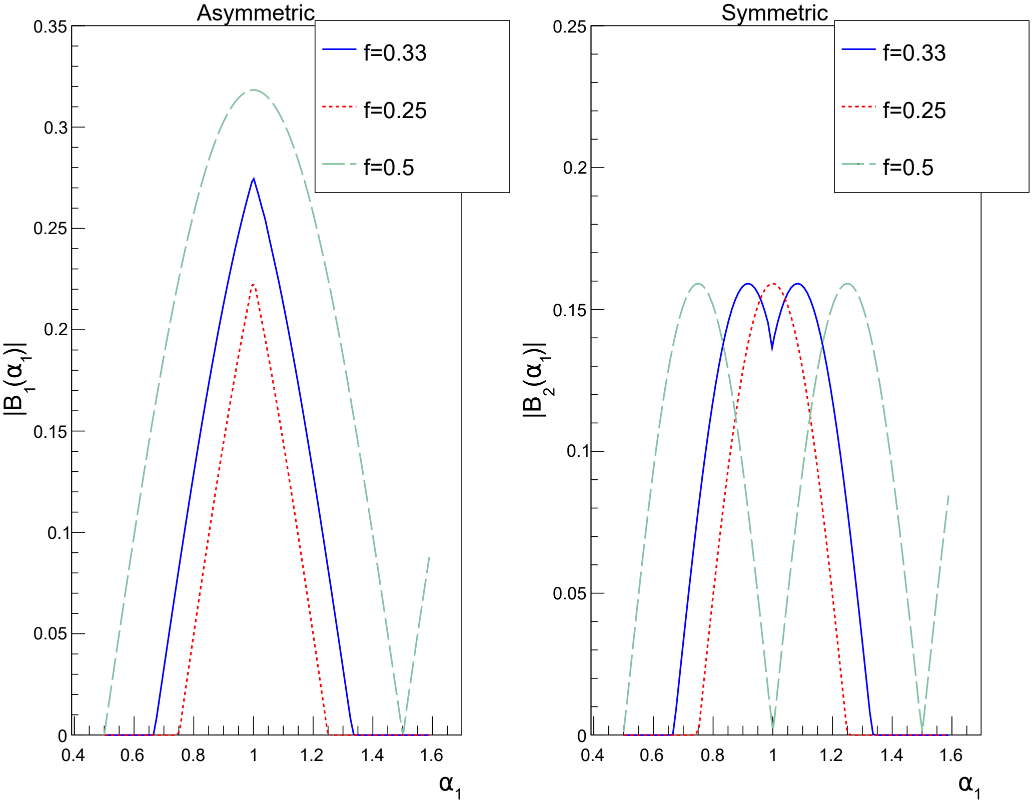

Figure 4.2. Plots of the functions $|B_1(\alpha_1)|$, on the left, and $|B_2(\alpha_1)|$, on the right, for three values of the open fraction $f = 0.25, 0.33, 0.5$. This results have been calculated by truncating the summation of equation (4.16) to $|n| < 20$. It is apparent that the shape of the functions $|B_q(\alpha_1)|$ for the symmetric case ($q = 2$), strongly depends on the open fraction f. The functions are always symmetric and periodic with respect to $\alpha_1 = 1$, reflecting the properties of the underlying Talbot effect.

The constant coefficients A_0 are the zeroth-order Fourier coefficients of $|\mathcal{T}_1(x)|^2$, the intensity transmission function of the first grating (for the case $z = 1$ and $w = 0$ it coincides with the transmission function itself). Equation (4.22) suggests the modulus of the q-th Talbot coefficient as a good estimator of the pattern visibility. The requirement that q, defined in equation (4.18), is an integer allows to enumerate different families of *resonance conditions* as a function of the physical parameters. If we consider the lowest values of q we have:

$$q = 2 \Rightarrow \frac{d_1}{d_2} = \frac{(1+\eta)}{2\eta}, \tag{4.23a}$$

$$q = 1 \Rightarrow \frac{d_1}{d_2} = \frac{(1+\eta)}{\eta}. \tag{4.23b}$$

The optimal value of η is related to the ratio of the two grating periods. The most common standard *symmetric* Talbot-Lau setup belongs to the case $q = 2$ and has $\eta = 1$, implying that $d_1 = d_2$. In the following we will study the interesting properties of the case $q = 1$ and $\eta > 1$. We will refer to this choice as the *asymmetric setup*. The value of q determines the relevant Talbot coefficients influencing the visibility, respectively $B_1(\alpha_1)$ for the asymmetric case, and $B_2(\alpha_1)$ for the standard symmetric setup. We now turn our attention to the α dependence of $|B_1(\alpha_1)|$ and $|B_2(\alpha_1)|$. The two functions are plotted in Fig. 4.2 for different values of the open fraction f. The position of the relative maximum of the relevant Talbot coefficient sets the *resonance* condition on the length. For instance we see that for the $B_1(\alpha_1)$, this always occurs for $\alpha_1 = 1$, whereas the behaviour of $B_2(\alpha_1)$ is more irregular and depends on the open fraction. Assuming for definiteness that the maximum occurs for $\alpha_1 = 1$, and using the definition (4.17), we obtain the resonance condition:

$$L = \frac{d_1}{d_2} L_T = \frac{d_1 d_2}{\lambda}, \tag{4.24}$$

where the periods of the gratings and magnification factor η have to satisfy either of the conditions (4.23) (or any other combination corresponding to an integer value of q, defined by (4.18)). Quantum diffraction takes place at the second grating, so in this general configuration with $d_1 \neq d_2$, it is d_2 that sets the relevant length scale trough the Talbot length $L_T = d_2^2/\lambda$. Furthermore, as a manifestation of the underlying Talbot effect, resonance is possible also at higher integer multiples of L_T. This is reflected in the periodicity of the Talbot coefficients in their argument α_1.

The case of a standard symmetric setup ($q = 2, \eta = 1, d_1 = d_2$) with $f = 0.5$ is peculiar, and does not satisfy the same resonance conditions, since it is evident from Fig. 4.2 that it achieves a maximum visibility for $\alpha \neq 1$. The case $f = 0.5$ is also critical in the classical case: the visibility of a moiré deflectometer with $f = 0.5$ is exactly zero [117]. It is interesting to see that if an asymmetric setup is employed, all the chosen values of open fraction, including $f = 0.5$, behave similarly. This property has favourable consequences, which motivate our choice to study the $q = 1$ family of resonances.

4.1.2 Asymmetric setups and period magnification

The features of the interference pattern produced by the asymmetric configuration are best illustrated with an example. For the resonance condition (4.23b), the intensity pattern is given by the general equation (4.15). The relevant properties of the interference patterns can be summarised in a *carpet* as shown in Fig. 4.3. This is a two dimensional density plot where each section is the intensity distribution $I(x)$ for a given value of L/L_T and x is the transverse coordinate: the carpet can be scanned by tuning the particle energy (or the de Broglie wavelength) to adjust L_T. Note that in this case we are assuming that the parameter η is fixed, thus both distances are scaled keeping their ratio constant. We will adopt a more general point of view where we investigate the behavior off-resonance in the next chapter. A plot of the visibility as a function of L/L_T is shown in Fig. 4.4. The features of the asymmetric Talbot-Lau setup are generally described as follows:

- The maximum fringe period is magnified and given by $d_3 = \eta d_1$. Fractional revivals are also present and are peculiar of the Talbot effect (see Fig. 4.3).
- The total length is given by $L^{(\mathrm{TOT})} = L(1+\eta)$. Imposing the appropriate resonance conditions on the grating periods (4.23b) yields:

$$L^{(\mathrm{TOT})} = (1+\eta)\frac{d_1}{d_2} L_T = (1+\eta)\frac{d_1 d_2}{\lambda}. \tag{4.25}$$

Figure 4.3. Plot of the intensity $I(x)$ (in arbitrary units), from equation (4.15), also as a function of the de Broglie wavelength which varies along the y-axis. For definiteness we set realistic parameters for low energy ($10\,\mathrm{keV}$) positrons (or electrons): $d_2 = 1\,\mu\mathrm{m}$, $d_1 = 4/3\,d_2$, $\eta = 3$, $L = 0.11\,\mathrm{m}$ and $f = 0.3$. As predicted we see the main interference fringes appear at $L/L_T = d_1/d_2$ and have a magnified period $d_3 = \eta d_1$. It is worth noting that only the adimensional ratios L/L_T and d_1/d_2 appear in (4.15), thus our plot shows the general form of the *Talbot carpet* for the $\eta = 3$ configuration with $f = 0.3$ material gratings. We specialized on particles of mass m_e only to give a sense of the physical scales.

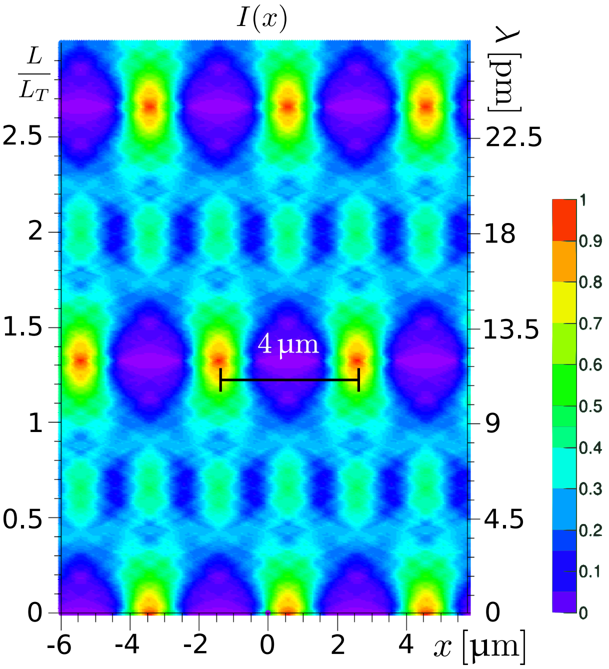

Figure 4.4. Visibility of the interference pattern of Fig. 4.3, in the neighborhood of the main interference peak, calculated with equation (4.21). The maximum occurs at $L/L_T = d_1/d_2$, as predicted in section 4.1. Note that the shape of the peak differs from the plots of Fig. 4.2. Those curves are proportional to the sinusoidal visibility, which is only an approximation, while here there are contributions from higher orders of the Fourier series (4.15).

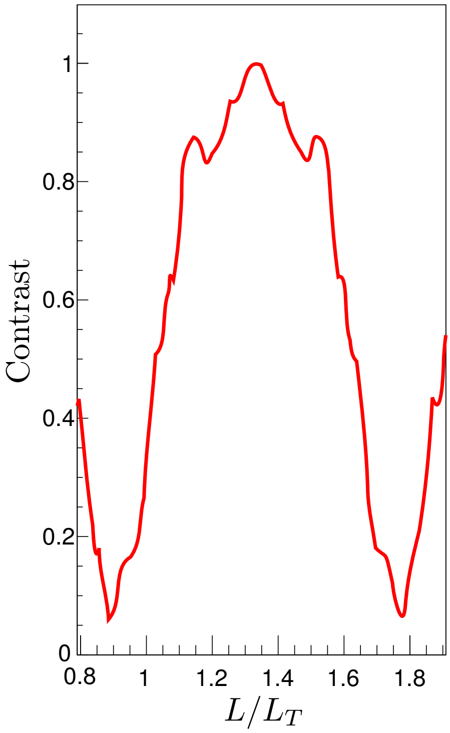

The properties of the two configurations relevant for the calculations to follow are summarised in Table 4.1.

	Symmetric	**Asymmetric**
$L^{(\mathrm{TOT})}$	$2\dfrac{d_{2,\mathrm{s}}^2}{\lambda}$	$\dfrac{(\eta+1)^2}{\eta}\dfrac{d_{2,\mathrm{a}}^2}{\lambda}$
d_3	$d_{2,\mathrm{s}}$	$(\eta+1)d_{2,\mathrm{a}}$

Table 4.1. Summary of the relevant properties $L^{(\mathrm{TOT})}$ and $d_3 = \eta d_1$ for the standard symmetric setup (4.23a) with $d_1 = d_2 = d_{2,\mathrm{s}}$, and the asymmetric setup (4.23b) with $d_2 = d_{2,\mathrm{a}}$ and $d_1 = (\eta+1)d_{2,\mathrm{a}}/\eta$.

It is possible to prove that for a given energy (wavelength) and at a fixed total interferometer length, asymmetric configurations allow to maximize the period of the interference fringes with respect to the standard setup. If the ratio $r = d_{3,\mathrm{a}}/d_{3,\mathrm{s}}$ is evaluated under the constraint that the two interferometers are of the same total length, namely,

$$\frac{d_{2,\mathrm{a}}^2}{d_{2,\mathrm{s}}^2} = \frac{2\eta}{(\eta+1)^2}, \tag{4.26}$$

the following result is obtained:

$$r\big|_{\text{Equal length}} = \frac{d_{3,\mathrm{a}}}{d_{3,\mathrm{s}}} = \eta \cdot \frac{\eta+1}{\eta}\frac{d_{2,\mathrm{a}}}{d_{2,\mathrm{s}}} = \sqrt{2\eta}. \tag{4.27}$$

So we see that asymmetric configurations provide a systematic improvement of the ratio $d_3/L^{(\mathrm{TOT})}$ that scales well with the magnification factor. This can be of interest experimentally for a variety of cases [1]. Magnifying configurations have been actually realized for low energy electrons [27], using however different resonance conditions and an extreme ($\eta = 100$) magnification factor, so that the observation plane was effectively in the far field of the second gratings. As a matter of fact that configuration requires different coherence conditions than the Talbot-Lau interferometer and is referred to as a *Lau interferometer* [26].

4.2 Inertial sensitivity and applications

We now turn our attention to the inertial sensitivity of Talbot-Lau interferometers. In section 4.1 we determined the displacement of the pattern induced by an external acceleration a, equation (4.19). This is a generalisation of the result from [33] that allows for gratings of different periods and a magnification factor η. If we set $\eta = 1$ we obtain the $\Delta x|_{\eta=1} = aT_1^2$, which is the well known displacement law for the the geometrical shadow pattern in a moiré deflectometer due to the same effect [117]. This correspondence will be further discussed, also in the asymmetric configuration, in section 4.2.1. The displacement (4.19) is quadratic in the magnification factor η. This interesting property might be helpful when the total length of the setup is limited by the properties of the interfering particles or the experimental apparatus. For example if the particles have a finite lifetime [1], or need to propagate in vacuum, under shielding from stray fields or in a cryogenic environment [1, 124]. An interesting potential application for a Talbot-Lau inertial sensor is the measurement of the gravitational acceleration g of the positronium atom. In this scenario all the experimental challenges we mentioned are relevant.

It is apparent from the geometry of the setup (Fig. 4.1) that increasing the asymmetry factor η at fixed total length $L^{(\mathrm{TOT})} = L(1+\eta)$, also reduces T_1. Equation (4.19) shows a quadratic dependence of the inertial displacement on both parameters. For this reason we apply the same reasoning of section 4.1.2 to find if there is a systematic gain in the inertial displacement from symmetric to asymmetric setups of the same length. We define the displacement per unit interferometer length as:

$$r_{\Delta x} = \Delta x / L^{(\mathrm{TOT})}$$

in the symmetric and asymmetric case under the constraint (4.26). Using the same notation of section 4.1.2, one can prove that (assuming $\eta > 1$):

$$\frac{r_{\Delta x,\mathrm{a}}}{r_{\Delta x,\mathrm{s}}} = \left.\frac{\Delta x_{\mathrm{a}}}{\Delta x_{\mathrm{s}}}\right|_{\text{Equal length}} = \frac{2\eta}{(\eta+1)} > 1. \tag{4.28}$$

Though this factor is greater than unity, it is limited to a maximum value of $\Delta x_{\mathrm{a}}/\Delta x_{\mathrm{s}} = 2$ for $\eta \gg 1$. However, already for $\eta = 3$ one can magnify the *fall* of the beam by 50% with respect to a symmetric configuration of the same length. This can already be a sizeable gain for some specific applications.

From a practical point of view, it can be proven [115], that the relative uncertainty σ_a/a with which the acceleration a can be measured by detecting a shift Δx in a fringe pattern with period d_3 and contrast C reads:

$$\frac{\sigma_a}{a} = \frac{1}{\sqrt{N}} \frac{1}{2\pi C\, \Delta x/d_3}, \tag{4.29}$$

where N is the number of data points forming the pattern, which depends on the beam intensity and the efficiency of the detector, for a given measurement time. Furthermore, the contrast is mainly influenced by the longitudinal velocity spread of the incoming particles. For a non-monochromatic beam the intensity pattern is recovered by integrating over the speed distribution. Generally this causes a loss in visibility that depends on the width of the speed distribution (see section 4.3). The chosen Talbot-Lau configuration directly influences the inertial sensitivity via the *relative displacement* $\Delta x/d_3$, where we recall that d_3 is the period of the interference fringes. It is thus useful to derive an expression for the ratio in the two cases of our interest. Starting from the asymmetric setup, defined by the resonance conditions (4.23b) and (4.24) we have

$$\frac{\Delta x_{\mathrm{a}}}{d_{3,\mathrm{a}}} = \frac{a T_1^2 \eta(\eta+1)}{2\eta d_{1,\mathrm{a}}} = \frac{a}{2} \frac{\sqrt{\eta}}{(\eta+1)} \sqrt{\frac{m}{h}} \left[T_{(\mathrm{TOT})}\right]^{3/2}. \tag{4.30}$$

The last equality follows from simple substitutions and algebraic manipulations using equation (4.25), the resonance conditions and the definitions of the Talbot length $L_T = d_2^2/\lambda$ and of the de Broglie wavelength. We introduced $T_{(\mathrm{TOT})}$ as the total flight time from the first grating to the detection plane, namely $L^{(\mathrm{TOT})}/v$.

On the one hand, equation (4.29) tells that to improve the sensitivity, the relative displacement $\Delta x/d_3$ should be maximised. On the other hand, equation (4.30) shows that this quantity increases monotonically with the total flight time, as expected, but also that it tends to zero as $\eta \gg 1$.

We can physically motivate the dependence of equations (4.30) and (4.31) from the particle mass: for a fixed total interferometer length and longitudinal speed v, any particle subjected to the same acceleration a, will undergo the same transverse displacement, according to equation (4.19). However, the heavier the particle, the smaller its de Broglie wavelength would be, thus leading to shorter periods for the two gratings and for the resulting fringe pattern. Following this line of reasoning, the ratio $\Delta x/d_3$ is expected to increase with the particle mass. The relative displacement for the standard setup instead reads:

$$\frac{\Delta x_{\mathrm{s}}}{d_{3,\mathrm{s}}} = a\frac{1}{2\sqrt{2}}\sqrt{\frac{m}{h}}\left[T_{(\mathrm{TOT})}\right]^{3/2}. \tag{4.31}$$

First we remark that it does not coincide with the result of equation (4.30) for $\eta = 1$. This is a consequence of the fact that the two configurations belong to two different sets of resonance conditions with different relevant Talbot coefficients, as discussed in section 4.1. As a matter of fact the "asymmetric configuration with $\eta = 1$" differs from the standard symmetric setup because $d_1 = 2d_2$ in the former, whereas $d_1 = d_2$ in the latter; as required by (4.23b). Even in this case we have $\Delta x_{\mathrm{a}}/d_{3,\mathrm{a}} < \Delta x_{\mathrm{s}}/d_{3,\mathrm{s}}$ at the same total length, so we see that the asymmetric setups we studied always provide a smaller relative displacement in the presence of a constant acceleration. This property, according to equation (4.29) can be a disadvantage if the aim is to measure the acceleration a with great accuracy. However, in some realistic experimental situations it may be preferable to have a larger absolute displacement at the expense of the relative shift (for instance, due to the finite detector resolution). A comparison of Eqs. (4.30) and (4.31) suggests that the impact of random external perturbations on the pattern visibility is effectively reduced by using a magnifying setup of the same length. An example is the Lorentz force acing on charged particle due to stray electromagnetic fields [1]. To summarise the results of this section, Fig. 4.5 displays the scaling with η of the parameters we introduced.

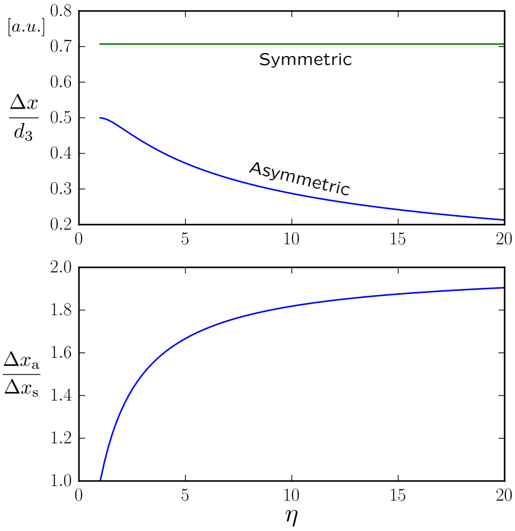

Figure 4.5. The top panel shows a comparison of Eqs. (4.30) and (4.31) (assuming arbitrary units in which $a = h = m = T^{(\mathrm{TOT})} = 1$). It is apparent that the asymmetric setup always provides a smaller relative displacement under the acceleration a. The absolute displacement is, however, always larger, as shown in the bottom panel. A smaller relative displacement is not desirable for inertial measurements, but also implies a reduced sensitivity to external disturbances. Generally the best trade off has to be found depending on the specific experimental application.

4.2.1 Comparison with moiré deflectometers

A moiré deflectometer, as described in [117], is a two-grating setup completely analogous to the one shown in Fig. 4.1. The crucial difference is that the grating periods $d^{(\mathrm{m})}$ and the length $L^{(\mathrm{m})}$ are chosen to satisfy the constraint [1]:

$$L^{(\mathrm{m})}\frac{\lambda}{d^{(\mathrm{m})}} \ll d^{(\mathrm{m})} \to L^{(\mathrm{m})} \ll L_T. \tag{4.32}$$

Therefore, quantum diffraction is negligible. We introduced the superscript (m) to denote the grating periods and length of the classical configuration. Equation (4.32) implies that a given resonant Talbot-Lau setup with parameters η, L, d_1, d_2 at fixed de Broglie wavelength λ, can be made into a classical device by changing the grating periods to larger values: $d_i^{(\mathrm{m})} \gg d_i$ for $i = 1, 2$. On the other hand one could decrease the length and keep the same gratings, so that $L^{(\mathrm{m})} \ll L$. However, since we are interested in inertial sensing application and the fringe displacement strongly depends on the length, in the following we always assume that the first route is taken when comparing the two devices.

For this reason, a moiré deflectometer will always produce a fringe system with a larger period than the Talbot-Lau setup of the same length tuned for the same particle beam.

We now derive in very simple terms the main features of the classical fringe pattern in the presence of an external acceleration a. Let us suppose that the incoming particle with speed v starts with a transverse position and speed (x_0, v_0), on a plane located at a distance $L_s = vT_s$ before the first grating. From the laws of uniformly accelerated motion it is then straightforward to write the following system of equations:

$$\begin{cases} x_1 &= x_0 + v_0 T_s + \frac{1}{2}aT_s^2 \\ x_2 &= x_0 + v_0(T_1 + T_s) + \frac{1}{2}a(T_1 + T_s)^2 \\ x_3 &= x_0 + v_0(T_1 + T_2 + T_s) + \frac{1}{2}a(T_1 + T_2 + T_s)^2. \end{cases} \tag{4.33}$$

Where x_1, x_2 , x_3 are the x-positions of the particle on the plane of G_1, G_2 and the detector respectively, T_1 and T_2 being the corresponding times of flight. After some algebraic manipulations we can eliminate the dependence on x_0 and v_0, solving for x_3 as a function of x_1 and x_2:

$$x_3 = x_2\left(1 + \frac{T_2}{T_1}\right) - x_1\frac{T_2}{T_1} + \frac{1}{2}a\left(T_2^2 + T_1T_2\right). \tag{4.34}$$

It is worth noting that equation (4.34) does not depend on the initial conditions x_0 and v_0: only the dynamics after the first grating are relevant. The same expression could have been obtained by assuming initial conditions on the plane of x_1. One also sees that the displacement due to a is the sum of two contributions depending on both times of flight, as expected since the force acts in both regions.

Equation (4.34) must be coupled with the requirement that the intermediate arrival positions onto the gratings are contained in the support of the gratings transmission function. To get an intuitive picture we implement this requirement by the simple replacements

$$x_1 = nd_1^{(\mathrm{m})} \quad \text{and} \quad x_2 = md_2^{(\mathrm{m})}, \tag{4.35}$$

that constrain the x-positions to be exact multiples n and m, respectively, of the grating periods. This substitution, together with $T_2 = \eta T_1$ yields:

$$x_3 = m d_2^{(\mathrm{m})}(1+\eta) - n d_1^{(\mathrm{m})}\eta + \frac{aT_1^2}{2}\eta(\eta+1). \tag{4.36}$$

A physically interesting periodic pattern arises if the grating periods and η are chosen to cast equation (4.36) in the form: $x_3 = b d_3^{(\mathrm{m})} + \frac{1}{2}aT_1^2\eta(\eta+1)$, where b is an integer number that depends on m, n and $d_3^{(\mathrm{m})}$ is the period of the fringes, generally depending on η. For example, the standard moiré deflectometer, defined by $d_2^{(\mathrm{m})} = d_1^{(\mathrm{m})}$ and $\eta = 1$ is a suitable choice. However, we observe that also by using the asymmetric resonance conditions (4.23b) we obtain the following expression

$$x_3 = \eta d_1^{(\mathrm{m})}(m-n) + \frac{aT_1^2}{2}\eta(\eta+1), \tag{4.37}$$

meaning that the final position is a multiple of $d_3^{(\mathrm{m})} = \eta d_1^{(\mathrm{m})}$. As we anticipated, the last line shows that period magnification and a-dependent fringe displacement have the same features in the classical and quantum description of the setup of Fig.4.1. Given this similarity, all the considerations made about the sensitivity (see equation (4.29)) remain valid. An important remark is that all other parameters being equal, the requirement $d_i^{(\mathrm{m})} \gg d_i$ causes the classical configuration to always produce a smaller relative displacement $\Delta x/d_3$, thus generally lowering the sensitivity (4.29).

However, the properties of the quantum and classical fringe patterns are markedly different. For example in the moiré deflectometer the visibility is independent of the particle energy [1], as also shown in section 4.3. This is why we carefully referred to the output of the moiré deflectometer as *geometrical shadow* patterns, in contrast with the genuine quantum interference fringes of a Talbot-Lau interferometer.

4.3 Numerical analysis

In the Talbot-Lau interferometer, the parameters C and Δx appearing in equation (4.29) for the inertial sensitivity are dependent on the speed distribution $P(v)$ of the particle beam. We now analyze this dependence with a numerical simulation. For definiteness, we will assume that the function $P(v)$ is a Gaussian with variance σ_v^2. Hence we can write the general expression:

$$\left(\frac{\sigma_a}{a}\right)_{\mathrm{NM}}(\sigma_v) = \frac{1}{\sqrt{N}}\frac{1}{2\pi\, C(\sigma_v)\,\Delta x_{\mathrm{eff}}(\sigma_v)/d_3}, \tag{4.38}$$

where $C(\sigma_v)$ is the contrast, $\Delta x_{\mathrm{eff}}(\sigma_v)$ is an effective displacement and the subscript NM recalls that it applies to non-monochromatic beams. As Eqs. (4.15) and (4.2) suggest, the intensity for a non-monochromatic beam in the presence of an external force has the general structure:

$$I_{\mathrm{NM}}(x) = \int I(x - \Delta x(v)|v)P(v)dv \tag{4.39a}$$

$$\approx \int I(x - \Delta x_{\mathrm{eff}}|v)P(v)dv \tag{4.39b}$$

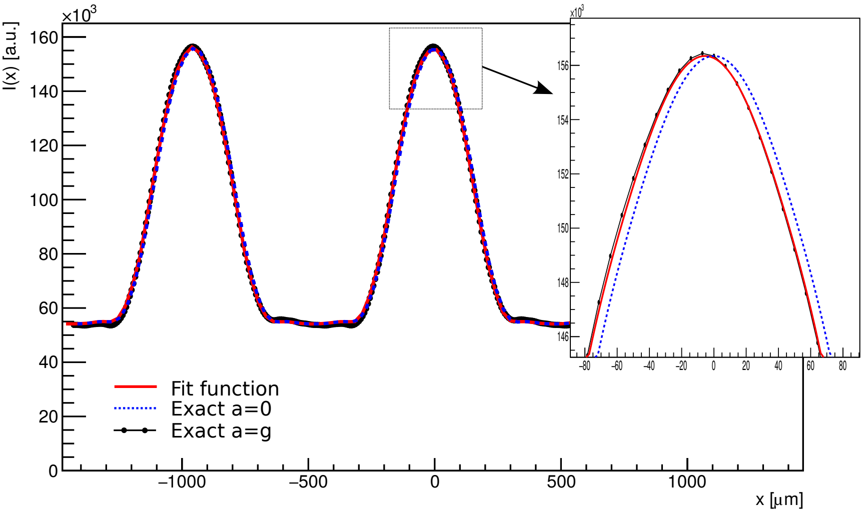

Figure 4.6. Example result of the fit procedure outlined in the text. In particular for the case $\sigma_v/\langle v\rangle = 0.3$ and the asymmetric configuration also described in sec 4.3. The box shows a detail of the portion around the peak to highlight the very small displacement of the interference pattern due to the gravitational acceleration with respect to the reference pattern with $a = 0$ (with the chosen parameters $\Delta x_{\text{eff}} = 4\,\mu\text{m}$). It is also evident the good agreement between the fit function, equation (4.39b), and the intensity (4.39a).

where $\Delta x(v)$ and $I(x|v)$ are given by Eqs. (4.19) and (4.15) respectively, and we highlighted the parametric dependence on v for clarity. Since there is a dependence on the integration variable both from the argument and in the functional form of $I(x)$, the second equality is in principle an approximation. The intensity distribution $I_{\text{NM}}(x)$ in the presence of the external force and a speed distribution $P(v)$ is evaluated as defined by equation (4.39a). A least squares fit procedure is then performed with the function:

$$I_{\text{fit}}(x, x') = \int I(x - x'|v)P(v)dv$$

with the displacement x' being the only free parameter. The displacement Δx_{eff} is then defined as the best fit value of x', and depends on $P(v)$, hence in our case, $\Delta x_{\text{eff}} = \Delta x_{\text{eff}}(\sigma_v)$. By inspecting the results of our numerical analysis (see Fig. 4.6), this is a reliable method to calculate the effective displacement, given the agreement between the fit function and the exact intensity[2].This method is indeed sensitive to the relative displacements smaller than 1% that we encountered. In order for the fit parameter to correspond exactly to the physical displacement we are after, an absolute reference frame has to be established. This is easily done in our computational simulation, by displacing the (monochromatic) intensity function $I(x)$ so that it has an interference peak for the speed $\langle v\rangle$ at $x = 0$. For example, for the asymmetric configuration it is necessary to apply a shift of $\eta d_1/2$.

A set of parameters suitable for a possible cold positronium beam was chosen: a mean speed $\langle v\rangle = 800\,\text{m/s}$, corresponding to a de Broglie wavelength $\lambda = 454\,\text{nm}$, and a total interferometer length $L^{(\text{TOT})} = 1\,\text{m}$. The expected fringe displacement due to the gravitational acceleration on the Earth surface $a = g = 9.81\,\mathrm{m/s^2}$ is thus of the order of a few microns. The chosen velocity distribution is a Gaussian normal:

---

[2] This agreement justifies the relation between equations (4.39b) and (4.39a).

$$P(v) = \frac{1}{\sqrt{2\pi}\sigma_v} \exp\left[-\frac{(v - \langle v\rangle)^2}{2\sigma_v^2}\right] \tag{4.40}$$

whose variance σ_v^2 has been chosen so that $\langle v\rangle - 3\sigma_v > 0$, to ensure that the Gaussian function is not truncated, to a very good approximation. Therefore in the plots of section 4.3, we are always comparing distribution of the same functional form. The Talbot-Lau setups analyzed are at resonance for the mean speed $\langle v\rangle$. We focus in particular on two configurations: a symmetric setup (4.23a) with $d_1 = d_2 = 476\,\mu\mathrm{m}$, and an asymmetric setup (4.23a) with $d_1 = 1.5d_2 = 476\,\mu\mathrm{m}$ and $\eta = 2$. We chose this low magnification setup because, according to equation (4.30), the relative displacement of the asymmetric configuration is decreasing with η. As a matter of fact, this choice of parameters produces a particularly challenging case where the relative gravitational displacement is very small ($\Delta x/d_3 < 1\%$), due to the small mass of the positronium atom (see equation (4.30)). For different experimental conditions (like heavier atoms) with a more sizable relative displacement, high magnification setups could also be advantageous. A simple Monte Carlo simulation of a moiré deflectometer was also used to provide a comparison with the classical setup. It is based on a direct calculation of the particles trajectories with the law of motion (4.33), taking into account the transmission properties of the gratings. The intensity factor N in equation (4.38) can always be defined as $N = \mathcal{M}T_{\mathrm{int}}$, where $\mathcal{M}$ is the beam intensity at the detector and a T_{int} is the integration time. As we will show, the visibility of a Talbot-Lau pattern is very sensitive to the v-distribution, so in many realistic particle beams, a velocity selection could be needed. In these cases the factor $\mathcal{M}$ (and in turn N) depends on σ_v as well, and the best trade-off between visibility (decreasing with σ_v) and statistics (increasing with σ_v) has to be found. Since this study is specific to each experimental situation, in the following we only focus on the functions $C(\sigma_v)$ and $\Delta x_{\mathrm{eff}}(\sigma_v)$. We also considered the dependence on the open fraction f of the gratings, since the form of the Talbot coefficients indicates that not only the visibility generally depends on f, but also that the behavior of the asymmetric and symmetric setups can be very different for certain values of f. In particular, Fig. 4.2 suggests that at $f \approx 50\,\%$ the asymmetric setups could provide an advantage in the visibility. This property is confirmed by our simulations and is physically relevant: in applications where the beam intensity is low (e.g. the inertial sensing of antimatter beams), it is most desirable to employ large open fractions ($f > 30\,\%$), in order to maximize the flux.

The contrast C of the intensity patterns was calculated via equation (4.21) and the result is shown in Fig. 4.7 and Fig. 4.8, alongside the visibility of the relevant moiré setups for comparison.

In particular, Fig. 4.7 reports results for $f = 0.3 = 30\,\%$: the asymmetric ($\eta = 2$) configuration provides a marginally higher visibility than the standard symmetric setup of the same length. In the highly monochromatic case ($\sigma_v/\langle v\rangle = 1\%$) both setups match the classical visibility of the moiré setup, which is close to unity at this open fraction. As expected, there is no dependence on the speed distribution in the classical case.

In Fig. 4.8 the contrast is shown for the case $f = 50\%$. Note that the periodicity of the symmetric setup has been adjusted to satisfy the appropriate maximum visibility condition at $f = 50\,\%$, that is $L/L_T \approx 1.33$ (see Fig. 4.2). In this situation the asymmetric setup provides a sizeable advantage in visibility, also compared to classical moiré deflectometers with $f = 50\,\%$ and $f = 40\,\%$. To make our description even more specific, the finite lifetime of positronium was finally accounted for. We recall that the longer lived

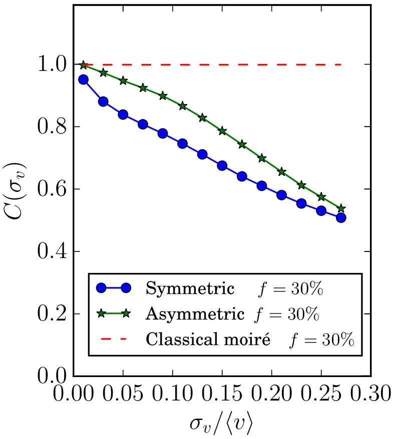

Figure 4.7. Visibility, equation (4.21), as a function of $\sigma_v/\langle v\rangle$. The symmetric setup has $d_1 = d_2 = 476\,\mu\text{m}$, $f = 0.3$, $L = 0.5\,\text{m}$, and $a = 9.81\,\text{ms}^{-2}$, whereas the asymmetric setup is defined by $d_1 = 1.5d_2 = 476\,\mu\text{m}$, $\eta = 2$ and $L = 0.33\,\text{m}$. These parameters are resonant for a $v = 800\,\text{ms}^{-1}$ positronium atom. Included for comparison a symmetric moiré setup of the same length with $d_1 = d_2 = 800\,\mu\text{m}$. We note that in equation (4.15) only the dimensionless ratios of the grating periods and the parameter $L_T/L \propto v$ appears,so the results should be sufficiently general.

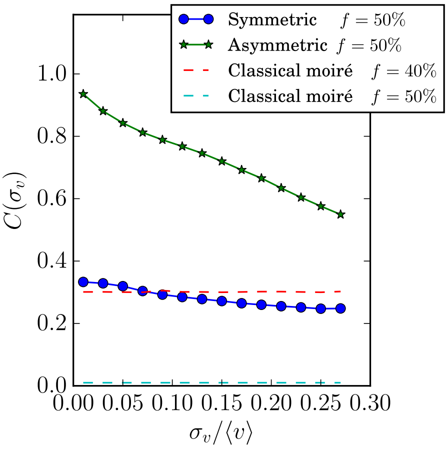

Figure 4.8. Visibility in the same conditions of Fig. 4.7, with an increased open fraction $f = 50\,\%$ and the period of the symmetric setup set to $d_1 = d_1 = 413\,\mu\text{m}$ (see text for details). The dashed lines show the visibility of classical moiré setups for three values of the open fraction: $f = 50, 40$ and $30\,\%$. Most importantly, we observe that the asymmetric Talbot-Lau setup provides considerably higher contrast than the symmetric setup, for which the value $f = 50\%$ is particularly critical, in analogy with the classical deflectometer [117] (see also Fig. 4.2).

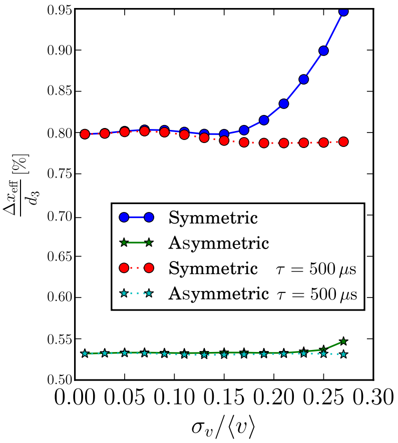

Figure 4.9. Relative displacement $\Delta x_{\text{eff}}/d_3$ for the same Talbot-Lau configurations described in Fig. 4.7. Both for ideal stable particles, and with a finite lifetime $\tau = 500\,\mu\text{s}$ that alters the effective speed distribution (see the text for details).

spin triplet ortho-positronium state has a lifetime $\tau_0 = 142\,\mathrm{ns}$ [85] in its ground state, and to devise a Talbot-Lau configuration yielding a measurable displacement under the gravitational acceleration for such a short lived particle is impossible. However the use of Rydberg states of Ps is feasible and has been proposed for this purpose [82, 125, 126]. In particular, for high-n Rydberg states [97], the lifetime scales as $\tau \propto n^2 l^3$ with n and l being the principal and angular quantum numbers respectively, so it is in principle possible to reach lifetimes of the order of $\tau \approx 500\,\mu\mathrm{s}$. We take the finite lifetime into account by assuming that atoms decaying before the detector plane (see Fig. 4.1) are not detected.

The relative displacement $\Delta x_{\mathrm{eff}}/d_3$ is analyzed both in the presence and in the absence of decay, focusing on the $f = 30\%$ case (the inertial displacement is unaffected by f). As seen in Fig. 4.9 the symmetric setup provides a larger relative displacement by the factor ≈ 1.3 predicted by Eq. (4.28) for $\eta = 2$. We also observe that, for the symmetric case in particular, there is a sizable dependence of the effective displacement on σ_v. This has a physical origin in the fact that, although the maximum variance σ_v has been carefully chosen, as the speed distributions widens the contribution from the slower particles starts to dominate. If one calculates the mean value of the displacement $\Delta x(v) \propto 1/v^2$, equation (4.19) for the distribution (4.40), a parameter that strongly correlates with Δx_{eff}, the same rise appears as a function of σ_v. The disappearance of this increase when the particles decay confirms this conclusion: the exponential decay with lifetime τ produces an effective speed distribution $P_{\mathrm{eff}}(v)$, different from the one the atoms were initially produced with, namely $P(v)$. This function has the following form:

$$P_{\mathrm{eff}}(v) \propto P(v) \exp\left(-\frac{L^{(\mathrm{TOT})}}{\tau v}\right), \tag{4.41}$$

it is peaked on a higher speed than $\langle v\rangle$, and the slower end of the spectrum is suppressed.

4.3.1 Inertial sensitivity comparison

In this chapter we investigated the inertial sensitivity of several Talbot-Lau configurations representative of the general features of this type of interferometer. In particular, we considered the asymmetric configuration ($\eta = 2$, $L^{(\mathrm{TOT})} = 1\,\mathrm{m}$), and the symmetric setup of the same length, at resonance for positronium atoms at $v = 800\,\mathrm{m/s}$. In both cases two values of the open fractions: $f = 30\%$ and $f = 50\%$ were studied, and the grating periods chosen to achieve the maximum visibility, according the results of section 4.1. The parameter f, in addition to the visibility, also affects the particle flux. In particular it is reasonable to assume that the intensity is proportional to the square of f, namely $N = f^2 N_0$. Thus we can define a significant estimator for the inertial sensitivity as:

$$\sqrt{N_0}\,\frac{\sigma_a}{a}\bigg|_{N=f^2N_0}, \tag{4.42}$$

where σ_a/a is defined by equation (4.38), performing the substitution $N = f^2 N_0$. The impact of the open fraction is thus taken into account, and the rescaling is meant to remove the dependence on the integrated flux. In Fig. 4.10, we plot the function (4.42) in the absence of decay, that is, for purely Gaussian speed distributions. Throughout most of the σ_v range, the best performing configuration is the asymmetric $f = 50\%$ configuration. Moreover, the inertial sensitivity is not the only figure of merit to be considered: the asymmetric setup also provides a larger absolute displacement Δx_{eff} and interference fringes period d_3 by a factor $2\eta/(\eta+1)$, and $\sqrt{2\eta}$ respectively (see equations (4.28) and (4.26)). These parameters are relevant when a finite experimental resolution is taken into account.

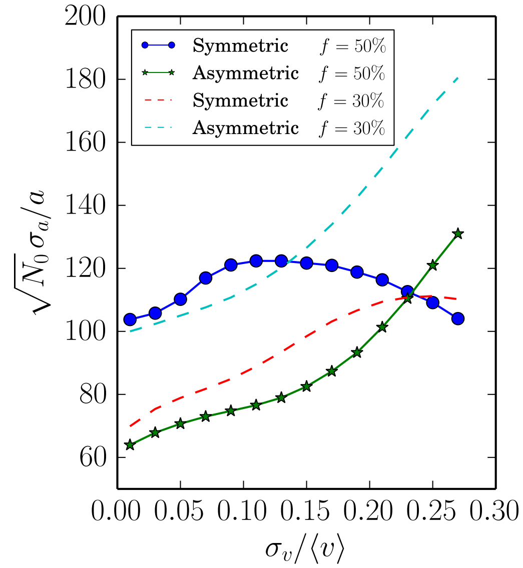

Figure 4.10. Rescaled inertial sensitivity, defined in equation (4.42). We compare the four Talbot-Lau configurations of the same total length, $L^{(\mathrm{TOT})} = 1\,\mathrm{m}$, defined in Figs. 4.8 and 4.7.

By virtue of their more regular behavior (see Fig. 4.2 and the associated discussion), asymmetric setups can employ higher open fractions, while still matching the visibility of the standard Talbot-Lau layout. To showcase this general behavior, we selected a realistic set of parameters that represent the best compromise between visibility and grating transmission for each setup. Our analysis suggests how to perform a fine tuning to find the optimal configuration for the specific experimental conditions. In particular the form of the speed distribution can vary widely between different applications [83]. The magnifying resonance conditions we described were known to exist for the Talbot-Lau interferometer [31, 105], but were never studied in detail especially with respect to their inertial sensing capabilities. Of particular interest, naturally relevant for the QUPLAS project, is the application of Talbot-Lau quantum interferometry to the measurement of the gravitational acceleration of neutral antimatter. In this emerging field of research [82, 112] the requirements on the optimization of the interferometric schemes are more stringent, therefore the advantages provided by the asymmetric configurations can be relevant.

In regards to the QUPLAS-0 setup for positron interferometry, the relevant figure of merit to be optimized is the interference fringe period for a given total interferometer length. We have shown how period-magnifying setups are best suited for this purpose. An asymmetric setup with $\eta = 5$ can produce $d_3 = 6\,\mu\mathrm{m}$ interference fringes in a total length of less than $70\,\mathrm{cm}$, at resonance for $E = 14\,\mathrm{keV}$ positrons. This fringe periodicity enables direct detection with nuclear emulsions, and is achieved with micrometric periodicity diffraction gratings. Therefore, this layout was chosen for the QUPLAS-0 phase, and will be described in details in the following chapters.

CHAPTER 5

Talbot-Lau interferometry with partially coherent beams

So far we made the assumption of a fully incoherent beam, implemented mathematecally by the requirement of a wide transverse speed (or momentum) distribution. This description is appropriate for weakly collimated beam with a large angular divergence. The Talbot-Lau setup still admits resonance conditions with high visibility even in this condition. This statement is valid as long as all the physical parameters (grating periods, distances) are taken to be exact and free of experimental uncertainty. To better evaluate the expected contrast of an interferometer when alignment errors are taken into account, a more realistic description of the particle beam is needed. A suitable model is proposed in [26]. We will start from a review of the required formalism, which we will prove to be fully equivalent to the Wigner function approach previously employed. The main difference which introduces more generality is a more accurate choice of the initial state Wigner function. A finite coherence length (i.e. a finite width of the transverse momentum distribution), as well as the convergent or divergent nature of the beam are taken into account. Moreover, we will move to a two dimensional description in the transverse plane, to account for relative rotations of the gratings, which have a sizable impact on the visibility.

The model [26] exploits the analogy with classical optics we already established. The particle beam is described as a *Gaussian Schell-model* (GSM) beam: a statistical distribution of Gaussian beam modes [127] that lends itself to a fully analytical treatment. Given a field $\phi(\mathbf{x}, z, t)$, we define its *mutual intensity function* as:

$$J(\mathbf{x}_a, \mathbf{x}_b; z) = \langle \phi^*(\mathbf{x}_a, z, t)\phi(\mathbf{x}_b, z, t)\rangle_t$$

where the vector $\mathbf{x}$ denotes coordinates in the plane transverse to the propagation direction z, and the angular brackets denote a time average over the statistical fluctuations of the field. The intensity on a plane at constant z is given by:

$$I(\mathbf{x}; z) = J(\mathbf{x}, \mathbf{x}; z)$$

In analogy with chapter 4, the mutual intensity is propagated through free space and through the two gratings. Specifically, free propagation follows *Zernike's propagation law* [128, 129]:

$$J(\mathbf{x}, \Delta\mathbf{x}; z) = \frac{1}{\lambda^2 z^2} \int d\Delta\mathbf{x}' \int d\mathbf{x}' e^{-(i2\pi/\lambda z)(\mathbf{x}'\Delta\mathbf{x}' - \mathbf{x}'\Delta\mathbf{x} - \mathbf{x}\Delta\mathbf{x}' + \mathbf{x}\Delta\mathbf{x})} J(\mathbf{x}', \Delta\mathbf{x}'; 0), \quad (5.1)$$

where the convenient set of variables $\mathbf{x} = (\mathbf{x}_a + \mathbf{x}_b)/2$ and $\Delta\mathbf{x} = \mathbf{x}_b - \mathbf{x}_a$ has been introduced. The parameter λ is the wavelength of the classical field, to be identified with the de Broglie wavelength in a semi-classical description of a matter-wave beam. The grating, given its transmission function $\mathcal{T}(\mathbf{x})$ acts on J as:

$$\widetilde{J}(\mathbf{x}, \Delta\mathbf{x}; z) = \mathcal{T}^* \left(\mathbf{x} - \frac{\Delta\mathbf{x}}{2}\right) \mathcal{T} \left(\mathbf{x} + \frac{\Delta\mathbf{x}}{2}\right) J(\mathbf{x}, \Delta\mathbf{x}; z), \tag{5.2}$$

using the tilde notation in analogy to chapter 4. However, a comparison of equation (5.2) with the grating transformation for the Wigner function (4.6), suggests that the analogy is more profound. The two expressions would look formally identical (apart from the vector nature of the arguments which was disregarded in the previous one-dimensional treatment) if the following relation holds:

$$J(\mathbf{x}, \Delta\mathbf{x}; z) = \int e^{-\frac{i\mathbf{p}\Delta\mathbf{x}}{\hbar}} W(\mathbf{x}, \mathbf{p}; z) d\mathbf{p}, \tag{5.3}$$

namely the mutual coherence and Wigner functions are linked by Fourier transformation. This formal correspondence is not surprising given that the Wigner function description is fully equivalent to a solution of the Schrödinger equation. Recall then the analogy between the latter and the Helmholtz equation of scalar diffraction theory, from which the mutual coherence formalism and the related propagation laws descend. As an additional consistency check one should prove that the evolution equation (5.1) induces the correct propagation law for the Wigner function. Starting from (5.1), taking the Fourier transform on both sides yields:

$$\begin{aligned} \int e^{-\frac{i\mathbf{p}\Delta\mathbf{x}}{\hbar}} W(\mathbf{x}, \mathbf{p}; z) d\mathbf{p} = \frac{1}{\lambda^2 z^2} \int d\Delta\mathbf{x}' \int d\mathbf{x}' \int d\mathbf{p}\, e^{-(i2\pi/\lambda z)(\mathbf{x}'\Delta\mathbf{x}' - \mathbf{x}'\Delta\mathbf{x} - \mathbf{x}\Delta\mathbf{x}' + \mathbf{x}\Delta\mathbf{x})} \times \\ \times\, e^{-\frac{i\mathbf{p}\Delta\mathbf{x}'}{\hbar}} W(\mathbf{x}', \mathbf{p}; 0). \end{aligned}$$

Grouping terms proportional to $\Delta\mathbf{x}'$ in the exponential phase factor on the right and performing the integration (a change of variables is convenient $d\Delta\mathbf{x}' = \frac{\lambda^2 z^2}{4\pi^2} d\mathbf{s}$) yields a Dirac delta function and the factor $\frac{1}{\lambda^2 z^2}$ simplifies:

$$\int e^{-\frac{i\mathbf{p}\Delta\mathbf{x}}{\hbar}} W(\mathbf{x}, \mathbf{p}; z) d\mathbf{p} = \int d\mathbf{x}' \int d\mathbf{p}\, \delta \left(\mathbf{x}' - \mathbf{x} + \frac{\mathbf{p}\lambda z}{2\pi\hbar}\right) e^{-(i2\pi/\lambda z)(-\mathbf{x}'\Delta\mathbf{x} + \mathbf{x}\Delta\mathbf{x})} W(\mathbf{x}', \mathbf{p}; 0).$$

Integration over $d\mathbf{x}'$ gives:

$$\int e^{-\frac{i\mathbf{p}\Delta\mathbf{x}}{\hbar}} W(\mathbf{x}, \mathbf{p}; z) d\mathbf{p} = \int e^{-\frac{i\mathbf{p}\Delta\mathbf{x}}{\hbar}} W \left(\mathbf{x} - \frac{\mathbf{p}\lambda z}{2\pi\hbar}, \mathbf{p}; 0\right) d\mathbf{p},$$

which is almost the desired result. To complete the connection we use the definition of the de Broglie wavelength $\lambda = \frac{2\pi\hbar}{mv} = \frac{2\pi\hbar z}{mt}$, where the usual assumption of classical point-particle like propagation along the z direction is exploited. Finally, we are left with:

$$W(\mathbf{x}, \mathbf{p}; z = vt) = W \left(\mathbf{x} - \frac{\mathbf{p}t}{m}, \mathbf{p}; 0\right), \tag{5.4}$$

completely equivalent to equation (4.4) for the evolution of the Wigner function under the free particle Hamiltonian ($a = 0$ in equation (4.4)).

This result confirms that the interpretation of the mutual coherence function as a Fourier transform of a Wigner function is sound in this context, and that this formulation is thus fully consistent with our previous treatment. Moreover, the correspondence ensures that the influence of an external acceleration (which was not considered in [26]) is unchanged for partially coherent beams.

5.1 Analytical expression for the intensity

We now focus on the specific choice of a *Gaussian Schell-model* beam as the initial state, following [26]. The mutual intensity function reads[1]:

$$J(\mathbf{x}, \Delta\mathbf{x}; 0) = e^{-\pi\left[\mathbf{x}^2/w_0^2 + \Delta\mathbf{x}^2/l_0^2 + 2i\mathbf{x}\Delta\mathbf{x}/(\lambda r_0)\right]} \tag{5.5}$$

Three parameters define the initial state and are an input to the model:

- w_0, the *beam width*
- l_0, the *transverse coherence length*
- r_0, the *radius of curvature* of the wavefront

More insight on the physical meaning of these parameters will be given in section 5.2 where we discuss how they can be measured experimentally. Via Fourier transformation (see 5.3), the Wigner function corresponding to this choice can be calculated exactly as a standard Gaussian integral:

$$W(\mathbf{x}, \mathbf{p}; 0) = \frac{l_0^2}{4\pi\sqrt{\pi}\hbar^2} e^{-\pi\mathbf{x}^2\left(\frac{1}{w_0^2} + \frac{l_0^2}{\lambda^2 r_0^2}\right) - \frac{\mathbf{p}^2 l_0^2}{4\pi\hbar^2} + \frac{\mathbf{x}\mathbf{p} l_0^2}{\hbar\lambda r_0}} \tag{5.6}$$

One can take the limit $r_0 \to \infty$ and $w_0 \to \infty$ (plane wave with flat envelope) to obtain:

$$W(\mathbf{x}, \mathbf{p}; 0) = \frac{l_0^2}{4\pi\sqrt{\pi}\hbar^2} e^{-\frac{\mathbf{p}^2 l_0^2}{4\pi\hbar}}, \tag{5.7}$$

namely the transverse momentum distribution has a Gaussian form with $\sigma_p \propto \hbar/l_0$. We thus recover the notion that the coherence length is inversely proportional to the width of the transverse momentum distribution. In chapter 4 we started from a generic distribution and eventually took the limit $\sigma_p \to \infty$. It is apparent that this choice of initial state is more general and effectively describes a *partially coherent* beam ($l_0 > 0$).

Having established the form of the initial state, either the Wigner function or the mutual intensity function evolution formalism has to be applied. In the latter case, a useful property of GSM beams [26] is that free propagation for a distance z results in the same functional form of equation (5.5), with the evolved parameters:

$$\begin{aligned}
w(z) &= w_0\sqrt{\left(1 + \frac{z}{r_0}\right)^2 + \left(\frac{\lambda z}{w_0 l_0}\right)^2} \\
l(z) &= l_0\sqrt{\left(1 + \frac{z}{r_0}\right)^2 + \left(\frac{\lambda z}{w_0 l_0}\right)^2} \\
r(z) &= z\left(\frac{(1 + z/r_0)^2 + (\lambda z/w_0 l_0)^2}{(z/r_0)(1 + z/r_0) + (\lambda z/w_0 l_0)^2}\right)
\end{aligned} \tag{5.8}$$

in place of w_0, l_0, r_0. Therefore for a general distance z the J function reads:

$$J(\mathbf{x}, \Delta\mathbf{x}; z) = e^{-\pi\left[\mathbf{x}^2/w(z)^2 + \Delta\mathbf{x}^2/l(z)^2 + 2i\mathbf{x}\Delta\mathbf{x}/(\lambda r(z))\right]}. \tag{5.9}$$

---

[1] To simplify the notation, an isotropic beam (that is, cylindrically symmetric along the optical axis) is assumed. We will clarify the different impact of beam coherence in the two transverse directions on alignment requirements in the next chapter.

Intensity on the transverse plane is calculated in this formalism as:

$$I(\mathbf{x}) = J(\mathbf{x}, 0; z). \tag{5.10}$$

The lengthy calculation of the intensity after interaction with the two gratings and propagation to the detector plane is described in [26]. In particular the full result assuming an anisotropic two-dimensional Gaussian beam ($w_{x0} \neq w_{y0}$, and similarly for the other parameters), and a rotation of the second grating along the optical axis by an angle ϕ, is given. However, in an attempt to reproduce the results reported in [26], I discovered that the formula was unable to replicate several of the many examples provided (see Fig. 5.1, for an example). Therefore I independently performed the full analytical calculation and found out that the expression contains a few typos. Nevertheless, I remark that all the results contained in the paper and the associated analysis are correct[2]. Following the notation of [26], the intensity distribution after crossing the two gratings and propagation to the observation plane (see Fig. 4.1) is in the form of a quadruple sum:

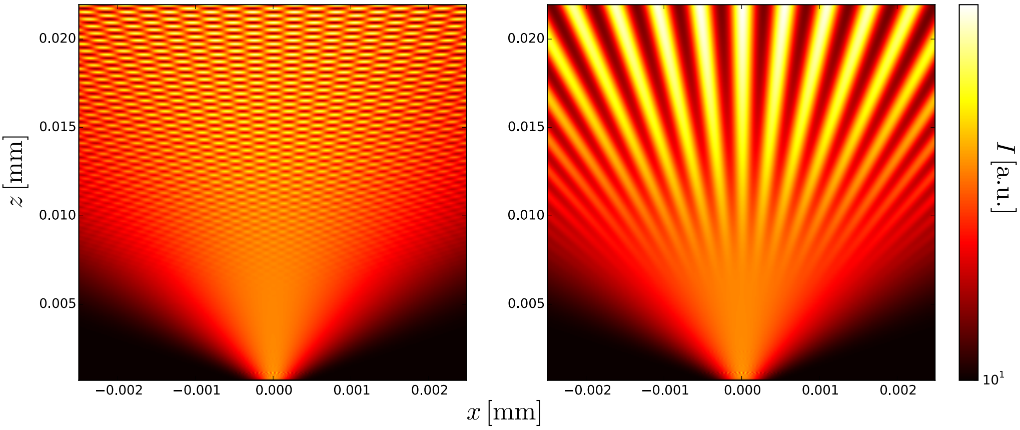

Figure 5.1. On the left, an attempt to reproduce Figure 6 from [26] with equation 18 from the same paper. On the right, results correctly reproduced with the correct phase factor given in equation (5.12) (full expression reported in Appendix B).

$$I(\mathbf{x}; z_3) = \frac{w_{x0} w_{y0}}{w_y(z_3) w_x(z_3)} \sum_{m,m',n,n'=-\infty}^{\infty} a^*_{m'} a_m b^*_{n'} b_n D^{\overline{m}}_{\overline{n}}(\mathbf{x}, z_3, w_{x,y}(z_3)) F^{\Delta m}_{\Delta n}(\mathbf{x}, z_3, r_{x,y}(z_3)) \times \\ \times P^{\overline{m},\Delta m}_{\overline{n},\Delta n}(z_3, r_{x,y}(z_3)) V^{\Delta m}_{\Delta n}(\mathbf{x}, z_3, l_{x,y}(z_3)). \tag{5.11}$$

The evolved parameters, different in the two directions (for instance $w_x(z)$ is the beam width along x at the distance z from the plane on which the initial value $w_{x0} = w_x(0)$ is measured) are given in equation (5.8). The coefficients a_k, b_k are Fourier series expansion coefficients of the transmission function of the first and second grating respectively (see for instance equation (4.20)). Auxiliary indexes $\Delta m = m - m'$ and $\overline{m} = (m + m')/2$ (similarly for n, n') are introduced for convenience. The distance z_3 is measured from the initial plane located at $z = 0$ to the observation plane.

---

[2] The PhD thesis of one of the authors of the paper is available [130] and contains the numerical code used to carry out the simulations in [26]. The analytical expression that I was able to infer from the code agrees with the result of my independent calculation, while it differs from the equation published in [26].

The expression for the four phase factors is complicated and can be found in equations 18b-18e in [26]. However, given the aforementioned issues, we report here the correct expression for the factor $P^{\overline{m},\Delta m}_{\overline{n},\Delta n}(z_3, r_{x,y}(z_3))$ (equation 18d in [26]), and for the sake of completeness, the full expression is also given in Appendix B together with some details on the numerical implementation.

$$P^{\overline{m},\Delta m}_{\overline{n},\Delta n}(z_3, r_{x,y}(z_3)) = \exp\left[\frac{2i\pi\lambda z_{13}\Delta m}{d_1}\left(\frac{\overline{n}\cos\phi}{d_2}\frac{z_{23}}{z_{13}} + \frac{\overline{m}}{d_1}\right)\left(1 - \frac{z_{13}}{r_x(z_3)}\right)\right] \times$$
$$\times \exp\left\{\frac{2i\pi\lambda z_{23}\Delta n}{d_2}\left[\frac{\overline{m}\cos\phi}{d_1}\left(1 - \frac{z_{13}}{r_x(z_3)}\right) + \frac{\overline{n}}{d_2} - \frac{\overline{n}z_{23}}{d_2}\left(\frac{\cos^2\phi}{r_x(z_3)} + \frac{\sin^2\phi}{r_y(z_3)}\right)\right]\right\} \quad (5.12)$$

The distances $z_{13} = L(\eta + 1)$ and $z_{23} = \eta L$ are measured from the observation plane to the first (period d_1) and to the second (period d_2) grating respectively. To make the connection with the notation of section 4, the distances are easily expressed in terms of L and η. As a final consistency check for the equivalence of this formalism with the Wigner function description it can be proven that the full expression, equation (5.11), in the limits of a fully incoherent wide beam with no divergence ($l_0 \to 0$, $w_0 \to \infty$, $r_0 \to \infty$) and $\phi = 0$ reduces exactly to equation (4.15) for the intensity. The calculation is lengthy and not particularly instructive, therefore it is not reported in this thesis.

5.2 Measuring the input parameters

Application of the model to a realistic experimental setup requires the measurement of the input parameters w_0, l_0, r_0. To this end, we propose a method that exploits the free evolution equations (5.8) to infer the coherence length from the transverse beam size alone. For a freely evolving, isotropic, GSM beam described by equation (5.9), the transverse intensity profile has the following Gaussian form:

$$I(\mathbf{x}; z) = J(\mathbf{x}, 0; z) = e^{-\pi\frac{\mathbf{x}^2}{w(z)^2}}. \quad (5.13)$$

This is usually a good approximation for electron beams (and for the L-NESS positron beam as well [14]), and also captures the relevant features of slit collimated atomic beams [131]. Note that with the chosen conventions $w(z) = \mathrm{FWHM(z)}\sqrt{\frac{\pi}{\log 2}}\frac{1}{2} \approx 1.06\,\mathrm{FWMH(z)}$, where the usual definition of full width at half maximum is implied. A close look at equations (5.8) reveals that the $l(z)$ and $w(z)$ have the same functional dependence on z. For this reason a good figure of merit of the overall *degree of coherence* is the ratio [26] $\beta = \frac{l(z)}{w(z)} = \frac{l_0}{w_0}$, which is left unchanged as the beam propagates. In Figure 5.2 an example of the behaviour of the functions $w(z)$, $r(z)$ and $l(z)$ is reported. Numerical values are chosen to represent the L-NESS positron beam, yet the qualitative features apply to most collimated particle beams. The beam width parameter $w(z)$ has a minimum (*beam waist* using the terminology of classical optics) at the position z_w. Differentiation with respect to z yields:

$$\left.\frac{dw(z)}{dz}\right|_{z=z_w} = 0 \iff \left(1 + \frac{z_w}{r_0}\right)\frac{1}{r_0} + \frac{\lambda^2 z_w}{w_0 l_0} = 0.$$

At the position z_w which satisfies the condition above, the denominator of $r(z)$ in equation (5.8) vanishes. Therefore if we set the reference plane (where initial conditions for

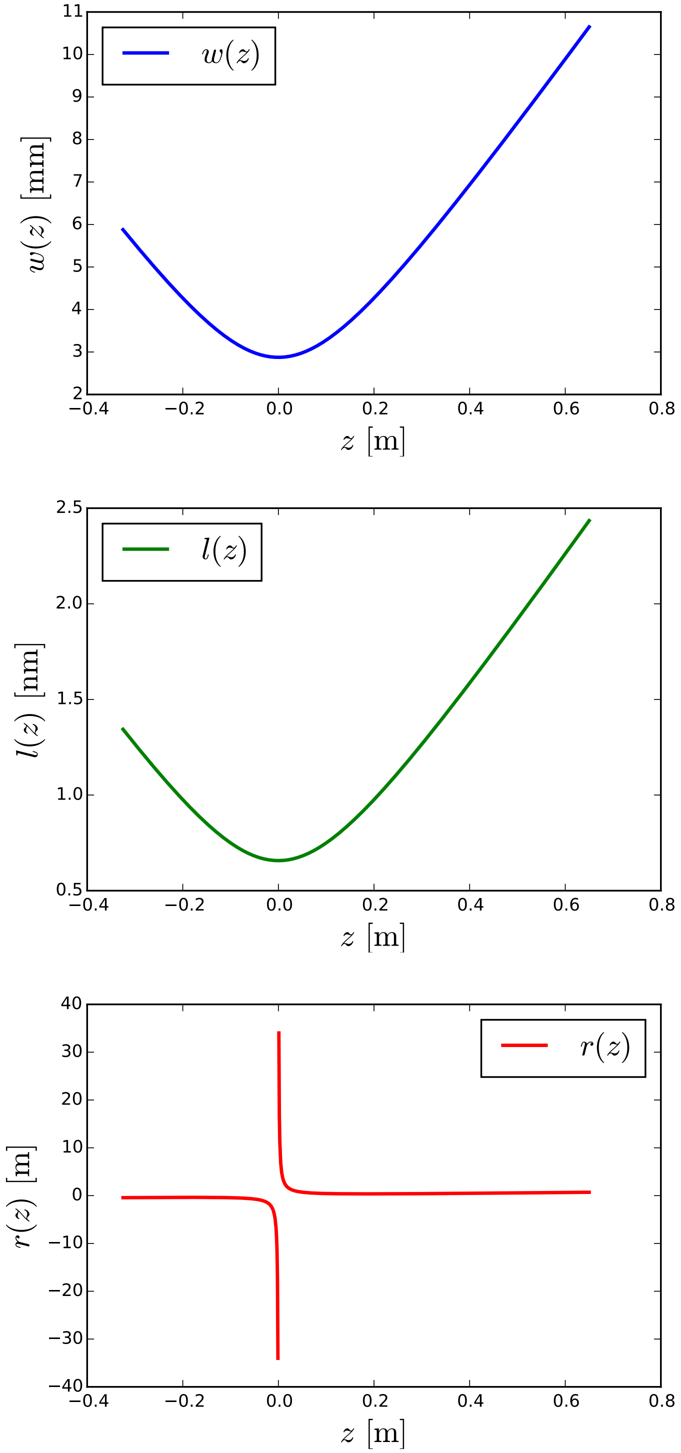

Figure 5.2. Plot of the evolution of the model parameters given by equations (5.8). The chosen initial values are chosen to be compatible with the L-NESS beam, specifically at $z = 0$ the numerical values are $l_0 = 0.65\,\text{nm}$ and $w_0 = 2.8\,\text{mm}$. At the beam waist (see text for a discussion) the radius of wavefront curvature diverges to $\pm\infty$.

the propagation are evaluated) to coincide with the position of the beam waist z_w, the $w(z)$ and $l(z)$ evolution equations onwards from that plane simplify to:

$$w(z) = w_0^* \sqrt{1 + \left(\frac{\lambda z}{w_0^* l_0^*}\right)^2}$$
$$l(z) = l_0^* \sqrt{1 + \left(\frac{\lambda z}{w_0^* l_0^*}\right)^2}. \tag{5.14}$$

The initial values w_0^* and l_0^* are taken on the beam waist plane. If one can locate the waist plane experimentally, and measure both w_0^* and the width $w(z_r)$ on a plane located z_r downstream the waist, then the first line of equation (5.14) can be solved for l_0^*.

Another interesting link between the model parameters and physically measurable properties is given by the divergence angle θ, measured far away from the beam waist (see Fig.5.3), namely:

$$\tan\theta = \lim_{z\to\infty} \frac{w(z)}{z} = \frac{w_0^*}{z}\frac{\lambda z}{w_0^* l_0^*} = \frac{\lambda}{l_0^*}.$$

This result is consistent with the classical intuition for the coherence length of optical radiation far away from an incoherent source. Via the Wigner function formalism the coherence length is also seen to be inversely proportional to the width of the transverse momentum distribution, revealing a sensible interpretation in the context of particle beams. To get a grasp of the length scales involved, typical input values of l_0^* and w_0^* measured for the L-NESS beam without any additional collimation are:

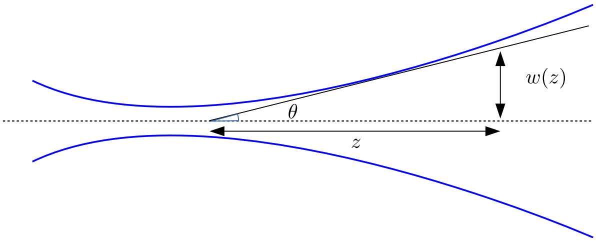

Figure 5.3. Schematic depiction of the geometrical propagation of a partially coherent particle beam. The divergence angle θ is typycally in the range of a few mrad for weakly collimated incoherent beams such as the L-NESS beam.

$$\begin{cases} w_0^* & \approx 2.4\,\mathrm{mm} \\ l_0^* & \approx 0.7\,\mathrm{nm} \qquad \text{(L-NESS beam reference parameters)} \end{cases} \tag{5.15}$$

Additional detals on the measurement techniques are discussed in Part III. By tuning the beam focusing these values can be controlled and slightly tuned, but not in such a way to significantly alter the features of the interferometric visibility. It is apparent that the global degree of coherence, $\beta \approx 10^{-6}$ is very small. As a matter of fact the β parameter is several orders of magnitude smaller with respect to similar experiments with partially coherent electron beams [132]. Those small-size beams were produced with electron guns adapted from electron microscope columns.

CHAPTER 6

Modelling QUPLAS-0 on the L-NESS beam

6.1 The reference QUPLAS-0 interferometer

A period-magnifying asymmetric Talbot-Lau configuration was chosen for the QUPLAS-0 phase of the experiment. The choice was motivated by the properties highlighted in chapter 4: the capability to produce the largest interference fringe period (sufficiently large for direct detection with nuclear emulsions) when total length is limited (to approximately $80\,\mathrm{cm}$ in our chamber). Asymmetric setups are also able to work with large open fraction gratings, useful to reduce intensity losses. An alternative option fulfilling some of the above requirements is the so-called *lau interferometer* regime [26]. This layout essentially corresponds to what we call asymmetric Talbot-Lau regime, with very large ($\eta \approx 500$ [132]) magnification factors. This idea was discarded because it required a more coherent beam (see the discussion in [26]), and gratings with approximately $200\,\mathrm{nm}$ periodicity. Such gratings were initially considered to be difficult to obtain commercially and impossible to manufacture in our facilities.

With regards to the issue of coherence, the paper [26] suggests that in the *Lau interferometer* regime, where the observation plane is in the far field of the second grating, the following requirement applies to the coherence length at the detector plane $l_{\mathrm{det}} > \frac{L_1\lambda}{d_1}$, whereas the standard Talbot-Lau setup does not need to meet this criterion. The magnification factor η can vary continuously, thus one expects that the transition between the two regimes should be smooth. In fact numerical simulations suggest that for low ($\eta \lesssim 10$) magnification factors the device indeed operates in an intermediate regime where some magnification is provided but the less demanding coherence requirements of the standard Talbot-Lau interferometer still apply. However, although it is appropriate to state that a Talbot-Lau interferometer works with a fully incoherent beam, there is a delicate interplay between beam coherence, knowledge of experimental parameters

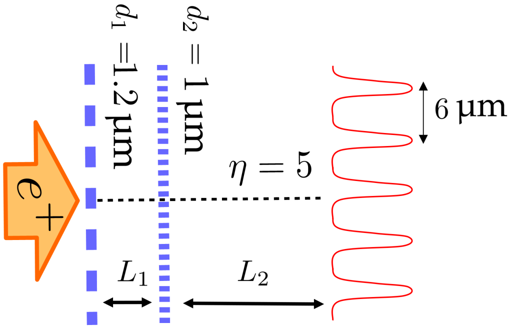

Figure 6.1. Scheme of the chosen final configuration for the QUPLAS-0 interferometer and nominal values of the parameters.

such as the grating periods, and alignment requirements. In this chapter we will tackle this issue in details, focusing specifically on our reference configuration and beam parameters. The nominal values defining the ideal QUPLAS-0 configuration which will be used for the numerical simulations are defined as follows (see also Fig. 6.1):

$$\begin{cases} d_1 = 1.2 d_2 = 1.2\,\mu\mathrm{m} \\ E = 14\,\mathrm{keV} \\ \lambda = 1.03 \times 10^{-11}\,\mathrm{m} \\ L_T = \frac{d_2^2}{\lambda} = 9.71\,\mathrm{cm} \\ L_1 = \frac{d_1}{d_2} L_T = 11.65\,\mathrm{cm} \\ L_2 = \frac{L_1}{d_1/d_2 - 1} = 5L_1 = 58.25\,\mathrm{cm} \\ d_3 = \frac{d_1}{d_1/d_2 - 1} = 6.0\,\mu\mathrm{m} \end{cases} \qquad \text{(QUPLAS-0 nominal parameters)} \qquad (6.1)$$

The above expressions are consistent with the resonance conditions discussed in section 4.1.1, adapted to the notation of Fig. 6.1, more suited to a discussion of alignment from an experimental point of view.

The grating periods are fixed input values known with experimental uncertainty. To achieve maximum visibility, the ratio of the two distances $\eta = \frac{L_2}{L_1}$ should satisfy the resonance conditions (4.18) with $q = 1$, namely: $\eta^* = \frac{1}{d_1/d_2 - 1}$. It is worth noting that the small spread in λ of our beam (of the order of 1% or less) was found to be completely negligible by numerical simulations, therefore the beam will be considered monochromatic throughout all the analysis.

6.2 Alignment requirements

The theoretical model discussed in the previous sections will now be applied to the QUPLAS-0 setup (6.1), using the reference parameters for the partially coherent L-NESS beam (5.15). The goal is to estimate the needed requirements on the alignment of the interferometer.

Longitudinal alignment

We start by addressing the issue of longitudinal alignment, that is how precisely the distances L_1 and L_2 should be controlled.

So far we assumed for simplicity an isotropic beam, that is with cylindrical symmetry along the propagation axis. However, for the discussion to follow it is necessary to distinguish the role of beam coherence in the two directions orthogonal to the optical axis. In keeping with the notation of the previous chapters, x labels the coordinate parallel to the grating periodicity, while y is the direction parallel to the grating slits. First of all, the predicted shape of the interference pattern at resonance is shown in Fig. 6.2. This is a one-dimensional pattern, as the approximation of indefinitely extended slits is still adopted. The expected contrast in ideal conditions is very high ($C \approx 94\%$), and the periodicity is exactly $d_3 = 6\,\mu\mathrm{m}$ as expected. We now examine contrast as a function of the total length $L^{(\mathrm{TOT})} = L_1 + L_2$ of the setup, assuming that resonance conditions are satisfied ($L_2 = \frac{L_1}{d_1/d_2 - 1} = \eta^* L_1$). The relevant plot is shown in Fig. 6.3. In Fig. 6.4 the contrast as a function of the two lengths L_1 and L_2 separately is also shown. The result

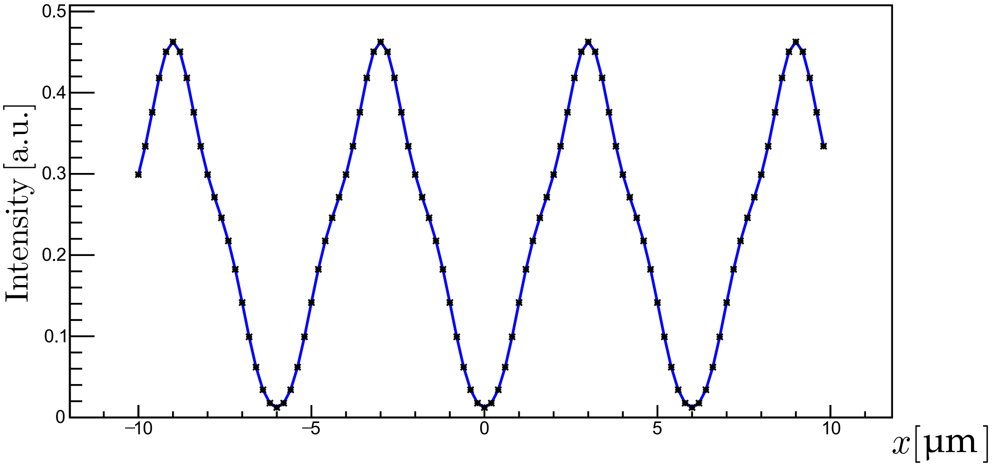

Figure 6.2. Calculated shape of the interference pattern at resonance using the QUPLAS-0 nominal values (6.1) and the reference L-NESS beam parameters (5.15), assuming that the first grating is placed on the beam waist. Translational invariance in the direction of the slits is assumed, therefore the pattern is presented as a one dimensional function of position in the x direction transverse to the optical axis.

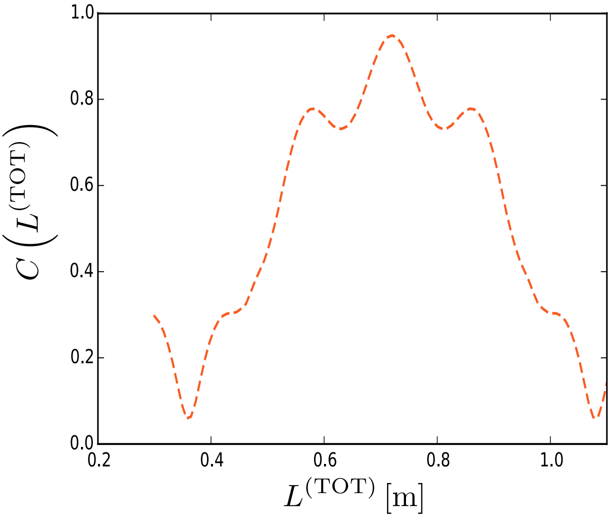

Figure 6.3. Contrast as a function of total length, fixing L_1/L_2 to resonance conditions, $C\left(L^{(\mathrm{TOT})}\right)\Big|_{\eta=\eta^*}$. Peak visibility occurs at the expected nominal value. The function is however very broad. Therefore, for fixed λ, small errors in the total length weakly affect visibility. The only relevant parameter is effectively the ratio L_2/L_1 (see Fig. 6.4). Similarly, a broad peak would be observed for $C(\lambda)$ at fixed geometry, which justifies the assumption of a monochromatic beam.

clarifies how the apparatus is robust with respect to errors in the total length, while the ratio L_2/L_1 strongly affects the visibility. It is therefore appropriate to adopt a point of view where L_1 is fixed to a sensible value (see eq. (6.1)), measured experimentally to a given uncertainty[1], namely $L_1 = \overline{L}_1 \pm \delta_{L_1}$. The relevant quantity to consider is then the contrast as a function of the distance of the detector plane from the second grating, namely $C(L_2)$. This function for the nominal parameters is displayed in Fig. 6.7, which shows that the behavior is well described by a Gaussian shape of the form:

Figure 6.4. Contrast as a function of L_1 and L_2.

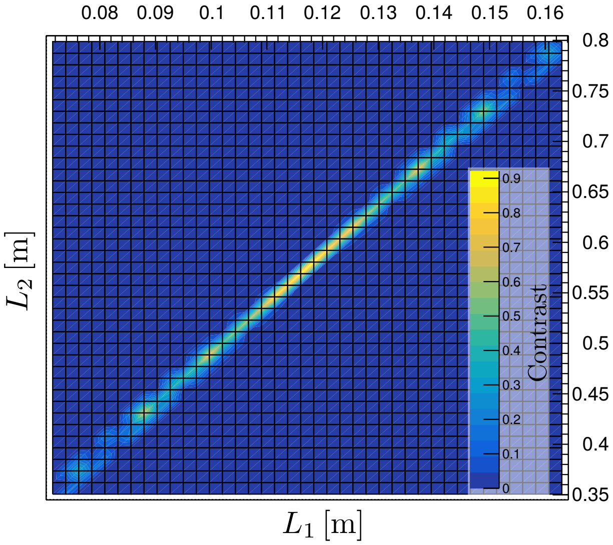

Figure 6.5. Point of view adopted for discussing tolerance to longitudinal misalignments.

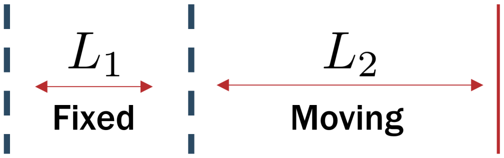

$$C(L_2) = C_0 e^{-\frac{(L_2-\overline{L}_2)^2}{2\sigma^2_{L_2}}}, \tag{6.2}$$

where C_0 is the peak contrast value. The location of the mean value of the Gaussian, $\overline{L}_2$, physically corresponds to the center of the region along the optical axis where high contrast fringes are visible: the optimal position of the detector plane. The width of this region is proportional to σ_{L_2}, hence this parameter quantifies the robustness of the interferometer with respect to detector positioning. Fig. 6.6 should illustrate the physical intuition underlying this statement. The parameter $\overline{L}_2$ is naturally the distance which satisfies the resonance conditions. It depends, as stated in equation (6.1), on the grating periods, which are affected by an experimental error. Therefore, setting $d_{1,2} = \overline{d}_{1,2} \pm \delta_{d_{1,2}}$, we obtain

$$\overline{L}_2 = \frac{\overline{L}_1}{\overline{d}_1/\overline{d}_2 - 1}.$$

---

[1] In this section experimental uncertainties will be denoted with the letter δ.

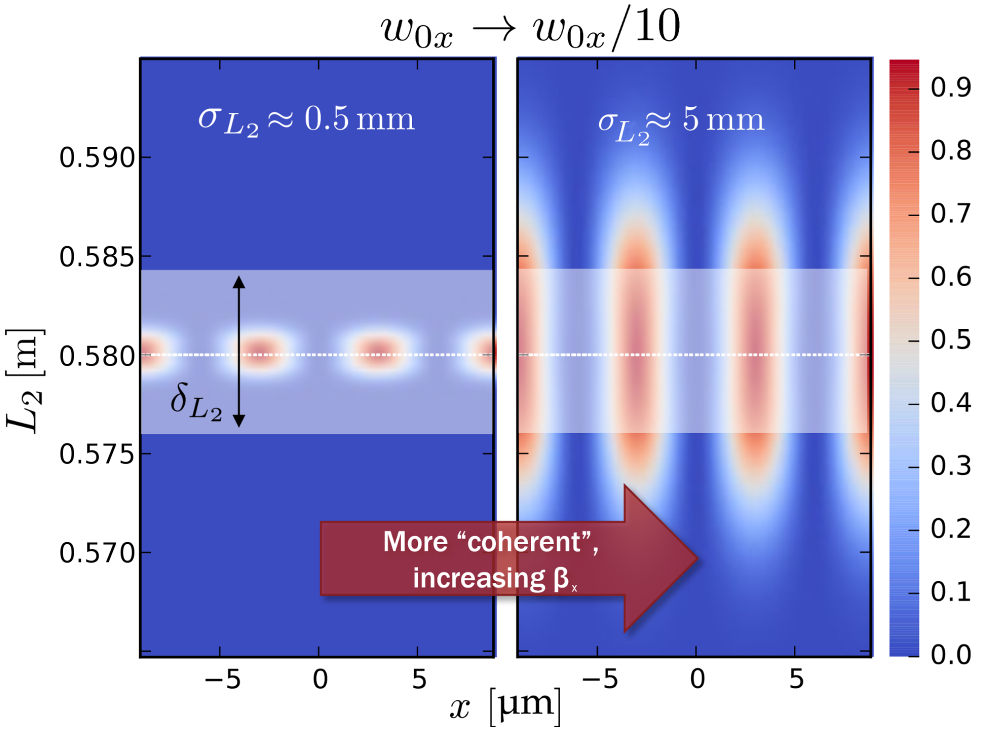

Figure 6.6. Intensity in color scale is represented as a function of the transverse coordinate x and of detector position L_2, in the region of the main resonance, using the reference beam and interferometer parameters from Eq. (6.1). From the left to the right panel the beam width is reduced ($w_{0x} \rightarrow w_{0x}/10$) to show the effect of increased coherence. The shaded white band represents schematically the region over which the contrast peak ($\overline{L}_2$, the ideal detector location) is expected, the width of said region is proportional to the experimental uncertainty δ_{L_2}. This depends on experimental errors on the measurements of L_1 and of the grating periods (see equation (6.3)).

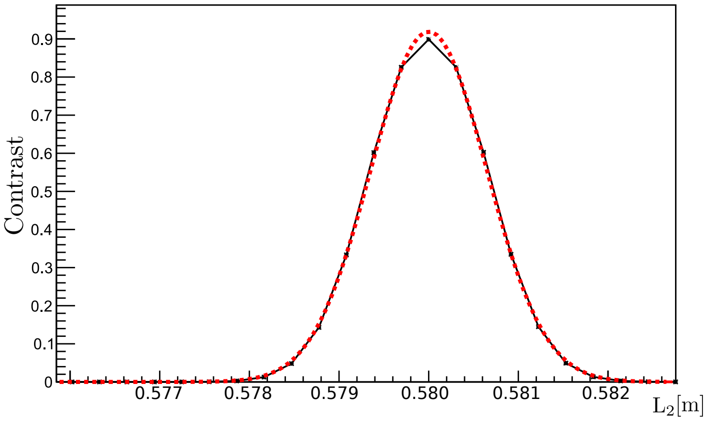

Figure 6.7. Contrast $C(L_2)$ as a function of detector position for L_1 fixed to the nominal value (6.1). The numerical result is well fit by a Gaussian function of the form of equation (6.2). Specifically, for the nominal QUPLAS-0 parameters, $\sigma_{L_2} \approx 0.6\,\mathrm{mm}$.

Applying standard error propagation, the uncertainty on $\overline{L}_2$, that is on the position where the detector should be placed, given all the other parameters, reads:

$$\delta_{L_2} = \overline{L}_2 \sqrt{\left(\frac{\delta_{L_1}}{L_1}\right)^2 + \left(\frac{\delta_r}{r-1}\right)^2} \tag{6.3}$$

where for convenience we introduced the ratio of the grating periods $r = \frac{\overline{d}_1}{d_2} \pm \delta_r$. The ideal detector position $\overline{L}_2$ acquires therefore an uncertainty that depends on the measurement precision of r and $\overline{L}_1$. The error parameter δ_{L_2} must be compared with the width of the high contrast region, σ_{L_2}, to estimate the feasibility of a single exposure experiment[2]. Consider the limiting cases: if $\sigma_{L_2} \ll \delta_{L_2}$, as sketched in the left panel of Fig. 6.6, the uncertainty on the theoretical ideal detector position is larger than the alignment error tolerated by the setup. Therefore, a single exposure experiment is essentially unfeasible. If the converse is true ($\sigma_{L_2} \gg \delta_{L_2}$) as suggested in the right panel, then high contrast can be retrieved with sizeable probability in a single attempt. The width σ_{L_2} is controlled by the parameters of the partially incoherent beam in the x direction. In figure 6.6, it is shown that by reducing the beam width w_{0x} by an order of magnitude, and leaving all other parameters intact, σ_{L_2} increases by approximately the same factor. In particular in Part III, we will show how σ_{L_2} is essentially proportional to the coherence length on the detector plane in the x-direction, namely l_x^{det}.

Rotational alignment

We now consider the issue of rotational alignment between the grating slits. The intensity given by equation (5.11) depends on the angle ϕ formed by the slits (see the sketch in the inset of Fig. 6.8), therefore it is possible to calculate numerically the contrast dependence on the angle $C(\phi)$. Alternatively, following [26], an useful approximate expression reads:

$$C(\phi) \propto e^{-\pi\left(\frac{\lambda L_2 \phi}{d_2 l_y^{\mathrm{det}}}\right)^2}. \tag{6.4}$$

A Gaussian dependence is predicted, with standard deviation

$$\sigma_\phi = \frac{1}{\sqrt{2\pi}} \frac{d_2 l_y^{\mathrm{det}}}{\lambda L_2}, \tag{6.5}$$

where l_y^{det} denotes the coherence length in the direction parallel to the length of the slits, on the detector plane. In Fig. 6.8 a comparison between equation (6.4) and the full numerical calculation shows very good agreement. For the nominal QUPLAS-0 beam and interferometer parameters the alignment tolerance is $\sigma_\phi \approx 200\,\mu\mathrm{rad}$. We remark that this is controlled by beam coherence in the y direction (see equation (6.5)). Results from a Monte Carlo simulated moiré deflectometer with the same geometrical features are also shown in Fig. 6.8. Although peak contrast is lower, the angular dependence is comparable. Therefore this phenomenon has a classical counterpart, and cannot be used to discriminate genuine quantum interference from moiré shadow effects (at least not without a very precise measurement and a more careful simulation of the moiré setup). It is also useful to compare expression (6.4) with the naive expectation based on purely

---

[2] We recall that for QUPLAS-0 we plan to use nuclear emulsion detectors, that do not provide an online feedback. Naturally, a scan of several exposures can be considered. Careful evaluation of the parameters δ_{L_2} and σ_{L_2} would allow to optimize the number of exposures needed to effectively cover a wide region along z.

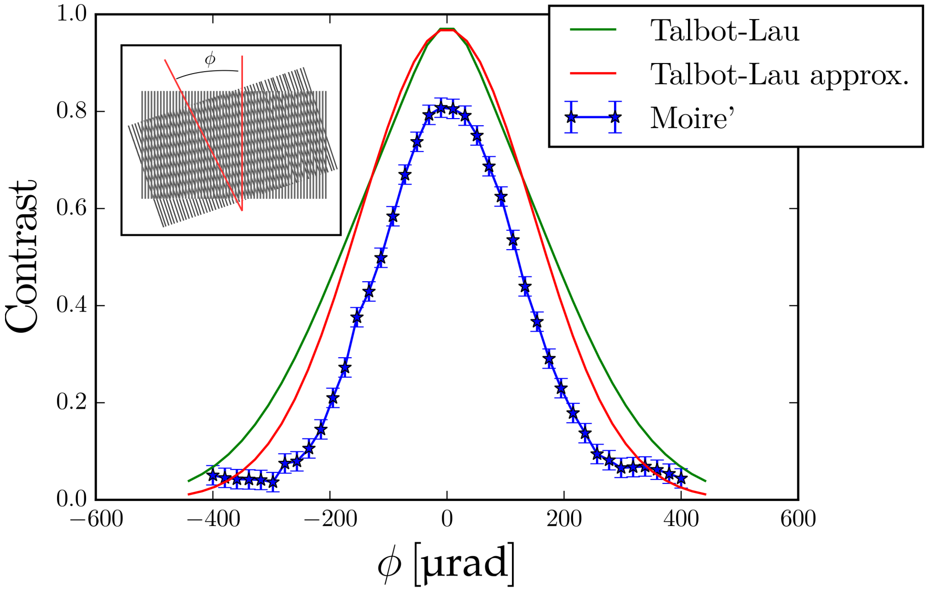

Figure 6.8. Contrast C as a function of the misalignment angle ϕ between the gratings, as sketched in the inset. For the Talbot-Lau setup, the nominal QUPLAS-0 parameters have been used. Results of a Monte Carlo simulated moiré deflectometer with the same geometrical features are also shown.

geometrical considerations. The slits of the first grating in a (standard, symmetric for symplicity) Talbot-Lau interferometer can be modeled as a collection of point sources which sum up incoherently to produce the interference fringes [1, 2]. It can be calculated [2, 21], that a transverse displacement Δx in the x direction of a point source induces a displacement Δx in the fringe pattern. A small rotation by an angle ϕ, if the slits have length h, produces a displacement $\Delta x \propto h\phi$. The maximum tolerable displacement is of the order of the fringe period, namely $d = d_1 = d_2$. Therefore, an alignment tolerance $\phi < \frac{d}{h}$ is estimated. Assuming that the beam is larger than h, then as a rough approximation, diffraction from an aperture with width h, produces a coherence length proportional to the distance $l_y^{\mathrm{det}} \approx L_2\lambda/h$. Substituting into Equation (6.5) reduces it to $\sigma_\phi \propto \frac{1}{\sqrt{2\pi}}\frac{d}{h}$, in qualitative agreement with the naive estimate.

To conclude this section we remark that, while it is correct to state that a Talbot-Lau interferometer produces high contrast fringes regardless of the coherence of the beam, it must be stressed that as $\beta \to 0$, the region of space where high contrast is detectable becomes narrower. Therefore requirements locating an positioning the grating and detector planes become very strict. Angular alignment requirements are similarly affected. More specifically, coherence length in the x direction controls the robustness of the apparatus with respect to longitudinal misalignments σ_{L_2}, whereas the coherence length in the y direction controls the tolerance to angular misalignments between the grating slits σ_ϕ. This behavior is not peculiar of the asymmetric setup and the same exact reasoning applies to the standard setup with the appropriate formulas for the resonance conditions.

6.3 Beam coherence and collimation slits

We established the connection between beam coherence and alignment requirements. In this section we discuss the most straightforward method for improving beam coherence, which consists in collimating the beam with narrow slits (narrow compared to the beam width). It has been suggested [131] that GSM beams are still effective in modeling slit-collimated atomic beams. In [131], it is assumed that a pair of slits is used to form a beam from a completely incoherent source. Here we introduce a simple generalization to the case where the input beam, before the collimating slit is already a GSM beam with known properties (w, l, r). As evidenced by the example of Fig. 6.9, this generalization is indeed needed to accurately model our system. Recalling the definition of the mutual coherence function (5.5), and considering only one coordinate (generalization to a round slit acting on both directions is straightforward), we have:

$$J(x, \Delta x) = e^{-\pi\left[x^2/w^2+\Delta x^2/l^2+2ix\Delta x/(\lambda r)\right]}.$$

A hard-edged slit of width s would have a transmission function of the form $t(x) = \chi_{[-s/2,s/2]}(x)$. It is however more convenient to assume a Gaussian transmission function

$$t(x) = e^{-\pi x^2/s^2}$$

This choice leads to a simple analytical result and at large distances from the slits compares well with exact numerical calculations [131]. The mutual coherence function after the slit is given by equation (5.2), and reads

$$J'(x, \Delta x) = t(x+\Delta/2)t^*(x-\Delta x/2)J(x, \Delta x) = e^{-\pi\left[x^2(2/s^2+1/w^2)+\Delta x^2(1/l^2+1/(2s^2))+2ix\Delta x/(\lambda r)\right]},$$

which is the functional form of a GSM beam with parameters

$$w' = \frac{sw}{\sqrt{2w^2+s^2}} \tag{6.6}$$

$$l' = \frac{\sqrt{2}ls}{\sqrt{2s^2+l^2}} \xrightarrow{s\gg l} l \tag{6.7}$$

We have highlighted the fact that in the typical scenario where the slit width is much larger than the coherence length ($l \approx 1\,\mathrm{nm}$ in the uncollimated L-NESS beam), a slit will not affect the coherence length but will, as expected, reduce the beam size. This is already sufficient, as suggested in Fig. 6.6, to loosen the alignment requirements (the global degree of coherence, β is increased $\beta' = l'/w' = \frac{\beta\sqrt{2w^2+s^2}}{s} > \beta$).

Two slits at a sizeable distance will however improve also the coherence length, as the free evolution of the beam in the space between them, with a reduced diameter thanks to the first aperture, has to be taken into account (recall the analytical expressions for the free evolution of the GSM beam given by equations (5.8)). A realistic example of collimation based on the nominal QUPLAS-0 parameters is displayed in Fig. 6.9. To give a sense of scale, collimation of this level already increases the calculated tolerance to longitudinal and angular misalignments by approximately a factor of four for the QUPLAS-0 setup (the improvement is found to be proportional to β'/β). The actual collimation system employed for the measurements will be described in the next chapter devoted to the experimental results.

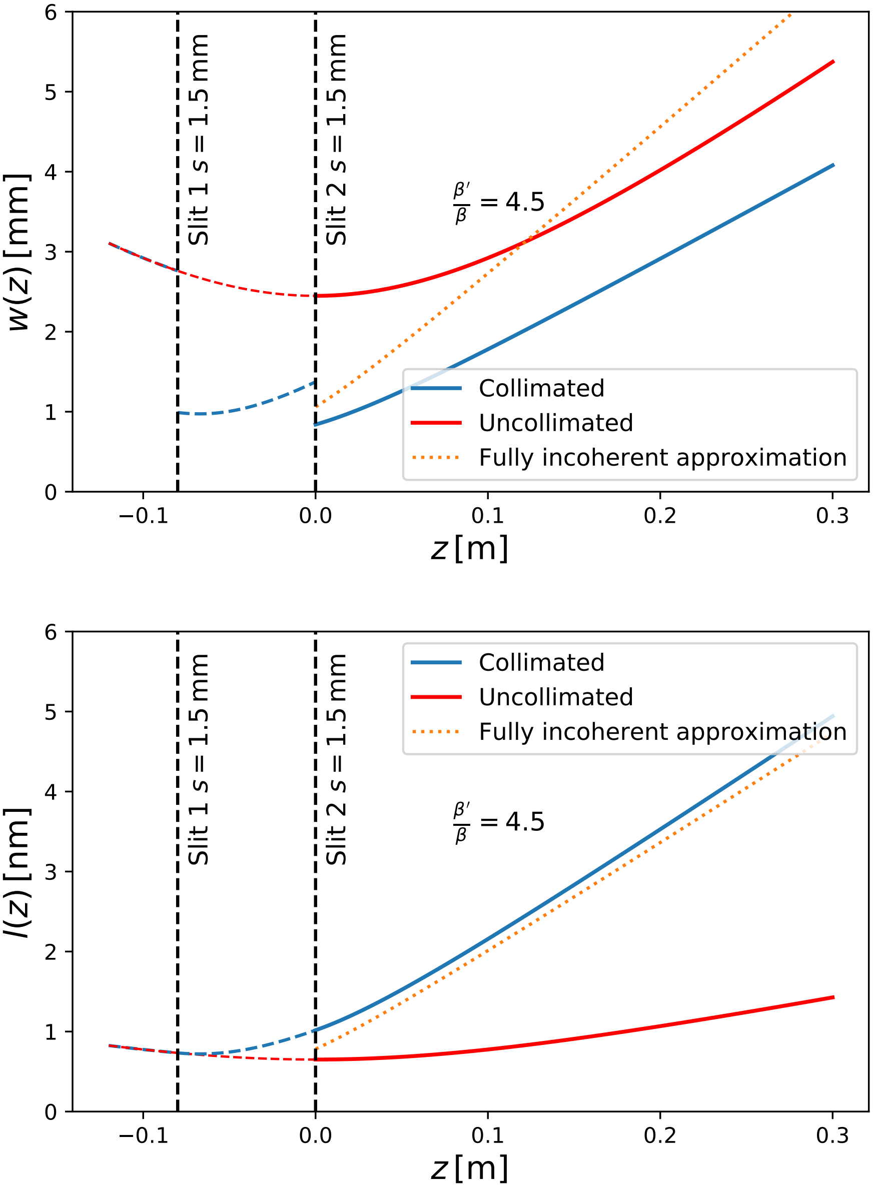

Figure 6.9. Effect on beam width w and coherence length l of two $s = 1.5\,\mathrm{mm}$ wide collimating slits (modeled with a Gaussian transmission function), placed on the L-NESS beam with nominal parameters. The second slit is located on the waist of the uncollimated beam, $8\,\mathrm{cm}$ after the first one. For comparison, the prediction assuming instead that the beam impinging on the slits is fully incoherent, which is not a good approximation in our set-up.

Part III

QUPLAS-0: experimental results

CHAPTER 7

An optical asymmetric Talbot-Lau interferometer

Before introducing the positron interferometer we report the results of a preliminary test of the chosen asymmetric configuration that was performed in the optical domain as a proof-of-concept using simple diffraction gratings produced with photographic films.

At the very beginning of our study of asymmetric Talbot-Lau interferometry in a period-magnifying configuration a simple optical experiment was realized to test the predictions of the models. To this end, we produced diffraction gratings of suitable periodicity by taking pictures of printed periodic masks with conventional black-and-white photographic film and a reflex camera. This allowed us to produce a set of gratings with a well known ratio between their periods (as the mask was changed but the camera stood stationary between exposures). Pictures characterising the gratings are shown in Fig. 7.1. Samples with a nominal open fraction $f_o \approx 30\%$ and periods $d_1 \approx 280\,\mu\mathrm{m}$ and $d_2 = 5/6 d_1$ were tested, to allow a magnifying setup with $\eta = 5$ in analogy with the foreseen QUPLAS-0 interferometer. Partially coherent illumination was provided by a He-Ne laser ($\lambda = 632.8\,\mathrm{nm}$) transmitted by a rotating ground glass disk (also known as an Arecchi's disk [133]); a sketch of the layout is shown in Fig. 7.2. The beam thus formed was described with the formalism of GSM beams. In particular, to apply equation (5.11) to predict the intensity, it is necessary to measure the beam parameters. Assuming an

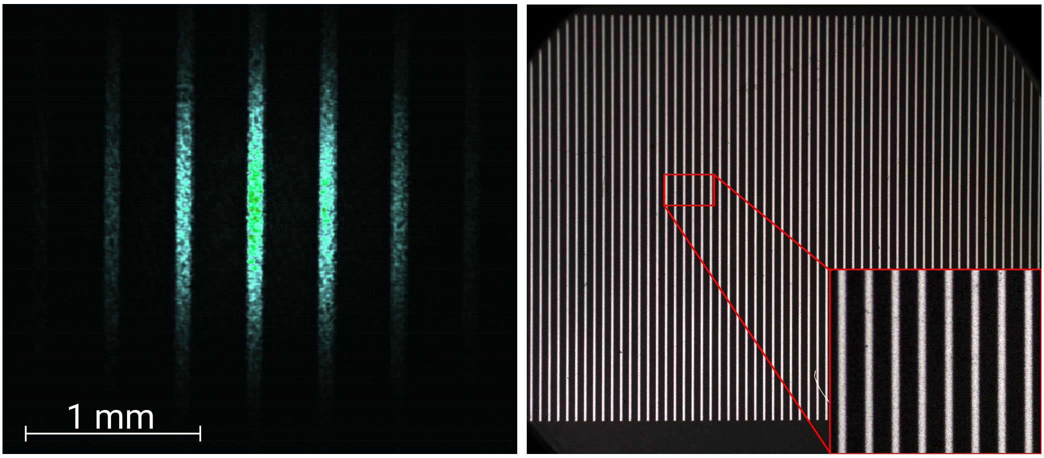

Figure 7.1. On the left, the $\approx 280\,\mu\mathrm{m}$ periodic grating imaged on a CMOS camera with coherent laser light and a single lens. On the right, natural light picture of the same grating, the inset shows a detail of the intensity periodic mask with higher magnification.

isotropic beam, the estimated parameters were $w_0 \approx 650\,\mu\mathrm{m}$, $l_0 \approx 2\times10^{-6}\,\mu\mathrm{m}$, $r_0 \approx 1\,\mathrm{m}$, on a plane $2.7\,\mathrm{cm}$ before the first grating. The distances L_1 and L_2 were optimized to find the best visibility. We stress that the apparatus in these conditions is much more robust to both angular and longitudinal misalignments compared to the foreseen QUPLAS-0 setup. For instance the above mentioned parameters imply $\sigma_\phi \approx 8.5°$, according to equation (6.5). The diffraction pattern was observed with a conventional CMOS camera; a representative result is shown in Fig. 7.3. Data show a fairly high contrast of 86%, which is lower compared to the 99% predicted by the model in the ideal resonance conditions. Several factors could be contributing to a reduction in contrast. For instance, the spatial quality of the gratings is compromised by distortions in the imaging system for producing the periodic pattern. Partial transparency of the absorbing region of the gratings could also reduce the visibility, as well as deviations from the ideal "square wave" profile of the grating transmission function assumed in the model. The latter effect naturally occurs as a result of the finite optical resolution of the film and camera system. In Fig. 7.3 we show a fit of the result with a function of the form $I'(x) = AI(x - x_0) + B$, where $I(x)$ is the intensity from equation (5.11), scaled and shifted, with an additional constant B to account for residual uniform background. Realistic sources of a constant background could be stray ambient light (also produced by diffusion of the laser itself) as well as residual electronic noise of the sensor which is not effectively subtracted. Besides the explicitly mentioned parameters (A, B, x_0), $I(x)$ depends on several physical quantities that could be extracted as fit parameters from the data. To this end L_1, L_2 and the beam parameters were constrained to a range centered on the measured values consistent with the measurement errors. The parameters f_o, d_1 resulting from the fit procedure are $f_o \approx 26\%$ and $d_1 \approx 286\,\mu\mathrm{m}$. The observed shape of the pattern is very well reproduced by the GSM model of equation (5.11). The introduction of a constant background was however necessary to account for the lower observed contrast.

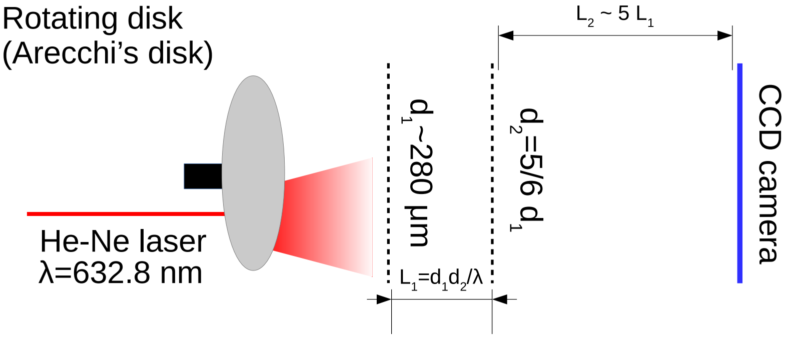

Figure 7.2. Sketch of the experimental setup for the measurement. The camera was equipped with a 1280×1024 pixel CMOS sensor, with a pixel size of $5.2\,\mu\mathrm{m}$.

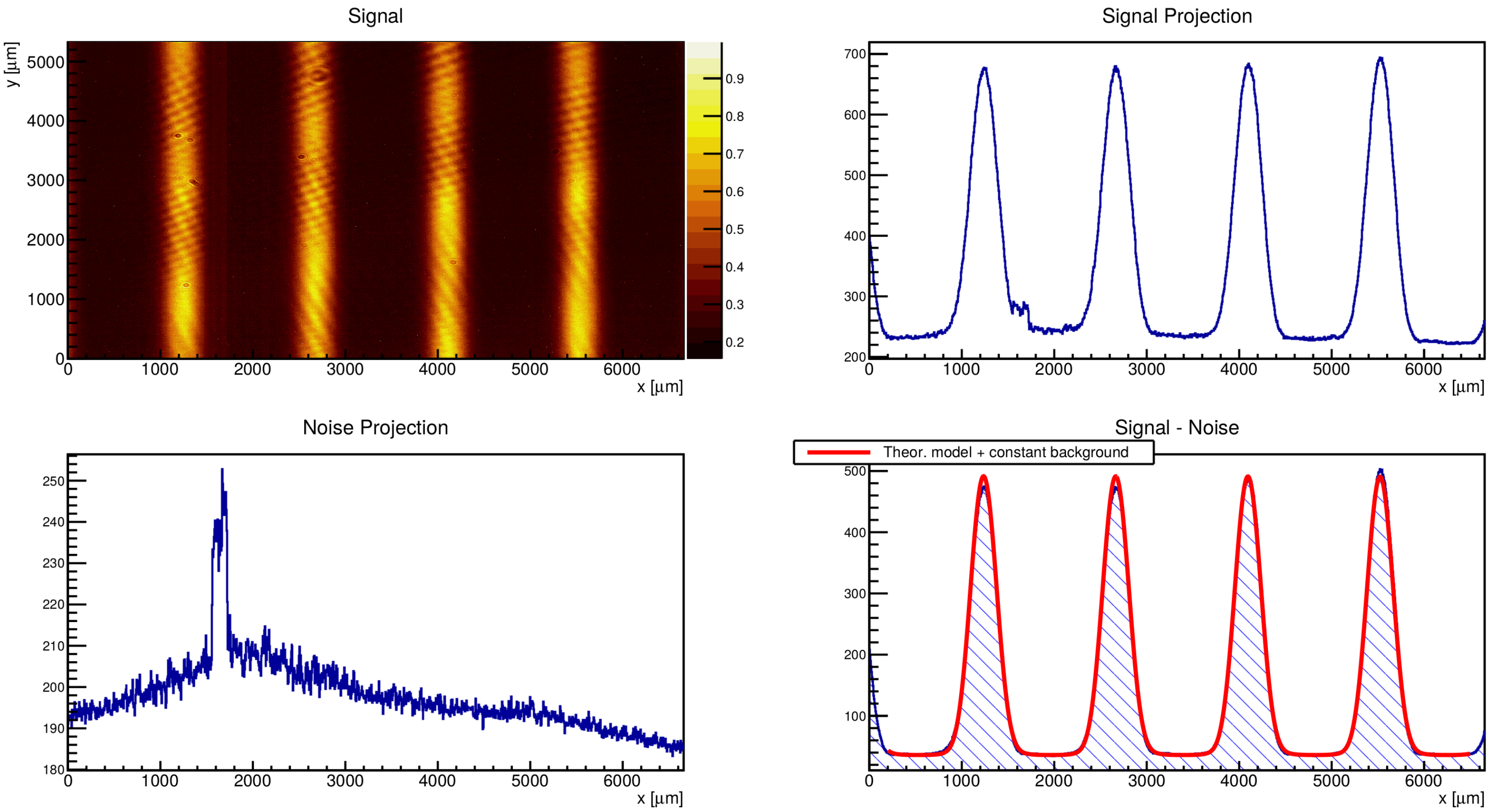

Figure 7.3. Optical interference pattern in an Asymmetric Talbot-Lau configuration with $\eta = 5$, performed with a He-Ne laser made partially coherent by means of a rotating ground disk. From top left in anticlockwise order: raw camera image, profile of the background noise (dark frame), final result with noise subtraction, profile of the raw camera image. The solid red line is a fit with the GSM beam model of equation (5.11), period of the first grating is $d_1 \approx 286\,\mu\mathrm{m}$, and the observed period is $d_3 \approx 1430\,\mu\mathrm{m}$ as expected from $d_3 = \eta d_1$. See text for details.

CHAPTER 8

The QUPLAS-0 interferometer and grating alignment

In this chapter we discuss the QUPLAS-0 apparatus from an experimental point of view, with emphasis on the rotational and longitudinal alignment techniques employed to meet the requirements introduced in the theoretical description of Part II.

8.1 Design and specifications of the apparatus

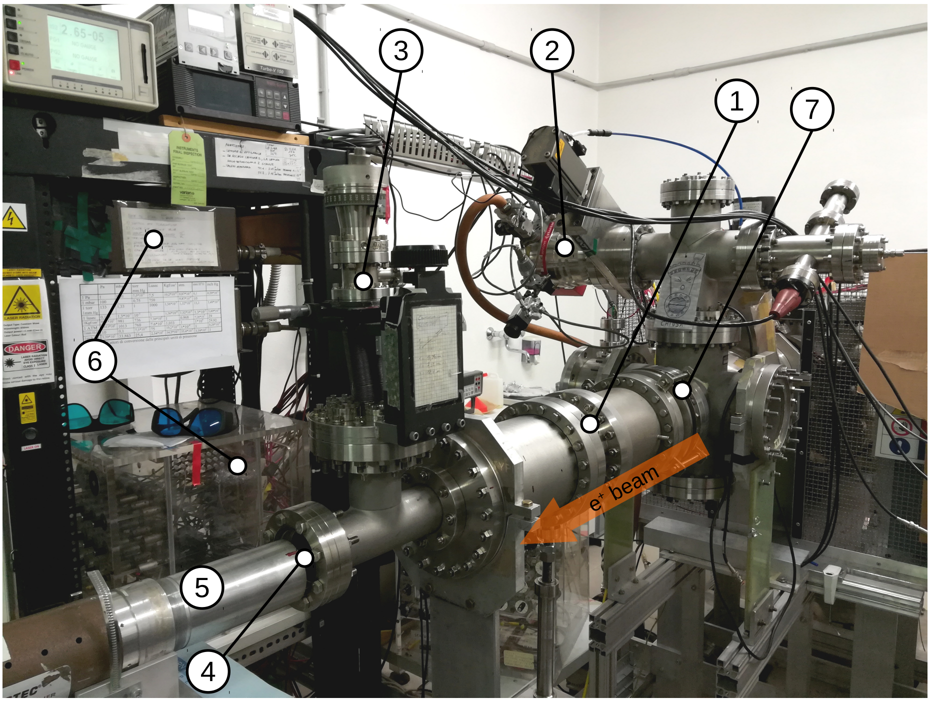

Figure 8.1. Picture of the L-NESS beam and experimental chamber configured for interferometry and beam characterization. The orange arrow is inserted to guide the eye on the direction of the e^+ beam. Labelled parts are: 1) Experimental chamber housing the interferometer inside a double-layer mu-metal shield. 2) Turbomolecular pump and valves. 3) x-y manipulator moving on the detector plane, used for beam characterization. 4) Transparent window which allows laser alignment. 5) BaF_2 detector. 6) High voltage control electronics. 7) Bellow allowing small adjustments of the chamber position and angle with respect to the beam optics.

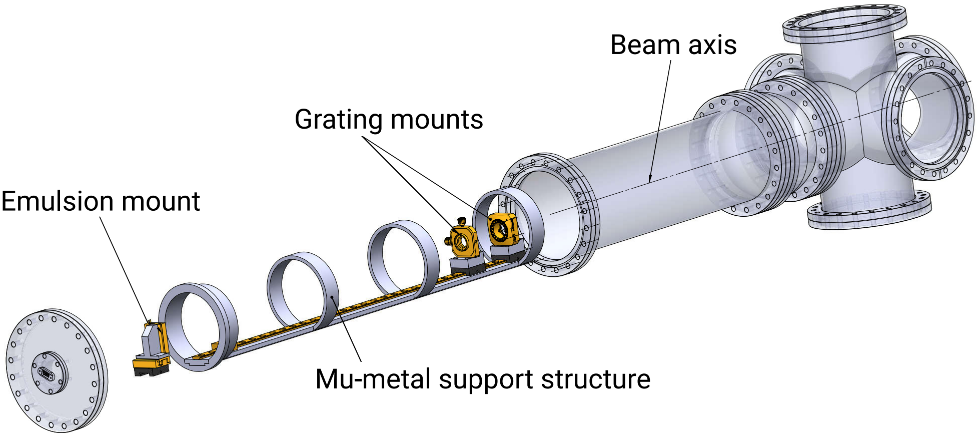

Figure 8.2. Drawing (courtesy of Marco Leone) of the interferometer tube coupled to the main experimental chamber. The mu-metal support structure is fixed inside the interferometer chamber (the mu-metal cylinders are not shown). Magnetic shielding (our double-layer shield is estimated to provide a reduction greater than a factor 100) against the field of the Earth is required to avoid sizeable deviations ($\sim 1\,\mathrm{cm}$) of the beam as it propagates $80\,\mathrm{cm}$. The rail supporting the interferometer slides out of the chamber to allow optical alignment (see Fig. 8.3).

In Fig. 8.1 a picture of the L-NESS beam and experimental chamber with the associated equipment is shown and described, a sketch of the interferometer structure is displayed in Fig. 8.2, while the interferometer components are pictured in Fig. 8.3. They are mounted on an optical rail that can be removed and inserted in the chamber with a sufficiently repeatable positioning. This is a necessary requirement, as the rotational and longitudinal alignment procedures take place on an optical table. We will describe in details these techniques in the following sections. The first grating holder is a mirror mount, made of fully non-magnetic materials by *Radiant Dyes Laser Acc. GmbH* [134], whereas the second grating is located on a piezoelectric rotator. Specifically, the unit was custom-made to our specifications by *MICRONIX USA, LLC* [135] with a fully non-magnetic construction[1]. It features an optical encoder with a nominal resolution of approximately $0.8\,\mu\mathrm{rad}$ and a bi-directional repeatability at the level of $3\,\mu\mathrm{rad}$. The gratings are mounted on aluminium disks which can be moved on the $x-y$ plane using the brass screws visible in Fig. 8.3 for fine-grained centering on the optical axis. The alignment laser is a *Thorlabs, Inc.*[136] CPS670F, $670\,\mathrm{nm}$, $4.5\,\mathrm{mW}$ diode laser with adjustable focus. Focusing on the camera plane yields the best visibility of the diffracted spots used for the rotational alignment. The camera used for this purpose is a Thorlabs DCC1545M, equipped with a 1280×1024 CMOS sensor (pixel size is $5.2\,\mu\mathrm{m}$). The total length of the interferometer rail is approximately $80\,\mathrm{cm}$, sufficient to fit the whole apparatus with geometrical parameters at resonance at the design positron energy of $14\,\mathrm{keV}$ (see Table 8.1). This geometrical configuration will be used for the QUPLAS-0 experimental campaign.

---

[1] To clarify the importance of this point, we found out that it is necessary to avoid parts containing ferromagnetic components. We tested a piezoelectric rotating mount with an aluminium body and observed complete loss of beam intensity at the end of the chamber. Although the main body was made of aluminium, steel parts contained inside had acquired a very strong magnetization (detected with a Hall probe), likely as a result of mechanical machining.

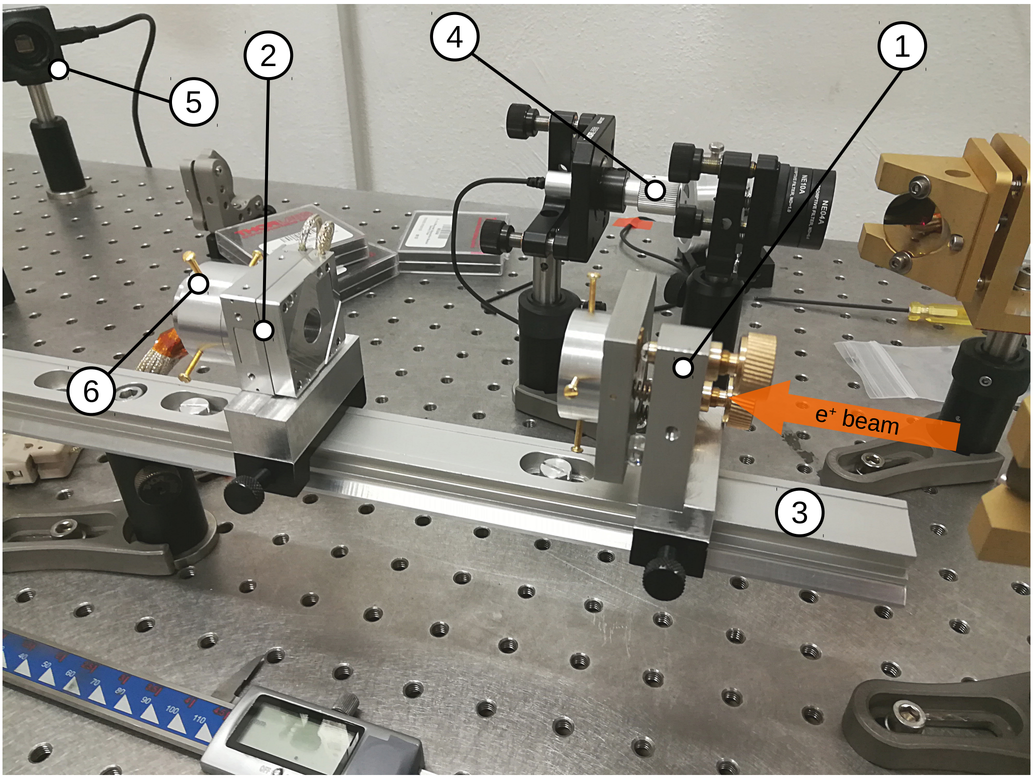

Figure 8.3. Picture of the two grating holders mounted on the main interferometer rail. Labelled parts are: 1) First grating holder. 2) Piezoelectric rotator housing the second grating. 3) Support rail. 4) Alignment laser. 5) Camera used for rotational alignment. 6) Screws for fine x-y grating positioning. Details on the components are discussed in the text.

8.2 Longitudinal alignment

Longitudinal alignment refers to the procedure of setting the correct distances between the planes of the two gratings and the detector. This alignment has to be carried out within a certain tolerance which is determined by beam coherence, as discussed in details in chapter 6 from a theoretical point of view. We now discuss the experimental implementation. First of all we report the most precise measurements of the grating periods at our disposal:

$$\begin{aligned} d_1 &= (1.2097 \pm 0.0003)\ \mu\text{m} \\ d_2 &= (1.0047 \pm 0.0003)\ \mu\text{m} \\ \frac{d_1}{d_2} &= 1.2040 \pm 0.0005 \end{aligned} \tag{8.1}$$

These values were provided by the manufacturer, and were obtained using far-field diffraction over a long baseline with a highly stable laser in a reflection geometry[2]. The above quantities are weighted averages of two measurements using different diffraction orders. We note that the sample variation in periodicity between gratings of the same batch is at the 10^{-6} level, therefore negligible with respect to the measurement error reported above. This feature is due to the peculiar manufacturing technique employed. From the measured grating periods the expected periodicity on the plane of resonance is obtained as:

---

[2] All information regarding the grating fabrication process and period measurement techniques comes from personal communications with Tim Savas (Lumarray).

$$d_3 = \frac{d_1 d_2}{d_1 - d_2} = (5.93 \pm 0.01)\,\mu\text{m} \tag{8.2}$$

We now recall the relevant equations from chapter 6 to discuss the alignment requirements. The distance between the second grating and the detector plane is:

$$\overline{L}_2 = \frac{\overline{L}_1}{\overline{d}_1/\overline{d}_2 - 1},$$

where $r = d_2/d_2$ and $\overline{L}_1$ is the experimentally measured distance between the two gratings, with uncertainty δ_{L_1}. As already motivated, we adopt the point of view of a fixed $\overline{L}_1$ distance and discuss the uncertainty δ_{L_2} on $\overline{L}_2$, that is on the ideal detector position. The latter reads:

E_{res} [keV]	λ [$\times 10^{-11}$ m]	L_1 [m]	L_2 [m]	L_{TOT} [m]
1	3.8764	0.0314	0.1537	0.1850
10	1.2205	0.0996	0.4881	0.5877
11	1.1631	0.1045	0.5122	0.6167
12	1.1131	0.1092	0.5352	0.6444
13	1.0689	0.1137	0.5574	0.6711
14	1.0295	0.1181	0.5787	0.6967
15	0.9941	0.1223	0.5993	0.7215
16	0.9621	0.1263	0.6192	0.7456
17	0.9329	0.1303	0.6386	0.7689

Table 8.1. Summary of the optimal geometrical parameters (rounded to the last significant digit, given the errors discussed in the text), as a function of the chosen design energy, that is the positron energy at which the Talbot-Lau configuration is to be at resonance. The de Broglie wavelength is calculated with the relativistic expression (2.1). We stress that, as motivated in chapter 6, the contrast for fixed wavelength depends essentially only on the ratio of the two lengths. The selected parameters for the QUPLAS-0 experimental campaign are highlighted.

$$\delta_{L_2} = \overline{L}_2 \sqrt{\left(\frac{\delta_{L_1}}{\overline{L}_1}\right)^2 + \left(\frac{\delta_r}{r-1}\right)^2}$$

Typical values of the distance L_1, calculated as $L_1 = \frac{d_1 d_2}{\lambda}$ are reported in table 8.1 for selected energies (assumed exact). We stress that the contrast for fixed wavelength only depends on ratio of the two distances, the optimal value of which is dictated by d_1/d_2. The best estimate of the ratio of the grating periods yields $\left(\frac{\delta_r}{r-1}\right)^2 \approx 6 \times 10^{-6}$. Since $\overline{L}_1$

is of the order of $10\,\mathrm{cm}$ in our energy range, an accuracy target of $\delta_{L_1} = 0.1\,\mathrm{mm}$ already makes the measurement error on the length largely negligible (since $\left(\frac{\delta_{L_1}}{L_1}\right)^2 \approx 7 \times 10^{-7}$). The dependence of δ_{L_2} as a function of δ_{L_1} is plotted in Fig. 8.4 for three reference energies using the best determinations of the grating periods and assuming a realistic range for δ_{L_1}. This plot provides very important information: the uncertainty δ_{L_2} is of the order of $1 - 2\,\mathrm{mm}$. To assess the feasibility of a single exposure, this value must be compared with the longitudinal extent of the interference fringes σ_{L_2}. The latter depends on beam coherence, as discussed in chapter 6. In other words, the degree of coherence of the beam should be increased to the point that $\sigma_{L_2} \gtrsim \delta_{L_2}$. We will discuss how this target is reached by means of mechanical collimation slits in chapter 9. In addition, Fig. 8.4 also suggests that a requirement of $\delta_{L_1} = 0.1\,\mathrm{mm}$ is very conservative, as the dependence of the relevant parameter δ_{L_2} on δ_{L_1} is rather weak. This level of accuracy is easily achieved by standard mechanical workshop machining and measurement techniques. Therefore a system based on a reference plane which moves along the interferometer rail was devised. The position of the plane is read by a linear scale (*Mitutoyo* ABS AT715 series [137]) with a nominal accuracy of $7\,\mu\mathrm{m}$ and also moves orthogonally to the interferometer rail, to be able to move past the mounted grating holders. The orthogonality of the plane motion along the secondary axis with respect to the main direction of travel is ensured by means of standard mechanical measurements at the level of approximately $20\,\mu\mathrm{m}$ of displacement over the full length of the plane. This auxiliary plane is mounted on the optical table on an elevated support (see Fig. 8.5 for a picture of the components), and the interferometer rail is finely positioned using linear gauges so that it is parallel to the direction of movement of the reference plane at the level of $20 - 30\,\mu\mathrm{m}$ over the length of the rail (approximately $80\,\mathrm{cm}$). The reference plane can then be used to measure the distances between plane objects that touch its surface. For instance, the gratings are mounted in such a way that the silicon chip is exposed and can be put in contact with the reference plane. Measurements thus performed, between the two grating planes, were found to be repeatable at the level of at least $0.05\,\mathrm{mm}$. This is mainly limited by the residual mechanical play in the carriages supporting the moving plane. Furthermore,

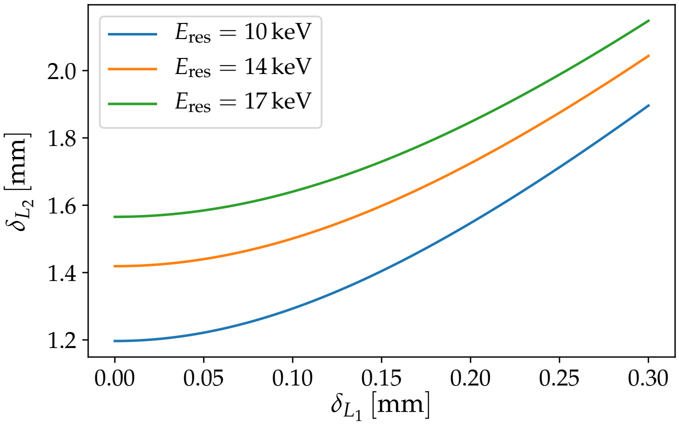

Figure 8.4. Plot of δ_{L_2} as a function of δ_{L_1} for three reference energies, using the nominal parameters of table 8.1, and the best estimates of the grating periods.

there could be systematic errors induced by the loss of parallelism between the reference plane and the grating planes. To perform the rotational alignment, an optical axis defined by the alignment laser is set to be parallel to the interferometer rail at the level of $1\,\mathrm{mrad}$ (a $0.5\,\mathrm{mm}$ positioning error of the laser spot over a length of $80\,\mathrm{cm}$). Using the back-reflected spots, the gratings will be tilted [3] to be orthogonal to the laser axis again at a level of a few mrad. The result of these measurements, which must be consistent with one another is to ensure the grating faces will be parallel to the reference plane at the level of (conservatively) at least $\theta = 10\,\mathrm{mrad}$. Given that the silicon chip is a square of side $l = 1\,\mathrm{cm}$, this would induce an error on distances measured with the reference plane of approximately $\frac{l}{2}\tan\theta \approx 0.05\,\mathrm{mm}$. In conclusion, the alignment setup devised is able to provide the required accuracy, as both sources of systematic errors and the observed statistical fluctuations of repeated measurements are at the level of $0.05\mathrm{mm}$. The general measurement protocol is as follows:

1. With the aid of the reference plane, gratings are positioned at a distance approximately[4] equal to the value suggested in table 8.1. This yields $\overline{L}_1 \pm \delta_{L_1}$.
2. The optimal value of L_2 is calculated: $L_2 = \frac{\overline{L}_1}{d_1/d_2 - 1}$.
3. The detector plane is then placed at a distance from the second grating $\overline{L}_2 = L_2$.

---

[3] Either using the degrees of freedom of the mirror mount for the first grating or the play built for this purpose into the x-y positioning system.

[4] We recall once again that discrepancies with respect to the optimal value even at the level of several mm would not affect the visibility in any measurable way (see Fig. 6.4).

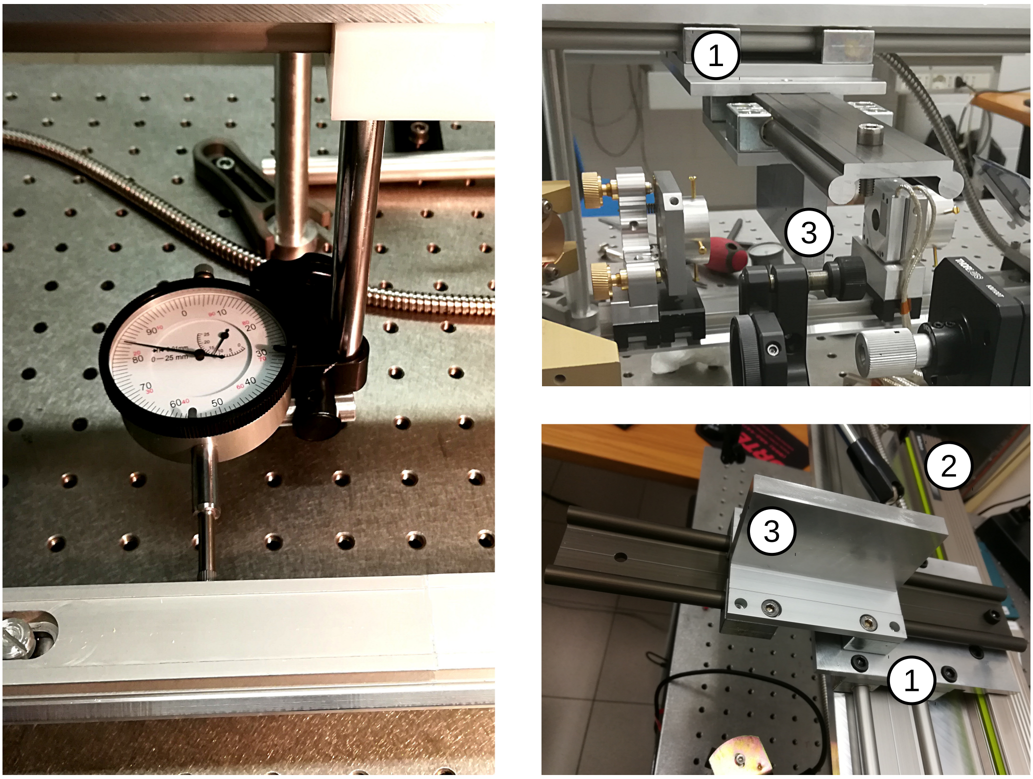

Figure 8.5. Right (top and bottom): two views of the reference plane (3) which moves on a carriage mounted on a linear guide (1), and can be retracted on an orthogonal axis to move past the interferometer components. The plane position is read by an optical linear scale (2). Left: the parallelism between the direction of movement of the reference plane and the interferometer rail is ensured by means of a standard dial indicator (a linear gauge).

8.3 Rotational alignment

As discussed in Part II, chapter 6, the reciprocal rotational alignment between the grating slits is a critical parameter. In particular we estimated that with the nominal L-NESS beam and QUPLAS-0 parameters, given in equations (5.15) and (6.1), the visibility drops rapidly as a Gaussian function of the angle ϕ with a standard deviation of the order of $\sigma_\phi \approx 200\,\mu\mathrm{rad}$. The misalignment angle must therefore be controlled at the level of tens of $\mu\mathrm{rad}$ for optimal results. A straightforward approach would be to rotate one of the gratings while monitoring the contrast of the interference fringes in real time. However, this is not viable in our system due to the extremely low intensity of the positron beam which prevents real-time measurements. Therefore, an indirect method that can be performed on an optical table with an alignment laser has been devised. Although the working principle is simple, in this section we attempt to discuss in details its effective accuracy by examining the main sources of systematic alignment errors.

The typical far field diffraction pattern produced by the QUPLAS-0 micrometric gratings is sketched in Fig. 8.6. Along the horizontal axis, diffraction by the $d \approx 1\,\mu\mathrm{m}$ apertures is observed, while the more closely spaced points in the vertical direction are produced by the $7\,\mu\mathrm{m}$ periodicity support structures. The first order diffraction maxima projected on a plane are arranged on an hyperbola, as explained by geometrical optics: the angular direction of the n-th diffraction maximum in a diffraction grating illuminated by a plane wave, with respect to the normal to the surface, reads

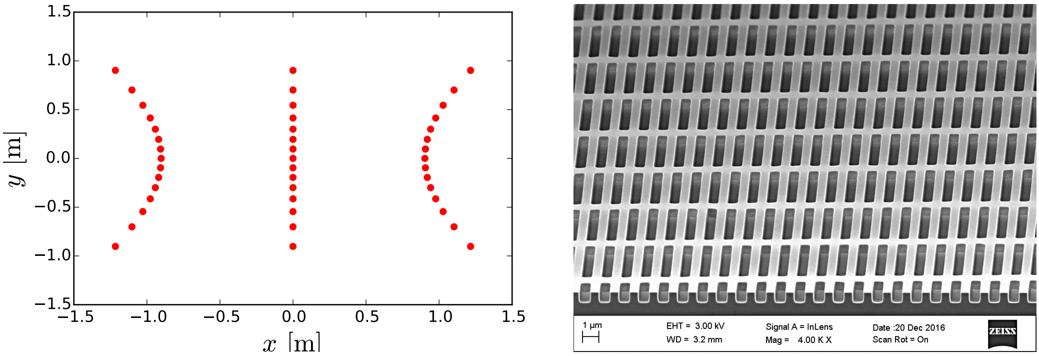

Figure 8.6. Left: calculated diffraction pattern of a $d = 1\,\mu\mathrm{m}$ grating obserbed at a distance of $L = 1\,\mathrm{m}$ illuminated by a $\lambda = 670\,\mathrm{nm}$ diode laser. Right: SEM image (courtesy of Tim Savas of Lumarray Inc. [138], who manufactured the gratings) of the $d = 1.2\,\mu\mathrm{m}$ silicon nitride diffraction gratings used for QUPLAS-0, showing the approximately $7\,\mu\mathrm{m}$ periodic support structure that produces diffraction along the y-axis in the left panel. More details on the structure are discussed in chapter 10.

$$\theta_n = \arcsin\left(m\frac{\lambda}{d} + \sin\theta_i\right) \tag{8.3}$$

where d is the periodicity of the slits, and θ_i is the angle of incidence of the incoming plane wave. For the grating and laser mentioned in Fig. 8.6, the diffraction angles in the vertical and horizontal direction respectively turn out to be $\theta_x = 42.0°$ and $\theta_y = 5.5°$. On a plane a distance L away from the grating surface the effective distance travelled by the light rays increases as you increase the y-direction diffraction order as $L' = L/\cos(\theta_v) = \sqrt{L^2 + y^2}$, so when one projects the two symmetric first order maxima of the $d \approx 1\,\mu\mathrm{m}$ diffraction, their distance on the screen increases as well. The diffraction angle in the horizontal direction is large enough that when the two gratings are put at their working distance for positron interferometry (approximately $11.5\,\mathrm{cm}$ at resonance for $E = 14\,\mathrm{keV}$), the two first order maxima are able to pass geometrically beyond the second grating and its support. Furthermore, it is observed that the central zero order maximum (defining the optical axis) is able to produce a diffraction pattern from the second grating as well.

Therefore, the two diffraction patterns can be simultaneously detected on a plane located beyond both gratings. If one is mounted on a rotating support, its diffraction image rotates independently from the other allowing the alignment procedure.

A schematic view from the top of the two grating arrangement is shown in Fig. 8.7. An interesting feature of the asymmetric setup chosen is that the first grating has a larger period ($d_1 \approx 1.2 d_2$), thus diffracts light at a smaller angle. This guarantees the existence of an intersection between the propagation direction lines of the first order maxima. The intersection points are marked by black dots in Fig. 8.7 and are located at a distance $D \approx 30\,\mathrm{cm}$ from the optical axis and $L \approx 30\,\mathrm{cm}$ downstream the second grating. If one of the gratings is rotated by an angle ϕ along the optical axis, the diffracted laser spots move on a circle of radius D on the plane orthogonal to the optical axis which contains the points of intersection. Obviously the ideal rotational alignment condition is met when the two pairs of spots (two on the left side and two on the right side) coincide. If the laser spots on both sides are superimposed with an uncertainty δx, the error on the alignment angle is estimated as:

$$\sigma_\phi \approx \frac{\delta x}{D}. \tag{8.4}$$

To achieve a reasonable $\sigma_\phi \lesssim 100\,\mu\mathrm{rad}$ accuracy one must ensure $\delta x \lesssim 30\,\mu\mathrm{m}$. In the

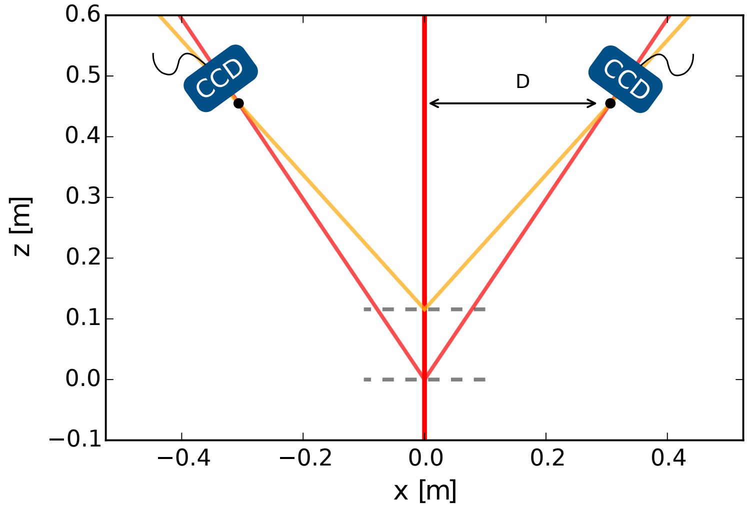

Figure 8.7. Sketch of the two gratings viewed from the top. Gratings are oriented so that strong diffraction takes place along the x-direction. The direction of the optical axis defined by the zero order maximum and the two first order maxima for each grating are represented by straight lines. The intersection points are monitored with two cameras to perform the alignment.

following sections several sources of error arising in a practical implementation of this idea are presented, to quantify the ultimate accuracy limit of the procedure.

8.3.1 Limits to the alignment accuracy

First of all, it could be argued that D should be increased to improve the accuracy of the procedure, for example by rotating the system 90° and performing the alignment using the light diffracted by the support structure. However it was observed that the two periodic patterns are not orthogonal, to a level of a few mrad, an order of magnitude larger than the required accuracy. This deviation from orthogonality is due to the fabrication process and was also confirmed by the manufacturer.

Orthogonality of the alignment laser to the surface of both gratings was found to be critical for good alignment, depending on the direction in which the tilt of the gratings takes place. A simple geometrical optics reasoning provides a satisfactory treatment of the observed effect: consider equation (8.3), if the angle of incidence is non-zero then the zero order maximum $(m = 0)$ comes out at the same incidence angle, but the two first order maxima $(m = \pm 1)$ are no longer emitted symmetrically. Schematically, this produces the effect shown in Fig. 8.8 when one of the gratings is tilted with respect to the laser along the y-axis. The system becomes asymmetric, but there are still unique intersections and an optimal rotation alignment condition can be found. Tilting, for instance, the first grating by $1\,\mathrm{mrad}$ introduces a mismatch between D and D' of $6\,\mathrm{mm}$, so orthogonality of the laser in this direction can be kept under control by checking for left-right symmetry to the level of a few mrad. To a first degree of approximation, this error does not affect significantly the accuracy of the rotational alignment along the z-axis. Of course if the gratings are not parallel the contrast of the positron interference fringes can be affected.

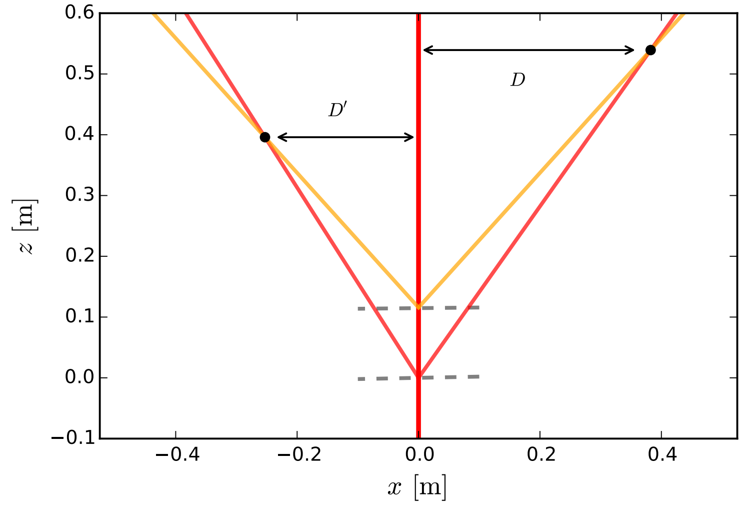

Figure 8.8. Tilting one of the two gratings with respect to the laser in the direction of the large angle diffraction angle makes the system geometry asymmetric.

If the gratings are instead tilted along the x-axis by an angle θ_t, then an effect which limits the alignment accuracy occurs. If $\theta_t = 0$, the three maxima of order $m = 0, \pm 1$

produced by each gratings should lie on a straight line as it is expected. However, these three points are also zero order maxima for the diffraction in the orthogonal direction (diffraction by the support structure), therefore they are propagating with the angle θ_t. Assume that the laser propagates purely along the z-axis, and the grating is tilted, then $\mathbf{v}_0 = \hat{u}_z$ is a vector representing the propagation of the zero order maximum. The first order maxima are obtained by rotating this vector as follows:

$$\mathbf{v}_{\pm 1} = \hat{R}_x(\theta_t)\hat{R}_y(\theta_{\pm 1})\hat{u}_z$$

where $\hat{R}_{x_i}(\alpha)$ denotes a standard rotation matrix around the coordinate axis x_i and the angles $\theta_{\pm 1}$ are given by equation (8.3). As a result of this, when the vectors are propagated to a plane away from the grating, the intersections with the plane do not lie on a straight line, as shown in Fig. 8.9. The difference in height Δy arising from the grating tilt can be computed from the explicit expression of the vectors and reads:

$$\Delta y = L \tan\theta_t \left(1 - \frac{1}{\cos\theta_d}\right). \tag{8.5}$$

The distance of the observation plane from the grating is denoted by L, and θ_d is the appropriate diffraction angle ($\theta_d = \theta_{\pm 1}$). This formula obtained with simple ray optics consistently describes the physics observed in practice by tilting the gratings. By inspection

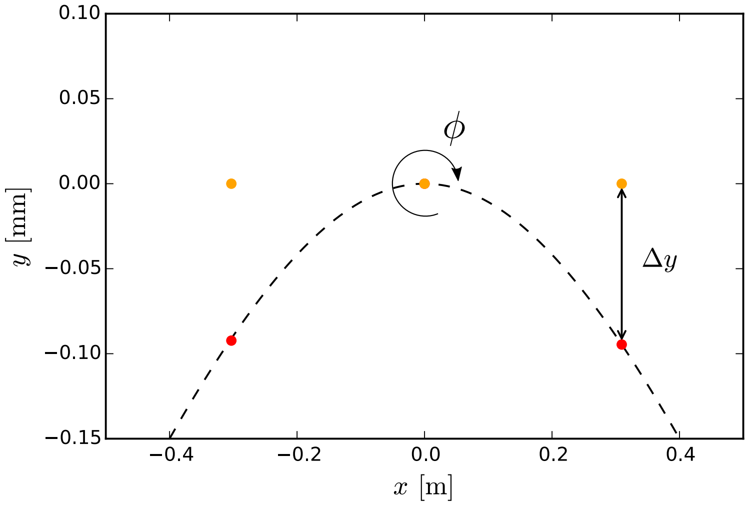

Figure 8.9. Diffraction maxima produced by two gratings in the arrangement of Fig. 8.7, one of which rotated around the x-axis by an angle $\theta_t = 1\,\mathrm{mrad}$, on the plane where superposition of the spots is expected. The dimensions are realistic as the drawing uses all the parameters from the real experimental layout.

of figure 8.9, where the gratings are supposed to be rotationally aligned ($\phi = 0$) but tilted, it is apparent that if, for instance, the two maxima on the right hand side are brought to coincide by rotating the grating, this deviates from the correct alignment condition. For this reason it is crucial to monitor the superposition of both pairs of spots simultaneously with two independent cameras. For $\theta_t \neq 0$ improving the *apparent* alignment on one side moves the spots farther away on the other. Thus by a series of iterative steps, the direction of the laser and the orientation of the grating mounted on the mirror mount can be adjusted to minimize this asymmetry effect. Actually this effect can be exploited to devise a robust repeatable protocol that rapidly converges to a good, symmetric alignment, as it will be described. On the other hand, the ideal alignment condition could also be generalized to having an equal Δy on both sides, which would work also for tilted gratings. However this is hardly convenient and this source of misalignment is correlated to other sources of asymmetry like the one discussed before which can combine to give unpredictable results. The rotational alignment procedure complements the mechanical measurements to ensure this condition. For reference, supposing the orthogonality of the laser to the gratings is controlled at the level of $\theta_t \approx 1\,\mathrm{mrad}$, then $\Delta y = 100\,\mu\mathrm{m}$, which would produce an alignment error $\sigma_\phi \approx 300\,\mu\mathrm{rad}$ if left-right symmetry was ignored. We will show that with our setup it is possible to ensure superposition of the laser spots on both sides at the level of a few microns.

In a first pre-alignment phase, the first grating (not mounted on the piezoelectric mount) is rotated manually so that the diffracted spots lie on the same height as the optical axis with respect to the plane of the optical table, namely an *horizontal* plane is defined (labelled the x-axis in Fig. 8.10, in keeping with the notation used so far: that is the direction where positron diffraction will take place). Small rotations from the ideal conditions by the angle ϕ would then produce displacement of the spots primarily in the orthogonal y-axis. Therefore, rotational alignment will be performed by ensuring optimal superposition of the y coordinate of the spots centres. Suppose however that the reference frame of the camera sensor is tilted[5] by an angle α with respect to these ideal axes, and also that the sensor is not placed exactly on the points of intersection of the diffraction spots, so that the spots centres acquire a distance l. The situation is sketched in Fig. 8.10, where the distances are greatly exaggerated for the sake of clarity. In the absence of such tilt ($\alpha = 0$), then rotating the gratings until the spot centres coincide in y yields a correct alignment even if $l \neq 0$, that is if the camera is not placed exactly on the intersection plane.

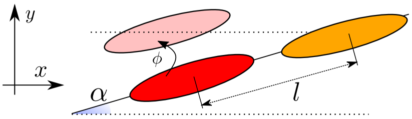

Figure 8.10. Sketch of a camera frame taken with a tilted camera and far from the ideal intersection plane. See text for a discussion.

If this strategy was instead applied in the presence of a small angle α, one would rotate the mount until the red spot moves upwards by $\Delta y = l \sin \alpha$. Assuming a worst-case scenario where $\alpha = 10\,\mathrm{mrad}$, and that the distance is at the level of the x-direction spot size (see Fig. 8.11) $l = 250\,\mu\mathrm{m}$ the resulting misalignment angle is:

$$\delta_\phi = \frac{\Delta y}{D} \approx 8\,\mu\mathrm{rad}$$

which is a very small contribution, completely negligible if the spots are superimposed also in the x-direction with the same $\mu\mathrm{m}$-level accuracy as in y. The procedure is indeed observed to be very robust with respect to this misalignment.

---

[5] The level of control on the rotation of the first grating, not on a dedicated rotation mount, is at the level of approximately $3\,\mathrm{mrad}$: horizontal alignment is obtained by rotating the grating manually and moving a ruler on the optical table until the zero and first order maxima are at the same height.

8.3.2 Measurement protocol and implementation

We now describe a repeatable protocol that is able to achieve $\mu\mathrm{rad}$ level accuracy in rotational alignment. A Gaussian fit (see Fig. 8.11) converges very well with a sub-pixel statistical error on the single frame, and the fitted peak position is stable across frames with fluctuations of the order of $1-2\,\mu\mathrm{m}$ (using the pixel size provided by the manufacturer). The laser spots are elliptical (and the laser has was oriented in such a way that the shortest semi-axis lies in the y direction where the utmost accuracy is needed), and have been focused on the plane of the cameras for the best visibility. The resulting spot size is of the order of $540\,\mu\mathrm{m} \times 120\,\mu\mathrm{m}$ FWHM. The image reported has both laser spots superimposed in a "perfect" rotational alignment condition. The accuracy of this superposition is however not limited by the spot size, taking advantage of the fact that the diffraction maxima coming from the two gratings travel spatially separated paths (see Fig. 8.7). It is possible to mask one spot at a time with an obstacle and ensure superposition on the y-axis at a level limited only by the stability of the Gaussian fit and the ability co control the tilt of the mirror mount to remove left-right asymmetry (the piezoelectric rotator itself is capable of sub-microradians adjustments). We now provide a step-by-step description of the measurement protocol, starting from the mounting and pre-alignment of the gratings:

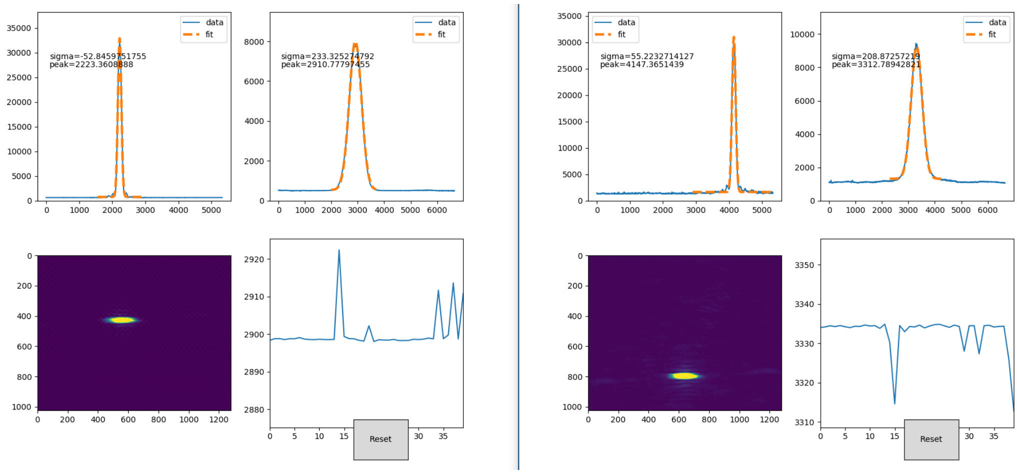

Figure 8.11. Example of the real-time analysis software implemented for the alignment procedure (using Python, the OpenCV [139] library to interact with the cameras through the DirectShow interface). The left and right panels are relative to the two cameras. For each cameras, from bottom left in clockwise order: raw image (units in pixels), integral of the image along y direction (units in microns), integral along x. The bottom right plot is used for other purposes unrelated to rotational alignment. Note that the unequal heights of the spots is just due to the cameras being installed on different mounts.

- **Definition of the optical axis:** using a moving pinhole mounted on a suitable support the alignment laser is made parallel to the interferometer rail. This procedure can be performed at the level of $1\,\mathrm{mrad}$.
- **Preliminary alignment of the gratings:** gratings are mounted on the supports, centered on the x-y plane with respect to the optical axis. The first grating is also

rotated manually within the support to define the horizontal plane. Then the pinhole is put before each grating mount, and the grating tilt is adjusted so that the back-reflected spot from the membrane coincides with the pinhole. This ensures orthogonality of both gratings with the laser.

- **Positioning of the grating supports:** the grating mounts are positioned in their final position at the correct distance (this step can be performed again after rotational alignment, which is then repeated, in an iterative fashion if necessary).

- **Positioning of the cameras:** the piezo mount is rotated until rotational alignment is obtained to the naked eye on a screen. The cameras are then moved on the plane of the optical table until the intersection plane of the laser spots is found. The process is aided by monitoring the variance of the Gaussian fit of the x-projection, which is displayed in real time, and has an absolute (and local) minimum on the intersection plane.

- **Finely adjusting grating parallelism:** this step conveniently exploits the phenomenon outlined in Fig. 8.9 to ensure left-right symmetry in a robust manner. The piezo mount is rotated relatively far from the alignment condition. In this condition all four spots are observable on the cameras (see Fig. 8.12), and the distance between pairs on the same side can be monitored in real time. Tilting the first grating vertically controls the aforementioned distance. The mount can thus be adjusted until equal distances are observed on the right and left side. This in turn ensures good grating parallelism.

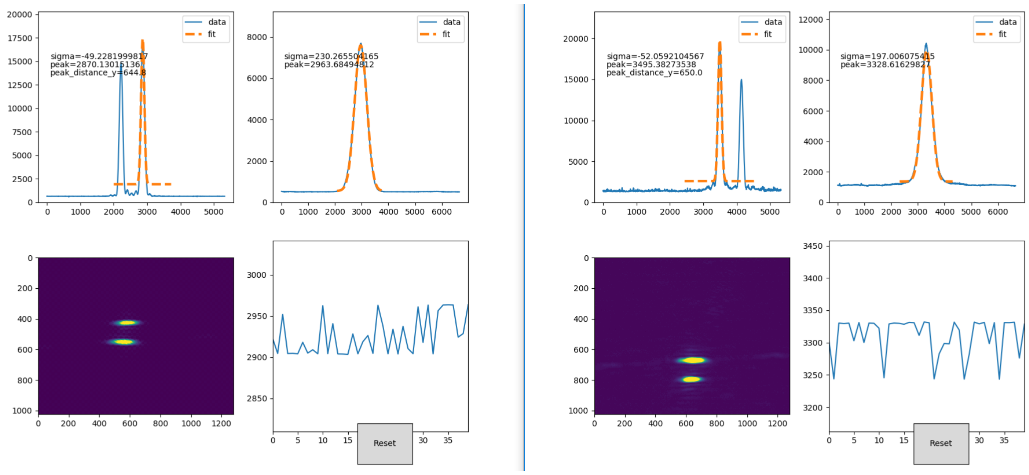

```
sigma=-49.2281999817
peak=2870.13015136
peak_distance_y=644.8
```

```
sigma=230.265504165
peak=2963.68494812
```

```
sigma=-52.0592104567
peak=3495.38273538
peak_distance_y=650.0
```

```
sigma=197.006075415
peak=3328.61629827
```

Figure 8.12. Condition ensuring parallelism of the two gratings: the distances between the two spots is equal in the left and right hand cameras. The distance is monitored in real time and is controlled by the vertical tilt of the mirror mount of the first grating, in a condition of poor rotational alignment. Note that the spots coming on each camera have to be filtered with unequal optical densities to achieve the same intensity (and avoid saturation, as unavoidably the intensity difference exceeds the dynamic range of the camera).

- **Finely adjusting rotation:** Finally, starting from the previous condition the piezo rotator can be moved back towards a superposition condition. Left-right symmetry should be obtained and is indeed observed experimentally (at least at the level of a few microns), confirming how this protocol ensures good parallelism between the gratings. Successive fine adjustments are done by masking one spot at a time until superposition is achieved.

The result after a few iterations of the last two steps is typically to obtain superposition of the spots at the level of $10\,\mu\mathrm{m}$ or better on both sides. This would correspond to a rotational alignment at the $30\,\mu\mathrm{rad}$ level. One order of magnitude smaller than the sensitivity of the apparatus in the worst-case scenario (uncollimated beam). This is however still an indirect procedure, and the validity of the above statement should ideally be checked with a real time interferometric measurement.

Stability of the self-locking rotation mount

The protocol described in the previous section is not applied directly in the experimental chamber, therefore the stability of the obtained alignment after the rail is removed from the optical table and inserted in the chamber must be kept into account. A careful experimental investigation was carried out and revealed that in spite of its *self-locking* capability, the piezoelectric rotator cannot guarantee long-term stability when power is removed, especially if it is moved or subjected to vibrations. Therefore, it is necessary to keep it connected and in a closed-loop feedback operation[6] during transportation of the rail to the chamber as well as during the measurement. This was technically feasible, and was routinely performed after it was confirmed experimentally that the magnetic field produced by the motor and sensor operation is negligible. The field was measured with a Hall probe and found in the center of the mount to be at a level indistinguishable from the Earth magnetic field B_E (which is still a perturbation over the background inside the mu-metal shield, which should be less than $B_E/100$). The spatial extent of the field is however limited, and ON/OFF comparison measurement of the beam position and intensity at the end of the chamber found no deviation within the experimental error of the procedure (which is described in the next chapter). Several week-long exposures were carried out during the QUPLAS-0 measurement campaign. The interferometer was rotationally alignment before each exposure, moved to the chamber, and the angular alignment checked after the exposure. Typically, the angular misalignment found after the measurement was at the level of $\phi_1 \approx 70\,\mu\mathrm{rad}$, starting from an initial condition of the order of $\phi_0 \approx 30\,\mu\mathrm{rad}$ or better. This figure is still sufficient to ensure good visibility even in the worst-case scenario of an uncollimated beam (which was, however, never used in practice except from an early test measurement). Furthermore, it is impossible to tell when the deviation from the initial alignment condition was introduced: whether it occurred as a gradual drift over the course of the measurement or was induced by moving the interferometer to and from the experimental chamber. Thus ψ_1 is only an upper limit to the effective misalignment condition in which the measurement took place.

---

[6] That is, absolute position is kept stable by the motor controller using the optical encoder reading as an input.

CHAPTER 9

Beam preparation and characterization

This chapter describes how the L-NESS beam was characterized and suitably prepared, by the addition of mechanical collimation slits, to carry out positron interferometry. In particular three main items will be discussed:

1. The protocol used to set up a reference laser to coincide with the beam and then to place the optical axis of the interferometer on the same axis.
2. The beam spot size on the plane of the detector and its dependence on the focusing voltage for various energies.
3. The impact of collimation and beam focusing on the tolerance of the interferometer to rotational and angular misalignments (using the theoretical tools developed in chapter 6).

9.1 Beam alignment and collimation

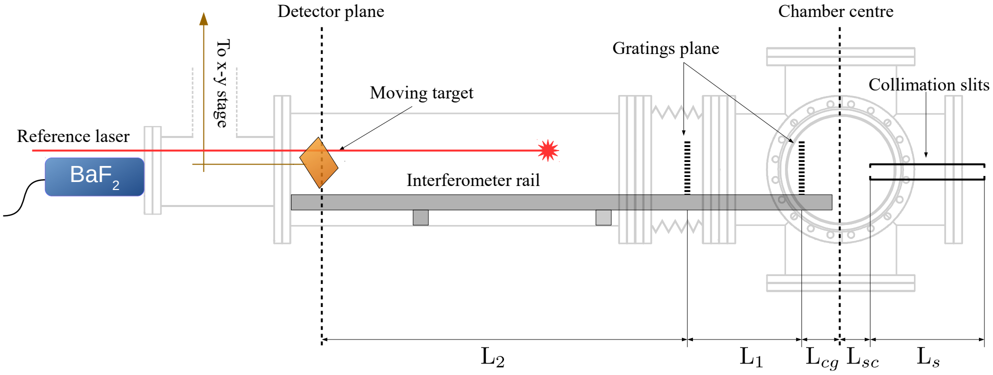

Figure 9.1. Scheme of the experimental chamber with collimation slits and beam position/size measurement apparatus in place at the end of the chamber. See text for a detailed description.

In Fig. 9.1 a sketch (cross-section) of the interferometer chamber is shown. The chamber is composed of two sections connected by a bellows: the main chamber on the right is rigidly connected to the rest of the beam chamber (containing the optics, source and moderator) and is stationary with respect to the laboratory reference frame. The elongated part of the chamber housing the interferometer rail, which is connected to this secondary chamber only, can be moved with respect to the main chamber (and thus the

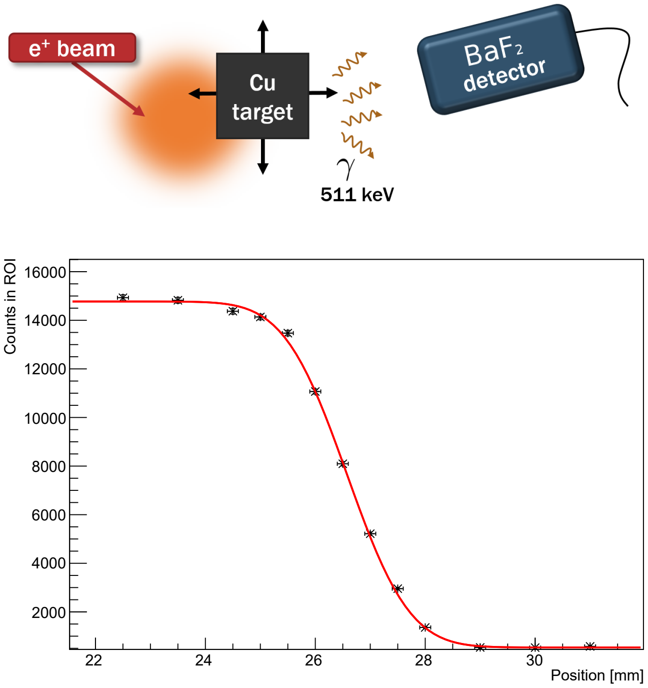

Figure 9.2. Scheme of the measurement process of the beam width used on the L-NESS beam. On the bottom panel a representative result is shown. Typically the statistical uncertainties from the fit with a sensible number of points is of the order of $\sigma < 1\,\mathrm{mm}$ both for the parameter x_0 and for σ_x. Two independent scans are required to locate the beam in the x-y plane.

beam optics). This degree of freedom allows to place the optical axis of the interferometer on beam axis. The bellows can then be firmly locked in place by means of four bolts. We describe the remaining items in Fig. 9.1 starting from the right-hand side. An aluminium tube with two circular collimation slits was placed so that the second slit is located $L_{sc} = 2\,\mathrm{cm}$ before the center of the main chamber, the length of the tube, hence the distance of the slits is $L_s = (10.2 \pm 0.1)\,\mathrm{cm}$, and the slit diameter is $r = 2\,\mathrm{mm}$. The plane of the first grating is located at a distance $L_{cg} = 3\,\mathrm{cm}$ from the center of the chamber, and the usual distances L_1 and L_2 define the detector plane. The distances reported without error are approximate and may change slightly depending on how the grating mounts are positioned and the bellow connection is locked in place. They are not crucial to the feasibility of the experiment, as it will be apparent from the following sections of this chapter. On the detector plane, an approximately $2.5 \times 2.5\,\mathrm{cm}^2$ copper target is moved in the x-y plane (transverse to the optical axis) and is used to measure the beam position and dimension (see Fig. 9.2 and the related description). The flange on the left end of the chamber is transparent and allows to see the spot of an alignment laser inside the chamber. The main reference laser is a collimated He-Ne laser located at a distance of approximately $4\,\mathrm{m}$ from the chamber, with a sub-mm spot size. A BaF$_2$ detector is used to monitor the intensity of the positron beam transmitted by the moving target (see 9.2 for an example). The measurement is based on the simple scheme shown in Fig. 9.2: an absorbing copper target larger than the full size of the beam is moved by means of an external manipulator. Assuming a Gaussian transverse intensity profile, of the form

$$n(x,y) = n_0 e^{-(x-x_0)^2/2\sigma_x^2-(y-y_0)^2/2\sigma_y^2},$$

then the intensity of the annihilation signal[1] I as a function of the target position as it moves for instance in the x direction, assumes the form

---

[1] The transmitted positrons will annihilate on the face of the glass flange that terminates the chamber, and

$$I(x) = a + b\left[1 - \text{erf}\left(\frac{x - x_0}{\sqrt{2}\sigma_x}\right)\right].$$

If the target position is scanned with the manipulator as shown in Fig.9.2, then the parameters σ_x and x_0 can be extracted from the fit, to estimate the beam position and transverse dimension. Once two independent scans are performed, the manipulator can be placed in the positions x_0 and y_0, and the edge of the square target coincides with the center of the beam. The spot of a secondary reference laser can be centered on the edge to indicate the beam position on the plane considered. The beam trajectory in the magnetic field of the Earth would be circular, with a curvature radius given by the well-known expression $R = m_{e^+}v/qB$. Assuming a conservative shielding factor of 100 from the mu-metal tubes, the radius for $v \approx 0.3c$ positrons is $R \approx 1200\,\text{m}$. It is therefore reasonable to make the assumption of straight line propagation between the two known points from which the beam passes: the measured position on the detector plane, defined by the secondary reference laser, and the center of the second collimation slit.

Alignment protocol

An alignment protocol can thus be performed according to the following steps:

1. Beam position (x_0, y_0) is measured on the detector plane and the spot of a secondary reference laser is placed on the beam center on that plane.
2. A pinhole located on the optical axis of the interferometer is mounted and positioned at the detector plane. The chamber is moved using the bellows (motion is controlled by a set of screws) to align the pinhole with the laser spot.
3. Then, the primary reference laser is adjusted until the beam passes through the pinhole and the second collimation slits.

This results in the alignment of the laser with the positron beam axis. The uncertainty of this superposition is estimated from two main contributions: the error of the experimenter in placing the laser spots on the targets, estimated to be $\sigma_l \approx 0.5\,\text{mm}$ and the statistical uncertainty from the fit parameters, typically $\sigma_{x_0,y_0} \approx 0.5\,\text{mm}$. We can therefore conclude that on each plane the laser spot should coincide with the beam spot at the level of $\sigma_{\text{alig}} \approx 1\,\text{mm}$, corresponding to an angular misalignment of $\sigma_\alpha \approx 2.5\,\text{mrad}$.

4. A second pinhole is placed at the beginning of the interferometer rail. The interferometer chamber is moved until the two pinholes are superimposed with the reference laser.
5. The bellows is locked in place carefully. This is necessary to avoid unwanted motion due to the atmospheric pressure once vacuum is obtained. It is possible to tighten the bolts which secure the bellows gradually while monitoring the laser alignment to ensure that it is not altered.

At the end of this procedure, alignment of the beam axis with the optical axis of the interferometer at the level of a few mrad should be achieved. Since many steps are

---

the detector placed in direct contact with the latter measures the $511\,\text{keV}$ gamma annihilation signal.

Figure 9.3. Sketch of the electrostatic optics configuration of the L-NESS beam. The 90° bend is required to get rid of the fast non-thermalized positrons escaping the moderator, and to reduce the flux of secondary γ directed from the ^{22}Na source to the experimental chamber. There are several deflection and focusing electrodes before and after the bend. In the inset the beam spot on a phosphor screen using an electron source is shown.

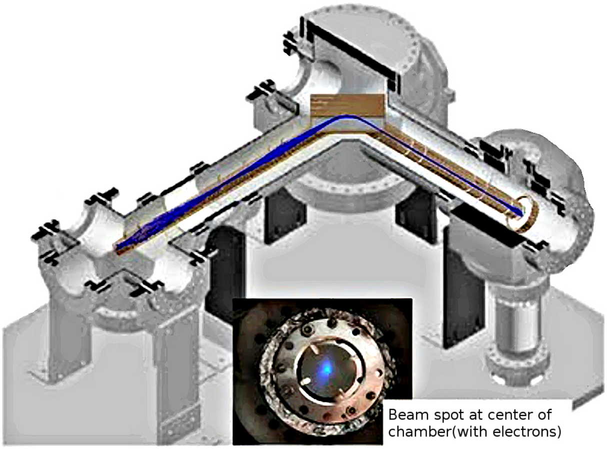

performed by visual inspection, it is difficult to provide a quantitative estimate of the uncertainty. A more careful estimate would also not be particularly helpful, since it is observed that in the time frame of several days, the beam position at the end of the chamber can undergo gradual drifts of the order of $0.5\,\mathrm{mm}$ due to slight instability of the beam optics. Those shifts are not detectable in real time during the measurements. Nevertheless, to a first degree of approximation traversing the gratings with a small angle β, for instance on the x-axis, could be modelled by a rescaling of both the periods $(d \to d\cos\beta)$ and the lengths $(L_{1,2} \to L_{1,2}/\cos\beta)$, which preserves the ratios d_1/d_2 and L_1/L_2, therefore the visibility should not be significantly affected.

9.2 Beam spot size and beam focusing

Several measurements of the beam spot size on the detector plane were made in the time frame of several weeks, using the technique we described. The beam has many deflection and focusing electrodes, both before and after the 90° bend (see Fig. 9.3). Before the measurement campaign the voltages of the deflection electrodes were adjusted to maximize the intensity transmitted through the two collimation slits. This condition should correspond to the best possible parallelism between the beam axis and the axis of the collimators. During the spot size measurement the intensity was monitored and small corrections applied if necessary to correct for possible drifts in the voltages. The spot size, expressed by its FWHM was studied as a function of the voltage of the last focusing electrode (the one nearest to the experimental chamber), namely V_F, for various positron energies. The energy is controlled by the potential V_E, following the relation:

$$E = e[V_E + V_M] = e[V_E + 1\,\mathrm{kV}],$$

where $V_M = 1\,\mathrm{kV}$ is the fixed potential of the moderator with respect to the target (at ground). It was found out experimentally that it is convenient to introduce the adimensional ratio

$$R = \frac{V_F}{V_E}$$

since the beam size $\mathrm{FWHM}(R)$ as a function of R is well approximated by a linear fit, independently on the positron energy. The experimental results with the best fit are reported in Fig. 9.4 for the y-coordinate. The same information could be extracted for

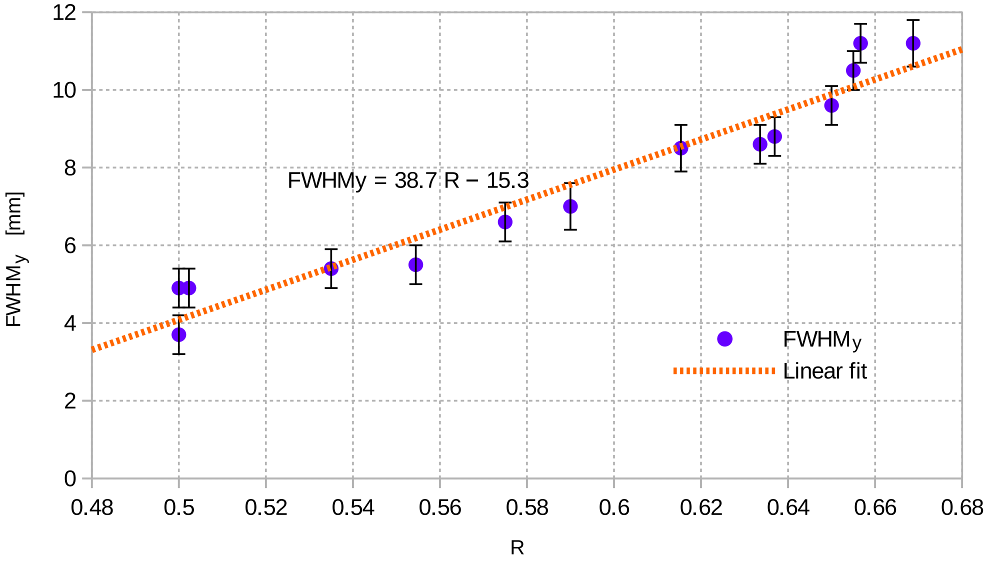

Figure 9.4. Spot size in the y-direction, $\mathrm{FWHM_y}$ as a function of the focusing voltage V_F.

the dimension $\mathrm{FWHM_x}$, and the *aspect ratio*[2] of the beam $\mathrm{FWHM_x}/\mathrm{FWHM_y}$ is approximately 1.2 (weakly dependent on beam focusing). The linear fit suggests a universal empirical formula for the beam dimension as a function of R:

$$\mathrm{FWHM}_y(R) \approx \alpha R - \beta \tag{9.1}$$

with $\alpha = (39 \pm 2)\,\mathrm{mm}$ and $\beta = (15 \pm 1)\,\mathrm{mm}$. This allows to conveniently set the focusing voltage to the suitable value, for instance to keep the beam dimension stable as the energy is scanned in consecutive interferometric measurements. Due to the presence of the collimators, beam dimension on the detector plane is correlated to the beam intensity. This follows from a simple geometrical argument: when the beam has the smallest spot size it is being focused far from the center of the chamber, therefore its size will be larger in the vicinity of the collimators, which will then filter out a larger fraction of the total intensity. Depending on the focusing voltage, the two collimation slits will transmit a fraction of the original beam intensity in the $10 - 20\%$ range. This behaviour can be studied with a series of measurements of total intensity (by means of the $\mathrm{BaF_2}$ detector located at the end of the chamber) at different energies. A typical result is shown in Fig. 9.5: a fit is performed on the experimental data (on each peak independently) with a function of the form

$$I(V_F) = Ce^{-\frac{(V_F - V_{F_0})^2}{2\sigma_V^2}} + C'. \tag{9.2}$$

This modulation is due to the presence of the collimators: there is an optimal focusing V_{F_0} for each energy which maximizes the transmission. From purely geometrical considerations, this arguably corresponds to the voltage for which the beam waist would be located roughly in the center of the collimator tube in the absence of the slits. Intensity drops symmetrically on both sides of the peak, where the uncollimated beam would be

---

[2] It is expected that the beam could be elliptical, and in particular that it can be larger in the x direction as a consequence of the 90° bend.

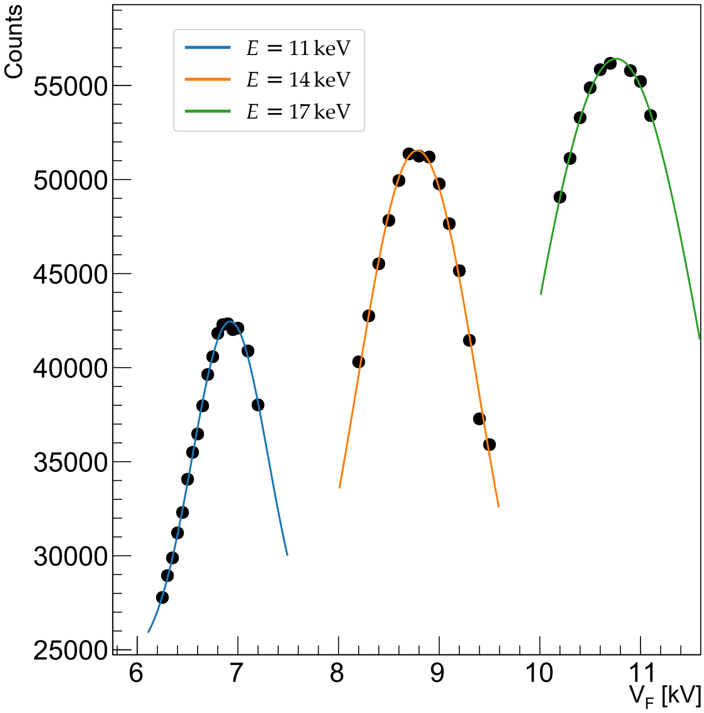

Figure 9.5. Typical example of a *focusing plot*: total intensity is measured as a function of V_F for different positron energies (and thus acceleration voltages V_E). Solid lines are least squares fit with a Gaussian function plus a constant background. Measurement time for each point was set to 1000 s.

focused before ($V_F > V_{F_0}$) or after ($V_F < V_{F_0}$) the aforementioned plane. The slight drop in peak intensity at decreasing energy is due to an energy-dependent transport efficiency of the beam optics and cannot be avoided. The empirical expressions (9.1) and (9.2) can be combined to estimate the average positron density on the detector plane as a function of V_F. To this end we define a parameter $D(V_F)$ as:

$$D(V_F; E) = \frac{I(V_F)/I(V_{F_0})}{[\mathrm{FWHM}_y(V_F/V_E)]^2} \tag{9.3}$$

which is proportional to the positron density, as the area covered by the spot scales quadratically with $\mathrm{FWHM_y}$, and we have normalized the intensity to the maximum value for each given energy. The parameter is plotted (in arbitrary units, as only relative changes are significant) in Fig. 9.6. All three energies display a similar trend: as the focusing voltage is decreased below V_{F_0} the density has a local maximum followed by a local minimum, then starts to increase up to a factor of two with respect to $D(V_{F_0}; E)$. Analytically the function is unbounded, but we have restricted our analysis to physically meaningful values of V_F. A factor of two increase is not negligible considering that (as we will discuss) typical exposure times with the collimated beam are of the order of days and the density, rather than the total number of positrons impinging on the emulsion is the figure of merit that should be maximized. Therefore, the analysis of experimental data suggests that the best working condition for positron density is achieved when the beam is focused towards the detector plane, to minimize the spot size. To supplement this information, in the following section we will estimate the impact of beam focusing on its coherence, and thus on the feasibility of the experiment. Density should in fact be maximized, as long as it is not detrimental for the expected tolerance to misalignments.

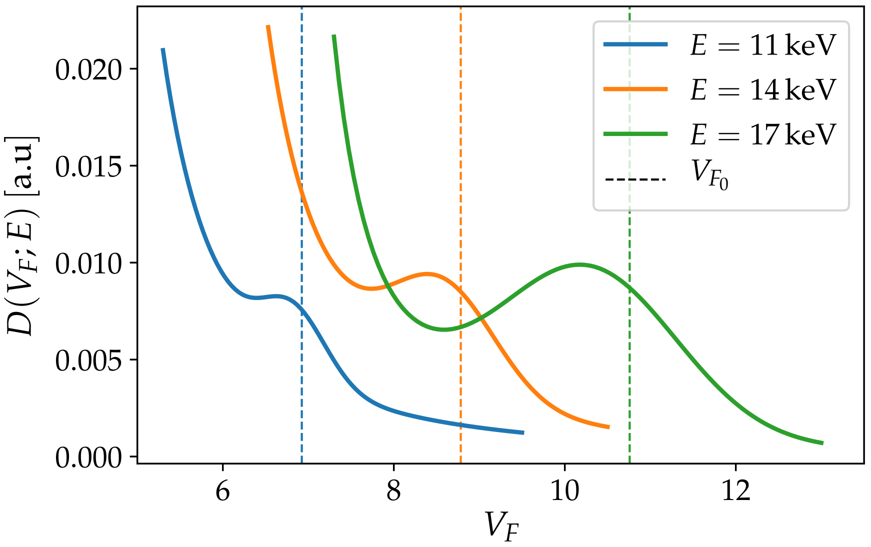

Figure 9.6. Plot of the density parameter $D(V_F; E)$ for three reference energies. The dashed lines indicate the voltages corresponding to maximum intensity V_{F_0}.

9.3 Beam coherence and interferometric visibility

We now discuss the influence of beam focusing on beam coherence, and thus on the tolerance to positional and rotational misalignments of the gratings. We will make extensive use of the concepts already introduced in Part II. We will support the conclusion that when the beam is collimated with two slits the relevant parameter, namely transverse coherence length on the detector plane l_{det}, is very weakly dependent on beam focusing. Slit geometry (distance and size) is the dominant contribution to determine beam coherence. To get a grasp of this behaviour, we focus on two reference beam configurations with and without collimation, characterized by a realistic set of nominal parameters:

- ***Focused mode*** which assumes the beam, when uncollimated, is focused in the center of the chamber (approximately where the second slit is located) to a beam spot of $\mathrm{FWHM}_0 = 2.3\,\mathrm{mm}$ that diverges to $\mathrm{FWHM}_{\mathrm{det}} = 10.0\,\mathrm{mm}$ on a plane $70\,\mathrm{cm}$ after the beam waist[3].
- ***Unfocused mode*** which assumes a beam with $\mathrm{FWHM}_{\mathrm{det}} = 5\,\mathrm{mm}$ and $\mathrm{FWHM}_0 = 8\,\mathrm{mm}$, on the same reference planes. This configuration can be achieved by lowering the focusing voltage V_F in comparison to the previous case.

---

[3] The chosen parameters are the best estimates from a set of measurements obtained in the early stages of the experiment. Due to a change in the chamber configuration it was later not viable to characterize at the same time beam width at the center and at the end of the chamber. Also note that we assume an isotropic beam for simplicity, but we recall that beam coherence on the x-axis influences robustness to longitudinal misalignments whereas y-axis coherence is related to rotational alignment.

In these two representative situations we calculate the beam evolution with and without a pair of $2\,\mathrm{mm}$ collimation slits placed $10.2\,\mathrm{cm}$ apart, using the approach of section 6.3. The results are displayed in Fig. 9.7 and Fig. 9.8. As already discussed in Part II, the contrast has a Gaussian dependence both on the angle between the gratings ϕ and the position of the detector L_2 (for fixed L_1). In each of the above four cases we evaluated the variances σ_ϕ and σ_{L_2} with the analytical expression (6.5) and with a numerical simulation using equation (5.11) respectively. The relevant parameters are summarized in Table 9.1. We recall from section 8.2 that the uncertainty on the determination of the ideal detector position δ_{L_2} is of the order of $1.5\,\mathrm{mm}$, and that for a single-exposure experiment to be realistically feasible the condition $\sigma_{L_2} > \delta_{L_2}$ must be satisfied[4]. From Table

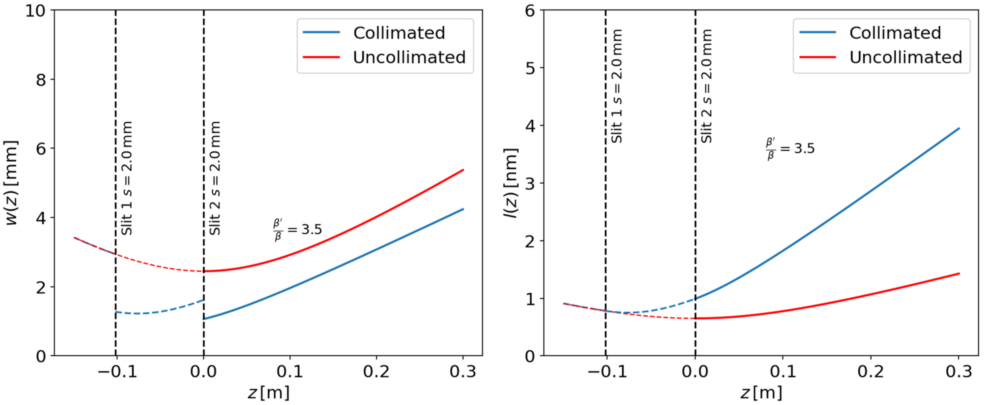

Figure 9.7. Evolution of the beam width parameter $w(z)$ (left) and of the transverse coherence length $l(z)$ (right) for the *Focused mode* configuration with and without collimation. Improvement in the global degree of coherence brought by collimation β'/β is also shown.

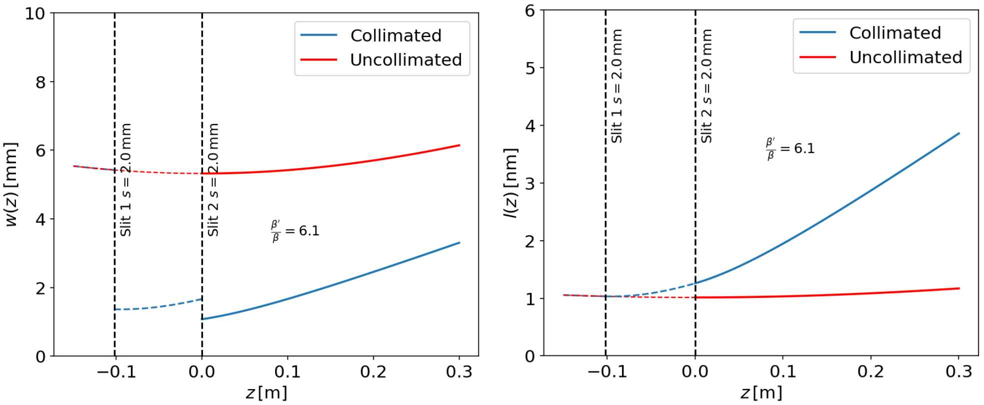

Figure 9.8. Evolution of the beam width parameter $w(z)$ (left) and of the transverse coherence length $l(z)$ (right) for the *Unfocused mode* configuration with and without collimation. Improvement in the global degree of coherence brought by collimation β'/β is also shown.

---

[4] The issue is discussed in details in Part II, however the intuitive meaning is that the tolerance to longitudinal misalignments must be greater than the uncertainty on the ideal detector position.

Configuration	l_0 [nm]	w_0 [mm]	l_{det} [nm]	σ_ϕ [µrad]	σ_{L_2} [mm]
Focused / Uncoll.	0.65	2.4	2.6	210	0.7
Unfocused / Ucoll.	1.00	5.3	1.5	116	0.4
Focused / Coll.	0.99	1.0	8.3	579	2.0
Unfocused / Coll.	1.25	1.0	7.9	552	1.9

Table 9.1. Summary of the relevant parameters for the four combinations of beam modes discussed in the text whose evolution is plotted in Fig. 9.7 and Fig. 9.8. See text for a discussion.

9.1 it is apparent that the uncollimated beam in both configuration does not provide the required degree of coherence[5]. This fact motivated the introduction of collimation slits, which are able to significantly improve the coherence length on the detector plane (the true figure of merit for comparing different configurations). The parameter σ_ϕ is increased well above the estimated accuracy of our alignment procedure which is of the order of a few tens of µrad, and the condition $\sigma_{L_2} > \delta_{L_2}$ is satisfied. For this reason the slit geometry configuration outlined in Fig. 9.1 was considered the best compromise between an adequate residual beam flux and a limited necessity to scan the detector position over a large area (which would be needed if $\sigma_{L_2} < \delta_{L_2}$). With our current measurement techniques it is not feasible to perform a scan along the z-axis to measure beam size evolution accurately. An interesting trend observed from the data in Table 9.1 is that collimation reduces the difference in l_{det} between the two modes from a factor ~ 1.7 to a factor of ~ 1, which suggests that once the slits are in place, it is their geometry to effectively control the coherence length on the detector plane regardless of beam focusing. This observation motivates the introduction of an approximate but convenient treatment to estimate the coherence properties of the beam based on its size on the detector plane alone. As it can be appreciated from Fig. 9.7 and 9.8, in both modes the collimated beam can be considered as having its waist on the second slit plane, and the size w_0 looks very weakly dependent on the size and focusing of the beam before the introduction of the slits. This fact can also be appreciated with an analytical calculation. Applying the first line of equation (6.7) two times subsequently, for two identical slits of width s, assuming an initial beam size w yields:

$$w'' = \frac{ws^2}{\sqrt{4s^2w^2 + s^4}} \tag{9.4}$$

This function for our range of realistic parameters $w \in [2.4\,\text{mm}, 10\,\text{mm}]$ and $s = 2\,\text{mm}$ depends weakly on w as it evaluates to $w'' = 0.92$ and $w'' = 0.99$ at the extremes of the interval (basically $w'' \approx s/2$ for $w > s$). Therefore it is sensible to approximate the size of the beam outgoing from the second slit with a constant value, for instance the average value $w_0 = \langle w'' \rangle = 0.96\,\text{mm}$ over the interval considered, and to assume that the beam waist is indeed located on the second slit, as the beam is always observed to have a size larger than w_0 downstream the collimation slits. Therefore the approach of equations (5.14) can be applied and for a given spot size[6] on the detector plane w_{det} the full evolution of the beam can be computed analytically (including l_{det}) to estimate the parameters

---

[5] For the Unfocused/Uncollimated mode, the spot size in the region of the two gratings will be significantly larger than their size ($3 \times 3\,\text{mm}^2$, whereas the model assumes it to extend indefinitely), therefore their action as effective collimation slits cannot be neglected, and would arguably bring the actual performances closer to the Focused/Uncollimated mode.

[6] We recall that the actual measured parameter will be the beam FWMH that is related to what we refer to

σ_ϕ and σ_{L_2}. Results of this calculation are shown in Fig. 9.9, where a weak dependence of the tolerance parameters is observed over the full range of beam sizes (controlled by focusing voltage) available in our setup. The parameters σ_ϕ and σ_{L_2} have the same functional behaviour, as they are approximately linear in the l_{det} (more precisely the linear dependence is predicted analytically for σ_ϕ by Equation (6.5) and was observed numerically for σ_{L_2}). There is good qualitative agreement between the values calculated with this approximation and the results of Table 9.1, although the former technique predicts a higher value of l_{det} for the *unfocused* mode rather than for the *unfocused* mode. We stress that we are estimating *tolerances* that are not intended to be measured accurately. In this context the only relevant conclusion is that a collimated beam should provide $\sigma_\phi \approx 550\,\mu\mathrm{rad}$, almost an order of magnitude larger than the sensitivity of our alignment procedure, and $\sigma_{L_2} \approx 1.95\,\mathrm{mm} > \delta_{\mathrm{L}_2}$, regardless of the beam focusing mode. One can therefore chose the focusing voltage that maximizes the flux density on the emulsion detector without compromising the feasibility of a single exposure experiment.

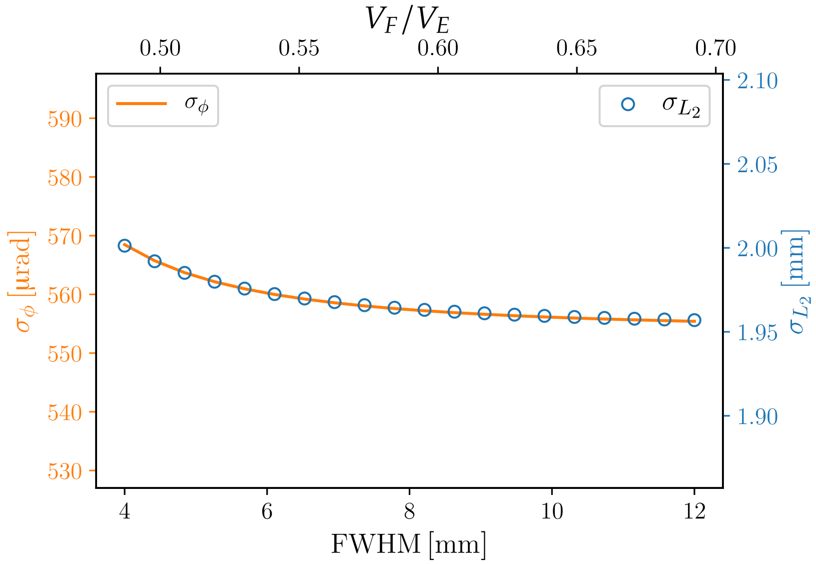

Figure 9.9. Plot of the parameters σ_ϕ and σ_{L_2} as a function of the spot FWHM on the detector plane (measured with the slits in place) and of the corresponding focusing voltage assuming the linear depdendence of equation (9.1). The description is approximate, as a fixed beam size $w_0 = 0.96\,\mathrm{mm}$ after the second slit is assumed (see text for details).

Finite-size effects of the gratings

All theoretical models introduced in Part II do not consider gratings of finite size. This approximation is sensible as long as the surface of the grating is significantly larger than the beam spot on the grating plane. In our experiment, this condition is barely satisfied given that the grating membranes span a surface of $3 \times 3\,\mathrm{mm}^2$ whereas the spot size is expected to be of the order of $1-2\,\mathrm{mm}$ FWHM. The actual size cannot be directly measured in our setup, and it can be roughly inferred either from the geometrical propagation of the beam (the spot size on the detector plane is known as well as the size of the slits)

---

as the size w by $w = \mathrm{FWHM}\sqrt{\pi/\ln(2))}/2$.

or from the theoretical evolution of the beam (with the approach outlined in the last section). In the latter case it must be kept in mind that to allow an analytical treatment a Gaussian shape for the slits transmission function was assumed (see 6.3). This approximation is known to yield reliable results far away from the slit [131]. This is useful for instance when the model is used to estimate the coherence length at the detector plane, but might underestimate the beam size in close proximity to the collimation slits. Nevertheless, we will exploit this convenient analytical treatment to extract useful qualitative information to aid the choice of the best focusing configuration for interferometry. To

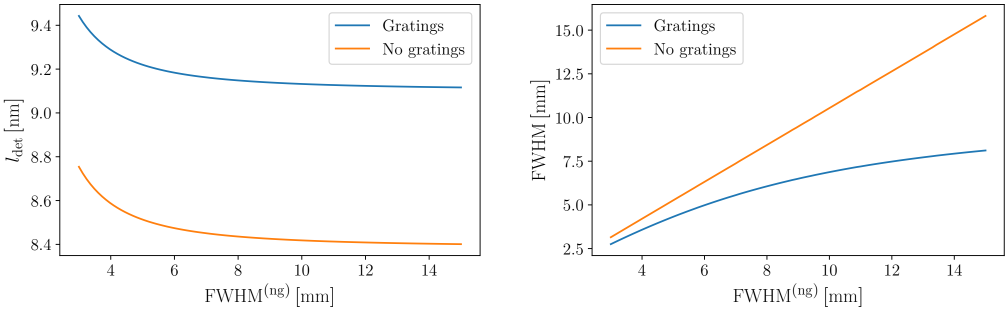

Figure 9.10. Left: coherence length $l_{\rm det}$ as a function of spot size FWHM$^{\rm (ng)}$ (measured without the gratings) on the detector plane. Finite-size diffraction gratings, when considered as additional collimation slits, introduce an improvement on $l_{\rm det}$ of a factor ≈ 1.08, essentially independent on beam focusing. Right: gratings also reduce the spot size, the strength of this effect is of course increasing with FWHM$^{\rm (ng)}$ as the beam is expected to be larger on the plane of the gratings.

this end we make a simplifying assumption and treat the gratings as an additional set of two collimation slits of size $s_g = 3\,\mathrm{mm}$, separated by a distance $L_1 = 118.1\,\mathrm{mm}$ (following the nominal parameters in Table 8.1). The first grating is assumed to be located a distance $L_{sg} = 4\,\mathrm{cm}$ from the second collimation slit, where we again assume the beam waist is located with $w_0 = 0.96\,\mathrm{mm}$. Then the evolution of the beam through the two gratings can be computed analytically to extract the coherence length on the detector plane ($L_2 = 578.7\mathrm{mm}$ after the second grating). As a first approximation[7] it is reasonable to assume that the proportionality $\sigma_\phi, \sigma_{L_2} \propto l_{\rm det}$ still holds, and that $l_{\rm det}$ is still a good figure of merit for the tolerance to misalignments, regardless of the fact that the beam undergoes a form of mechanical collimation at the same time as it interacts with the gratings. The length $l_{\rm det}$ and FWHM width of the beam on the detector plane were studied as a function of the size of the beam without accounting for the grating. To avoid ambiguity, we have labelled this parameter FWHM$^{\rm (ng)}$ in this section, and the results are shown in Fig. 9.10. As it could be expected, finite-size gratings acting as collimation slits slightly improve the coherence length $l_{\rm det}$ by a factor of approximately 1.1, independent on beam focusing. The reduction of the spot size is instead dependent on beam focusing, as it is expected from a simple geometrical picture.

For the same reasons, it is also expected that the flux transmitted by the gratings de-

---

[7] To perform a full analytical calculation in the spirit of [26] and generalize the model to gratings of finite size would be out of the scope of this work. As a matter of fact it might even be impossible to obtain a relatively compact fully analytical expression if the infinite-size approximation is dropped. In this case a computationally heavy numerical treatment would be the only option.

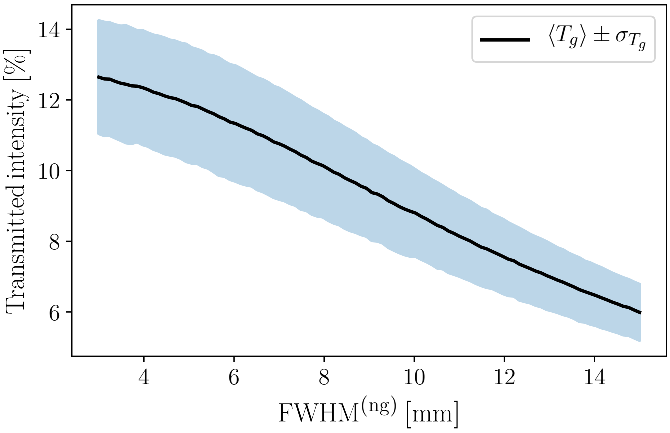

Figure 9.11. Estimated intensity transmission T_g of the two gratings. The shaded region represents a width of ± 1 standard deviation from the mean, assuming a grating positioning error of $\sigma_g = 0.5\,\mathrm{mm}$. An exact open fraction $f_o^T = 0.38$ was assumed.

pends on beam focusing. To estimate this effect we calculated the transmitted intensity through the two gratings using the beam size estimated by the model and performing (analytically) on the plane of the two gratings Gaussian integrals[8] of the form

$$T_g(a, b, \sigma_x, \sigma_y) = \frac{f_o^T}{2\pi\sigma_x\sigma_y} \int_{-d/2+a}^{d/2+a} \exp\left[-x^2/(2\sigma_x^2)\right] \mathrm{dx} \int_{-\mathrm{d}/2+\mathrm{b}}^{\mathrm{d}/2+\mathrm{b}} \exp\left[-\mathrm{y}^2/(2\sigma_\mathrm{y}^2)\right] \mathrm{dy}, \tag{9.5}$$

where a and b are possible displacements of the gratings with respect to the beam axis, f_o^T is the area open fraction of the grating[9] and d is the side of the square membrane. Since the error on grating positioning is sizeable (we assumed a realistic estimate $\sigma_{gp} = 0.5\,\mathrm{mm}$) a standard Monte-Carlo simulation was performed by drawing normally distributed displacements $a_{1,2}$ and $b_{1,2}$, independently for the two directions for each of the two gratings. Total transmission is calculated as $T_g = T_g(a_1, b_1, \sigma_x^1, \sigma_y^1) T_g(a_2, b_2, \sigma_x^2, \sigma_y^2)$ and averaged over the distribution of the displacement. The result is plotted in Fig. 9.11, where the shaded region represents a width of ±1 standard deviation from the average value. The configuration focused on detector plane undergoes significantly smaller losses due to the gratings. This could further enhance advantage in terms of density per unit exposure time of this operating mode, discussed in Fig. 9.6. However, this effect is partly compensated by a less appreciable reduction in spot size due to the mechanical effect of the gratings, as apparent in the right panel of Fig. 9.10. One can estimate the change in the density parameter D, defined in equation (9.3) and taken here as a function of FWHM$^{(\mathrm{ng})}$, as follows:

$$D'\left(\mathrm{FWHM}^{(\mathrm{ng})}\right) = D\left(\mathrm{FWHM}^{(\mathrm{ng})}\right) T_g\left(\mathrm{FWHM}^{(\mathrm{ng})}\right) \times \left(\frac{\mathrm{FWHM}^{(\mathrm{ng})}}{\mathrm{FWHM}}\right)^2 \tag{9.6}$$

This is motivated by a linear scaling of the flux with the parameter T_g, while the area is quadratic in the transverse size of the beam. The ratio D'/D is plotted in Fig. 9.12

---

[8] Accounting for the known asymmetry of the beam, its size was multiplied by a factor 1.2 (the average measured aspect ratio $\mathrm{FWHM_x}/\mathrm{FWMH_y}$) in one direction to produce a more realistic result. This asymmetry was neglected for simplicity in discussing the coherence properties of the beam.

[9] It is assumed that positrons which interact with the closed portion of the membrane are either absorbed with unit probability (which is approximately correct only for energies below 10 keV) or scattered to random angle with a wide enough distribution that they do not contribute significantly to the signal in the spot region.

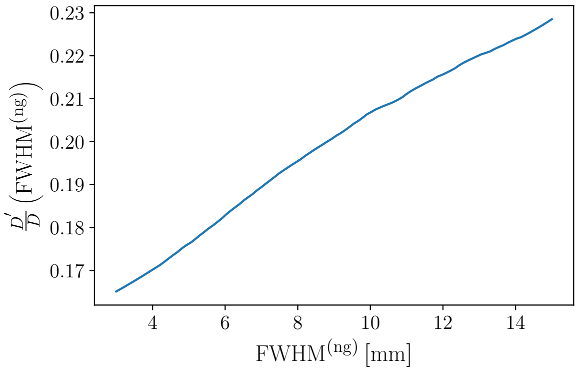

Figure 9.12. Ratio of the density parameters D' and D, that is respectively with and without the contribution of the gratings in terms of membrane transmission and change in the spot size. The functional dependence on $\mathrm{FWHM}^{(\mathrm{ng})}$ is defined in equation (9.6).

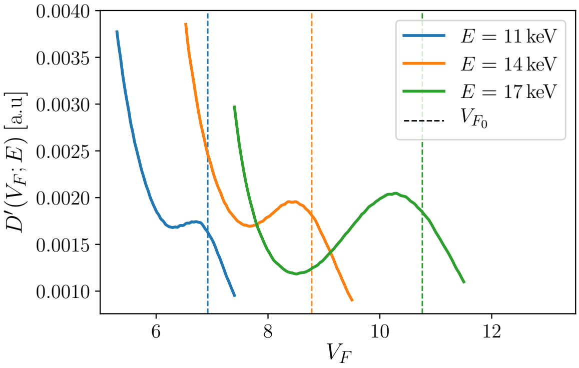

Figure 9.13. Plot of the density parameter $D'(V_F; E)$, accounting for the effect of finite-size gratings, for three reference energies. The dashed lines indicate the voltages corresponding to maximum intensity V_{F_0}.

for the range of interest. The function is not constant and an increase is observed that favours configurations focused closer to the center of the chamber (corresponding to larger values of $\mathrm{FWHM}^{(\mathrm{ng})}$). By combining this information with the dependence of beam width on beam focusing a plot analogous to Fig. 9.6 can be constructed, and is shown in Fig. 9.13. Higher density is still obtained by lowering the focusing voltage with respect to the value that maximizes the flux (V_{F_0}). The advantage obtainable within a realistic range of parameters is however slightly reduced if the effect of the gratings is taken into account, as suggested by the increasing behaviour of the function D'/D.

CHAPTER 10

Emulsion detectors

This chapter contains the results of preliminary studies on various aspects of the emulsion detectors developed for the QUPLAS-0 experiment. In particular, a first experimental run was aimed at evaluating the efficiency in detecting positrons in the energy range of interest ($10 - 20\,\mathrm{keV}$). These results were published in the paper *"Detection of low energy antimatter with emulsions"* [14]. Subsequently, the capability to detect and reconstruct micrometric-scale periodic patterns, even when operating in high vacuum (HV) conditions for several days was assessed. The results of these analysis are contained in the paper *"Nuclear emulsions for the detection of micrometric-scale fringe patterns: an application to positron interferometry"* [15].

10.1 The QUPLAS-0 emulsion detector

A hit position resolution for positrons significantly better than $1\,\mu\mathrm{m}$ is required on the detector plane to resolve the $6\,\mu\mathrm{m}$ interference with a sizeable contrast. The sinergy of a high resolution detection and a detailed theoretical model of the signal could allow to extract more information from the interference pattern with respect to the commonly used approach of moving grating masks in a three-grating interferometer [86]. The intrinsic position resolution of nuclear emulsions is known to be at the level of $0.1\,\mu\mathrm{m}$ [140] when detecting grains left by high energy cosmic rays. This feature makes nuclear emulsion a promising option for positron interferometry studies.

Nuclear emulsions are composed by silver-bromide microcrystals with a diameter of approximately $0.2\,\mu\mathrm{m}$, embedded in a gelatine matrix. The latent image left by the passage of ionizing particles is developed, via a chemical process, to silver grains approximately $1\,\mu\mathrm{m}$ in diameter, visible through an optical microscope. A review of the technology can be found in [141]. The emulsion gel used for the QUPLAS-0 experiment was produced at the Nagoya University in Japan. It features a content of silver bromide crystals of approximately 55% in volume, and a low background of thermally induced grains, at the level of $1 - 2\,\mathrm{grains}/1000\,\mu\mathrm{m}^3$.

Typically the gel is poured on plastic supports, but for this application glass plates were used. Glass has a thermal expansion coefficient one order of magnitude smaller than plastic and ensures the necessary stability at a sub-micrometric level for the detection of patterns covering a surface of some mm^2.

A $(1.0 \pm 0.1)\,\mu\mathrm{m}$ thick gelatin layer is then applied on the active emulsion surface, to protect it from mechanical stress during handling and transportation, which would result in an increased background. Glycerine is also added to the gel at a concentration of 1.5% to allow operation in vacuum. This is a particularly critical point, given that exposures with a duration of several days could be needed to collect the necessary statistics in the QUPLAS-0 measurements. A picture of emulsion detectors after development is shown in Fig. 10.1.

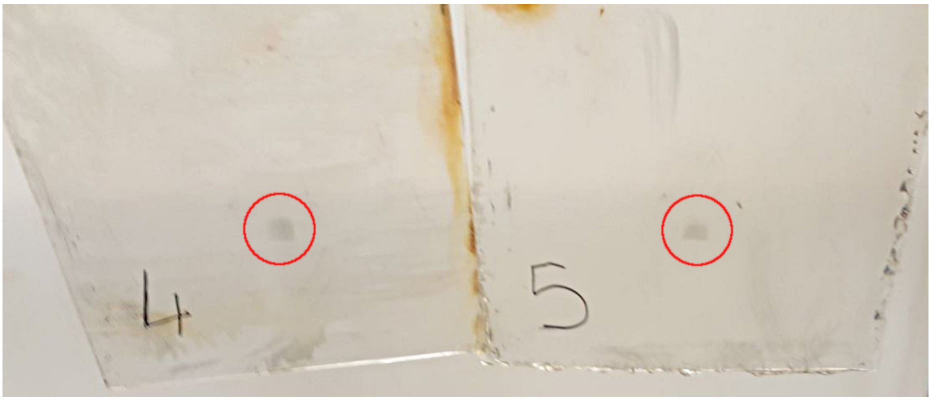

Figure 10.1. Picture of the glass-supported emulsion films after development. Red circles mark the position of the positron beam spot, visible as a faint black region in this picture.

10.2 Emulsion efficiency studies

A series of exposures to the L-NESS positron beam on the same emulsion film, moved by means of an external manipulator, was performed at the energies of $3, 6, 9, 12, 15, 18\,\mathrm{keV}$. In order to estimate the detection efficiency, the positron rate at the target during the measurement at $18\,\mathrm{keV}$ was estimated to be $n_0 = (7.6 \pm 0.9) \times 10^3\,\mathrm{s}^{-1}$. This estimate was performed by measuring the intrinsic efficiency of HPGe detectors for photons of $511\,\mathrm{keV}$ using a calibrated ^{22}Na source and taking into account the solid angle of the detector, the attenuation of the vacuum chamber, the emulsion and the aluminium holder, the positron backscattering, etc. [14]. A linear increase in flux, estimated at 8% for $9\,\mathrm{keV}$, was measured for lower energies. Therefore the observed counts on the emulsions has been suitably rescaled and the flux is considered to be a constant. Exposure was performed at a pressure in the $10^{-6} - 10^{-7}\mathrm{mbar}$ range, which is the standard requirement for the correct operation of the L-NESS beam. Note that when working with emulsions both cold and hot cathode pressure gauges cannot be employed, as it was observed that stray light can be absorbed by the detector and produce a significant background increase.

Absorption of positrons by the emulsion protective layer must to be taken into account, and this was performed by adapting a semi-empirical model [142, 143] based on the parametrization of Monte Carlo simulations, which has been widely used for modelling positron stopping profiles in several materials. It is expected that the total rate detected on the emulsion $n_{\mathrm{emu}}(E)$ depends on the incoming rate n_0 as follows:

$$N_{\mathrm{emu}}(E) = n_0 T(E) \varepsilon_{\mathrm{emu}}(E), \tag{10.1}$$

where $T(E)$ is the transmission percentage of the protective layer at the energy E, calculated with the above mentioned method, and $\varepsilon_{\mathrm{emu}}(E)$ is a (possibly energy dependent) intrinsic emulsion efficiency. The product $N^*_{e^+}(E) = n_0 T(E)$ obviously represents the predicted rate of positrons actually reaching the active emulsion layer.

$E\,(\mathrm{keV})$	$T\,(\%)$	$N^*_{e+}\ (\times 10^3\,\mathrm{s}^{-1})$	$N_{\mathrm{emu}}\ (\times 10^3\,\mathrm{s}^{-1})$	$\varepsilon_{\mathrm{emu}}\,(\%)$
9	35 ± 6	2.7 ± 0.6	2.08 ± 0.04	78 ± 16
12	66 ± 6	5.0 ± 0.7	3.98 ± 0.06	79 ± 11
15	80 ± 3	6.1 ± 0.8	4.73 ± 0.07	78 ± 10
18	86 ± 2	6.5 ± 0.8	5.67 ± 0.07	87 ± 11

Table 10.1. Summary of the experimental results of the test run to evaluate emulsion efficiency, which is defined by equation (10.1) as the ratio $N_{\mathrm{emu}}/N^*_{e+}$ The content of this table is adapted from [14].

Experimental results of this test are summarized in Table 10.1 and Fig. 10.2. No positrons were observed at energies below $9\,\mathrm{keV}$; calculations with the semi-empirical model indeed show that the transmission probability is essentially zero already at $6\,\mathrm{keV}$.

The calculated efficiency inherits the large errors that affect the determination of the initial flux n_0 and of the function $T(E)$ (the latter in turn arises from a large 10% uncertainty on the thickness of the protective layer). If a linear regression is performed on the efficiency data, assuming the linear dependence $\varepsilon(E) = A + BE$, the estimated fit parameters are $A = 0.7 \pm 1$ and $B = (0.008 \pm 0.006)\,\mathrm{keV}^{-1}$. The coefficient of the energy dependent part is compatible with zero. Within the large uncertainties, this analysis supports the conclusion that the intrinsic emulsion efficiency is weakly dependent on the energy in this range. All experimental points (see the inset of Fig. 10.2) are indeed compatible, and suggest an efficiency of the order of 80%.

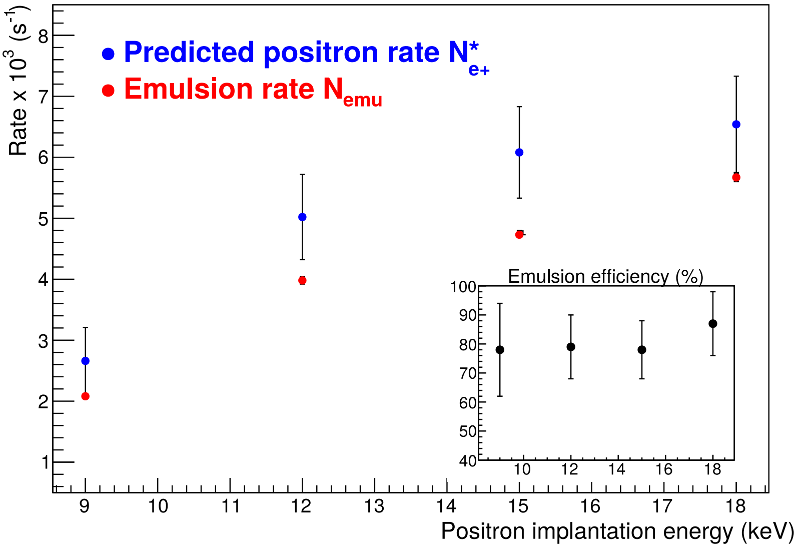

Figure 10.2. Plot of the results of Table 10.1, reported for ease of visualization.

10.3 Detection of micrometric fringe patterns with nuclear emulsion

10.3.1 Experimental setup

To assess the performance of emulsions in a scenario comparable to the detection of periodic fringes produced by the QUPLAS-0 interferometer, an experimental test was devised and implemented. This consisted in placing diffraction gratings with periodicities of $6, 7$ and $20\,\mu\mathrm{m}$ in close contact with the emulsion surface to act as absorption masks for the incoming positrons, thus producing a periodic pattern.

In particular, two different silicon nitride diffraction gratings were exposed to the positron beam:

- **Grating A** is part of the samples produced by LumArray Inc. [123, 138], specifically for QUPLAS-0. Here we recall their specifications: the transmissive region is a free standing silicon nitride (SiN) membrane, approximately $700\,\mathrm{nm}$ thick, coated on both sides with a $10\,\mathrm{nm}$ thick gold layer to prevent charge build-up. The free standing area has a surface of $3 \times 3\,\mathrm{mm}^2$, and is patterned with a system of rectangular apertures. Slits with a periodicity $d_1 = (1209.7 \pm 0.3)\,\mathrm{nm}$ and an approximately 50% open fraction run along the horizontal direction (see figure 10.3). In the orthogonal direction, the pattern has a period $d_2 = (7.00 \pm 0.05)\,\mu\mathrm{m}$ and an open fraction of $(79 \pm 3)\%$.

- **Grating B** was produced at the L-NESS laboratory with a technique based on electron beam lithography. This free standing silicon nitride membrane is $325\,\mathrm{nm}$ thick, and spans several adjacent but disconnected regions, each one $300 \times 300\,\mu\mathrm{m}^2$ wide. This sample is also gold coated with a $10\,\mathrm{nm}$ gold layer. A system of slits is patterned in two orthogonal directions, in analogy with the previous case. Periods are $d_3 = (6000.0 \pm 0.5)\,\mathrm{nm}$ (open fraction of $(58 \pm 3)\%$) and $d_4 = (20000.0 \pm 0.5)\,\mathrm{nm}$ (open fraction of $(54 \pm 1)\%$).

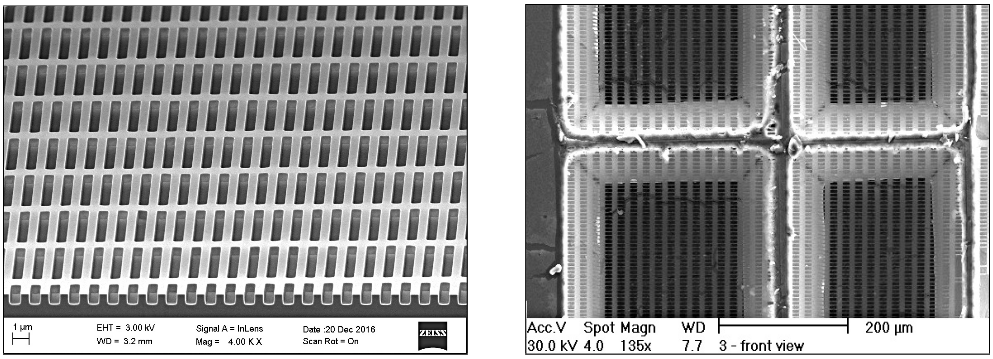

Figure 10.3. SEM images of Grating A (**left**) and Grating B (**right**).

The gratings were positioned in close contact with the emulsion surface by means of a carefully aligned grating holder (see figure 10.4), with the necessary degrees of freedom for the grating to seat flat on the emulsion surface[1]. In the case of sample B, the membrane-to-emulsion distance was limited by the thickness of the silicon wafer, which was mounted as shown in figure 10.4. Therefore we estimated a distance of the order of $\Delta X_B \approx 0.3\,\mathrm{mm}$. For Grating A, an arbitrarily small distance was possible. However a spacing of $\Delta X_A \approx 0.1\,\mathrm{mm}$ was set to avoid breakage of the thin membrane.

---

[1] Practically, the aluminium disk supporting the grating was given some mechanical play inside its holder and was fastened with a single nut. Therefore it was possible to bring a test glass plate close to the grating holder kept horizontal, release the nut to let the grating surface lie flat on the glass plate by gravity. The

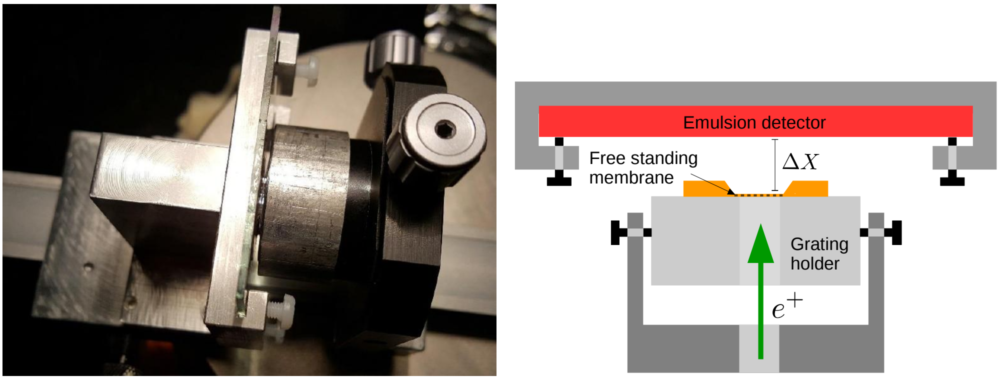

Figure 10.4. Picture (left) and sketch (right) of the system used to put the grating membranes in *contact* with the emulsion detector. The grating holder was mounted on an x-y translation stage to allow alignment of the grating membrane with the beam by means of a reference laser. The membrane-to-emulsion distance is defined as ΔX.

For these measurements the beam was delivering a nearly Gaussian beam spot, and two different configurations were tested. In a "focused" mode of operation the beam was focused on the emulsion/grating plane, and had a diameter of approximately $2.3\,\mathrm{mm}$ FWHM. An "unfocused" mode where the beam was focused after the sample, thus delivering a larger $\approx 5\,\mathrm{mm}$ FWHM spot was tested. In both cases the total positron flux was approximately $5 \times 10^3\, s^{-1}$. The grating membrane was centered on the peak intensity of the beam by means of the reference laser in the "focused" mode.

10.3.2 Pattern detection techniques

Emulsions were scanned at the automated scanning facility of the University of Bern. We now briefly describe the scanning procedure: the microscope camera is equipped with a 1280×1024 pixels CMOS sensor and grabs images corresponding to $378 \times 294\,\mu\mathrm{m}^2$ emulsion surface. The center portion of one of these images selected from exposure of grating A is shown in figure 10.5 (a). A positioning stage moves the microscope on the horizontal (x-y) plane and for each given position a sequence of 35 images is taken by shifting the focal plane vertically along the z-axis (the pitch between consecutive images is $1.5\,\mu\mathrm{m}$). The silver grains are reconstructed as clusters by a specific algorithm which assigns them their corresponding (x, y, z) coordinates both in a coordinate system local to the view, and in a global reference frame that takes into account the stage position. In figure 10.5 (b) the distribution of the cluster coordinates from all the images taken at a given horizontal position is shown, and in the following we will refer to these sets of data as *views*. The volume of interest is scanned by repeating this procedure for adja-

---

emulsion and grating holders were mounted on a piece of rail similar to the main interferometer guide, which allowed sufficiently repeatable positioning. To perform the measurements, the emulsion support with the active detector was then gently pushed towards the grating mount.

cent views. The following analysis will make use of the local coordinates only[2]. Global coordinates are however used to examine the large scale features of the exposures such as the beam profile. Positrons in the $E < 20\,\mathrm{keV}$ energy range can penetrate less than $1\,\mu\mathrm{m}$ in the active volume of the emulsion detector before annihilation takes place, therefore a sharp peak close to the surface is a clear signature of positron annihilation grains. The peak is clearly evident in the histogram of the z coordinate shown in figure 10.5 (c). Background grains detected in the emulsion are due to various sources: an intrinsic noise due to thermal effects, cosmic rays and Compton electrons from the $511\,\mathrm{keV}$ gammas produced in positron annihilation events. To isolate the signal, a Gaussian fit is performed on the peak of the histogram and a cut on the z coordinate is made using the standard deviation σ_z and mean z_0 from the fit results, namely $|z_0 - z| < 1.5\sigma_z$.

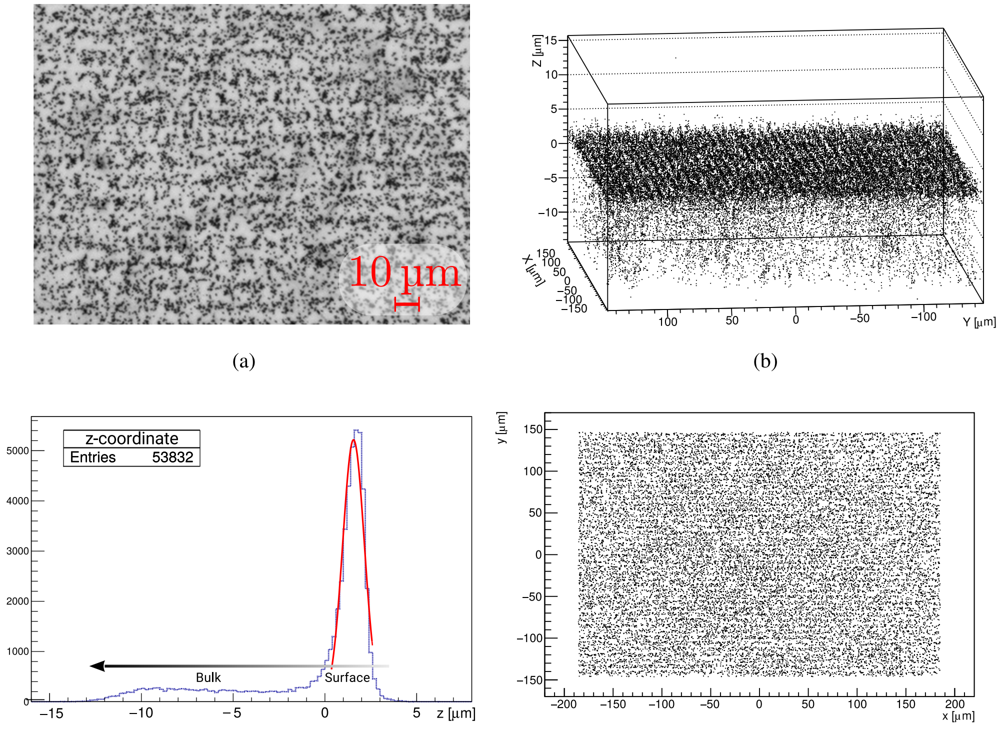

(a) (b)

(c) (d)

Figure 10.5. Center portion of a raw microscope frame at fixed z position (a), (x, y, z) position of the reconstructed clusters in the view (b), histogram of the z coordinate of the clusters and Gaussian fit used for the selection procedure (c). The arrow indicates the direction of incoming positrons. Note that the origin of the z-axis is arbitrary and different for each view; the cut is determined independently for each single view. Plot of the (x, y) position of the clusters (d). All the above images refer to the same view, from the exposure of Grating A.

Close to the edge of the microscope frames, optical aberrations are not negligible. The decrease in sharpness and contrast in that region could worsen the performance of the clustering algorithm, therefore a cut is also performed in (x, y), to an area of $340 \times 270\,\mu\mathrm{m}^2$. Furthermore, aberrations result in a slight curvature of the average positron implantation depth over the surface of the view, artificially enlarging the width of the peak in z. The (x, y, z) coordinates are thus fit with a polynomial of the form $f(x, y) = (x - a)^2 + (y - b)^2 + c$, and the z positions corrected accordingly. This improves the effectiveness of the cut on z and consistently improves the measured contrast. The grain positions on the (x, y) plane are not altered as this would require a more detailed model of the optical distortion profile. The following discussion will show that regardless of optical aberrations, accurate distance measurements at least at the level of 1%, which is more than sufficient for our purposes, can be obtained. Figure 10.6 shows an example of the effect of the correction of aberrations on the z coordinate on a selected view. The final (x, y) distribution in a single view after aberration correction and the application of the above mentioned selection criterion on z coordinate is shown in figure 10.5 (d) where a hint of a periodic structure (with the expected $7\,\mu\mathrm{m}$ periodicity) is appreciable even by visual inspection.

---

[2] Attempts to make use of all the statistics in the global coordinate system were unsuccessful and lead to measuring much lower contrasts. The motion of the microscope is not accurate enough to define a reference frame that is consistent at the sub-micrometric level on the full scanning surface.

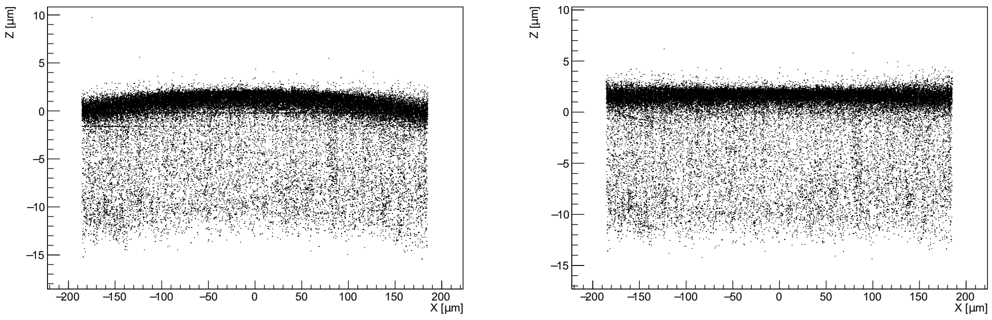

Figure 10.6. Example of the (x, z) distribution of grains in a single view before (left) and after (right) correction of optical aberrations is applied.

The analysis of emulsion data needs to take into account the rotation angle α between the laboratory and the microscope reference frames. Therefore, the periodic signal is expected in a linear combination of the (x, y) coordinates, that we define for instance as $t = -x \sin\alpha + y \cos\alpha$, with the rotation angle α to be determined. The shape of the intensity pattern produced by the gratings as absorption masks is well approximated by a *square wave*. This assumption neglects the fact that gratings have a finite thickness, therefore positrons transmitted through the closed portions of the periodic structure would undergo multiple scattering. The resulting smearing effect would then distort the profile. However, in a regime of relatively strong absorption (as it will be inferred from the data, the contrast produced by absorption only was $> 65\%$), this effect can be neglected without significantly impacting the results. For a period d, and an open fraction f_o, the general intensity profile, modulo an overall normalization constant reads:

$$I(t) = \sum_{k=-\infty}^{\infty} \chi_{[kd,(f_o+k)d]}(t) + A(C_0)\chi_{[(f_o+k)d,(1+k)d]}(t), \tag{10.2}$$

where $\chi_{[a,b]}(t)$ is the characteristic function of the interval $[a, b]$, and the parameter $A(C_0) < 1$ is related to the contrast by $A(C_0) = (1 - C_0)/(1 + C_0)$. The contrast C_0 depends on the (energy-dependent) positron transmission rate through the closed portion of the grating periodic structure and the protective emulsion layer. It represents the contrast of the signal before the introduction of finite resolution effects, and can be estimated by a Monte Carlo simulation with the *PENELOPE* (Penetration and ENErgy LOss of Positrons and Electrons) package [144]. Specifically the *pyPenelope* interface [145] was used, and more details and examples will be discussed in the following section.

The effective resolution of the emulsion-grating system, defined as a Gaussian smearing of the (x, y) position of the clusters has three main contributions: the intrinsic resolution of the scanning and clustering procedure $\sigma_{\mathrm{INT}} \approx 0.1\,\mu\mathrm{m}$, the multiple scattering in the emulsion protective layer ($\sigma_{\mathrm{MSL}} \approx 0.3\,\mu\mathrm{m}$)[3], and finally $\sigma_{\mathrm{DIV}} = \sigma_\theta \Delta X$. The latter is due to the angular divergence of the beam, projected through the emulsion-membrane distance ΔX. The beam divergence for the "focused" mode was estimated to be $\sigma_\theta \approx 6\,\mathrm{mrad}$, by measuring its diameter on two planes $65\,\mathrm{cm}$ apart (one of which is the beam waist), as discussed in section 5.2. This makes σ_{DIV} the dominant contribution to the total resolution already for $\Delta X > 0.05\,\mathrm{mm}$. The total effective resolution is therefore given by:

$$\sigma = \sqrt{\sigma_{\mathrm{INT}}^2 + \sigma_{\mathrm{MSL}}^2 + \sigma_{\mathrm{DIV}}^2}, \tag{10.3}$$

and the signal, including smearing effects, is obtained by convolving the square wave $I(t)$ with a Gaussian function. The integral $I_\sigma(t) = \int \exp\left[-(t-s)^2/(2\sigma^2)\right] I(s)\,\mathrm{d}s$ is easily performed and reads:

$$\begin{aligned} I_\sigma(t) = \sum_{k=-\infty}^{\infty} B \Bigg[&(1-A)\,\mathrm{erf}\left(\frac{d(f_o+k)-t+t_0}{\sqrt{2}\sigma}\right) + \\ &+ A\,\mathrm{erf}\left(\frac{d(1+k)-t+t_0}{\sqrt{2}\sigma}\right) - \mathrm{erf}\left(\frac{kd-t+t_0}{\sqrt{2}\sigma}\right)\Bigg], \end{aligned} \tag{10.4}$$

where the sum can be truncated to $|k| \leqslant 2$ given that $\sigma \ll d$ is expected for successful detection of the periodic signal. Overall constants are absorbed into the parameter B, and t_0 accounts for a phase shift (displacement) of the periodic signal. The measured contrast follows from the usual definition:

$$C_\sigma = \frac{I_{\max} - I_{\min}}{I_{\max} + I_{\min}}, \tag{10.5}$$

where $I_{\max}$ ($I_{\min}$) is the absolute maximum (minimum) of the $I_\sigma(t)$ function. It is worth noting that it would be possible to derive a similar analytical expression also if the smearing effect of multiple scattering by the grating is not neglected. The parameters σ and A (or C_0) in equation (10.4) are strongly correlated. Typically a good fit to the data is obtained with different combinations of these two parameters. Essentially a poorer resolution can mimic the effects of a lower initial contrast and vice versa. This ambiguity is eliminated by suitable constraints on the fit parameters, consistent with a realistic estimate of C_0 via Monte Carlo simulation. The analytical expression (10.4) also allows to conveniently estimate the required resolution to detect a given periodic pattern. Several examples are shown in figure 10.7, which suggests that a resolution significantly better than $1\,\mu\mathrm{m}$ is required to detect the $6\,\mu\mathrm{m}$ positron interference pattern with sizeable contrast. Emulsion detectors are among the few detectors capable of this resolution.

---

[3] Estimated with a Monte Carlo simulation in the relevant energy range for these exposures, given the density and composition of the protective layer [14]. We do not give a detailed discussion of the error, which is dominated by the 10% uncertainty on the thickness of the layer.

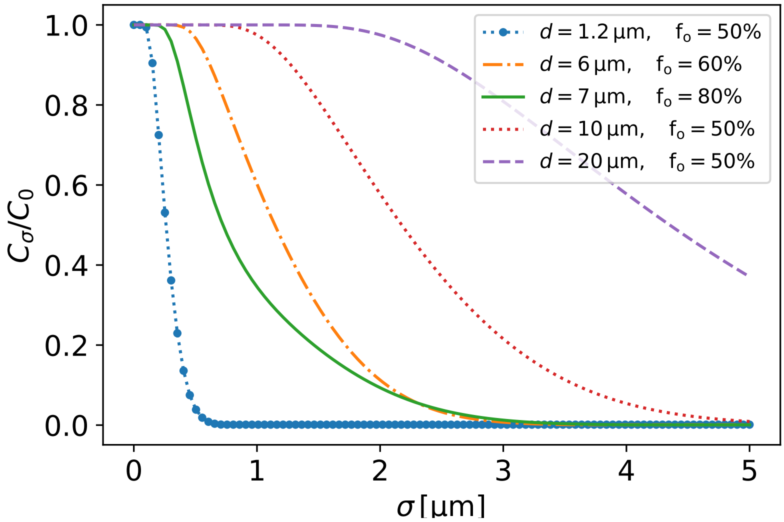

Figure 10.7. Plot of the ratio C_σ/C_0, obtained with equation (10.4) for some representative combinations of periods and open fractions. The parameter C_0 is the original contrast of the periodic pattern, while C_σ is the contrast after smearing with a resolution σ (as defined in equation (10.5)). The ratio is largely independent on the choice of initial contrast C_0.

Equation 10.4 should fit the observed intensity profile, however, to enhance the visibility of the pattern, it is convenient to *fold* the data over one single period d_{fold}, by constructing a histogram of $t' = t \bmod d_{\text{fold}}$. A fit of the resulting histogram with the equation 10.4 is then performed with the constraint $d = d_{\text{fold}}$. An example is shown in figure 10.8. The goal of the analysis is then to find the optimal combination of parameters $(\alpha^*, d^*_{\text{fold}})$ that maximize C_σ, therefore d^*_{fold} is the best estimate of the signal periodicity. A two-parameter blind search is performed on a coarse-grained grid; a representative example is shown in figure 10.8, where C_σ is plotted as a function of $(\alpha, d_{\text{fold}})$. The optimal values $(\alpha^*, d^*_{\text{fold}})$ are then determined by means of a standard minimization algorithm. The described analysis is performed independently on each *view* of the analyzed emulsion surface.

An alternative method based on the so-called Rayleigh test [146] was applied. This approach is effective in finding periodicities in unbinned data even with low statistics, and does not depend on a specific model for the shape of the expected signal. The test statistic, R, is defined as [146]

$$R(\alpha, d_{\text{fold}}) = \left| \frac{1}{n} \sum_{j=1}^{n} \exp\left(i \frac{2\pi t_j(\alpha)}{d_{\text{fold}}} \right) \right| . \tag{10.6}$$

where $t_j(\alpha)$ labels the rotated coordinate of the j-th cluster in a view. For large n, the quantity $2nR^2$ is distributed as χ^2 with two degrees of freedom [146], and this information can be used to evaluate the significance of a periodic signal from the hypothesis of uniformly distributed points. Therefore, in full analogy with the previous method, a two parameter search is made to find the optimal values $(\alpha^*, d^*_{\text{fold}})$ maximizing R.

Finally, it is worth noting that if the data from emulsion scans are used to measure

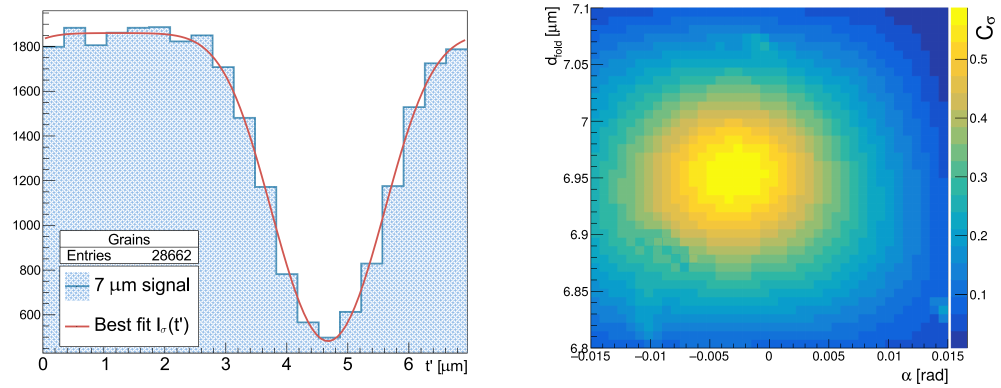

Figure 10.8. Left: example of a fit of the distribution of the grains for the same view of Grating A exposure displayed in figure 10.5. The measured contrast is approximately 50%. Right: C_σ as a function of $(\alpha, d_{\text{fold}})$.

length scales, such as the grating periods, the systematic error on the conversion factor between image pixels and actual position on the emulsion surface must be taken into account. This constant is estimated by moving the horizontal stage a few hundreds of microns and comparing the displacement of a pattern of clusters in microns (as it is measured by the stage encoder) and in pixels (as it is observed by the camera). We have estimated an uncertainty of approximately 0.8% on the measurement of this parameter. A more detailed discussion will follow in the results section.

10.3.3 Monte Carlo simulation of positron transport

As mentioned in the previous section, Monte Carlo simulations with the PENELOPE code were used to evaluate the transport of positrons through several materials. This approach will also be applied in other parts of this thesis, therefore we will now briefly discuss the results produced by this software package. More specifically, the *pyPenelope* graphical user interface [145] for the PENELOPE code was used. This software allows to conveniently define the materials and the geometry of the substrate through which positrons must be propagated. A run of the program performs a full Monte Carlo simulation of an ensemble of positron trajectories, allows graphical visualization of the simulated particles (see Fig. 10.9, left panel), and outputs a detailed result file with all the scattering events for each trajectory. Each positron is also tagged according to its final state (backscattered, transmitted, absorbed). Relevant information that can be inferred from this file include the energy or exit angle distribution of transmitted positrons (see Fig. 10.10). In the paper [143] results of a Monte Carlo simulation specifically tuned for positrons were reported, and phenomenological analytical models for the stopping profile (distribution of the positron implantation depth in a given sample), called *generalized Mahkov profiles* were obtained from the simulations. As a cross check on the results of the general-purpose *PENELOPE* software, we (successfully) reproduced the results from [143]. An example is shown in the right panel of Fig. 10.9: the stopping profile for a multilayer of aluminium ($113\,\text{nm}$) and platinum ($113\,\text{nm}$) over a silicon substrate, obtained from the *PENELOPE* simulation is superimposed to the analytical model with the parameters reported in [143], displaying very good agreement.

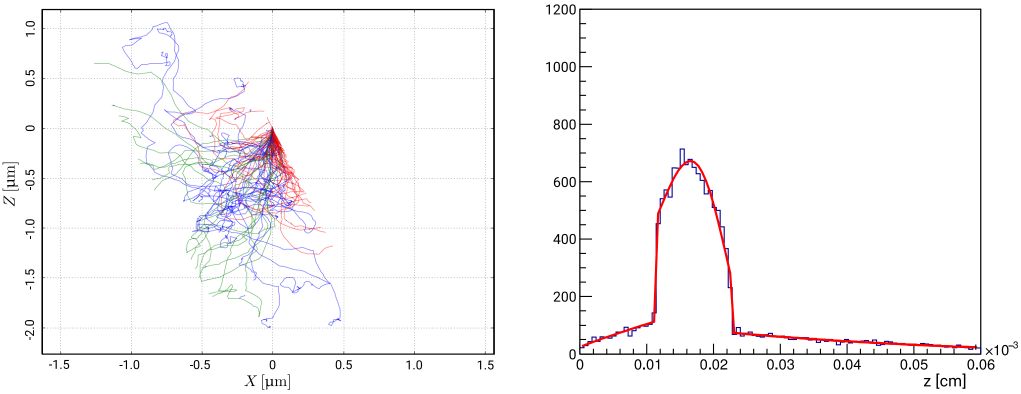

Figure 10.9. Graphical output (trajectories) of a typical *pyPenelope* simulation (left). Stopping profile of $10\,\mathrm{keV}$ positrons in a multilayer of aluminium ($113\,\mathrm{nm}$)/platinum ($113\,\mathrm{nm}$)/silicon, on the (right). A total of 20000 trajectories were simulated to obtain this result, which is shown as an example of the good agreement between *pyPenelope* simulations and the literature. The solid line is an analytical model developed in [143], based on Monte Carlo simulations performed with a specifically tuned code.

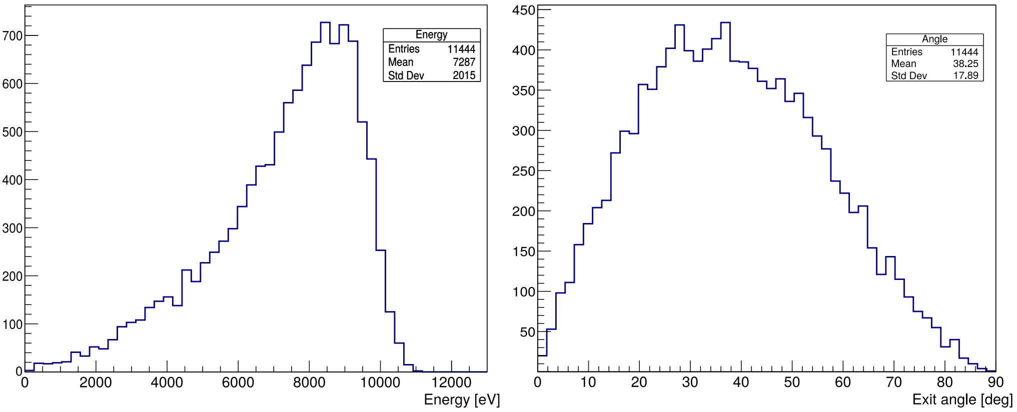

Figure 10.10. Distribution of the energy (left) and exit angle (right) for positrons at $12\,\mathrm{keV}$ initial energy, transmitted through a $700\,\mathrm{nm}$ thick silicon nitride layer, with a $10\,\mathrm{nm}$ gold coating, representing the membrane of the QUPLAS-0 diffraction gratings. The exit angle β is defined as $\beta = \tan^{-1}(\sqrt{x^2+y^2}/z)$, where the z-coordinate is normal to the exit surface from the membrane.

10.3.4 Results of the exposures

For each grating sample, a main $30\,\mathrm{min}$ long exposure with the beam in "focused" mode (we recall, focused on the grating/emulsion plane) was performed. Subsequently, the emulsion detector was replaced and a $2\,\mathrm{hour}$ long exposure performed with the beam in "unfocused" mode. The "unfocused" mode of operation could theoretically feature a significantly reduced beam divergence, therefore this repeated test was aimed at finding evidence for a variation in the observed resolution brought by changes in the σ_{DIV} parameter (which could also be an interesting way of measuring the divergence of a beam with an exposure on a single plane). For several reasons the measurements were not conclusive in this regard (which I stress was not the main aim of the exposures). We recall from the definition of the smearing parameter $\sigma_{\mathrm{DIV}} = \Delta X \sigma_\theta$ that it is directly proportional to the distance. Therefore failure to repeat the reciprocal positioning of the emulsion and the membrane with sufficient accuracy might have hidden any contrast increase brought by reduced beam divergence. Furthermore, the beam position was characterized in the "focused" mode, and laser alignment of the gratings performed accordingly. It was however found that changing the potential on the focusing electrodes induced a displacement of the beam spot, therefore the membrane was exposed to the tails of the beam which could first of all feature different divergence characteristics (there could be local correlations between spatial position in the beam spot and mean divergence angle of positrons in that position). Secondly, due to the unintended drop in intensity caused by the displacement, the signal density was lower than expected. The resulting decrease in signal-to-noise ratio naturally introduces a spurious loss of contrast. For this reasons, the following analysis covers the main exposures in "focused" mode. It is however important to stress that the pattern was successfully recovered with similar contrast in both cases. The beam spots on the emulsion surface are shown in Fig. 10.11 for the two ("focused" and "unfocused") exposures of Grating A. The square shape of the membrane is clearly visible, as well as the aforementioned displacement of the beam spot with respect to the membrane.

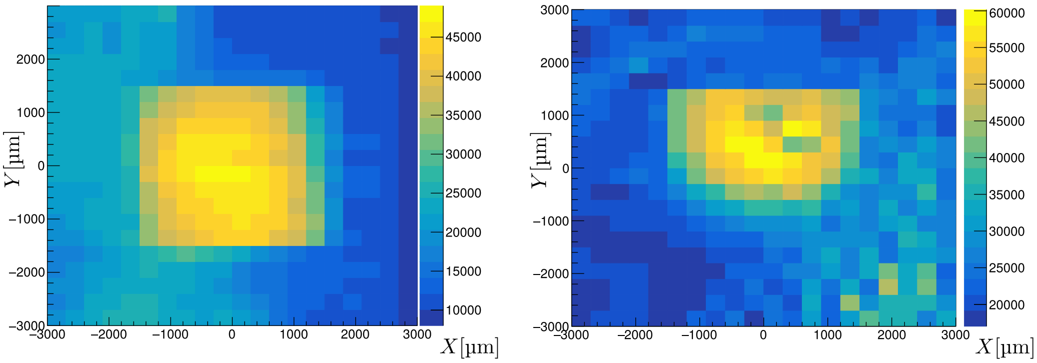

Figure 10.11. Beam spots (as 2D histograms) on the emulsion for the two exposures of Grating A. The square shape of the $3 \times 3\,\mathrm{mm}^2$ membrane is clearly visible. Each bin covers a surface of $300 \times 300\,\mu\mathrm{m}^2$.

Grating A exposure

Exposure of Grating A was performed at the positron energy $E_A = 12\,\mathrm{keV}$. Transport through the multilayer of gold and silicon nitride (Si_3N_4) was simulated with the method described in 10.3.3, to extract the energy distribution of the transmitted positrons. This distribution is then multiplied by the function $T(E)$, defined (we recall from section 10.2) as the the probability for a positron of energy E to be transmitted through the emulsion protective layer. The integral of the resulting distribution allows one to calculate the fraction F_C of positrons impinging on the active emulsion surface having traversed the closed part of the grating. The corresponding fraction for the open part of the grating is simply $T(E_A)$. Therefore, the estimated contrast is $C_0 = [T(E_A) - F_C] \,/\, [T(E_A) + F_C]$. Accounting for the errors on the protective layer thickness, a contrast range $0.75 < C_0 < 0.85$ for C_0 was estimated, and serves as a useful constraint for the fit parameters in equation (10.4).

An analysis software was written to apply the folding technique outlined in section 10.3.2 to all the views in a region of interest. The software makes use of ROOT [147] scripts managed as parallel jobs with the aid of GNU Parallel [148] and Python scripts. The parameters $(C_\sigma, \alpha^*, d^*_{\mathrm{fold}}, \sigma, f_o)$ are extracted by means of this analysis, which searched for the expected periodicity of 7 µm. The $1.2\,\mu\mathrm{m}$ pattern is instead undetectable with this setup, as the following discussion will clarify. Figure 10.12 shows the maps of the contrast C_σ and the angle α^* as a function of the coordinates of the geometrical center of the view on the emulsion surface $(\mathrm{X_v}, \mathrm{Y_v})$.

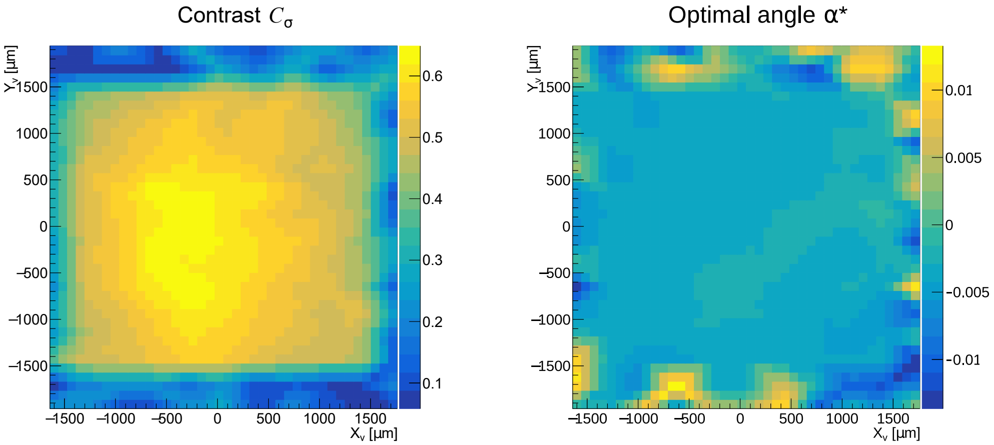

Figure 10.12. Maps of the contrast C_σ (left) and of the optimal angle α^* (right), as a function of the coordinates of the geometrical center of the views $(\mathrm{X_v}, \mathrm{Y_v})$.

The shape of the membrane is clearly visible in the contrast plot (left panel of Fig. 10.12, compare with the beam spot in the left panel of Fig. 10.11). The contrast modulation within the surface is due to several factors, as for example the intensity fall-off of the beam (FWHM $\approx 2.3\,\mathrm{mm}$) that reduces the signal-to-noise ratio near the edge of the membrane. Misalignments between the membrane and the emulsion plane, or correlations between transverse position within the beam spot and the angular spread of incoming positrons could also be responsible for a position-dependent resolution effect. Contrast does not drop abruptly near the boundary of the membrane region since the edge of the views is not necessarily aligned with the edges of the membrane itself.

The right panel of Fig. 10.12 shows an equally coherent result for the angle α^* as expected for a genuine periodic signal.

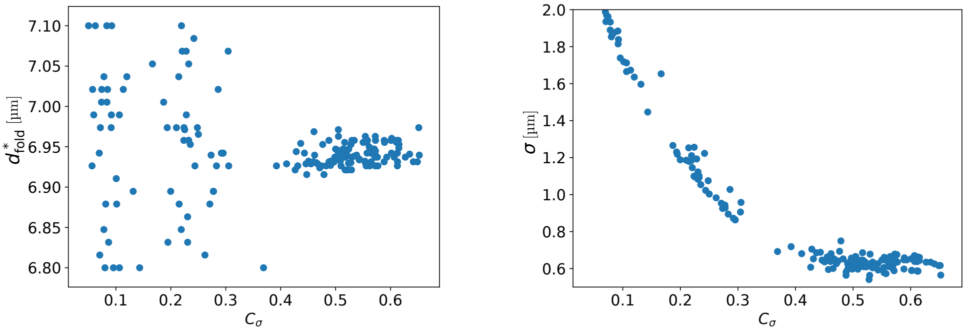

Figure 10.13. Scatter plots of the optimal period d^* (left) and resolution σ (right), versus the contrast C_σ

In Fig. 10.13 the scatter plot of the periodicity (left) and resolution (right) versus the contrast are shown for each view. In the left panel, there is clear evidence of a coherent periodic signal in a portion of the region analyzed: points with contrast $C_\sigma > 40\%$ belong to views which fall entirely inside the membrane region, where fit results are physically meaningful and reliable. The remaining points are low contrast views outside of the membrane. An interesting behaviour can be appreciated in the right panel of figure 10.13, and is explained as follows: the function $I_\sigma(t)$, defined in equation 10.4, formally reduces to a constant (that is, a periodic signal with $C_\sigma = 0$) either in the limit $C_0 \to 0$ or $\sigma \to \infty$. In this analysis the parameter C_0 is bounded to the range obtained by Monte Carlo simulation. In low contrast views a good fit is obtained for larger values of σ, as the parameter C_0 cannot approach zero. Therefore a correlation between low contrast and high estimated σ arises. In analogy with the previous discussion, no correlation is present for $C_\sigma > 40\%$, that is on views well within the membrane region with a sizeable contrast and clear periodic content.

	Period Folding	Rayleigh test
d^*_{fold}	$(6.944 \pm 0.002_{\text{stat}} \pm 0.050_{\text{syst}})$ µm	$(6.942 \pm 0.002_{\text{stat}} \pm 0.050_{\text{syst}})$ µm
α^*	(-0.0034 ± 0.0002) rad	(-0.0036 ± 0.0002) rad
C_0	$(75.5 \pm 0.2)\%$	-
C_σ	$(56.2 \pm 0.5)\%$	-
f_o	$(75.5 \pm 0.2)\%$	-
σ	$(0.630 \pm 0.004_{\text{stat}} \pm 0.005_{\text{sist}})$ µm	-

Table 10.2. Best estimate of the relevant parameters for the exposure of Grating A. Results for the optimal angle and period found by the folding and Rayleigh test methods are fully compatible. Systematic errors stems from the calibration of the optical imaging system, as discussed in section 10.3.2.

The best estimates of the parameters have been obtained by restricting the calculation to the views which fall completely inside the membrane region: $|\mathrm{X_v}| < 1\,\mathrm{mm}$ and $|\mathrm{Y_v}| < 1\,\mathrm{mm}$, and are summarized in table 10.2.

As a consistently check the Rayleigh test method was also applied to the same set of data. The two parameter search in the $(\alpha, d_{\mathrm{fold}})$ plane has yields compatible results on single views (compare the left panel of Fig. 10.14 with the right panel of Fig. 10.8). A scatter plot of the optimal values $(\alpha^*, d^*_{\mathrm{fold}})$ found on the set of views within the membrane with both methods is shown in the right panel of Fig. 10.14. The best estimates of the two parameters produced by the methods are compatible. We can conclude from this analysis that a periodic pattern with an average contrast of approximately 56% was detected, with features consistent with the theoretical model of equation 10.4. The measured period and open fraction are compatible with the nominal specifications provided by the manufacturer. Furthermore, the measured overall resolution of $0.63\,\mathrm{\mu m}$ reported in table 10.2 is fully compatible with expectations, as described in section 10.3.2, and such a value prevents the detectability of the $1.2\,\mathrm{\mu m}$ pattern. This also means that with a more optimized setup, with smaller membrane-to-emulsion distance and possibly a thinner protective layer, the detection of periodic patterns down to the $\approx 1\,\mathrm{\mu m}$ length scale in a genuine interferometer, where no spurious smearing effects are present, is likely feasible.

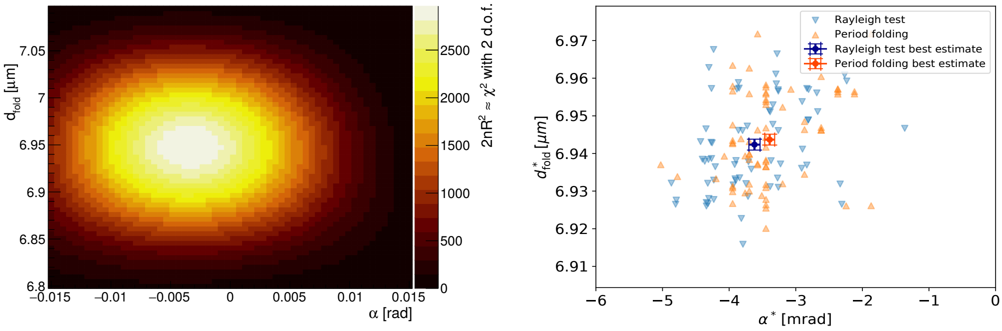

Figure 10.14. Left: plot of the function $2nR^2(\alpha, d_{\mathrm{fold}})$, defined from equation 10.6, for the same view shown in figure 10.8. Right: scatter plot of the optimal values $(\alpha^*, d^*_{\mathrm{fold}})$ for the views in the membrane region for both the period folding and the Rayleigh test methods.

Grating B exposure

For Grating B a positron energy of $E_B = 10\,\mathrm{keV}$ was chosen as the best compromise to minimize the amount of positrons transmitted by the closed parts of the membrane (significantly thinner than that of Grating A) and maximize the detection efficiency (see section 10.2). As described before Grating B is composed of several disconnected regions, therefore an extensive analysis of the whole surface was not meaningful. A total of 6 views displaying a clear periodic signal with the $20\,\mathrm{\mu m}$ periodicity were considered, and a typical raw microscope frame from one of such regions is shown in Fig. 10.15 (left panel). Each contains two detectable periodic patterns, and this feature can be exploited to improve the results of the analysis. Fig. 10.7 suggests that the contrast of the $20\,\mathrm{\mu m}$ pattern is essentially independent of the smearing resolution σ up to $\sigma \approx 2\,\mathrm{\mu m}$, therefore $C_\sigma(20\,\mathrm{\mu m}) \approx \mathrm{C}_0(20\,\mathrm{\mu m})$. On the contrary, the $6\,\mathrm{\mu m}$ signal is highly sensitive to this parameter. Furthermore, the parameters C_0 and σ are independent of the periodicities

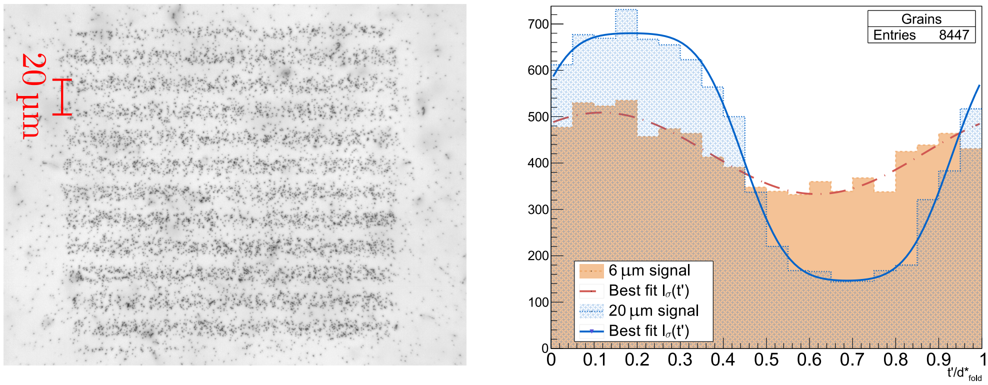

Figure 10.15. Left: raw microscope image from a single view containing one of the open regions of the diffraction grating (see figure 10.3). The 20 μm support structure is clearly visible, whereas the 6 μm periodicity in the orthogonal direction cannot be distinguished. Right: folded signal of a single view for both periodicities at their optimal values of period and angle, compared with the best fit with equation 10.4.

of the patterns and should therefore have the same value for both periodic signals. As it is apparent in comparing the raw microscope pictures, the signal density was much lower for this exposure, and the less consistent spatial quality of the periodic structure across the surface lead to larger fluctuations in contrast and in the measured geometrical parameters between the views. Therefore the more robust approach of first applying the Rayleigh test method was to find the optimal values $(\alpha^*, d^*_{\text{fold}})$, and then fitting with equation 10.4 was devised. Taking advantage as explained of both patterns, in particular a first fit the 20 μm signal is made to extract a reliable estimate of $C_0 = \overline{C}_0 \pm \sigma_{\overline{C}_0}$ (the uncertainty $\sigma_{\overline{C}_0}$ is obtained from the fit). Subsequently, equation 10.4 is fit to the 6 μm pattern with the constraint $|C_0 - \overline{C}_0| < \sigma_{\overline{C}_0}$ to obtain an estimate of all the parameters, including σ. Finally, a fit of the 20 μm pattern is performed again with suitable constraints on both C_0 and σ. The results of this procedure averaged over the views are summarized in table 10.3. Folded signals at the optimal angles and period are shown for a representative view in the right panel of figure 10.15, and compared to the best fit with equation 10.4.

	20 μm pattern	6 μm pattern
d^*_{fold}	$(19.2 \pm 0.1_{\text{stat}} \pm 0.2_{\text{syst}})$ μm	$(5.93 \pm 0.02_{\text{stat}} \pm 0.05_{\text{syst}})$ μm
C_σ	$(60 \pm 2)\%$	$(17 \pm 1)\%$
C_0	$(60 \pm 2)\%$	$(60 \pm 2)\%$
f_o	$(53 \pm 1)\%$	$(57 \pm 1)\%$
σ	(1.58 ± 0.05) μm	(1.52 ± 0.05) μm

Table 10.3. Best estimate of the relevant parameters for the exposure of Grating B, for the two periodic patterns with nominal periodicities of 20 μm and 6 μm.

The angle α^* is not reported, since for this grating the disconnected regions do not have the same orientation. The procedure effectively yields self-consistent results between the two patterns as the values of C_0 and σ are compatible.

10.3.5 Long exposure in High Vacuum

As apparent from the results above, with the full intensity of the beam and a single diffraction grating, $30\,\mathrm{min}$ of exposure are fully sufficient to obtain a signal density much higher than the intrinsic or induced background noise, as evidenced by the sizable contrast detected. However, as discussed in section 6.2, for the actual QUPLAS-0 exposures it could be necessary to collimate the beam to improve its spatial coherence. This would introduce an intensity loss of about one order of magnitude, in addition to the transmissive loss with two gratings in place, which amounts to approximaly another order of magnitude. This could mean that exposure times of the order of one or more days are required. It was reported in the past that emulsion films undergo an increase of background when kept in High Vacuum (HV) conditions (namely pressures lower than $10^{-6}\,\mathrm{mbar}$) for several days [149]. However, the detector developed for QUPLAS-0 features a new gel composition, therefore the background increase was investigated by repeating the exposure of Grating A at the same positron energy, after the emulsion was kept in the vacuum chamber at a pressure of the order of $10^{-6} - 10^{-7}\,\mathrm{mbar}$ for 1 week. The pressure cannot be monitored in real time but only estimated[4], since both cold and hot cathode pressure gauges can produce stray light and increase emulsion background grains.

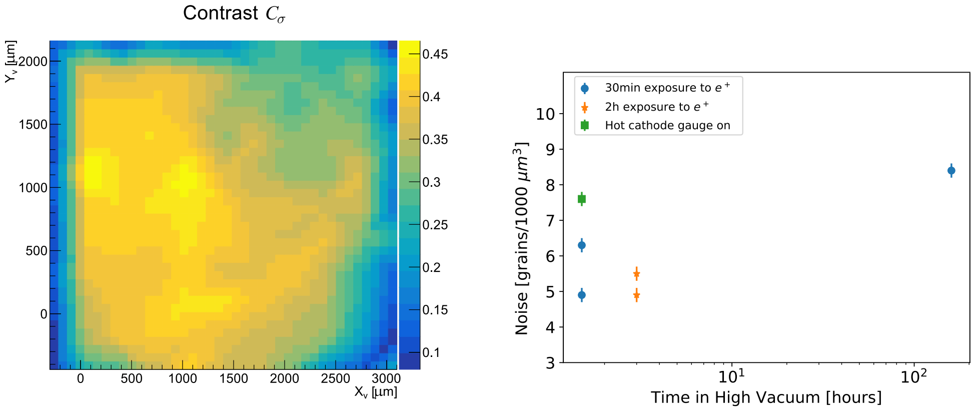

Figure 10.16. Left: contrast map covering the membrane surface, for an exposure performed after 1 week in High Vacuum (HV) conditions, at a pressure $\gtrsim 10^{-7}\,\mathrm{mbar}$. Right: density of grains measured at a distance of about $4\,\mathrm{mm}$ from the center of the beam spot, for different emulsion samples and positron exposure times as a function of the total time spent in HV.

The contrast map in the left panel of Fig. 10.16 confirms that the periodic structure is still well resolved after the emulsion was left in vacuum. A direct comparison with the previous results would be misleading since the membrane/emulsion positioning was altered. The background measurements are summarized in the right panel of figure 10.16. Each data point represents a different emulsion detector sample, specifically an average value of the grain density measured at a distance of about $4\,\mathrm{mm}$ from the center of the beam spot in four different corners. This distance is sufficient to give a good estimate of intrinsic noise which is independent on the positron exposure time. As a matter of fact, close to the beam spot, a background increase arises from the Compton electrons. The reported data also confirm that the hot cathode gauge (which was in this case left on for only 1 hour) introduces a measurable background increase.

---

[4] The typical time for our chamber to reach the working pressure of$10^{-6}\,\mathrm{mbar}$ is well known. We also performed a specific test with an emulsion film to better estimate the time needed to reach the target pressure in the presence of additional outgassing by the emulsion detector.

The main result is that an increase of exposure time to high vacuum by two orders of magnitude induces an increase in background of a factor around 1.5 with respect to the average of the other four observations. This indicates that the background level is not directly proportional to the time spent in vacuum, therefore long exposure times can effectively increase the signal-to-noise ratio in our experiment.

CHAPTER 11

Positron interferometry: preliminary measurements

11.1 Planned measurement campaign and goals

A series of measurements was planned with the goal of observing matter-wave interference in the Talbot-Lau interferometer: the setup was first configured to be at resonance for a positron energy of $E = 14\,\mathrm{keV}$ (see Table 8.1) using the rotational and longitudinal alignment techniques described in chapter 8. The first objective was then to observe sizable contrast on the emulsion at the resonance energy. The incoming positron energy could then be tuned in the $11 - 17\,\mathrm{keV}$ range. A modulation in contrast due to the change in $\lambda_{\mathrm{dB}}(E)$ is the signature of quantum interference effects as opposed to moiré (geometrical shadow) phenomena. The suggested range is limited from below by the sensitivity of standard emulsions with the protective layer applied. Although positrons could be detected down to $9\,\mathrm{keV}$ energy in our previous tests (see Table 10.1), a transmission loss by more than a factor of two with respect to $E = 14\,\mathrm{keV}$ would make a measurement at $E = 9\,\mathrm{keV}$ prohibitively long. The upper limit to the energy range is instead dictated by the capability of stable operation of the electrostatic optics for long measurement times.

The contrast dependence on positron energy is shown in the left panel of Fig. 11.1 for ideal angular and longitudinal alignment. The expected peak contrast is in excess of 90%, and the functional dependence on E displays a peculiar structure with a local minimum at $E \approx 11\,\mathrm{keV}$ and a small contrast revival for lower energies (the same feature could be appreciated also in Fig 6.3, where the total length was being varied instead of the energy). The modulation in contrast in this energy range, expressed for instance by the ratio:

$$\frac{C(11\,\mathrm{keV})}{C(14\,\mathrm{keV})} \equiv \frac{C_{11}}{C_{14}}$$

is however fairly small, with a minimum value of approximately 0.78. A sizable angular misalignment, as displayed in the right panel of Fig. 11.1 will reduce the observed modulation in contrast even further. The same effect is produced by carrying out the measurements away from the ideal detection plane. This is the main reason why it is necessary to find the optimal alignment by maximizing the contrast at resonance before the scan in energy is attempted. The dependence of the maximum contrast modulation C_{11}/C_{14} as a function of both L_2 and ϕ is plotted in Fig. 11.2.

This analysis suggests that in the worst case scenario one must be able to reconstruct the contrast of the interference signal with a relative uncertainty at the level of a few percent. A good understanding of the relevant sources of noise is therefore required.

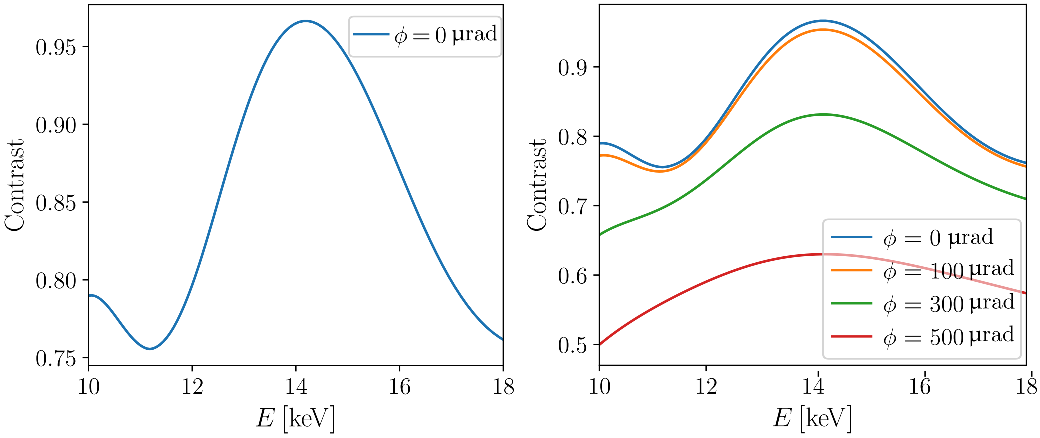

Figure 11.1. Left: contrast of the interference pattern as a function of incoming positron energy for optimal rotational alignment $\phi = 0$. Parameters used for the beam were $w_0 = 1\,\mathrm{mm}$ and $l_0 = 1.25\,\mathrm{nm}$ on the beam waist, located $5\,\mathrm{cm}$ before the first grating. Right: the same function is plotted for different relative angular positions of the gratings. The characteristic structures as well as the relative contrast modulations in the considered range are dampened as ϕ increases.

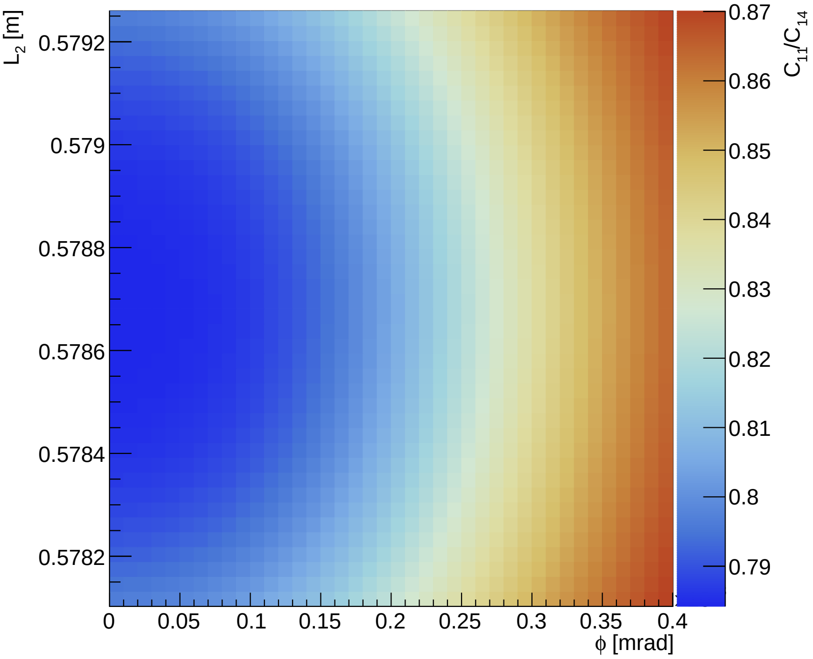

Figure 11.2. Plot of the contrast modulation parameter C_{11}/C_{14} as a function of ϕ and L_2.

11.2 Background noise estimation

In this section we will evaluate the relevance of the two main sources of background noise in the interferometric measurement. We first consider the contribution of positrons transmitted from the closed portion of the grating membrane (that we will also refer to as the grating bars). Intrinsic emulsion noise is discussed in the following section.

11.2.1 Grating membrane transmission

Although the QUPLAS-0 gratings[1] are a factor of three thicker than gratings used in the past for similar experiments [38, 132], our energy is also significantly higher. A series of Monte Carlo simulations has been performed with the *pyPenelope* software for a range of incoming positron energies (from $1\,\mathrm{keV}$ to $18\,\mathrm{keV}$ in steps of $1\,\mathrm{keV}$). From the Monte Carlo simulated trajectories, the energy distribution of the transmitted positrons can be calculated, and an example for $14\,\mathrm{keV}$ incoming energy is shown in the left panel of Fig. 11.3. The right panel of Fig. 11.3 shows the distribution of the emission angle from the surface in the x-direction, namely β_x, defined as $\tan^{-1}(x/z)$ where the z-axis is normal to the exit surface from the membrane. The emission has rotational symmetry along the z-axis, therefore an analogous result is obtained for β_y. The angular distribution can be approximated by a Gaussian function with $\sigma_\beta \approx 0.57\,\mathrm{rad}$. This parameter is observed to be essentially independent of the incoming positron energy. The pyPenelope software [145] should realistically account for surface effects at the membrane exit, and in the literature there are experimental results [150] (angle-resolved cross-section measurements) as well as independent Monte Carlo calculations [151] that indicate that a broad angular distribution can indeed be expected.

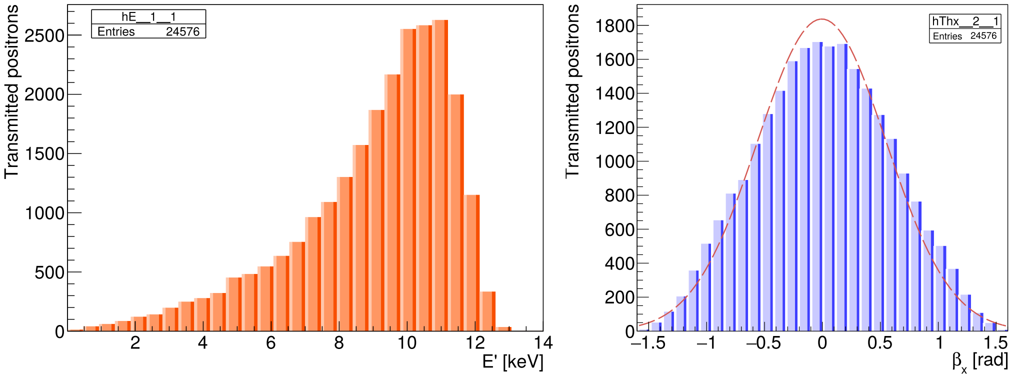

Figure 11.3. Energy and angle distribution of $14\,\mathrm{keV}$ positrons transmitted by the $700\,\mathrm{nm}$ thick grating membrane (details on the membrane are reported in section 10.3.1). The simulation was carried out for 50000 incoming positrons.

Positrons transmitted by the grating bars will produce on the emulsion a uniformly distributed pattern (with at most a Gaussian modulation on a large scale) that is superimposed over the interference signal. By virtue of the broad angular distribution, a simple geometrical argument suggests that this source of noise can be neglected: if positrons are propagated as ballistic particles from the plane of the second grating with a Gaussian angular distribution with $\sigma_\beta = 0.57\,\mathrm{rad}$, they are found to be distributed on the detector plane with $\mathrm{FWHM}_{\mathrm{noise}} \approx 0.8\,\mathrm{m}$. On the other hand the typical size of the detected positron spot in the interferometric measurements we performed is $\mathrm{FWHM}_{\mathrm{signal}} \approx 6.5\,\mathrm{mm}$. Therefore, in terms of surface density, the contribution of this source of noise is suppressed by a factor proportional to $(\mathrm{FWHM}_{\mathrm{noise}}/\mathrm{FWHM}_{\mathrm{signal}})^2 \approx 10^4$. Although we established that this is a negligible contribution by several orders of magnitude, for completeness we report the additional results extracted from the Monte Carlo simulations. We define the function $T_1(E)$ as the fraction of positrons transmitted by the silicon nitride membrane with a well-defined initial energy E. The function $T_2(E)$ is instead defined as the transmitted fraction assuming a non-monochromatic input energy distribution given by the distribution outgoing from an identical membrane hit by positrons with energy E. Both functions are displayed in Fig. 11.4. With the above definitions the product $T_1(E)T_2(E)$ essentially represents the transmission probability through two consecutive identical membranes with initial positron energy E. A positron incoming on the first grating can follow one out of four different paths to the detector plane. It can go through the open parts of both gratings, this constitutes the interference signal that we model analytically. The probability of this event is $P_{OO} = \left(f_o^T\right)^2$. The parameter f_o^T is the surface open fraction of the grating and the geometrical cut introduced by the frame of the second grating is neglected given the small angular divergence of the beam. Alternatively the particle can be transmitted by the closed portion of both the first and second grating, with probability $P_{CC} = \left(1 - f_o^T\right)^2 T_1(E)T_2(E)T_g$, where T_g is the probability for a positron scattered by the first membrane with the angular distribution of Fig. 11.3 to fall inside the $3 \times 3\,\mathrm{mm}^2$ frame of the second grating (otherwise the positron is absorbed). Finally it can go unperturbed through the slits of the first grating and be

---

[1] The geometry of the membrane for the QUPLAS-0 gratings has already been described in section 10.3.1, where it was labelled "Grating A".

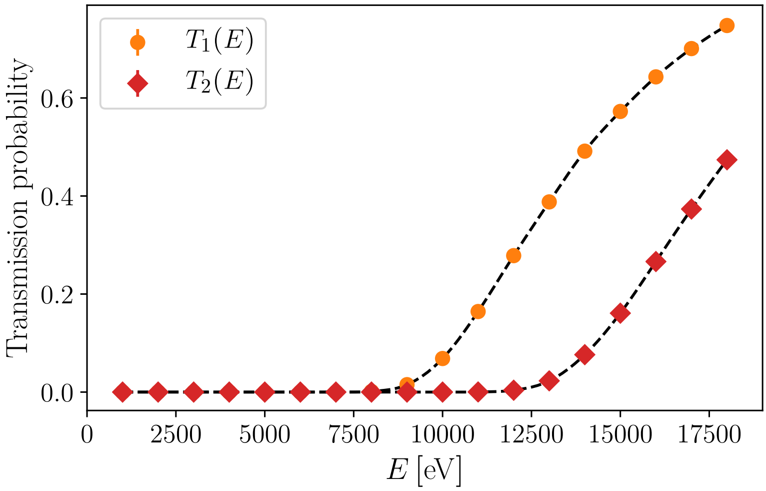

Figure 11.4. Transmission probability $T_1(E)$ through one grating membrane with a monochromatic input energy E. The function $T_2(E)$ is the transmission probability for an input energy distribution given by the output distribution produced by an identical membrane hit by positrons of energy E.

transmitted by the membrane of the second, or vice-versa. The corresponding probabilities are respectively $P_{OC} = \left(1 - f_o^T\right) f_o^T T_1(E)$ and $P_{CO} = \left(1 - f_o^T\right) f_o^T T_1(E) T_g$. Given these quantities, a signal-to-noise ratio in terms of flux can be defined as:

$$\mathrm{SNR_f(E)} = \frac{\mathrm{N_0 P_{OO}}}{\mathrm{N_0 \left(P_{CC} + P_{OC} + P_{CO}\right)}} = \frac{\left(\mathrm{f_o^T}\right)^2}{\mathrm{T_1 \left(1 - f_o^T\right) \left[\left(1 - f_o^T\right) T_2 T_g + f_o \left(1 + T_g\right)\right]}} \tag{11.1}$$

where we suppressed the E dependence. A more interesting figure of merit is however the signal-to-noise ratio in terms of average flux density, that is related to equation (11.1) as follows:

$$\mathrm{SNR_d(E)} = \mathrm{SNR_f(E)} \frac{\mathrm{S_{signal}}}{\mathrm{S_{noise}}} \tag{11.2}$$

where the parameters S_{signal} and S_{noise} are the surface covered by the signal and noise spots respectively. Assuming both are well approximated by Gaussian distributions they are proportional to the square of the FWHM parameter. Using Monte-Carlo simulation of ballistic trajectories one can estimate $T_g \approx 0.3\%$, so most of the positrons scattered through the bars of the first grating are stopped by the frame of the second gratings. The functions (11.1) and (11.2) are shown in Fig. 11.5 assuming $S_{\text{signal}}/S_{\text{noise}} \approx 10^{-4}$ as mentioned before. The SNR due to residual transmitted positrons is energy-dependent and changes by an order of magnitude in the energy range of interest. However, strong suppression due to the wide angular distribution of scattered positrons ensures that this contribution is effectively negligible in terms of flux density on the emulsion surface. This feature is particularly relevant, as the effects of a sizeable energy-dependent contribution to background noise would have to be carefully discriminated from the genuine contrast modulation shown in 11.1.

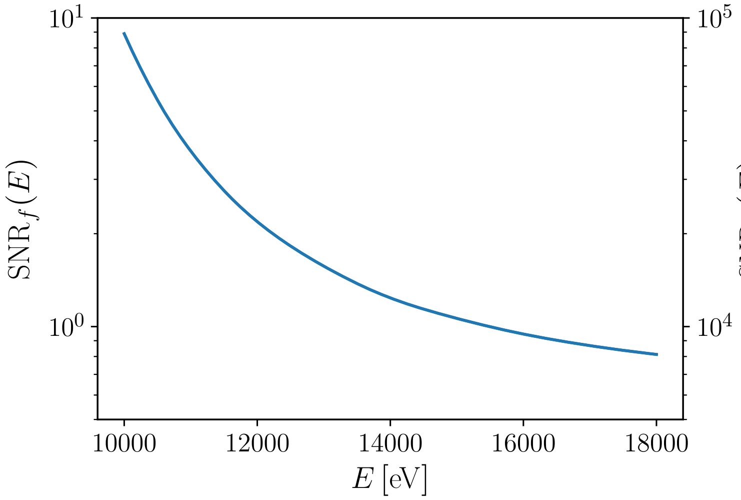

Figure 11.5. Signal-to-noise ratio in terms of flux and flux density (as defined in equations (11.1) and (11.2) as a function of positron energy E. The decresing trend is due to the increased transmission through the grating bars at higher energies.

11.2.2 Intrinsic emulsion noise

A more sizable, but energy-independent source of noise is due to thermally induced grains that naturally appear in emulsion films, as mentioned in chapter 10. This contribution is difficult to estimate precisely, as it manifests non-negligible sample variation between emulsion batches, and it also depends on factors such as emulsion storage and transportation conditions and time spent in vacuum. The thermal component is by far dominant with respect to sources such as cosmic rays and the tracks left by Compton electrons generated by the $511\,\mathrm{keV}$ gammas which come both from positrons annihilating directly on the emulsion and from the ^{22}Na radioactive source. In measuring experimentally a density of background grains, which are sensibly assumed to be uniformly distributed, one naturally accounts also for these negligible contributions. Intrinsic noise density, as it is suggested by the experimental data in Fig. 10.16, is not directly proportional to the exposure time or to the time spent in vacuum, at least up to times of the order of 100 hours that were tested.

Therefore increasing the exposure time will generally result in an improved signal-to-noise ratio. Exposure time must be selected to obtain sufficient grain density while avoiding saturation. To aid this process, a preliminary measurement was first performed, with the diffraction gratings removed, but the collimators in place and the emulsion in its final position for the interferometric measurement. The result of a 6 hours long exposure at $E = 14\,\mathrm{keV}$ and $V_F = 7\,\mathrm{kV}$ is shown in Fig. 11.6 in the form of a two-dimensional histogram. A $7\,\mathrm{\mu m}$ deep region of interest on the z-axis (normal to the surface of the emulsion) was selected to produce Fig. 11.6, and the region $|x| < 180\,\mathrm{\mu m}$, $|y| < 135\,\mathrm{\mu m}$ was considered for each view (coordinates x and y are in the local reference frame of the single view). This cut is necessary to remove the overlapping regions from adjacent views thus avoiding double-counting of grains. An approximately Gaussian beam spot with FWMH $= (6.5 \pm 0.5)\,\mathrm{mm}$ is clearly visible. This result is in good qualitative agreement with the expected width estimated at $V_F = 7\,\mathrm{kV}$ from the empirical linear relation (9.1): FWMH $= (6.0 \pm 1.4)\,\mathrm{mm}$. The grain density drops from about

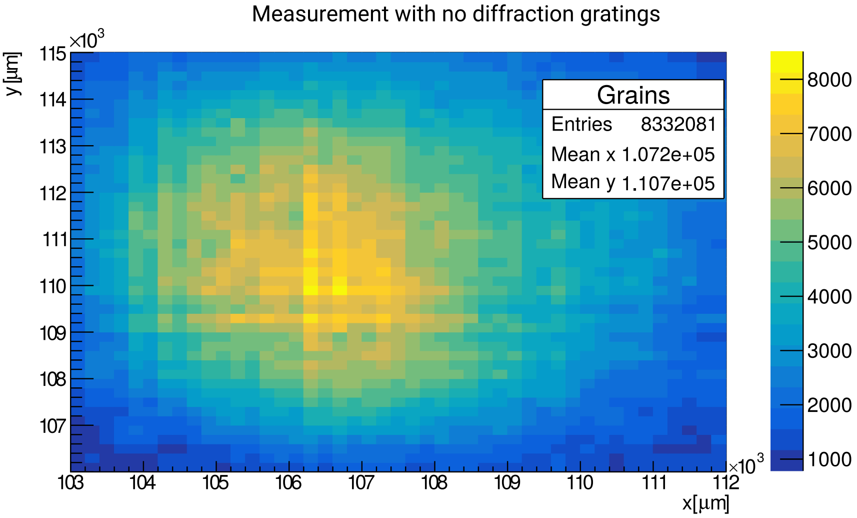

Figure 11.6. Two-dimensional histogram of the distribution of detected grains on the emulsion surface after 6 hours of exposure at $E = 14\,\mathrm{keV}$ and $V_F = 7\,\mathrm{kV}$. Bin size is $200 \times 200\,\mathrm{\mu m}^2$.

$28.5\,\text{grains}/1000\,\mu\text{m}^3$ at the center of the peak to approximately $3.5\,\text{grains}/1000\,\mu\text{m}^3$ far away from the spot. Therefore, assuming a uniform noise density, we can estimate a peak signal-to-noise ratio, with respect to the intrinsic and gamma-induced background of approximately $\text{SNR}_\text{int} \approx 7$ in these conditions.

11.3 Interferometric measurement

The positron flux during the measurement with no gratings was monitored with an HpGe detector located to the side of the emulsion holder. Gratings were then mounted and properly aligned, and an interferometric measurement was started with a new emulsion film located in the exact same position. By the counting rate of the HpGe detector (with careful subtraction of the laboratory background), the percentage of flux transmitted through the gratings was estimated as $T_g = (11 \pm 1)\%$. This corresponds to a satisfactory alignment between the interferometer and the beam axes, as suggested by Fig. 9.11 for the observed spot size. Knowledge of the actual flux relative to the no-gratings measurement allows one to tune the exposure time for the desired grain density. To match the density at which the test $7\,\mu\text{m}$ geometric fringe patterns were detected in chapter 10, an exposure time $T_\text{exp} = 120\,\text{h}$ was estimated. The beam spot on the emulsion after exposure is shown in Fig. 11.7. The peak density of grains is about $55.5\,\text{grains}/1000\,\mu\text{m}^3$ and drops to approximately $7.5\,\text{grains}/1000\,\mu\text{m}^3$ outside the beam spot. Consistently with the results reported in Fig. 10.16, an increase in noise density is expected for longer exposures to vacuum (at the level of $10^{-6}\,\text{mbar}$ during the measurement, inferred from the current draw of an ion pump, as all conventional pressure gauges have to be left off).

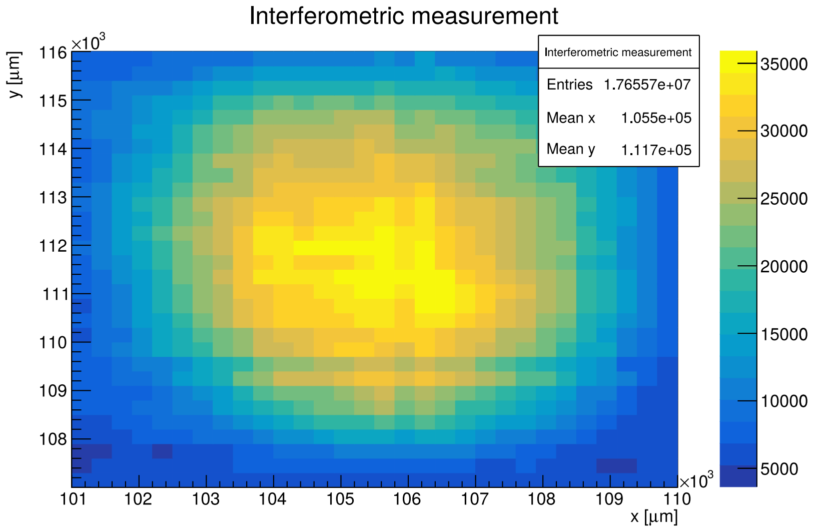

Figure 11.7. Distribution of detected grains on the emulsion surface after 120 hours of exposure at $E = 14\,\text{keV}$ and $V_F = 7\,\text{kV}$. Bin size is $300 \times 300\,\mu\text{m}^2$. A depth of $7\,\mu\text{m}$ around the positron signal peak along the z-axis was selected.

11.3.1 Data analysis: pattern finding

The following geometrical parameters were measured using the alignment techniques outlined in chapter 8:

$$\begin{aligned} L_1 &= (118.1 \pm 0.1)\,\mathrm{mm} \\ L_2 &= (578.8 \pm 0.1)\,\mathrm{mm} \\ \phi_0 &= (30 \pm 10)\,\mu\mathrm{rad} \\ \phi_1 &= (70 \pm 10)\,\mu\mathrm{rad} \end{aligned} \tag{11.3}$$

Distances are set for resonance at $E = 14\,\mathrm{keV}$ given the measured grating periodicities (see equation (8.1), Table 8.1 and the related discussion). The angular grating alignment ϕ_0 was estimated on the optical table (8.1) before the interferometer was inserted into the chamber. After the week-long measurement the interferometer was put on the measurement system[2] and the rotational alignment evaluated as ϕ_1. In both cases $\phi \ll \sigma_\phi \approx 500\,\mu\mathrm{rad}$, therefore sizable contrast was potentially expected. Nevertheless, we will conclude that no periodic signal was detected in this exposure. This conclusion is supported by the analysis methods outlined in chapter 10, in particular the Rayleigh test, coupled with a comparison with Monte Carlo generated signals. In Fig. 11.8 we show a two dimensional plot of the function $R_T \equiv 2nR^2(\alpha, d_{\mathrm{fold}})$, defined from equation 10.6. The number of generated points $n = 30000$ is the typical number of grains detected in a single microscope view at the center of the beam spot in the real measurement. A clear peak in the $(\alpha, d_{\mathrm{fold}})$ search is well visible (compare also with the experimental result of Fig. 10.14). The statistical significance of the result can be estimated by observing that Rayleigh test function $R_T = 2nR^2$ calculated for an ensamble of uniformly distributed points is distributed as $\chi^2(R_T; 2)$: the chi-square distribution with two degrees of freedom [146]. One can define a function $P_{\mathrm{rd(R_T)}}$ as follows:

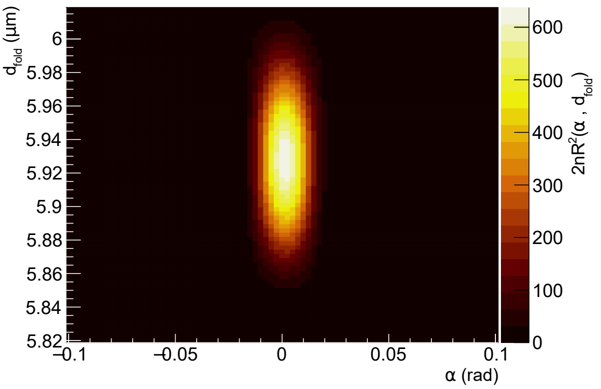

Figure 11.8. Plot of the function $R_T \equiv 2nR^2(\alpha, d_{\mathrm{fold}})$, defined from equation 10.6 as a function of the rotation angle α and folding period d_{fold} for a Monte Carlo generated periodic signal with 20% contrast, $\alpha = 0$ and $d = 5.93\,\mu\mathrm{m}$. The periodic pattern with $n = 30000$ points was generated using the full analytical expression (5.11).

$$P_{\mathrm{rd}}(R_T) = \int_{R_T}^{+\infty} \chi^2(x; 2)\,\mathrm{d}x, \tag{11.4}$$

---

[2] The interferometer support allows sufficiently repeatable positioning, however one cannot exclude that part of the observed drift is due to moving the apparatus between the chamber and the optical table. The estimated variation in the quality of rotational alignment can therefore be considered an upper limit to the actual shift occurred during the measurement.

which represents essentially the probability that a uniformly distributed signal (with no periodicity) produces a value of the Rayleigh test greater or equal than R_T by random chance. In other words, $P_{\rm rd}$ is the p-value relative to the null hypothesis of a uniform distribution. In Fig. 11.9 the calculated R_T for Monte Carlo generated periodic signals with varying contrast C is shown together with a parabolic fit of the form $R_T(C) = aC^2 + b$. Note that in this case a single search on the expected period was performed, therefore $P_{\rm rd}$ consistently represents a p-value, as no corrections for multiple trials are necessary. The function $P_{\rm rd}(R_T(C))$ is also plotted (using the parabolic fit $R_T(C)$). It becomes vanishingly small already for contrasts of the order of 10% (with the chosen statistics, that matches the grain density observed experimentally). This feature ensures the reliability of the Rayleigh test to detect periodic signals with small contrasts which are undetectable by visual inspection or direct fitting techniques.

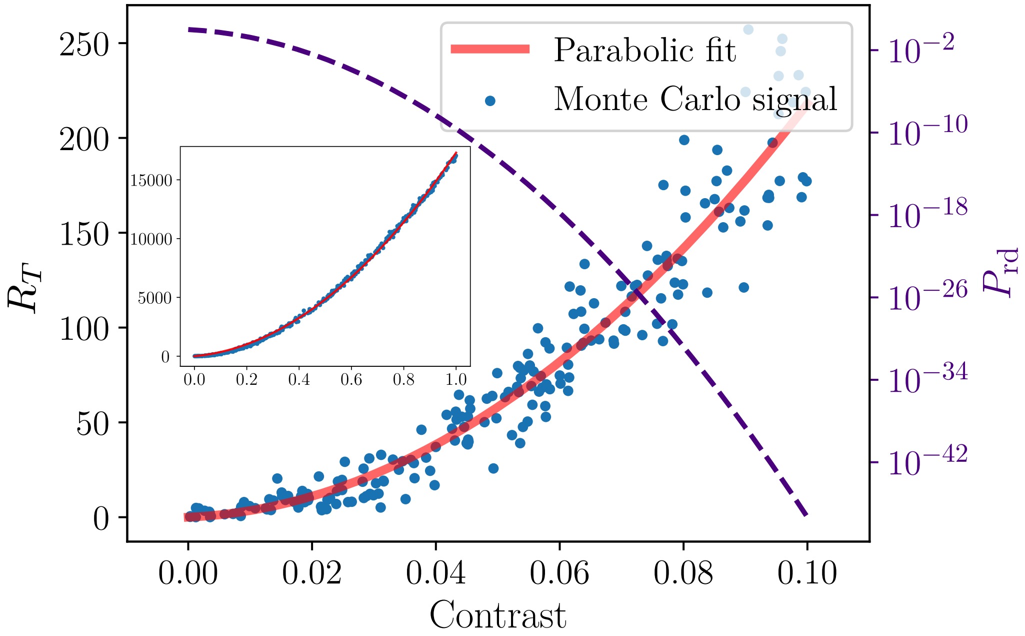

Figure 11.9. Scatter plot of R_T vs. contrast C for an ensemble of Monte Carlo generated periodic signals, each with $n = 30000$ points. In the inset the full range $C \in [0, 1]$ is shown, and the data are in good agreement with a parabolic fit. The dotted line shows the probability that the observed R_T is due to a statistical fluctuation: $P_{\rm rd}$, as defined in equation (11.4).

The two-parameter Rayleigh test-based search was applied systematically on the emulsion surface, as it was done to detect the test fringe patterns. In Fig. 11.10 we compare the result of three representative views (labelled a,b,c) taken at the center of the beam spot with three other candidates: a Monte Carlo generated view with comparable statistics and 3% contrast, a single view from the blank measurement with no diffraction gratings and a Monte Carlo generated view with uniformly distributed grains. By visual inspection one can readily appreciate that the three views, although adjacent, do not display any recognizable peak near the same values of $(\alpha, d_{\rm fold})$. Furthermore, comparable maximum values of R_T are observed in a view from the blank exposure with no diffraction gratings, Fig. 11.10**(e)**, as well as for a Monte Carlo generated uniformly distributed view, Fig. 11.10**(f)**. We already mentioned that for independent realizations of uniformly

R_T **two-parameter search**

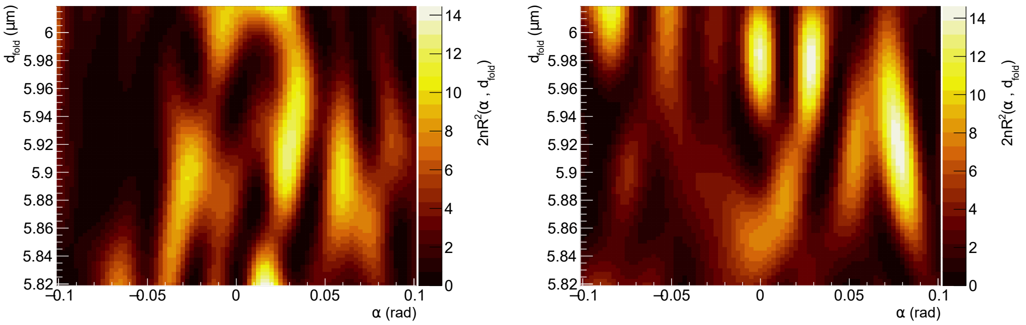

(a) Interferometer,
view "a", $n \approx 30000$.

(b) Interferometer,
view "b", $n \approx 30000$.

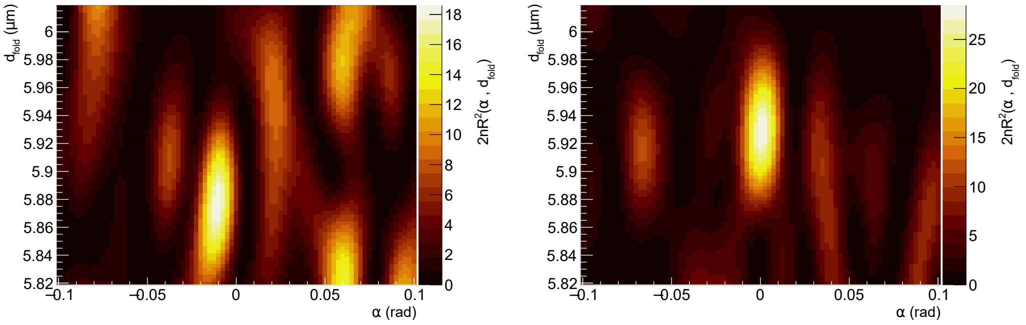

(c) Interferometer,
view "c", $n \approx 30000$.

(d) Monte Carlo generated
$C = 3\%$, $n = 30000$.

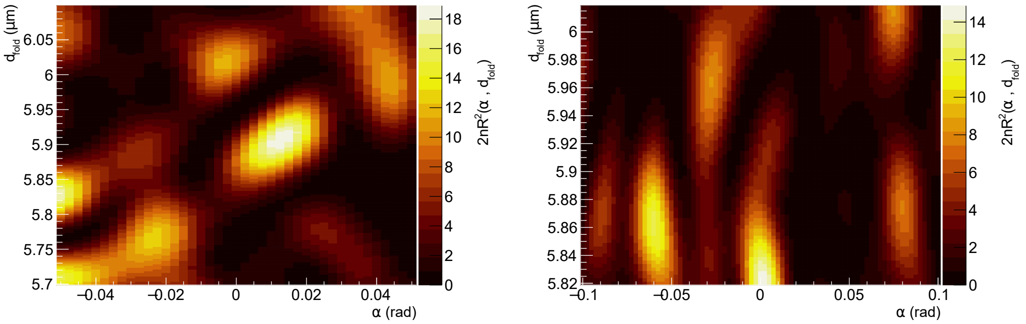

(e) No gratings
one view $n \approx 18000$.

(f) Monte Carlo generated
Uniform, $n = 30000$.

Figure 11.10. Comparison of two-parameter searches based on the Rayleigh test function $R_T = 2nR^2(\alpha, d_{\text{fold}})$, defined from equation 10.6, where n is the number of points forming the pattern. The data considered in each case are indicated in the sub-captions. See text for a discussion of the results.

distributed points the expected distribution of R_T is $\chi^2(R_T;2)$. In Fig. 11.10**(f)**, R_T is calculated on a grid of 6400 combinations of the parameters $(\alpha, d_{\text{fold}})$. Although they are not strictly independent realizations (as they are related by rotations), the observed distribution of R_T agrees reasonably well with $\chi^2(R_T;2)$ (see Fig. 11.11). Under the approximation that they are independent realizations, the probability to exceed the value $R_T = 14$, is 0.091%, yet the probability that at least one uniformly distributed realization out of 6400 yields $R_T \geq 14$ is 99.7%. The realizations are strongly correlated with their nearest neighbours, therefore an extended peak tends to develop around the single combination of parameters that by chance produces a sizeable value of R_T. Correlations therefore explain the formation of structures even for uniformly distributed data. This qualitative reasoning explains how several peaks that might appear significant at a first glance arise in two-parameter searches even in the absence of contrast. On the contrary, the Monte Carlo signal with non-zero contrast shown in Fig. 11.10**(d)** is the only example to display a single well-defined peak within the parameter space. The two-parameter search was applied to 130 views covering the region of the peak, and the optimal values $(\alpha^*, d^*_{\text{fold}})$ maximizing R_T are shown in Fig. 11.12 for the interferometric measurement. For comparison we also show the results of the same analysis applied to the views rotated by $\pi/2$, and to a set of Monte Carlo generated views with $\alpha = 0$, $d = 5.93$ µm and 3% contrast. The rotated views are a sensible choice as a comparison signal as they have the same grain count yet should not contain any periodic component. It is apparent that

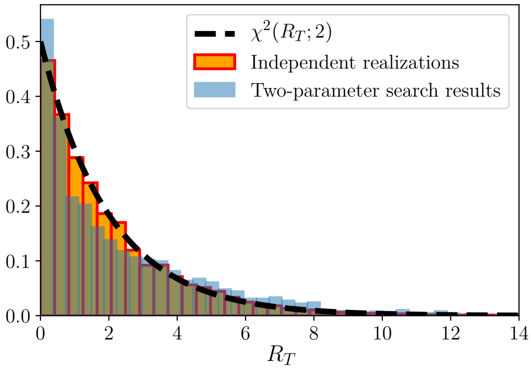

Figure 11.11. For independent realizations of uniformly distributed points, the Rayleigh test variable R_T follows a $\chi^2(R_T;2)$ distribution. The results of the two-parameter search shown in Fig. 11.10**(f)** are only approximately distributed as $\chi^2(R_T;2)$, due to correlations.

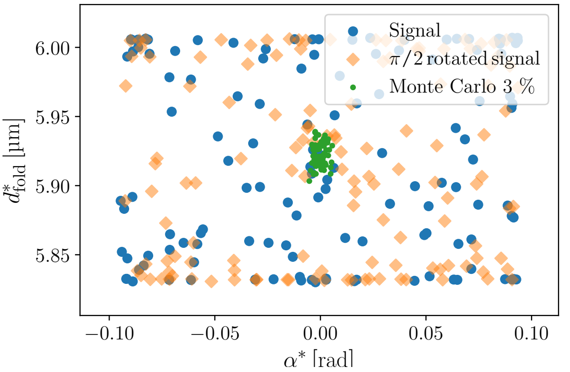

Figure 11.12. Scatter plot of the optimal values $(\alpha^*, d^*_{\text{fold}})$ maximizing R_T found in the two-parameter search on single views, for three different cases: interferometric measurement, the same measurement rotated by $\pi/2$ and Monte Carlo generated views with $\alpha = 0$, $d = 5.93$ µm and 3% contrast.

the results for the real data are randomly scattered and there is no evidence of a coherent signal. The rotated views also display the same behaviour, unlike the Monte Carlo generated signal with 3% contrast. In the latter case the results are clustered around the expected values, as it was observed for the successful experimental measurements reported in Fig. 10.14 (right panel).

11.3.2 Single-exposure distance scan

Several reasons could be put forward to justify absence of a periodic pattern. If the predictions of the analytical model on the tolerances to misalignment are considered realistic, then both longitudinal and rotational alignment should have been well under control. However, as we already mentioned, the ideal detector position is very sensitive to the ratio of the grating periods. A systematic error at the level of $1\mathrm{nm}$ can shift the detector position by several mm. To perform a scan in L_2 would be prohibitively long, therefore we implemented a solution that exploits the features of the emulsion detector. A holder to place the emulsion at a 45° angle was devised, and is shown in Fig. 11.13.

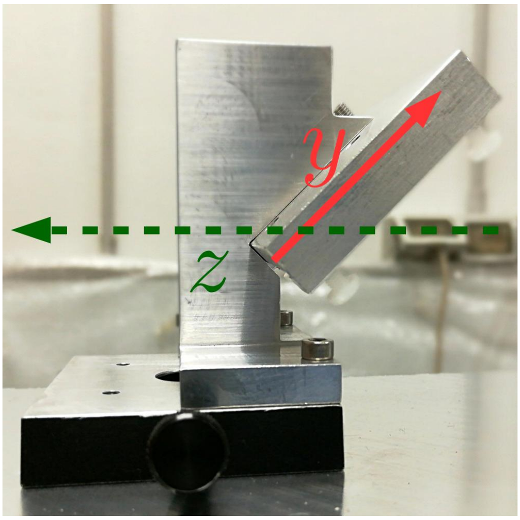

Figure 11.13. Picture of the emulsion holder modified to keep the film at a 45° angle with respect to the optical (z) axis.

The vertical position on the emulsion surface, namely along the y-axis in Fig. 11.13 thus becomes correlated with the distance along the optical (z) axis. This in a certain sense allows one to simultaneously perform the experiment at different L_2 using different horizontal slices of the emulsion covered by the $\sim \mathrm{cm}$ wide beam spot. This solution could allow to observe the contrast modulation with L_2 predicted by the theoretical model. Naturally each sector on the emulsion will not be performing a fully independent experiment, as non negligible beam divergence will mix together components at different L_2. One thus expects that the maximum observed contrast with this method could be lower compared to an orthogonal detector. Nevertheless, preliminary results indicate that this technique is effective to detect measurable contrast even a few mm away from the center of the beam spot. These results are reported in the next chapter.

CHAPTER 12

First evidence of a periodic pattern

12.1 Measurement summary

Several exposures were performed with the tilted emulsion support in different experimental conditions. In this chapter we focus on two measurements at $E = 14\,\mathrm{keV}$ ($V_F = 7\,\mathrm{kV}$). In a first attempt with the emulsion located at the nominal distance $L_2^* = 578.8\,\mathrm{mm}$, an indication of a periodic signal consistent with the expected features was found at the edge of the beam. A second measurement was then carried out moving the emulsion in the direction suggested by the position of the observed signal, which resulted in a dramatic improvement in contrast. In summary, two exposures will be considered in the following:

A. $L_2 = L_2^*$, $E = 14\,\mathrm{keV}$, **uncoated emulsion**, $T \approx 120\,\mathrm{h}$

B. $L_2 = L_2^* - 4\,\mathrm{mm}$, $E = 14\,\mathrm{keV}$, **uncoated emulsion**, $T \approx 116\,\mathrm{h}$

For these measurements, we employed emulsion films prepared without the $1\,\mu\mathrm{m}$ thick protective layer. The lack of protective layer makes the films more sensitive to damage due to external agents. For this reason some areas of the film were found to display an increase in background density, especially close to the emulsion surface. However, on average no significant background increase with respect to standard emulsion films was measured. In particular the grain density in the bulk of the emulsion in the region of the positron spot was measured at approximately $7.5\,\mathrm{grains}/1000\,\mu\mathrm{m}^3$, consistent with previous experimental results for similar exposure times. The capability to work with no protective allows to extend the range of available energies, thus gaining access to a much more sizeable contrast drop. The measured distances and rotation angles, denoted with the same symbols as equation (12.1) were as follows:

$$\begin{aligned} L_1 &= (118.1 \pm 0.1)\,\mathrm{mm} \qquad (12.1)\\ L_2^{\mathrm{A}} &= (578.8 \pm 0.5)\,\mathrm{mm}\\ L_2^{\mathrm{B}} &= (574.8 \pm 0.5)\,\mathrm{mm}\\ \phi_0 &= (30 \pm 10)\,\mu\mathrm{rad}\\ \phi_1 &= (60 \pm 10)\,\mu\mathrm{rad} \end{aligned}$$

where the distances L_2^{A} and L_2^{B} refer to the first and second exposures respectively. A larger error on L_2 is quoted with respect to the distances measured with the upright emulsion. This is due to the fact that with a tilted emulsion L_2 is correlated to the vertical position of the beam spot on the detector plane, which is known at the level of $0.5\,\mathrm{mm}$. Both measurements were performed in the usual pressure range of $10^{-6} - 10^{-7}\,\mathrm{mbar}$. The same analysis technique outlined in the previous chapter was applied to the full scanned surface in both exposures.

12.1.1 Results of exposure A

The optimal values $(\alpha^*, d^*_{\text{fold}})$ found for the 573 individual views analysed are shown in Fig. 12.1. From the projected histograms, an increase in the density of points clustered around $d^* \approx 5.9\,\mu\text{m}$ is visible. This feature was not observed in the previous interferometric measurements and is a first indication of the presence of a coherent periodic signal on the surface. A fit to the folded histogram at $(\alpha^*, d^*_{\text{fold}})$ was also performed with a sinusoidal function to evaluate the contrast. Views with a sinusoidal contrast $C > 7\%$ and $(\alpha^*, d^*_{\text{fold}})$ contained in the region displayed in Fig. 12.1 will be highlighted. This is particularly helpful to guide the eye in the following plots. First we show, in the left panel of Fig. 12.2 a scatter plot of the center position of the views in global emulsion surface coordinates (X, Y), superimposed to a heatmap of the number of grains entering the Rayleigh test analysis, labelled n. This quantity accounts for the cut on grain depth (z-axis), which is performed using a Gaussian fit as described in section 10.3.2, and indicates the shape of the beam spot. The highlighted views display a measurable contrast, consistent values of $(\alpha^*, d^*_{\text{fold}})$, and are located mostly in the $y > -112000\,\mu\text{m}$ region. Their distribution is not regular, but it is apparent that at the very edge of the beam spot the signal-to-noise ratio is at a minimum. Furthermore, the quality of the periodic pattern that could be produced is expected to decay far away from the optical axis. In the right panel of Fig. 12.2 a map of the sinusoidal contrast C over the emulsion surface is displayed. The view with the highest contrast and value of the Rayleigh test (which we

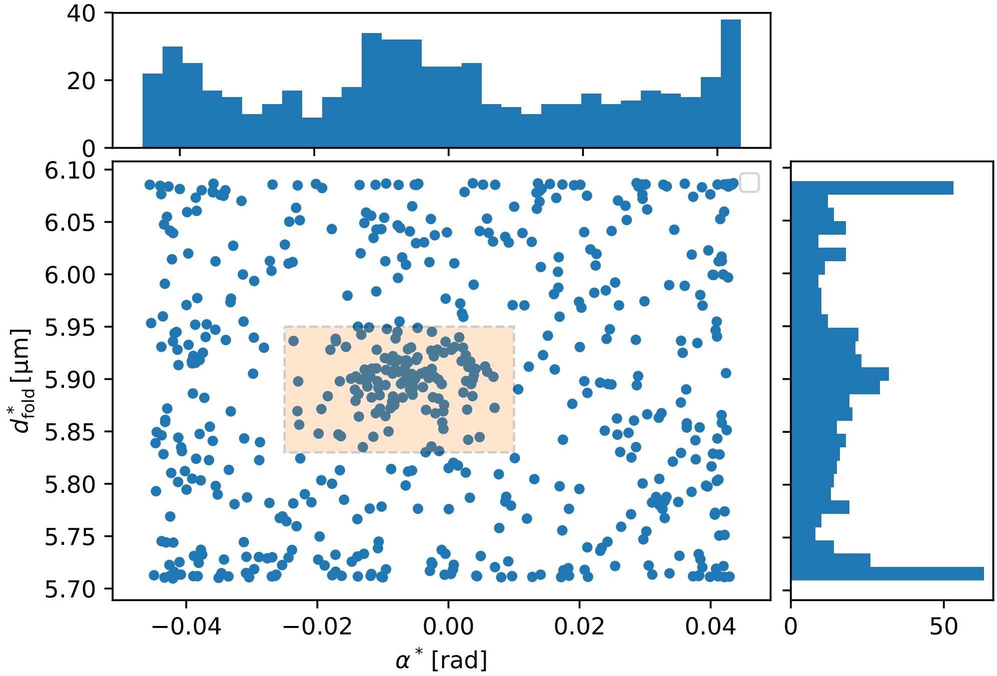

Figure 12.1. Scatter plot of the optimal period and angle $(\alpha^*, d^*_{\text{fold}})$ found via the Rayleigh test on individual views. An increase in density close to the center of the parameter space is appreciable from the projection histograms. A rectangular region of interest (ROI) around the peak density is highlighted for visualization purposes.

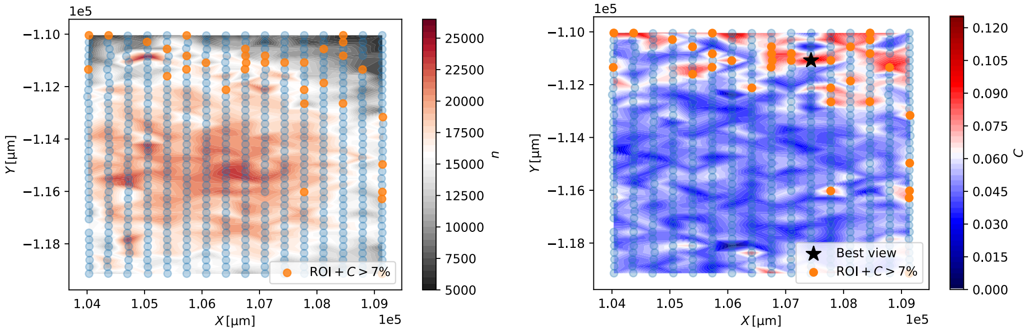

Figure 12.2. Left: scatter plot of the center position of each analyzed view. The color scale represents the number of points n selected for the analysis after the required cuts. This quantity is essentially proportional to the beam intensity. Right: sinusoidal contrast C is represented in color scale. The position of the single best view with the highest measured contrast (and also the highest value of the Rayleigh test, as shown in Fig. 12.3) is marked. Views with contrast greater than 7% are highlighted to guide the eye.

label *best view*) is marked, and is seen to be surrounded by a cluster of views with measurable contrast. The result of the two-parameter Rayleigh test search and of the resulting folding histogram is shown in Fig. 12.3 for the best view and for an adjacent view. To better highlight the shape of the *fringes* the histogram is folded on $3d^*_{\mathrm{fold}}$ to show three full periods. In the insets inside the histograms the measured parameters $(\alpha^*, d^*_{\mathrm{fold}})$ are reported, with error estimated as the standard deviation of a two-dimensional Gaussian fit on the peak of the two-parameter Rayleigh test search. The sinusoidal contrast C is also given, with error extracted from the least squares fit. The results outlined in this section allow one to conclude the following:

- In a region of at least $0.7 \times 0.3\,\mathrm{mm}^2$, the Rayleigh test provides strong statistical evidence of a departure from a uniform distribution at a periodicity $d = (5.88 \pm 0.02)\,\mu\mathrm{m}$ (weighted average of the two views). The p-value, corrected for multiple trials in the two-parameter search[1] is approximately 1×10^{-13} and 9×10^{-8}, respectively for the two views.

- Folding and fitting with a sinusoidal function gives a measured contrast of the order of $10 \pm 1\%$ (average of the two views) in the considered region.

- The center of this region is located at a vertical distance $\Delta y = (4.3 \pm 0.1)\,\mathrm{mm}$ from the center of the beam spot (the position of which is estimated with a Gaussian fit).

With the tilted emulsion geometry, one expect that a signal appearing at a distance Δy off-axis, could be detected on the beam axis by moving the emulsion a distance $\Delta y/\sqrt{2}$ (due to the $45°$ tilt) in the correct direction. In this specific case, given the orientation of the emulsion holder shown in Fig. 11.13, the data suggest to move the emulsion towards the second grating, to reduce L_2.

---

[1] We ignore the fact that the trials are correlated and multiply P_{rd} defined in equation (11.4) for the number of trials $M = 6400$. This gives a conservative estimate of the p-value.

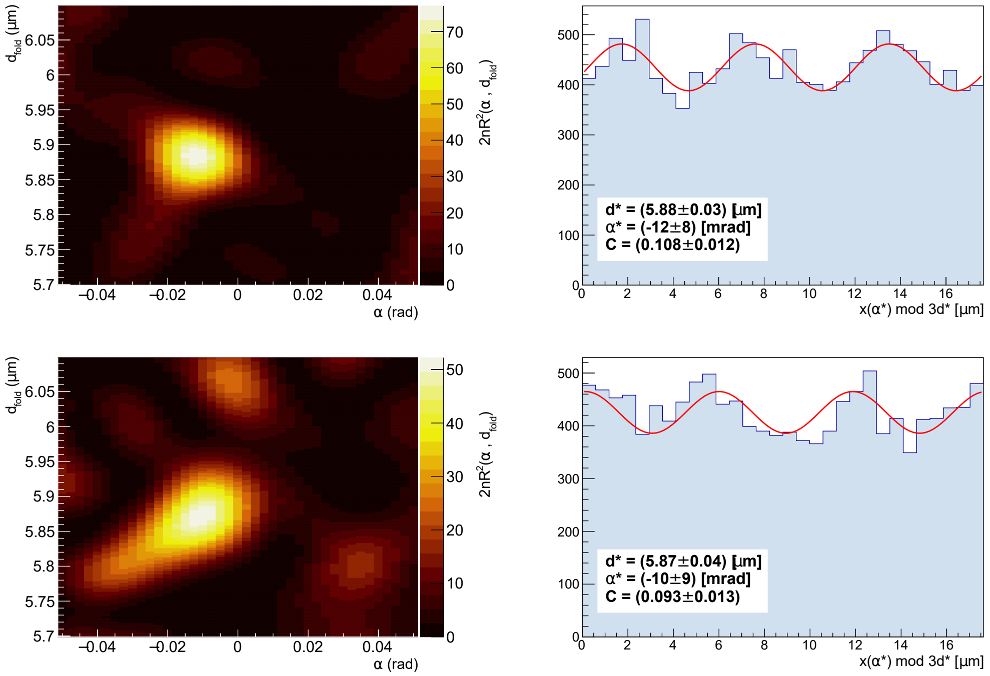

Figure 12.3. Two-parameter Rayleigh test search and folding histogram over $3d^*_{\mathrm{fold}}$ for the best view (top) at $E = 14\,\mathrm{keV}$, and an adjacent view (bottom). In the inset the parameters $(\alpha^*, d^*_{\mathrm{fold}})$ and the measured sinusoidal contrast C are reported. The number of points entering the analysis is $n \approx 13000$ in both cases.

12.1.2 Results of exposure B

For exposure B, the emulsion holder was moved $4\,\mathrm{mm}$, to obtain $L_2^{\mathrm{B}} = (574.8 \pm 0.5)\,\mathrm{mm}$. Before discussing the results it is worth noting that this emulsion film belongs to a different production batch than the film used for exposure A. Transportation conditions were also different, as emulsions from this batch were delivered in aluminium boxes in an attempt to reduce the possibility of surface damage[2]. The film displayed signs of surface contamination, which was successfully removed by cleaning after development. The observed efficiency was lower than expected (flux density reduced by almost a factor of two, in spite of the same emulsion time and no detectable change in incoming positron flux, as monitored by the HpGe detector). Intrinsic noise density was also higher than usual, measured at approximately $11\,\mathrm{grains}/1000\,\mu\mathrm{m}^3$. The data were analysed with the usual approach: in Fig. 12.4 the optimal angle and period $(\alpha^*, d^*_{\mathrm{fold}})$ is shown, found via the Rayleigh test on individual views. Clear peaks are visible in the projected histograms, which can be fit with a Gaussian function plus a linear background to locate the position of the peak. $d^0_{\mathrm{fold}} = (5.86 \pm 0.02 \pm 0.05_{\mathrm{syst.}})\,\mu\mathrm{m}$, where we report the variance of the Gaussian function as the uncertainty on the measured parameter, and we remind that a systematic uncertainty on distances measurements performed with emulsions at the level of 0.8% was estimated. Statistical error from the fit on the parameter d^0_{fold} would be $0.001\ \mu\mathrm{m}$, which is negligible with respect to the systematic error. Furthermore, due to the tilt of the emulsion, it is expected that the period at different Y, hence at different L_2, varies slightly as $d_3(L_2) = d_1 L_2/L_1$, as suggested by equations (4.14) and (4.15). Therefore, the variance of the Gaussian function is a more sensible choice for the uncertainty on d^0_{fold}, which serves as a semi-quantitative estimate of the average observed period. This is different (although compatible within the errors) from the expected value $d_3 = (5.93 \pm 0.01)\ \mu\mathrm{m}$ calculated in equation 8.2 from the measured grating periods. A

---

[2] In comparison to the standard packaging, which consists in a simple opaque plastic sleeve, sealed against light leaks.

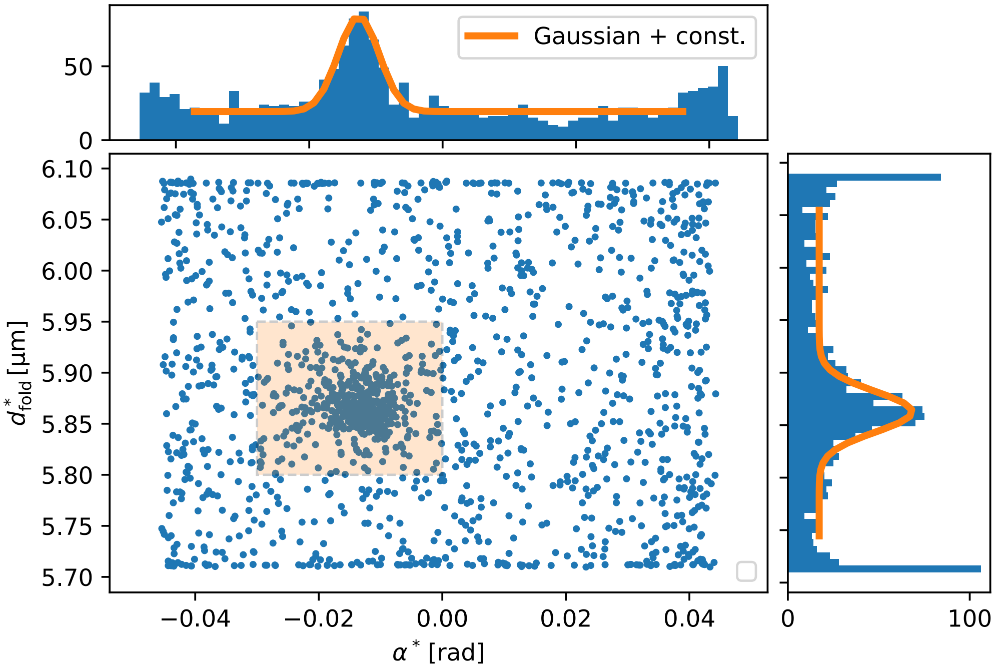

Figure 12.4. Scatter plot of the optimal period and angle $(\alpha^*, d^*_{\mathrm{fold}})$ found via the Rayleigh test on individual views. An increase in density close to the center of the parameter space is appreciable from the projection histograms, and a Gaussian fit is superimposed. A rectangular region of interest (ROI) around the peak density is highlighted for visualization purposes.

smaller period is fully consistent with the observed L_2 position of the fringes, as we will now discuss with the aid of Fig. 12.5: on the left panel the number of positrons in the view is shown, and the position of views with sinusoidal contrast $C > 15\%$ belonging to the region of interest displayed Fig. 12.4 is superimposed to the color scale plot. Sinusoidal contrast is also plotted on the right hand panel on the full scanned area. A large area (tens of square mm) with significant contrast, up to 32% is visible. By comparison with the left hand side plot, it is apparent that this region is populated by views with a consistent optimal period d^*_{fold} and angle. This already is a strong signature that a periodic signal has been successfully produced and detected on the emulsion surface. We recall that with an upright emulsion at the expected distance $L_2 = (578.8 \pm 0.1)\,\mathrm{mm}$ no periodic signal was detected. On the other hand, from the Y position of maximum contrast (see also Fig.12.6) one can infer that the effective position of the observed signal is $L_2^{\mathrm{obs}} \approx 572\mathrm{mm}$. Assuming for simplicity that this is indeed the position of maximum contrast (which has to be assessed with further measurements), the value of the ratio

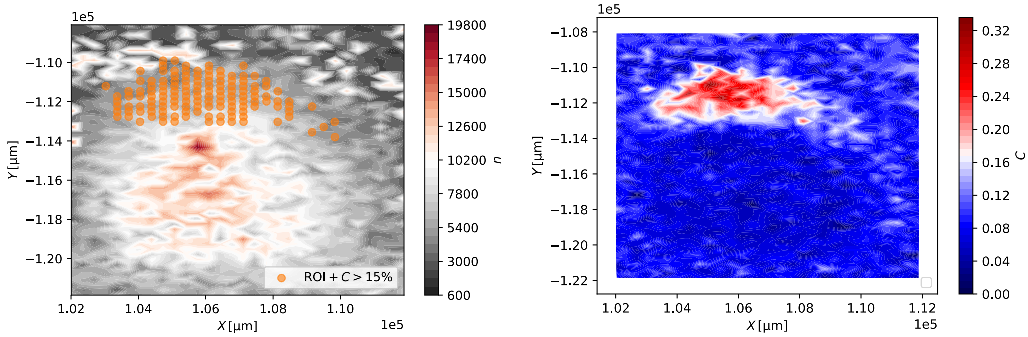

Figure 12.5. Left: scatter plot of the center position of each analyzed view. The color scale represents the number of points n selected for the analysis after the required cuts. Views with contrast greater than 15% and belonging to the period-angle region of interest displayed in Fig. 12.4 are highlighted to guide the eye. Right: sinusoidal contrast C represented in color scale.

$r = d_1/d_2$ compatible with the experimental is calculated from:

$$\eta^{\mathrm{obs}} = \frac{L_2^{\mathrm{obs}}}{L_1} = \frac{1}{r-1},$$

hence $r^{\mathrm{obs}} \approx 1.206$, while the expected value was $r = 1.2040 \pm 0.0005$. The experimental observation that a periodic signal appears for smaller L_2 than expected (and, consistently, with a smaller period) can be explained by a deviation on the expected d_1/d_2 of the order of 0.2%. It is plausible that either the experimental error on the determination of the periods ($\sigma_d = 0.3\,\mathrm{nm}$) has been underestimated or that there are systematic errors in the measurement procedure. A comparison with a different measurement technique is needed to assess the validity of these hypotheses. We recall that the optimal L_2 position is very sensitive to r: a systematic error of $1\,\mathrm{nm}$ (0.1% level) on one grating period would displace the ideal detector plane by approximately $3\,\mathrm{mm}$. In conclusion, the periodicity of the detected signal and the distance at which it appeared are fully consistent. It is interesting to examine the large-scale features of the high-contrast region, in particular its width in the Y-direction, which is connected to the ”longitudinal width” of the periodic fringes, predicted by the parameter σ_{L_2} appearing in equation (6.2), in the framework of a quantum-mechanical description. It is worth noting, however, that a contrast modulation along the optical axis is also predicted for a moiré deflectometer, with the particles assumed to follow simple ballistic propagation. We will further discuss this point with the aid of a Monte Carlo simulation in the Conclusion (see Fig. 13.2). To extract a contrast profile, views centered in the range $|X - X_0| < 500\,\mu\mathrm{m}$ were selected, where $X_0 = 1.05 \cdot 10^5\,\mu\mathrm{m}$ is the position of the view with the maximum observed contrast (see Fig. 12.8). A Gaussian fit (with a constant background) was then performed on the contrast of the selected views as a function of Y, as shown in Fig. 12.6. Fit results for the relevant parameters (variance and location of the maximum) are:

$$\sigma_Y = (910 \pm 50)\,\mu\mathrm{m} \tag{12.2}$$

$$Y_0 = (-111400 \pm 45)\,\mu\mathrm{m} \tag{12.3}$$

Given the emulsion tilt, the corresponding width of the contrast modulation as a function of longitudinal distance is $\sigma_z = \sigma_y/\sqrt{2} \approx 650\,\mu\mathrm{m}$. In comparison the predicted width σ_{L_2}, according to the quantum-mechanical model and realistic beam parameters, is of the order of $\sigma_{L_2} \approx 2\,\mathrm{mm}$. This is displayed in Fig. 9.9. One possible interpretation

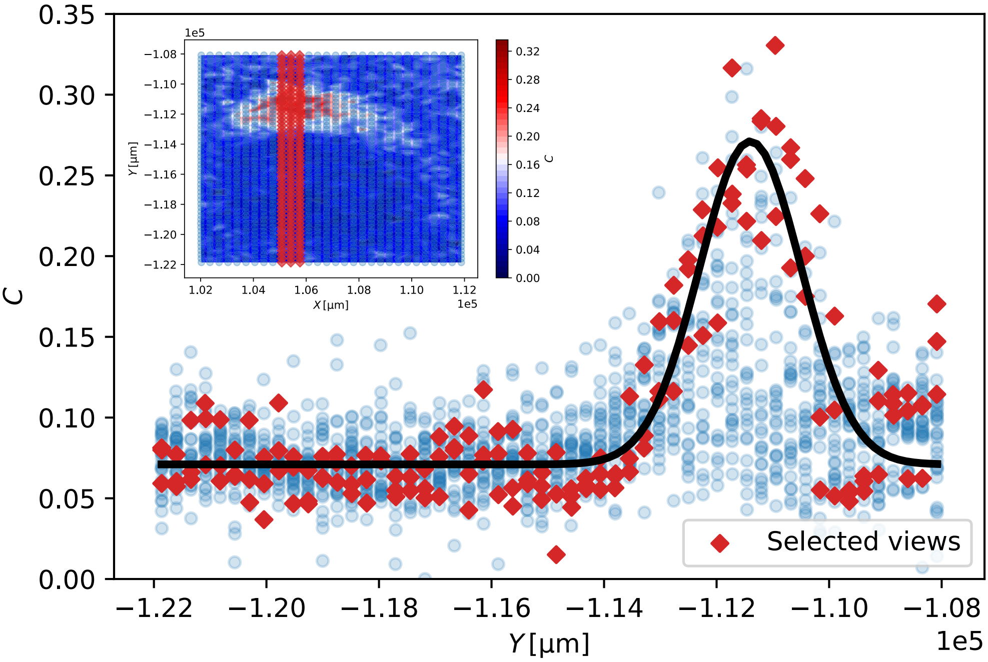

Figure 12.6. Sinusoidal contrast of each view as a function of Y- position of its center. A region of interest is selected, as shown in the inset, and the corresponding views are highlighted. The solid line is a fit with a Gaussian function plus a constant background, performed on the selected views only.

of this discrepancy is that contrast was still rising for increasing Y (thus decreasing L_2 along the z-axis), but positron density was also rapidly decreasing (the high-contrast region is close to the edge of the beam). The combination of the two effects could explain the observed approximately Gaussian shape with a smaller width than predicted. The soundness of this reasoning must be assessed experimentally by moving the emulsion further towards the second grating to perform a scan in the z direction. Furthermore, if this interpretation is correct, at the optimal emulsion position, the peak of the contrast modulation along Y should coincide with the center of the beam (peak beam intensity). On the other hand, there could be effects, unaccounted for by the analytical model, that produce a distortion of the focal plane of the interferometer, in such a way that high contrast is recovered only off-axis. In other words, the optical axis of the beam might not necessarily coincide with peak beam intensity. Several deviations from ideal conditions indeed appear in the experimental setup: lack of parallelism between the gratings (at the level of a few mrad), or between the gratings and the beam axis, an irregular (non Gaussian) beam profile, finite grating size.

We now focus on the results of the Rayleigh test: in Fig. 12.7 the distribution of the maximum value of R_T is shown. A sizable fraction of the views is above $R_T = 100$, a threshold for which the p-value against the null hypothesis of a uniform distribution is already vanishingly small ($P_{\mathrm{rd}} < 10^{-18}$).

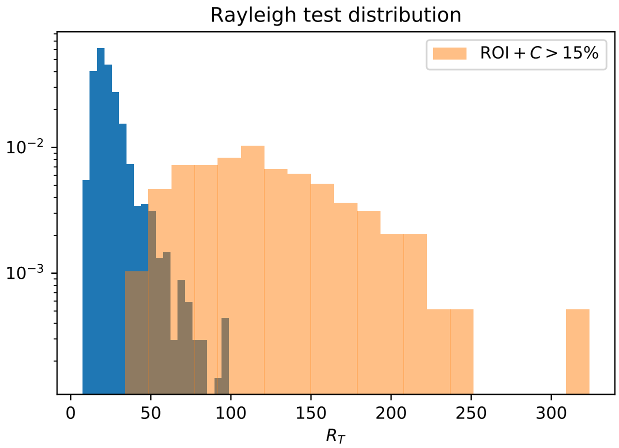

Figure 12.7. Distribution of the Rayleigh test results for the 1620 views analyzed. The selected views in the high-contrast region (see Fig. 12.5) and the remaining views are shown as two separate histograms (independently normalized to unit area).

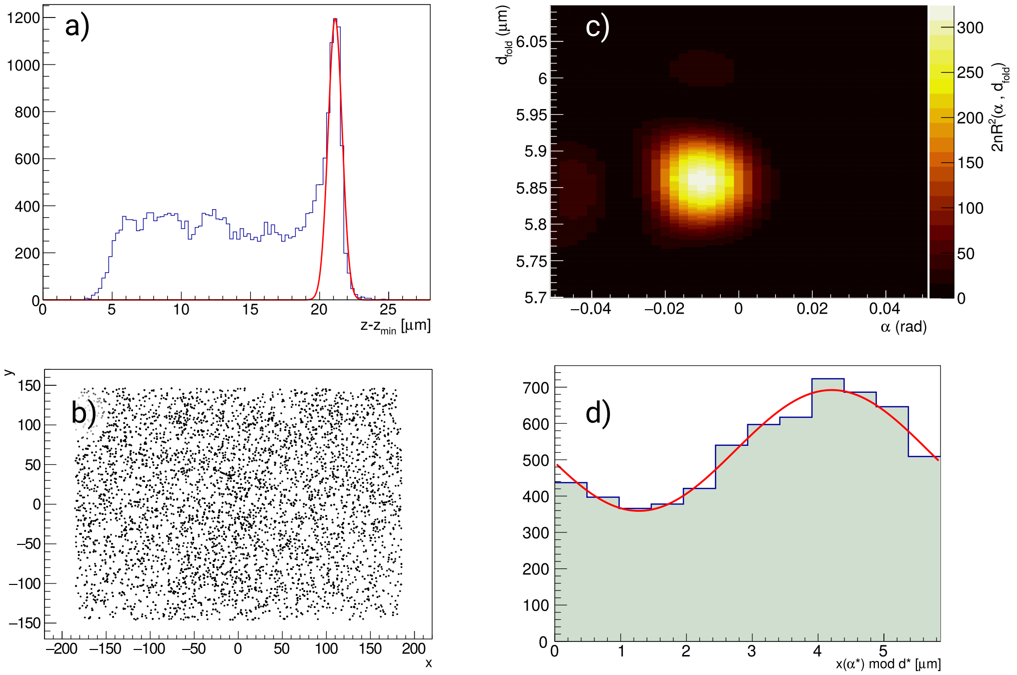

Figure 12.8. Panel (a) is the depth distribution of the clusters (or grains), showing a clear peak close to the surface of the emulsion. A Gaussian fit is used to estimate the width of the cut as explained in chapter 10. Panel (b) shows the x-y position (in local view coordinates) of the grains remaining after the cut in z. Panel (c) is the result of the two-parameter Rayleigh test search, and the folded histogram at the optimal angle and period $(\alpha^*, d^*_{\text{fold}})$ found via the Rayleigh test is shown in panel (d). Fit with sinusoidal fit yields a contrast of $32 \pm 2\%$.

The best result of $R_T = 323.8$ corresponds to a view with 32% contrast. Relevant plots for the analysis of this view are shown and described in Fig. 12.8 and Fig. 12.9 as a representative example. The number of grains entering the analysis after selecting a x-y-z region of interest following the usual approach is $n = 6321$. Average volumetric density of grains in the bulk of the emulsion in this view can be estimated as $11 \pm 1\,\mathrm{grains}/1000\,\mu\mathrm{m}^3$. Under the hypothesis that no significant increase in noise density occurs close to the surface (which is a conservative assumption), the number of background noise grains entering the analysis can be roughly estimated as $n_{\mathrm{bckg}} = 2800 \pm 300$. With this information one can estimate the original contrast of the interference fringes, before introducing noise and finite position resolution, for instance by means of a Monte Carlo simulation based on the profile predicted by the analytical expression (5.11). A x-y distribution, which includes uniformly distributed points to represent noise, and a position resolution ($0.1\,\mu\mathrm{m}$ was assumed) can be generated. The generated view is then analyzed with the same software used for the experimental data. The contrast C_0 of the analytical signal is controlled by[3] the parameter ϕ from equation (6.5). We do not attempt a quantitative estimate and only provide an example for comparison: with the measured signal-to-noise ratio, fringes with an initial contrast $C_0 = 0.6$ (60%) yield average detected sinusoidal contrast $\langle C \rangle^{C_0 = 60\%} = 0.32$, Normally distributed with standard

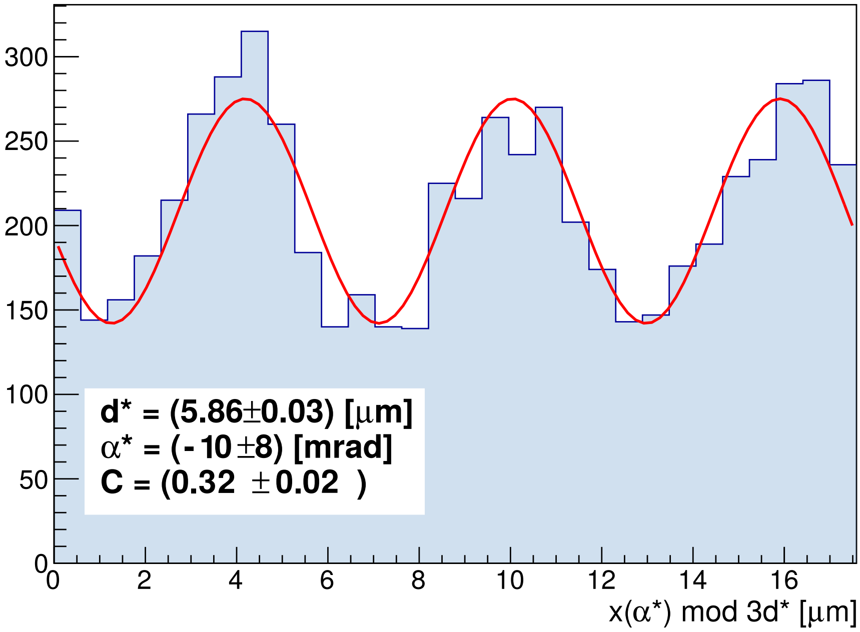

Figure 12.9. Two-parameter Rayleigh test search and folding histogram over $3d^*_{\mathrm{fold}}$ for the best view (top) at $E = 14\,\mathrm{keV}$, and an adjacent view (bottom). In the inset the parameters $(\alpha^*, d^*_{\mathrm{fold}})$ and the measured sinusoidal contrast C are reported. The number of points entering the analysis is $n \approx 13000$ in both cases.

---

[3] This choice is arbitrary and was made for convenience, the exact shape of the function weakly affects the result in this case.

deviation $\sigma_C^{C_0=60\%} = 0.01$. Fig. 12.9 shows an histogram folded over three periods obtained from the same view. The values reported in the inset for d^* and α^* are obtained via the Rayleigh test, while the sinusoidal contrast is taken from the fit on the folded histogram on a single period d^*. This is a more robust estimate of the contrast, however a sinusoidal fit over three periods is superimposed to guide the eye (which still yields a contrast compatible with the quoted value).

CHAPTER 13

Conclusion and future directions

QUPLAS-0: summary of the results

The design and experimental implementation a Talbot-Lau positron interferometer for the QUPLAS-0 experiment was the main goal of this thesis. In Part II a theoretical model able to account for the most relevant features of the beam was introduced, and a novel period-magnifying working regime was identified. As discussed in Part III, the capability to detect micrometric-scale fringe patterns with nuclear emulsion detectors was assessed experimentally with test patterns. This allowed to develop and validate effective analysis techniques which could be readily applied to the real interferometric signal.

In chapter 12, clear evidence of the detection of a periodic signal consistent with the theoretical expectations was provided. Based on these results, a measurement campaign could be arranged: first to perform a scan in detector position (taking full advantage of the tilted emulsion configuration), then to assess the quantum-mechanical origin of the signal. The unique signature of quantum matter-wave interference is the energy (or de Broglie wavelength) dependence of contrast at fixed interferometer geometry. The expected contrast modulation is shown in Fig. 13.1 for a wide range of energies. This peculiar functional dependence is markedly different from the constant behaviour predicted for a classical moiré deflectometer. Contrast for an angular misalignment much larger than the predicted accuracy of the alignment protocol is also shown in Fig. 13.1. The observed effect is to smooth out the secondary peaks around resonance. It is reasonable to expect that other deviations from the ideal conditions assumed in the model (such as indefinitely extended and perfectly parallel gratings) could produce a similar result. The region from $3\,\mathrm{keV}$ to $14\,\mathrm{keV}$ is particularly promising as two full contrast revivals could be observed. This region was initially believed to be impossible to study with emulsion detectors, as the protective layer would stop positrons below $E < 9\,\mathrm{keV}$. The latest results have shown that uncoated emulsions can operate reliably even for long data taking runs in high vacuum conditions. Therefore, it is likely that the rapid contrast drop in the low energy region can be exploited to obtain strong evidence of a non-constant behaviour. This result would have been very challenging to prove from an experimental point of view if positron energy were restricted to the $11 - 17\,\mathrm{keV}$ range. Regardless of its classical or quantum-mechanical origin, the observation of a periodic signal in the QUPLAS-0 apparatus is a significant result. As a matter of fact, the alignment requirements of a moiré deflectomer and of a Talbot-Lau interferometer with the same geometry are comparable. This statement applies both to rotational (see Fig. 6.8) and longitudinal (see Fig. 13.2) alignment. As a consequence, evidence that a periodic signal was generated from the two-grating arrangement and successfully detected in the QUPLAS-0 layout implies that the device fulfils the requirements in terms of alignment,

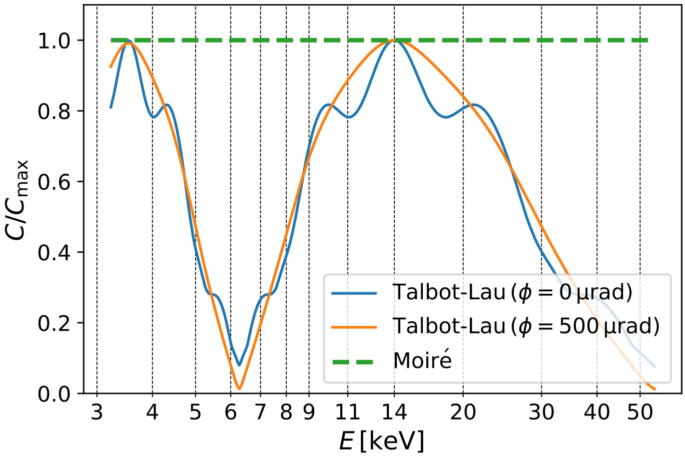

Figure 13.1. Fringe contrast as a function of energy, normalized to the resonance value. The QUPLAS-0 interferometer si considered at resonance for $E = 14\,\text{keV}$ and two representative rotational alignment conditions are considered. No contrast modulation with energy is expected, in principle, for a moiré deflectometer.

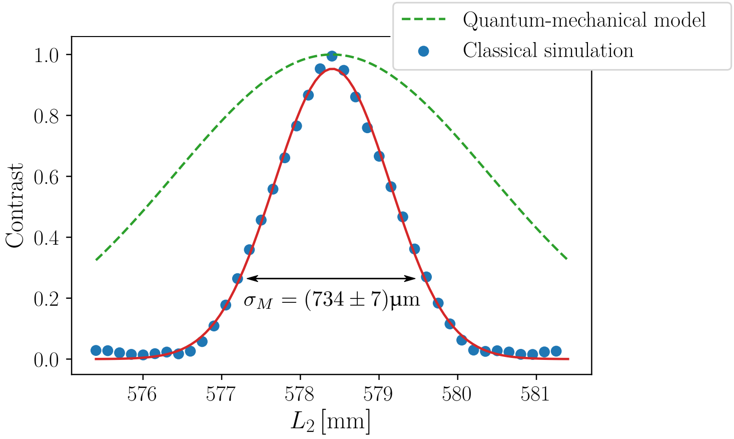

Figure 13.2. Contrast dependence on L_2 for a moiré deflectometer with the same geometry of the QUPLAS-0 setup. In the Monte Carlo simulation, a Gaussian transverse beam profile is assumed on the plane of the second slit, with a width matched to the quantum-mechanical model (see (9.4) and the related discussion). Ballistic trajectories are then propagated through the gratings acting as intensity masks. The angle with respect to the optical axis is drawn from a Normal distribution tuned to produce a beam spot on the detector plane with FWHM $\sim 6.5\,\text{mm}$, to match the observed size. An approximately Gaussian contrast profile with standard deviation σ_M is retrieved. The dashed line is the prediction of the quantum-mechanical model, significantly wider. Although model-dependent, this difference might be useful to discriminate classical from quantum. The tilted emulsion gives experimental access to a contrast profile with a single exposure.

beam quality and detector performance to observe matter-wave interference. The experimental results reported in chapter 12, although preliminary, prove that the QUPLAS-0 setup is working ″at least″ as moiré deflectometer for positrons.

Future directions

QUPLAS-0

Strong evidence to support the quantum-mechanical origin of the periodic pattern produced by the QUPLAS-0 interferometer was actually obtained with the experimental setup and techniques described here[1]. Improving the quality of the measurements requires several technical upgrades: first of all the current source intensity is $5\,\mathrm{mCi}$ therefore with a new $50\,\mathrm{mCi}$ source (the maximum intensity available), positron flux can be increased by an order of magnitude, to $\sim 4 \times 10^4\, e^+/\mathrm{s}$. The experiment will remain in the single-particle regime (transit time through the interferometer is of the order of nanoseconds), but shorter exposure times, coupled to a manipulator which moves the emulsion to perform multiple exposures on the same film will make possible a much finer optimization of the detector position. Impact of beam focusing and collimation could also be studied more in details. Furthermore, better characterization of the beam (thus determination of its parameters) would be achieved using an MCP detector coupled to a phosphor screen to image the beam directly, even performing a scan along the optical axis. This could likely improve the beam-interferometer alignment to maximize the transmitted intensity and potentially increase the observed contrast. The synergy of these improvements will hopefully allow to compare experimental results with the analytical model in a more quantitative fashion. A comparison with electrons in the same setup to search for potential discrepancies (for instance due to surface interactions with the gratings), could then become feasible.

QUPLAS-I and QUPLAS-II

Increased beam intensity is also crucial for the planned future phases of the experiment. In chapter 3 (see also Appendix A) we have already reviewed the technical developments needed to tackle positronium interferometry and, possibly, measure the gravitational acceleration of positronium. An interesting option that could be more promising in the short term is to exploit the negative positronium ion, Ps^-. This system can be produced by implanting slow positrons on metallic surfaces coated with alkali metals (such as Na [152]). Ps^- is very short-lived ($\tau \sim 0.47\,\mathrm{ns}$), but as a charged particle it can be accelerated electrostatically, and ortho-Ps can be produced via a laser-driven photodetachment process[152], to form an energy-tunable Ps beam. A Talbot-Lau interferometer for ground-state Ps atoms with kinetic energies of several keV could make use of the same gratings and configuration of QUPLAS-0. Slow ($v \sim 10^4\,\mathrm{m/s}$) Rydberg-excited positronium, with all the related complications, naturally remains the only viable option for gravity measurements based on Talbot-Lau interferometry. I am hopeful that the results contained in this thesis can be a tiny contribution towards this ambitious goal.

---

[1] I took part in all the process from data taking to data analysis, discussion and editing of the results. However, since the activity took place after the thesis draft was submitted to the referees (and also for the sake of brevity) detailed results are not included in the final version of this thesis. They are reported in the preprint titled **First observation of antimatter wave interference**, arXiv:1808.08901, 2018.

Appendices

APPENDIX A

Positronium in external fields

This appendix contains several results of interest for the QUPLAS experiment, related to the dynamics of (Rydberg) positronium atoms in external magnetic and electric fields. A semi-classical model, called the *classical trajectory Monte Carlo* (CTMC) [153] approach is introduced and used to evaluate the influence of stray magnetic field on a possible gravity measurement. Finally the motion in electric field (manipulation of Ps atoms via the Stark effect[154]) is discussed, both using the standard point-like description of the atom and CTMC simulations. Good agreement was found between these techniques. This result suggests that the CTMC approach could be used to simulate the motion of Ps also for very highly excited states in strong and rapidly varying electric fields where the point-like approximation might become unreliable. We also report the results of a calculation of ionization rates in external electric fields for highly excited states. These data are not readily available in the literature and could be necessary for the development of position-sensitive detectors for Ps. While many simulation results are essentially preliminary, they are useful to set future directions in the preparation of the following QUPLAS phases.

A.1 Theoretical background

To introduce the CTMC approach for the simulation of the trajectories of Ps atoms , we start from the Hamiltonian of two single particles (of charge e_1 and e_2), bound by the Coulomb potential $V(|\mathbf{r}|) = e_1 e_2/|\mathbf{r}|$. This semi-classical description is well-suited for the highly-excited Rydberg states, where the separation between the two particles is very large. Suppose that the bound particles are moving in an external magnetic and electric field, represented respectively by the vector and scalar potentials $\mathbf{A}(\mathbf{r})$ and $\phi(\mathbf{r})$. Then the Hamiltonian reads [153]:

$$H = \sum_{i=1,2} \left\{ \frac{1}{2m_i} \left[\mathbf{p}_i - e_i \mathbf{A}(\mathbf{r_i})\right]^2 + e_i \phi(\mathbf{r_i}) \right\} + V(|\mathbf{r_1} - \mathbf{r_2}|), \tag{A.1}$$

where the usual definitions of the canonical momenta $\mathbf{p}_i$ and coordinates $\mathbf{r}_i$ apply. The index $i = 1, 2$ labels the two interacting particles. We now specialize this equation to the case of positronium, so we fix $e_1 = e = -e_2$ and $m_1 = m_2 = m$. Furthermore we consider the case of a constant and uniform magnetic field $\mathbf{B}$ and fix the symmetric gauge for the vector potential:

$$\mathbf{A}(\mathbf{r}) = \frac{1}{2}\mathbf{B} \times \mathbf{r}$$

The Hamiltonian thus reduces to:

$$H = \frac{1}{2m}\left\{\left[\mathbf{p}_1 - \frac{e}{2}\mathbf{B}\times\mathbf{r}_1\right]^2 + \left[\mathbf{p}_2 + \frac{e}{2}\mathbf{B}\times\mathbf{r}_2\right]^2\right\} - \frac{e^2}{|\mathbf{r}_1 - \mathbf{r}_2|} + e\phi(\mathbf{r_1}) - e\phi(\mathbf{r_2}) \quad \text{(A.2)}$$

A change to a more convenient set of variables is usually performed [153]:

$$(\mathbf{r_1}, \mathbf{p_1}, \mathbf{r_2}, \mathbf{p_2}) \rightarrow (\mathbf{R}, \mathbf{K}, \mathbf{r}, \mathbf{p}),$$

where $\mathbf{K}$ is called the *pseudomomentum*. In the absence of an electric field (or for constant and uniform electric fields) it is a constant of motion. The exact definition of the coordinate transformation reads:

$$\begin{cases} \mathbf{R} = \dfrac{\mathbf{r}_1 + \mathbf{r}_2}{2} \\ \mathbf{K} = \mathbf{p}_1 + \mathbf{p}_2 + \dfrac{e}{2}\mathbf{B}\times(\mathbf{r}_1 - \mathbf{r}_2) \\ \mathbf{r} = \mathbf{r}_1 - \mathbf{r}_2 \\ \mathbf{p} = \dfrac{\mathbf{p}_1 - \mathbf{p}_2}{2} - \dfrac{e}{4}\mathbf{B}\times(\mathbf{r}_1 + \mathbf{r}_2) \end{cases} \quad \text{(A.3)}$$

It can be checked that equation (A.3) is a canonical transformation which preserves the correct commutation relations. For instance:

$$\begin{aligned} [\mathrm{p}_i, \mathrm{K}_j] &= \left[\tfrac{\mathrm{p_1}_i - \mathrm{p_2}_i}{2} - \tfrac{e}{4}\epsilon_{ilm}\mathrm{B}_l\left(\mathrm{r_1}_m + \mathrm{r_2}_m\right), \mathrm{p_1}_j + \mathrm{p_2}_j + \tfrac{e}{2}\epsilon_{jlm}\mathrm{B}_l\left(\mathrm{r_1}_m - \mathrm{r_2}_m\right)\right] \quad \text{(A.4)} \\ &= -\tfrac{e}{2}\mathrm{B}_l\left(\epsilon_{jlm}\delta_{im} + \epsilon_{ilm}\delta_{jm}\right) = 0. \end{aligned}$$

With similar calculations one can prove the following:

$$\begin{aligned} [\mathrm{R}_i, \mathrm{K}_j] &= \delta_{ij} \\ [\mathrm{r}_i, \mathrm{p}_j] &= \delta_{ij} \\ [\mathrm{r}_i, \mathrm{R}_j] &= [\mathrm{K}_i, \mathrm{R}_j] = [\mathrm{p}_i, \mathrm{R}_j] = 0 \end{aligned} \quad \text{(A.5)}$$

Equation (A.3) is easily inverted and introduced in the Hamiltonian (A.2) to yield, after some algebraic manipulation:

$$H = \frac{1}{2m}\left\{2\mathbf{p}^2 + \mathbf{K}^2/2 + \frac{e^2}{2}\left(\mathbf{B}\times\mathbf{r}\right)^2 - e\mathbf{K}\left(\mathbf{B}\times\mathbf{r}\right)\right\} - \frac{e^2}{|r|} + e\phi\left(\mathbf{R} + \mathbf{r}/2\right) - e\phi\left(\mathbf{R} - \mathbf{r}/2\right), \quad \text{(A.6)}$$

in accordance with the result quoted in [153], generalized with the addition of an external electric field term. The equations of motion following from (A.6) read:

$$\begin{cases} \dot{\mathbf{R}} = \dfrac{1}{2m}\left[\mathbf{K} - e\left(\mathbf{B}\times\mathbf{r}\right)\right] \\ \dot{\mathbf{K}} = -e\left[\nabla_{\mathbf{R}}\left(\phi\left(\mathbf{R} + \mathbf{r}/2\right) - \phi\left(\mathbf{R} - \mathbf{r}/2\right)\right)\right] \\ \dot{\mathbf{r}} = \dfrac{2\mathbf{p}}{m} \\ \dot{\mathbf{p}} = -\dfrac{e}{2m}\left(\mathbf{B}\times\mathbf{K}\right) + \dfrac{e^2}{2m}\mathbf{B}\times\left(\mathbf{B}\times\mathbf{r}\right) - e^2\dfrac{\mathbf{r}}{|\mathbf{r}|^3} - e\left[\nabla_{\mathbf{r}}\left(\phi\left(\mathbf{R} + \mathbf{r}/2\right) - \phi\left(\mathbf{R} - \mathbf{r}/2\right)\right)\right] \end{cases} \quad \text{(A.7)}$$

In the specific case of a constant and uniform electric field, namely $\phi(\mathbf{r}') = \mathbf{E}\cdot\mathbf{r}'$, the pseudomomentum is conserved, and a simple constant term $-e\mathbf{E}$ appears in the equation of motion for $\mathbf{p}$.

A.1.1 Selection of the Ps initial state

Positronium is a quantum-mechanical system. In the semi-classical approach we are establishing, it is needed to find appropriate initial conditions that well represent a specific quantum-mechanical state with well-defined quantum numbers. In the unperturbed case (i.e. without electric and magnetic fields), the Hamiltonian reduces to the familiar form:

$$H^{\mathrm{unp}} = \frac{\mathbf{p}^2}{2\mu} - \frac{e^2}{|\mathbf{r}|},$$

where $\mu = 0.5$ is the reduced mass of the system. This is the Hamiltonian of the well-known two-body Kepler problem. Angular momentum and energy are constants of motion in this setting, moreover closed trajectories are ellipses, and the momentum is orthogonal to the position vector at the aphelion and perihelion of the trajectory (see Fig. A.1 for a definition of the symbols). Conservation of energy and momentum implies the following relations:

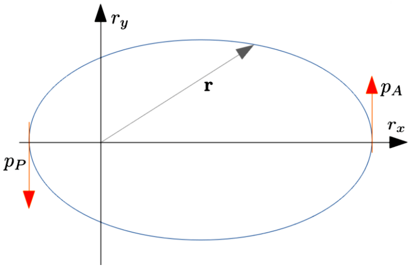

Figure A.1. Kepler orbit of the relative coordinate $\mathbf{r}$. The momenta $\mathbf{p}_P$ and $\mathbf{p}_A$ are orthogonal to the position vectors $\mathbf{r}_P$ and $\mathbf{r}_A$ at the perihelion P and aphelion A respectively.

$$\begin{cases} p_A^2 - \dfrac{1}{r_A} = p_P^2 - \dfrac{1}{r_P} = E_n \\ \quad p_A r_A = p_P r_P = L_l \end{cases} \tag{A.8}$$

which can be related to the quantum-mechanical expressions (in atomic units) for energy $E_n = -\frac{1}{4n^2}$ and modulus of the angular momentum $L_l = \sqrt{l(l+1)}$ as a function of the principal (n) and orbital (l) quantum numbers. Solving the above system of equations one obtains:

$$\begin{cases} r_A = 2n^2 + 2n^2\sqrt{1 - \dfrac{l(l+1)}{n^2}} \\ p_A = \dfrac{\sqrt{l(l+1)}}{r_A} \end{cases} \tag{A.9}$$

for the initial conditions as a function of the quantum numbers. For convenience we defined initial conditions on the aphelion, but to span all the phase space in a typical Monte Carlo simulation, the generated initial vectors will be rotated randomly in three-dimensional space. Furthermore, given that the period T_{orb} of the orbit is known, to generate initial conditions at any point on the allowed trajectory, a preliminary evolution with the unperturbed equations of motion for a randomly generated time $t_{\mathrm{preev}} \in [0, T_{\mathrm{orb}}]$ can be performed before the actual simulation of each atom starts. This procedure should provide sensible initial conditions that well represent the quantum state, at least in a weak field regime, where the assumption of an initially unperturbed state is sensible. For strong field regimes, a form of *adiabatic switch-on* of the external field on the states prepared with the recipe outlined above can be considered [155]. We now discuss the dynamics of Ps in some interesting cases using the CTMC formalism.

A.2 Homogeneous magnetic field

The assumption of a homogeneous magnetic field is adequate for the magnetic field of the Earth, which already has a sizeable impact on the motion of positronium. We start from the definition of the pseudomomentum **K** in terms of the physical velocity of the center-of-mass:

$$\mathbf{K} = M_{\mathrm{Ps}}\mathbf{v}_{\mathrm{Ps}} + e\mathbf{B} \times \mathbf{r}. \tag{A.1}$$

This result follows either from the fourth of equations (A.7) or from the definition of the mechanical momentum in terms of the canonical momentum, namely:

$$\mathbf{p}_i^{\mathrm{mech}} = \mathbf{p}_i - \frac{e}{2}\mathbf{B} \times \mathbf{r}_i$$

The motion of Ps in a homogeneous magnetic field has been studied in [153] in 1991, where the authors state that the equations cannot efficiently be solved in Cartesian coordinates, and a complicated change of variables and integration scheme is devised. However, I found that it is now possible to reproduce with little computational effort, all the results of the paper directly in Cartesian coordinates[1] (see Fig. A.2 for an example). The study [153] focuses on a high magnetic field regime ($B \approx 1T$) in which a chaotic behavior is possible[2]. Furthermore the constraint $\mathbf{K} = 0$ is imposed, however this is not

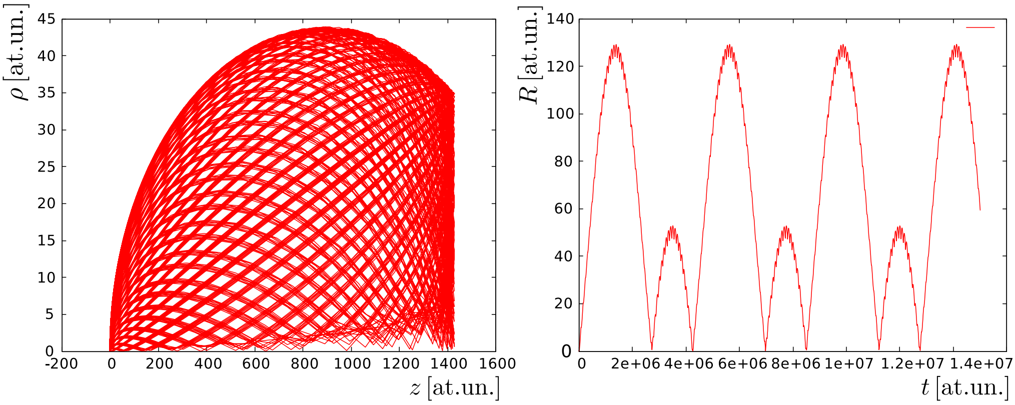

Figure A.2. Left: plot in the ρ-z plane of the relative coordinates, where $\rho = \sqrt{x^2 + y^2}$, for the same initial conditions of the reference paper [153]. Right: time dependence of the absolute value of the center of mass position, for the same trajectory. All axes are in atomic units. This result, reported in Figure 2 in [153] is reproduced in a fraction of a second directly in cartesian coordinates with the above mentioned methods.

---

[1] In particular, all the simulations were performed with standard numerical methods such as the *Dormand-Prince* [156] or *Fehlberg* [157] Runge-Kutta type solvers provided by the *Odeint* [158] C++ library.

[2] In the regime of interest for QUPLAS, no evidence of chaotic behaviour was found. We remark that in the same conditions considered in [153] direct integration in Cartesian coordinates still correctly predicts a chaotic behavior.

a particularly interesting choice. According to equation (A.1), fixing $\mathbf{K} = 0$ is equivalent to setting a particular value of the Ps velocity, that depends on the magnetic field and on the initial condition on the internal coordinate, $\mathbf{r}_0$ (since $\mathbf{K}$ is a constant of motion). The typical initial values chosen in [153] correspond to an extremely small (and experimentally unrealistic) Ps speed $V_{\mathrm{Ps}} \approx 10\,\mathrm{m/s}$.

We focus for definiteness on a Ps velocity $V_{\mathrm{Ps}} = 800\,\mathrm{m/s}$, and assume the atoms travel horizontally over a distance $L = 1\,\mathrm{m}$, in the magnetic field of the Earth. In a dipole approximation, the radial and tangential components of the magnetic field are given by the following expressions [159]:

$$B_r = -\frac{2B_0}{R^3}\sin\lambda \tag{A.2}$$

$$B_\theta = \frac{B_0}{R^3}\cos\lambda \tag{A.3}$$

where $B_0 = 3.12 \cdot 10^{-5}\,\mathrm{T}$ is an empirical constant, λ is the latitude and $R = r/R_E$ is defined in terms of the distance to the center of the Earth r and the mean Earth radius R_E. Inserting for instance the data of the L-NESS lab in Como (coordinates N$45°48'4.376''$, E$9°5'33.782''$ and an elevation of $219.4\,\mathrm{m}$ above sea level) we find:

$$B_r = -4.479 \times 10^{-5}\,\mathrm{T}$$

$$B_\theta = 2.177 \times 10^{-5}\,\mathrm{T}$$

Without loss of generality, we can fix a Cartesian laboratory reference frame with the

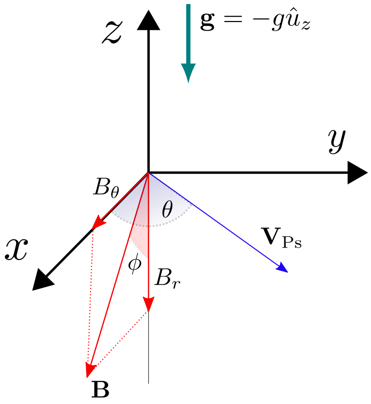

Figure A.3. Laboratory reference frame for Ps gravity measurement. Atoms travel in the horizontal direction forming an angle θ with the tangential component of the Earth magnetic field.

z-axis oriented vertically. That is the direction in which we would be observing the interference pattern for gravity measurements (see Fig. A.3). We can orient the frame so that the magnetic field reads:

$$\mathbf{B} = (B_\theta, 0, B_r)$$

The positronium atom then travels in the x-y plane. The solution of equations (A.7) is most conveniently carried out in a reference frame in which the magnetic field is oriented along one coordinate axis. So we just transform the initial conditions with a rotation about the y-axis of an angle $\phi = \mathrm{atan}(B_r/B_\theta)$, that orients $\mathbf{B}$ purely along z. The final position is then rotated back to the laboratory frame.

Trajectories in an homogeneous magnetic field

Evaluating the first of equations (A.7) with the initial conditions for the relative coordinates $r_0 = 1250$ and $p_0 = 0.02$, consistent (in atomic units) with a Rydberg state $n = 25$ and $l = 24$ yields:

$$\frac{|\mathbf{B} \times \mathbf{r}_0|}{|\mathbf{K}|} \approx 10^{-5} \tag{A.4}$$

where $\mathbf{K}$ is a constant of motion. So we expect an essentially linear motion on a large scale with small ($O(10^{-5})$) perturbations. The numerical solution confirms this prediction. Figure A.4 compares the law of motion $Y(t)$ of the y-coordinate of the center of mass for $B \approx B_0$ and $B = 1\,\mathrm{T}$. As discussed in Fig. A.4, small oscillations are invisible on macroscopic time scales in a weak field regime. Consider also that the field will be further reduced by applying a magnetic shielding of a factor 100 or 1000, feasible by means of a multi-layer mu-metal shield. The most sizable effect is what the the equation of motion already tells us: the center of mass moves with an effective velocity that is modified by the presence of the magnetic field:

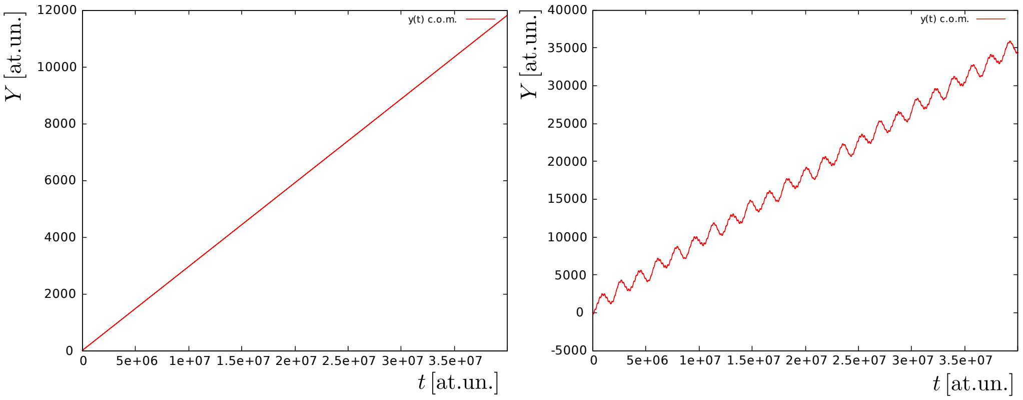

Figure A.4. Plot of the time evolution of the Y center of mass coordinate in a weak $B \approx B_0$ magnetic field (left) and in a strong $B = 1\,\mathrm{T}$ field (right). Time scale is in atomic units, the plotted range corresponds to approximately $1\,\mathrm{ns}$. On this time scale, as predicted, local periodic perturbation of linear motion are totally negligible in a weak field regime. Still in large fields, the perturbations appear periodic and if they are averaged out the trend is clearly linear.

$$\dot{\mathbf{R}} = \mathbf{V}_{\mathrm{Ps}} \to \dot{\mathbf{R}} = \mathbf{K}/M.$$

Thus we can expect a deviation from the unperturbed trajectory that we want to estimate. We will evaluate the deviation vector:

$$\Delta\mathbf{R} = \mathbf{R}^{(B)}_{\mathrm{Fin}} - \mathbf{R}^{(0)}_{\mathrm{Fin}} = (\Delta X, \Delta Y, \Delta Z) \tag{A.5}$$

where the unperturbed final position after a time T is simply $\mathbf{R}^{(0)}_{\mathrm{Fin}} = \mathbf{V}_{\mathrm{Ps}} \cdot T + \mathbf{R}_0$, and $\mathbf{R}^{(B)}_{\mathrm{Fin}}$ is the numerical solution of the equations of motion. In the following it is assumed that $\mathbf{R}_0 = \mathbf{0}$. Obviously both quantities will be taken in the laboratory frame of reference by performing the required inverse rotation on the output of the numerical algorithm. By the definition of $\mathbf{K}$, equation (A.1) we see that the deviation depends on the initial conditions, in particular $\mathbf{r}_0$, both in modulus and direction. It is thus necessary to look at the deviation of an ensemble of trajectories with a fixed initial positronium velocity, varying the orientation in space of the internal orbital motion. The velocity $\mathbf{V}_{\mathrm{Ps}} = V_{\mathrm{Ps}} \cdot (\cos(\theta), \sin(\theta), 0)$, lies on the x-y plane (see Fig. A.3).

To set appropriate initial conditions on the internal coordinates, we use the semi-classical correspondence established in equations (A.9). Thus we set initial position and momentum vectors as:

$$\mathbf{r}_0 = (r_a, 0, 0) \quad \mathbf{p}_0 = (0, p_a, 0).$$

The initial vectors are then rotated randomly, with a uniform sampling so that the normal to the orbital plane spans all directions in space; there are various algorithms to realize this sampling. In an axis/angle representation of three-dimensional rotations, one can extract the rotation angle from the following distribution [160]:

$$P(\alpha) = \frac{2}{\pi} \sin^2\left(\frac{\alpha}{2}\right)$$

in the interval $[0, \pi]$, and the rotation axis is taken as a unit vector uniformly distributed on the surface of a sphere [3]. The dependence on the orientation of the Ps velocity on the x-y plane (the angle θ in Fig. A.3) was also investigated. For the single trajectory (that is, a particular choice of $\mathbf{r}_0$ and $\mathbf{p}_0$) there is indeed a difference in the orientation of the deviation vector. However the form of its distribution is very weakly affected; we will present results from the cases $\theta = 0$ and $\theta = \frac{\pi}{2}$. In summary, the algorithm employed to evaluate the deviation vectors is as follows:

- Initial conditions $\mathbf{r}_0$, $\mathbf{p}_0$ are randomly rotated.
- The system is evolved with the equations of motion for a time much longer than the (negligible) oscillating behavior. A suitable time interval is found to be $T_{\mathrm{sol}} = 10^6$ (atomic units of time).
- The final position is found by normalizing the position at the end of the previous evolution step to the physical timescale for an $1\,\mathrm{m}$ long trajectory, namely $T_{\mathrm{phys}} = 10^{13}$ (assuming the motion is linear).
- Repeat the above steps on an ensemble of trajectories, sampling uniformly distributed initial conditions as described. The distribution of the deviation vector, defined in equation (A.5), is thus obtained.

In figures A.5 and A.6 we present a few representative results, assuming for definiteness a shielding factor of 100. The deviations are found to be linear in the magnetic field, so the expected deviations for any value of the shielding factor are readily estimated.

---

[3] This, in turn, is easily obtained for instance by normalizing three independent normally distributed points. Uniformity is ensured by the rotational invariance of the distribution $P(x, y, z) \propto \exp\left\{x^2 + y^2 + z^2\right\}$.

Displacement for $\mathbf{B} = \mathbf{B}^{\mathrm{Earth}}/100$

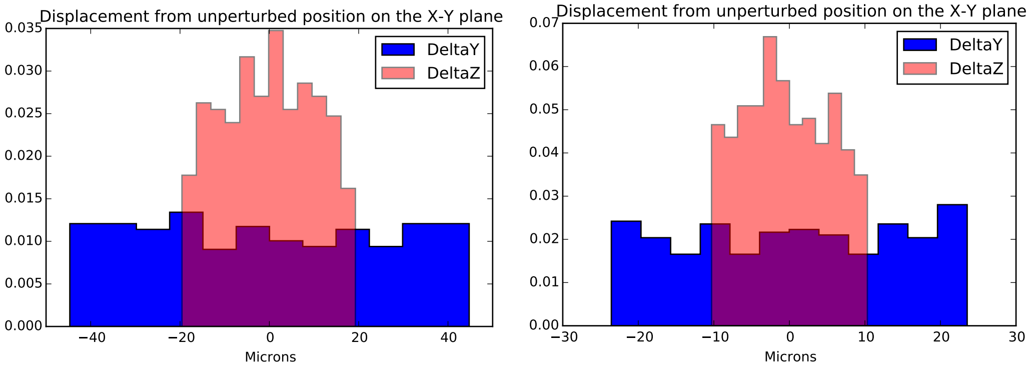

(a) $n = 90$ and $l = 89$ **(b)** $n = 90$ and $l = 1$

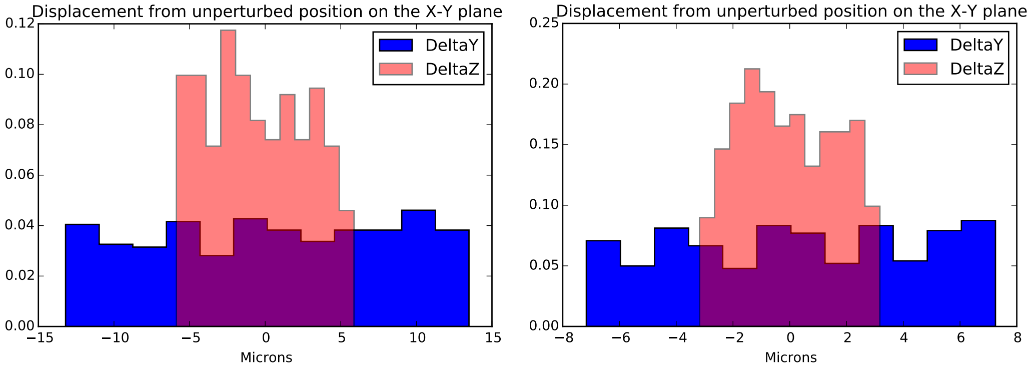

(c) $n = 50$ and $l = 49$ **(d)** $n = 50$ and $l = 1$

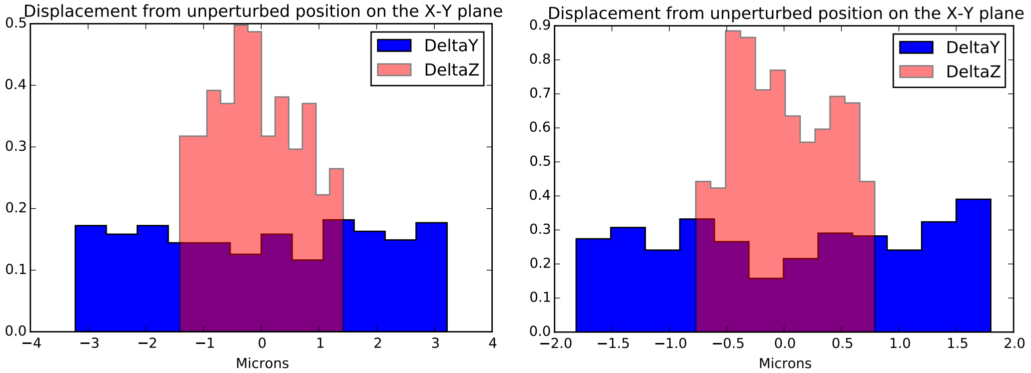

(e) $n = 25$ and $l = 24$ **(f)** $n = 25$ and $l = 1$

Figure A.5. Deviation on the plane transverse to the motion for $\theta = 0$ (so that $\mathbf{v}_{\mathrm{Ps}} = 800\,\mathrm{m/s}$ along the x axis), and the indicated quantum numbers. We assumed a magnetic shielding factor of 100. The histograms are normalized and each contains 400 trajectories.

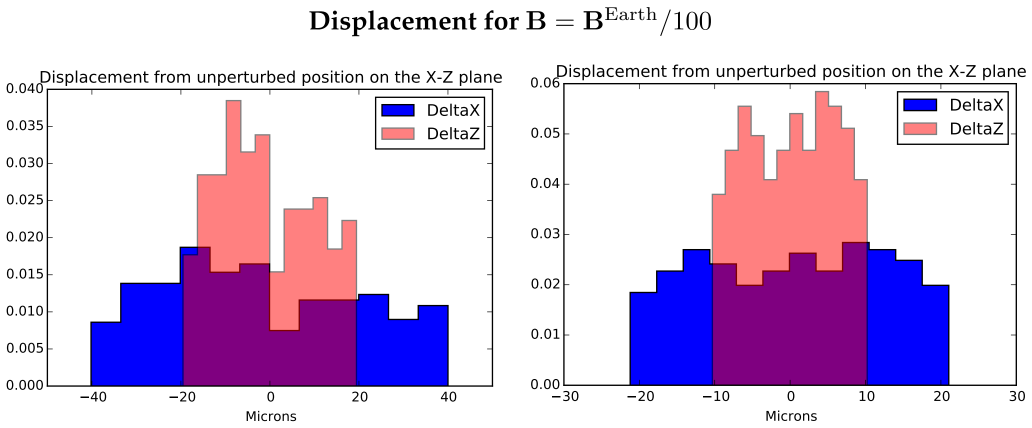

(a) $n = 90$ and $l = 89$ **(b)** $n = 90$ and $l = 1$

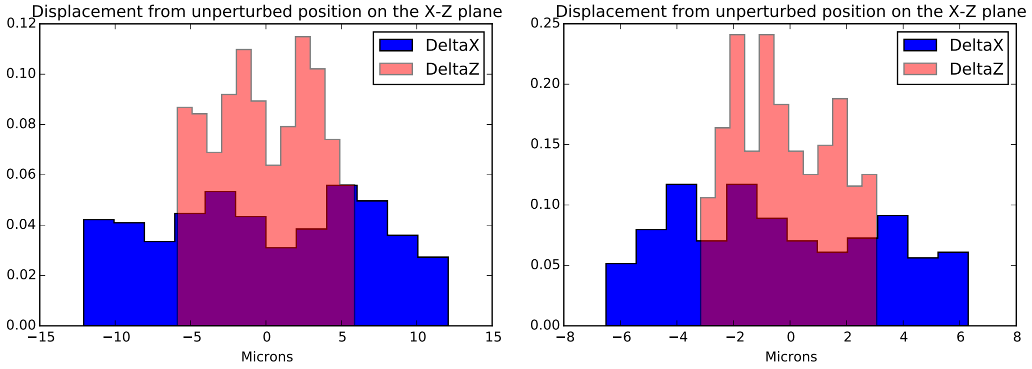

(c) $n = 50$ and $l = 49$ **(d)** $n = 50$ and $l = 1$

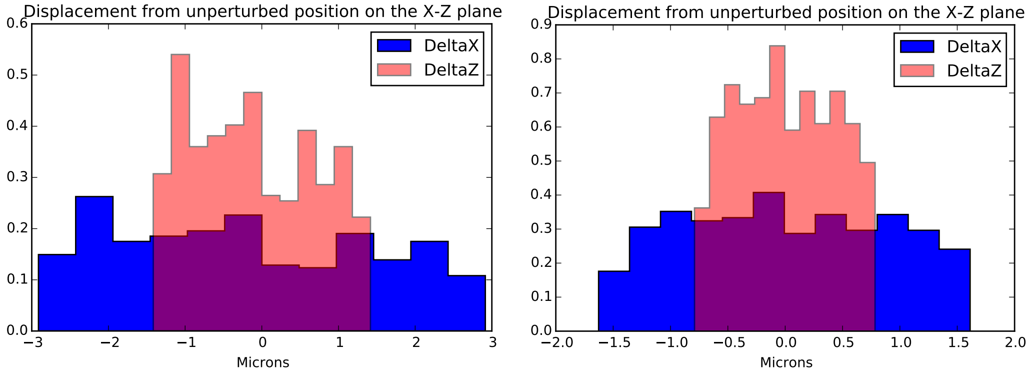

(e) $n = 25$ and $l = 24$ **(f)** $n = 25$ and $l = 1$

Figure A.6. Deviation on the plane transverse to the motion for $\theta = \pi/2$ (so that $\mathbf{v}_{\mathrm{Ps}} = 800\,\mathrm{m/s}$ along the y axis), and the indicated quantum numbers. We assumed a magnetic shielding factor of 100. The histograms are normalized and each contains 400 trajectories.

We observe that the distribution of the displacement in both directions is always symmetrical about the origin. Therefore there are no systematic effects that can compete with gravity. The deviation has been calculated for a flight length of $1\,\mathrm{m}$, however since we are concerned with linear motions, the results could be converted in deviation angles to be completely general. The width of the distribution increases both with n and with l, although the dependence on l is weaker. The width of the distributions is also linear in the magnetic field strength, so the effect of the shielding is easily taken into account. If we require, for definiteness, that the displacement on the z-axis (the only one relevant for a gravitational measurement), must be of the order $\Delta Z \approx 1\ \mu\mathrm{m}$ we see that it roughly requires a shielding factor $s \approx 1000$ for $n = 90$ and $s \approx 100$ for $l = 25$.

From a different point of view we can state that Ps is just propagating linearly with a modified effective velocity. Thus this deviation can be seen as an additional contribution to the transverse velocity spread of the particle beam (additional with respect to the intrinsic contribution). In Part II we have established the link between the transverse momentum distribution and what is typically referred to as the transverse coherence length. Its impact on the visibility of the pattern and on the robustness of the interferometer with respect to misalignments was studied. The observed deviations at the level of $10^2\ \mu\mathrm{m}$, correspond to deviations angles of approximately $0.1\,\mathrm{mrad}$, therefore negligible with the spread expected from a weakly collimated positronium beam (we recall for comparison that the L-NESS positron beam has a typical divergence angle of the order of $6\,\mathrm{mrad}$).

In conclusion, a constant and uniform magnetic field is found to produce an increase in the angular spread of the Ps beam, which is negligible for the case of the magnetic field of the Earth. Therefore, shielding requirements are not critical for a possible gravity measurements, as no systematic effects possibly competing with gravity arise. However, it must be stressed that although the motion remains linear on a large time scale, oscillations in the center of mass motion could affect the quantum mechanical description of the interference process, possibly reducing the visibility of the interference pattern. Standard models are not able to account for perturbations in the motion in a straightforward manner. The relative strength of the perturbation can be limited by an appropriate magnetic shielding, as suggested by equation (A.4).

A.2.1 A constant electric field

The case of a constant and uniform electric field $\mathbf{F}$, with $\mathbf{B} = 0$ is trivial, as the center-of-mass and the internal motion are completely decoupled and the center-of-mass trajectory is unaffected. Therefore we will consider the action of a constant electric field in addition to the Earth magnetic field. It is observed from simulations of a large number of trajectories that indeed the motion has the same linear character on a large scale that is associated to the magnetic field only case. Given this feature, it is sensible to employ the same reasoning introduced before and discuss the deviation from unperturbed trajectories in the presence of the additional electric field. Since the effect is very small we set a very large value of electric field $F = 1000\,\mathrm{V/m}$, $n = 25$, $l = 1$, and (in the same reference frame discussed in section A.2) consider six possible cases for the orientation of the $\mathbf{F}$, namely along the three coordinate axes combined with the two possible orientations of the $\mathbf{v}_{Ps}$ vector in the x-y plane. The results of simulations on an ensemble of trajectories are summarized in Fig. A.7 and can be compared with figures A.5 and A.6. The comparison reveals that in the z direction (the one relevant for our purposes) there is an increase in the spread of the trajectories (spread of the transverse velocities), but relatively limited considering the very strong value of the electric field. Moreover we see that there is no marked asymmetry in the distributions introduced by the additional external field. The strength of the coupling between the center of mass motion and the electric field is somewhat mediated by the magnetic field, in the sense that all information about the $\mathbf{F}$ field comes from the term $\mathbf{B} \times \mathbf{r}$ in the derivative of the center of mass coordinate. So shielding the magnetic field also effectively reduces the influence of stray electric fields.

A.3 Stark effect and motion in electric field gradients

Although positronium is neutral, high-n Rydberg states can be very sensitive to electric field gradients due to the large dipole moments they can acquire. The starting point for a description of this effect is the theory of the Stark effect. We now briefly recap the main equations relevant for our simulations. In an external electric field $\mathbf{F} = (0, 0, F)$ that we can assume directed along the z-axis with no loss of generality, the perturbed Hamiltonian of the Ps atom reads:

$$H = H_0 + eFz,$$

where H_0 is the hydrogenic part. This problem can be dealt with by solving the free Hamiltonian in "parabolic coordinates" (see [97, 161]), and evaluating the perturbation energy. The states are labelled by four quantum numbers (only three of which are independent):

$$|n, n_1, n_2, m\rangle$$

The two parabolic quantum numbers n_1 and n_2 satisfy $n = n_1 + n_2 + |m| + 1$. The energy of the eigenstates reads (to first order in F) [103]:

$$E_{n\, n_1\, n_2\, m} = -\frac{R_M hc}{n^2} + \frac{3}{2} n(n_1 - n_2) e a_0 F + \cdots$$

where $a_0 = \frac{m_e}{\mu} a_0^H$ is the Bohr radius corrected for the reduced mass, and $R_M = \frac{R_\infty \mu}{m_e}$ is the corrected Rydberg constant. The quantum number $k = (n_1 - n_2)$ is usually introduced. Putting all this together and adopting atomic units yields, for the special case of positronium ($\mu = 0.5 m_e$):

$$E^{\mathrm{Ps}}_{n\, k\, m} = -\frac{1}{4n^2} + 3nkF + \cdots \tag{A.1}$$

The idea behind Stark acceleration (or deceleration) of Rydberg atoms is that if a Stark state is created in an inhomogeneous electric field, then the states with $k > 0$ (called "low-field-seeking") will be attracted in the direction of decreasing electric field, and vice-versa for the states with $k < 0$. So if a an atom travels in a field gradient with a certain initial velocity, then energy transfer from the kinetic energy of the center of mass to the coupling with the electric field will take place, leading to a decelerating or accelerating effect depending on the sign of k and the direction of the gradient. The loss or gain in kinetic energy can be estimated as [101]:

$$\Delta E_k = 3nk\Delta F$$

In particular an approximation used in the literature is that the istantaneous force $\mathbf{f}$ acting on the atom is proportional to the gradiend of $|\mathbf{F}|$. We can justify this statement with the following reasoning: assume the field in the position where the Rydberg-Stark state is initially excited is $\mathbf{F}_0$, then as the atom moves the field will vary both in intensity

Displacement for B $= \mathrm{B}^{\mathrm{Earth}}/100$ and $F = 1000\,\mathrm{V/m}$

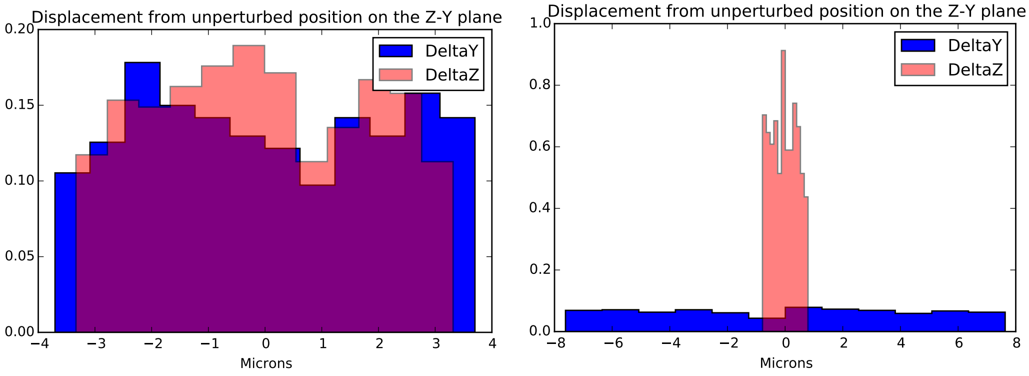

(a) $\mathbf{F} = F\hat{\imath}$, and $\mathbf{v}_{Ps} = v_{Ps}\hat{\imath}$ **(b)** $\mathbf{F} = F\hat{\jmath}$, and $\mathbf{v}_{Ps} = v_{Ps}\hat{\imath}$

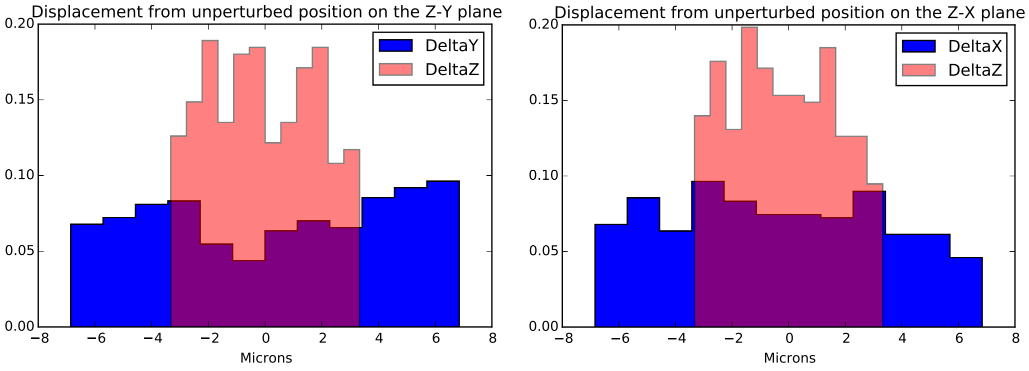

(c) $\mathbf{F} = E\hat{k}$, and $\mathbf{v}_{Ps} = v_{Ps}\hat{\imath}$ **(d)** $\mathbf{F} = F\hat{\imath}$, and $\mathbf{v}_{Ps} = v_{Ps}\hat{\jmath}$

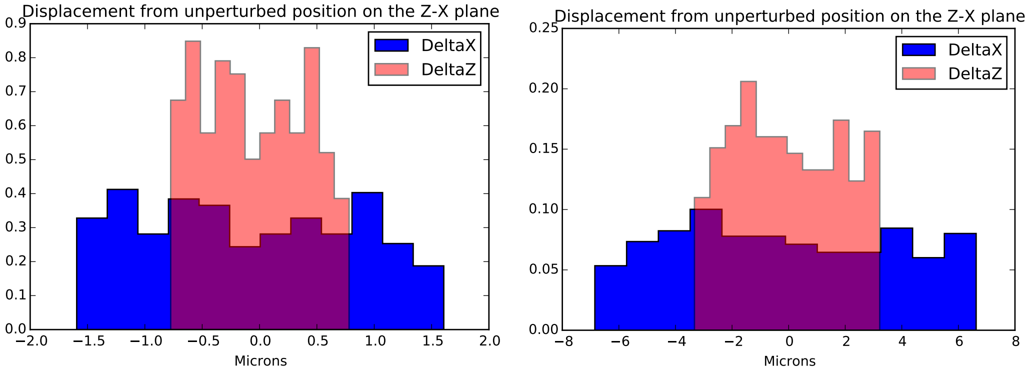

(e) $\mathbf{F} = F\hat{\imath}$, and $\mathbf{v}_{Ps} = v_{Ps}\hat{\jmath}$ **(f)** $\mathbf{F} = F\hat{k}$, and $\mathbf{v}_{Ps} = v_{Ps}\hat{\jmath}$

Figure A.7. Deviation on the plane transverse to the motion in the presence of the shielded (factor 100) Earth magnetic field and a strong electric field $V = 1000\,\mathrm{V/m}$, for the six orientation cases mentioned in the text .

and direction (generally). Physically it happens that the state acquires an electric dipole, whose modulus is proportional to $d \propto 3nk$, and is oriented along the field $\mathbf{F}_0$. In classical electromagnetism the force exerted on a dipole $\mathbf{d}$ in a field $\mathbf{F}$ is $\mathbf{f} = \nabla(\mathbf{d} \cdot \mathbf{F})$ [103]. If one assumes that the electric field varies (spatially) slowly enough so that the dipole moment of the atom remains parallel to the istantaneous field along the motion, then:

$$\mathbf{f} = \nabla(3nk\frac{\mathbf{F}}{|\mathbf{F}|} \cdot \mathbf{F}) = 3nk\nabla|\mathbf{F}| \tag{A.2}$$

so that the force is the gradient of the modulus of the electric field. This allows a computationally simpler approach (with respect to CTMC) for the simulation of trajectories in arbitrary electric fields by considering the atom as a point-like particle subjected to the force (A.2). Since the force depends on the quantum number, radiative decay of the Rydberg atom to the lower lying levels is a complication because the potential it feels changes as it decays. For the time being we assume that the typical travel time in a deceleration/acceleration stage is much shorter than the radiative lifetime ($\tau \approx 200\mu s$ for an $n = 20$ state) and neglect decay altogether.

A.3.1 Field ionization rate of Rydberg-Stark states

On the contrary, field ionization is not negligible. In the so-called classical approximation [103], the critical field scales rapidly with n^{-4}:

$$F_{\text{class}} = \frac{2hcR_M}{ea_0 9n^4} \approx \frac{1.4 \times 10^{10}}{n^4}\,\text{V/m} \tag{A.3}$$

where the quoted numerical constant is specific to positronium. This formula, in particular, gives the field at which the ionization lifetime is 10^{-8} s for the *extreme* Stark state with quantum numbers $(n_1, n_2, m) = (0, n-1, 0)$ [97]. The acceleration field should be everywhere much lower than this limit. Of course the mean force is increasing with the electric field, so the best compromise between the risk of field ionization and acceleration will have to be found. Experimental results for Hydrogen [101] suggest that it is possible to obtain accelerations as high as $a \approx 10^{11}$ m/s with fields below the classical ionization limits (Ps is 2000 times lighter than hydrogen).

It is interesting to consider the issue of field ionization of the Rydberg-Stark states of Hydrogenoid atoms in more details. The semi-empirical formula often reported in the literature [103, 162] states that the ionization rate for a a state with quantum numbers $|n, n_1, n_2, m\rangle$ is given by:

$$\begin{aligned}\Gamma_{n,n_1,n_2,m}(F) = \frac{E_h}{\hbar}\frac{(4C)^{2n_2+m+1}}{n^3 n_2!(n_2+m)!}\exp\left\{-\frac{2}{3}C - \frac{1}{4}n^3\frac{ea_0F}{E_h}\left(34n_2^2 + 34n_2m + \right.\right.\\ \left.\left. +46n_2 + 7m^2 + 23m + \frac{53}{3}\right)\right\},\end{aligned} \tag{A.4}$$

where $E_h = 2hcR_M$, with $R_M = R_\infty\mu/m_e$ the Rydberg constant corrected for the reduced mass, and

$$C = \frac{1}{ea_0\sqrt{E_h}}\frac{(-2E_{n,n_1,n_2,m})^{3/2}}{F}.$$

This approximate expression is valid only for weak fields and low n states [162] (the argument of the exponential factor can rapidly become very large and give unreliable results). Exact numerical calculations, which are not trivial, are generally needed to correctly assess the ionization rates. There is a rich literature on the subject (see for example [163, 164, 165, 166, 167]). Results based on numerical solution of the Schrödinger equations are reported in [164] for several combinations of quantum numbers, but the general algorithm presented is not easily implemented from the information contained in the paper and does not appear to be very robust for strong electric fields, where ionization lifetime approaches 10^{-12} s. I was able to reproduce the known results using the approach of [166] to provide initial values for the semi-classical algorithm of [165]. The combination of these two methods allowed to extend the calculation to very strong fields. Representative results for an $n = 25$ state with different combinations of the parabolic quantum numbers obtained with this method are shown in Fig. A.8.

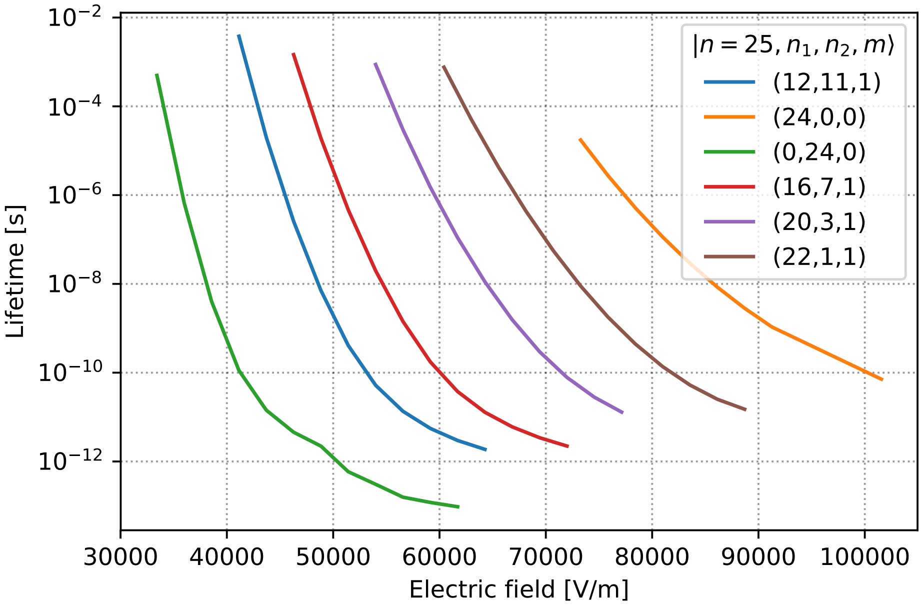

Figure A.8. Ionization lifetime of positronium as a function of the external field applied for $n = 25$ and several combinations of the parabolic quantum numbers. Note how the critical field predicted by equation (A.3) is $36\,\mathrm{kV/m}$, which indeed corresponds to the field at which the $n_2 = 24$ state has a lifetime of 10^{-8} s according to the exact numerical solution.

A.3.2 CTMC simulation in nonhomogeneous electric fields

We now perform a comparison of the CTMC approach with the point-like description of the motion in nonhomogeneous electric fields. In particular we focus on the simple configuration of a linearly varying field, oriented along the z-axis (which is also the direction of travel of the atoms). To set realistic initial conditions in a non-negligible external electric field, the technique of adiabatic switch-on was applied. We briefly describe the steps involved:

- **Preparation of the free initial state**. A suitable distribution of free-field initial states is prepared as previously discussed. A given n, l state is prepared in the perihelion, on a fixed plane. Then it is evolved with the free equations of motion for a uniformly sampled random fraction of the Kepler period ($T_K = \frac{1}{2}\pi(r_A + r_P)^{3/2}$):

$$\begin{cases} \dot{\mathbf{R}} = 0 \\ \dot{\mathbf{K}} = 0 \\ \dot{\mathbf{r}} = \dfrac{2\mathbf{p}}{m} \\ \dot{\mathbf{p}} = -e^2 \dfrac{\mathbf{r}}{|\mathbf{r}|^3} \end{cases} \tag{A.5}$$

This produces a distribution of points in the $(\mathbf{r}, \mathbf{p})$ phase space that define elliptical trajectories on a fixed plane with the appropriate energy and angular momentum. An uniformly sampled random rotation is then applied.

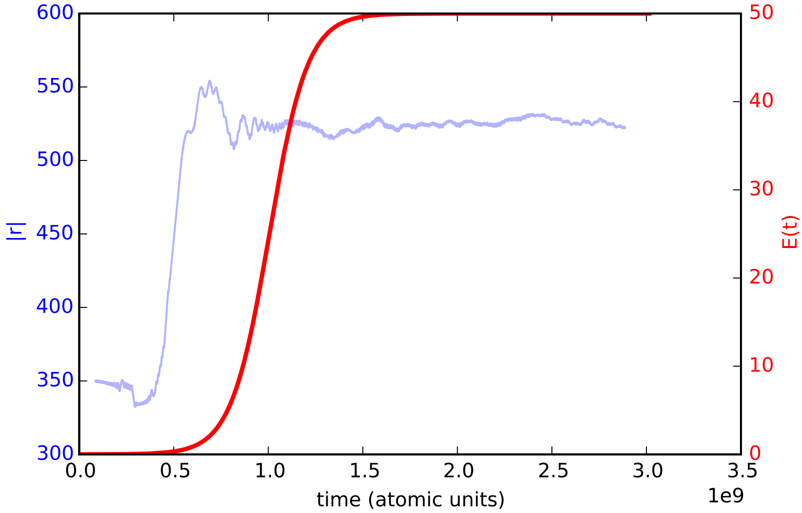

Figure A.9. Time dependence of $F(t)$ and of a moving average of $|\mathbf{r}|$, the modulus of the relative e^+/e^- position. The average value of $|\mathbf{r}|$ is changed by the electric field turn-on and then reaches a stable value. This suggests that indeed the state is approaching a condition that represents a well-defined quantum state. As far as the force in a field gradient is concerned, the behavior of the atom after E field switch on is consistent with the principal quantum number n being left unchanged, and a value of k being acquired depending on the precise initial conditions.

- **Adiabatic switching of the electric field**. To simulate the Rydberg-Stark states, the final state of the previous step is set as initial conditions for the evolution in a time-varying electric field slowly approaching the value F_0 (hence the name *adiabatic* *switching on*). In particular the evolution equations for this stage read:

$$\begin{cases} \dot{\mathbf{R}} = 0 \\ \dot{\mathbf{K}} = 0 \\ \dot{\mathbf{r}} = \dfrac{2\mathbf{p}}{m} \\ \dot{\mathbf{p}} = -e^2 \dfrac{\mathbf{r}}{|\mathbf{r}|^3} + eF(t)\hat{\mathbf{u}}_z; \end{cases} \tag{A.6}$$

(in previous equations it was assumed that $F = \nabla\phi$, here we adopt the usual convention $\mathbf{F}(\mathbf{x}) = -\nabla\phi(\mathbf{x})$, hence the plus sign in the last equation). The time dependence of the electric field was chosen to be a sigmoidal function (see Fig.A.9):

$$F(t,\tau) = \frac{F_0}{1 + \exp\{-(t - 10\tau)/\tau\}}$$

so that $F(0) \approx 0$ and $F(30\tau, \tau) \approx F_0$. The time constant τ is chosen so that it is much larger than the Kepler period, for example $\tau = 1000T_K$.

The resulting state after this step should correspond to one of the possible Rydberg-Stark states with the chosen principal quantum numbers. One must relate classical quantities to quantum numbers. In analogy with the free field case, it is useful to use the total energy to do so. Rearranging equation (A.1), one obtains:

$$k = (E + \frac{1}{4n^2})/(3nF_0) \tag{A.7}$$

the energy E is the classical energy evaluated at the end of the trajectory (when a constant field regime has been reached). In this case ($\mathbf{K} = 0$) it reads:

$$E = \frac{1}{2m} \cdot 2\mathbf{p}^2 - \frac{e^2}{|\mathbf{r}^2|} - F_0 ez. \tag{A.8}$$

The above equations suggest a way to calculate the k quantum number associated to a certain initial state. How to do the converse, that is decide the Rydberg-Stark quantum numbers beforehand, and produce a suitable set of classical initial conditions is not straightforward[4]. If time efficiency is not a concern, in a Monte Carlo simulation approach one could just generate a certain number of states and only retain results for the k states of interest.

- **Evolution in a constant direction field of varying intensity.** After the initial state is prepared in a well-defined n, k state, simulation of the motion in a field of the form:

  $$\mathbf{F}(\mathbf{x}) = F(z)\hat{\mathbf{u}}_z \quad \text{with} \quad F(z) = F_0 - z\frac{(F_0 - F_1)}{z_m}$$

  is performed. Field intensity decreases linearly from F_0 to F_1 over a length z_m, the length of an hypothetical acceleration/deceleration stage based on a linear field gradient. Such a field is given by the potential:

  $$\phi(\mathbf{x}) = -zF_0 + \frac{z^2(F_0 - F_1)}{2z_m}.$$

---

[4] Probably since the problem in a constant electric field (at the instant of time when the atom is excited to Stark states) is cylindrically symmetric, one could obtain more states of unchanged k by rotating initial conditions around the electric field axis, but this hypothesis has not been investigated yet.

The equations of motions then read:

$$\begin{cases} \dot{\mathbf{R}} = \dfrac{\mathbf{K}}{2m} \\ \dot{\mathbf{K}} = -e\dfrac{(F_0 - F_1)}{z_m} z\hat{\mathbf{u}}_z \\ \dot{\mathbf{r}} = \dfrac{2\mathbf{p}}{m} \\ \dot{\mathbf{p}} = -e^2\dfrac{\mathbf{r}}{|\mathbf{r}|^3} - e\left(-F_0 + \dfrac{(F_0 - F_1)}{z_m}R_z\right)\hat{\mathbf{u}}_z \end{cases} \tag{A.9}$$

If the CTMC approach is consistent with the point-like approximation the Ps atom should experience a constant force directed along z, whose sign depends on k, and on the sign of the gradient $(F_0 - F_1)/z_m$. For definiteness we set the parameters $F_0 = 50\,\mathrm{V/cm}$, $F_1 = 5\,\mathrm{V/cm}$ and $z_m = 0.3\,\mathrm{m}$. The choice of a very small distance is dictated by the substantial computational load of this method if high accuracy is required. The field gradient is then $\nabla F = (F_1 - F_0)/z_m = 1500\,\mathrm{v/cm^2}$, thus in the same range of the average gradients employed in stark decelerators [154] (where, however, the spatial dependence is nonlinear). The incoming Ps atoms are prepared with an initial velocity $\mathbf{v} = v\hat{u}_z$ with $v = 10^4\,\mathrm{m/s}$. Their quantum number k is calculated as explained and a CTMC simulation is run. As the field is decreasing along the trajectory in this example, states with positive coupling to the field ($k > 0$) are expected to be accelerated (low-field seeking states) whereas the $k < 0$ states should be decelerated.

Using equation (A.2) expressed in terms of the acceleration with the appropriate sign, then the expected acceleration in this field is

$$a = -\frac{3nk\nabla F}{2m_e} = -\frac{3nk\nabla F}{2} \text{ (all quantities in atomic units)} \tag{A.10}$$

the equation can be used as a consistency check to test if the simulated acceleration agrees with the expected value based on the previously outlined estimation of the k quantum number.

Results and future developments

Qualitative inspection of a large ensemble of trajectories confirms that the simulated motion is indeed a uniformly accelerated motion along the z axis, with the expected value of the acceleration. A typical example is shown in Fig. A.10. This result suggests that both techniques can be applied tu study the motion in arbitrary electric fields such as the one produced by the geometry sketched in Fig. 3.5 for a possible Stark decelerator. The CTMC approach, although computationally heavier, is expected to be more accurate in strong fields with respect to the point-like approximation.

Finally, we can consider an electric field gradient as a disturbance in a possible measurement of g, and calculate the gradient that produces an acceleration $a \approx 9.81\,\mathrm{m/s^2}$. Recalling equation (A.10), with the necessary conversion to atomic units, one obtains for a typical worst case scenario , that is $n = 25$ and $k = 24$:

$$\nabla F_g^{n=25,k=24} \approx 2\,\mathrm{mV/m^2} \quad \text{(field gradient that competes with gravity)}$$

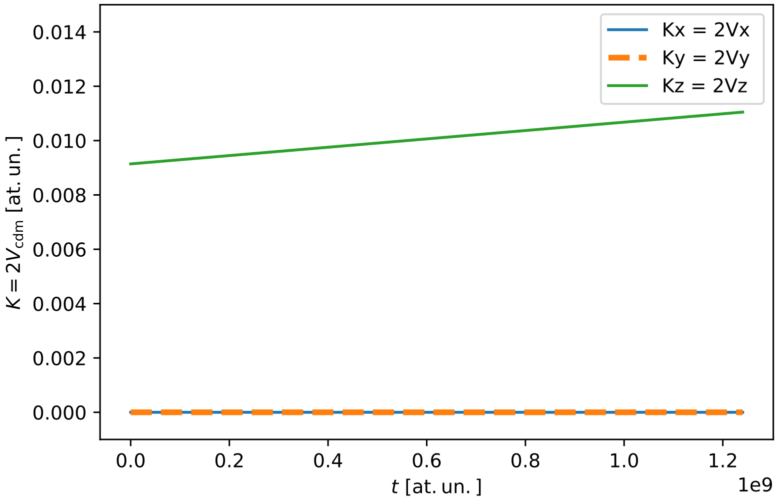

Figure A.10. Time dependence of the three components of $\mathbf{K} = 2\mathbf{V}_{\mathbf{Ps}}$ for a $=\approx 16$ atom (in this semi-classical approximation non-integer values are allowed), with the parameters described in the text. Constant positive acceleration along the z-axis is observed as expected for a ”low-field seeking” state and a decreasing electric field in the direction of travel. The observed acceleration is $a \approx 6.9 \times 10^{10}\,\mathrm{m/s^2}$, consistent with the value of k predicted by the point-like approximation for an initial state with the quantum number k (A.10).

So for the ”extreme Stark states” with $k = n - 1$ and $n > 25$ the required field uniformity is very high. Depending on their origin, nonhomogeneous stray fields might be fluctuating (even randomly) in time and space whereas the gravitational acceleration is exerted for the full time of flight along the same direction. Further studies are required to assess the feasibility of a possible gravitational measurement in known experimental conditions. The results of this appendix provide the foundation to carry out this investigation.

APPENDIX B

Full expression and implementation of equation (5.11)

For the sake of completeness the full expression of equation (5.11) is reported in this appendix. The formula has been verified with an independent calculation and correctly reproduces the results of the original paper [26]. As discussed in chapter 5 the equation displayed in the paper contained a few typos. The formula for the intensity reads:

$$I(\mathbf{x}; z_3) = \frac{w_{x0} w_{y0}}{w_y(z_3) w_x(z_3)} \sum_{m,m',n,n'=-\infty}^{\infty} a^*_{m'} a_m b^*_{n'} b_n D^{\overline{m}}_{\overline{n}}\left(\mathbf{x}, z_3, w_{x,y}(z_3)\right) F^{\Delta m}_{\Delta n}\left(\mathbf{x}, z_3, r_{x,y}(z_3)\right) \times$$
$$\times P^{\overline{m},\Delta m}_{\overline{n},\Delta n}(z_3, r_{x,y}(z_3)) V^{\Delta m}_{\Delta n}(\mathbf{x}, z_3, l_{x,y}(z_3)),$$

where a_k, b_k are the Fourier series expansion coefficients of the transmission functions of the first and second grating respectively. Convenient indexes are introduced and denoted $\Delta m = m - m'$ and $\overline{m} = (m' + m)/2$. Furthermore we recall that the distances z_i with $i = 0, 1, 2, 3$ represent respectively the position of an initial reference plane, the first and second grating plane and the detector plane. The evolution of the parameters $l(z), r(z), w(z)$ is computed with equations (5.8). The D function reads

$$D^{\overline{m}}_{\overline{n}}(\rho, z_3, w_{x,y}(z_3)) = \exp\left\{ \frac{-\pi \left[x - \lambda z_{23} \left(\frac{\overline{n}\cos\phi}{d_2} + \frac{\overline{m}}{d_1} \frac{z_{13}}{z_{23}} \right) \right]^2}{w_x(z_3)^2} \right\} \times \exp\left[\frac{-\pi \left(y - \frac{\overline{n}\sin\phi \lambda z_{23}}{d_2} \right)^2}{w_y(z_3)^2} \right],$$

and controls the overall envelope of the diffraction pattern. The functions F and P govern the periodicity of the interference fringes and their contrast modulations along the optical axis:

$$F^{\Delta m}_{\Delta n}(\rho, z_3, r_{x,y}(z_3)) = \exp\left\{ -2i\pi x \left[\frac{\Delta n \cos\phi}{d_2} \left(1 - \frac{z_{23}}{r_x(z_3)} \right) + \frac{\Delta m}{d_1} \left(1 - \frac{z_{13}}{r_x(z_3)} \right) \right] \right\} \times$$
$$\times \exp\left[-2i\pi y \frac{\Delta n \sin\phi}{d_2} \left(1 - \frac{z_{23}}{r_y(z_3)} \right) \right] \qquad ,$$

$$P^{\overline{m},\Delta m}_{\overline{n},\Delta n}(z_3, r_{x,y}(z_3)) = \exp\left[\frac{2i\pi\lambda z_{13}\Delta m}{d_1} \left(\frac{\overline{n}\cos\phi}{d_2} \frac{z_{23}}{z_{13}} + \frac{\overline{m}}{d_1} \right) \left(1 - \frac{z_{13}}{r_x(z_3)} \right) \right] \times$$
$$\times \exp\left\{ \frac{2i\pi\lambda z_{23}\Delta n}{d_2} \left[\frac{\overline{m}\cos\phi}{d_1} \left(1 - \frac{z_{13}}{r_x(z_3)} \right) + \frac{\overline{n}}{d_2} - \frac{\overline{n} z_{23}}{d_2} \left(\frac{\cos^2\phi}{r_x(z_3)} + \frac{\sin^2\phi}{r_y(z_3)} \right) \right] \right\} \qquad .$$

Finally, the V function describes the visibility of the interference fringes as a function of the relative position and orientation of the gratings.

$$V_{\Delta n}^{\Delta m}(z_3, l_{x,y}(z_3)) = \exp\left\{ \frac{-\pi\left[\lambda z_{23}\left(\frac{\Delta n\cos\phi}{d_2} + \frac{\Delta m}{d_1}\frac{z_{13}}{z_{23}}\right)\right]^2}{l_x(z_3)^2} \right\} \times \exp\left[-\pi\left(\frac{\Delta n \sin\phi\lambda z_{23}}{d_2 l_y(z_3)}\right)^2\right].$$

The above formula was implemented in a C++ code, the gratings were modelled as pure intensity masks with a well-defined open fraction f. The Fourier components are given by equation (4.20) in section 4.1.1:

$$a_n(f) = f\,\mathrm{sinc}(\pi n f)\left(\mathrm{e}^{i\pi n f}\right).$$

To speed up the evaluation the table of Fourier components is precomputed in a first initialization step. As suggested in [26], the summation was truncated to the first few Fourier orders, namely $-N \leq m, n, m', n' \leq N$. Typically a value $N = 4$ was chosen, as no significant differences in the calculated shape of the diffraction pattern (both transverse and longitudinal) were observed for larger N. The choice of $N = 2$ introduces a visible distortion of the diffraction pattern but considerably speeds up the calculation. Salient features of the pattern such as the contrast and its dependence on the relative angle and position of the gratings are correctly predicted only at a qualitative level. This mode is thus only useful for rapid visualization purposes.

Bibliography

[1] S. Sala, F. Castelli, M. Giammarchi, S. Siccardi, and S. Olivares. Matter-wave interferometry: towards antimatter interferometers. *J. Phys. B: At. Mol. Opt. Phys.*, 48:195002, 2015.

[2] S. Sala. Master's thesis: Antimatter wave interferometry with positrons, positronium and antiprotons., 2014.

[3] URL `http://www.lhep.unibe.ch/`. [Online; accessed 10-May-2018].

[4] See the list of references available on the official website of the laboratory. `http://lness.como.polimi.it/positron.php`. [Online; accessed 10-May-2018].

[5] M. Deutsch. Three-quantum decay of positronium. *Phys. Rev.*, 83:866–867, Aug 1951.

[6] A. Kellerbauer et al. Proposed antimatter gravity measurement with an antihydrogen beam. *Nucl. Instr. and Meth. in Phys. Res. B*, 266:351–356, 2008.

[7] C. Amole et al. Description and first application of a new technique to measure the gravitational mass of antihydrogen. *Nature Comm.*, 4:1785, 2013.

[8] P. Pérez et al. The gbar antimatter gravity experiment. *Hyperfine Interactions*, 233(1):21–27, Aug 2015.

[9] A. Tonomura. Demonstration of single electron buildup of an interference pattern. *Am.J.Phys.*, 57:117–120, 1989.

[10] P. G. Merli, G. F. Missiroli, and G. Pozzi. On the statistical aspect of electron interference phenomena. *Am . J. Phys.*, 44, 1976.

[11] A. Zeilinger et al. Single and double-slit diffraction of neutrons. *Rev.Mod.Phys.*, 60, 1988.

[12] M. Arndt et al. Wave-particle duality of C_{60} molecules. *Nature*, 401:680–682, 1999.

[13] S. Sala, M. Giammarchi, and S. Olivares. Asymmetric Talbot-Lau interferometry for inertial sensing. *Phys. Rev. A*, 94:033625, Sep 2016.

[14] S. Aghion, A. Ariga, T. Ariga, M. Bollani, E. Dei Cas, A. Ereditato, C. Evans, R. Ferragut, M. Giammarchi, C. Pistillo, M. Romé, S. Sala, and P. Scampoli. Detection of low energy antimatter with emulsions. *Journal of Instrumentation*, 11(06):P06017, 2016.

[15] S. Aghion, A. Ariga, M. Bollani, A. Ereditato, R. Ferragut, M. Giammarchi, M. Lodari, C. Pistillo, S. Sala, P. Scampoli, and M. Vladymyrov. Nuclear emulsions for the detection of micrometric-scale fringe patterns: an application to positron interferometry. *Journal of Instrumentation*, 13(05):P05013, 2018.

[16] G. Möllenstedt. *The History of the Electron Biprism*, pages 1–15. Springer US, Boston, MA, 1999. ISBN 978-1-4615-4817-1.

[17] Richard P. Feynman and Albert R. Hibbs. *Quantum Mechanics and Path Integrals: Emended Edition (Dover Books on Physics)*. Dover Publications, 2010. ISBN 0486477223.

[18] R. Rosa. The merli–missiroli–pozzi two-slit electron-interference experiment. *Physics in Perspective*, 14(2):178–195, Jun 2012.

[19] L. de Broglie. Recherches sur la théorie des quanta. *Ann. Phys. (Paris)*, 3, 1925.

[20] M. Arndt and K. Hornberger. Quantum interferometry with complex molecules. *arXiv:0903.1614v1*, 2008.

[21] M. Born and E. Wolf. *Principles of Optics: Electromagnetic Theory of Propagation, Interference and Diffraction of Light*. Cambridge University Press, 1999. ISBN 0521642221.

[22] J. Goodman. *Introduction to Fourier optics*. Roberts and Company Publishers, 2004. ISBN 9780974707723.

[23] R. Tumulka, A. Viale, and N. Zanghì. Reduced coherence in double-slit diffraction of neutrons. *Phys. Rev. A*, 75, 2007.

[24] A. S. Sanz, F. Borondo, and M. J. Bastiaans. Loss of coherence in double-slit diffraction experiments. *Phys. Rev. A*, 71, 2005.

[25] R. Bonifacio and S. Olivares. Young's experiment, schroedinger spread and spontaneous intrinsic decoherence. *Z.Naturforsch*, 56 a:41–47, 2001.

[26] B. McMorran and A. D. Cronin. Model for partial coherence and wavefront curvature in grating interferometers. *Phys. Rev. A*, 78:013601, 2008.

[27] A. D. Cronin and B. McMorran. Electron interferometry with nanogratings. *Phys. Rev. A*, 74: 061602, 2006.

[28] J. F. Clauser and M. W. Reinsch. New theoretical and experimental results in fresnel optics with applications to matter-wave and x-ray interferometry. *Appl. Phys. B*, 54:380–395, 1992.

[29] S. Nowak, Ch. Kurtsiefer, T. Pfau, and C. David. High-order talbot fringes for atomic matter waves. *Opt. Lett.*, 22(18):1430–1432, Sep 1997.

[30] E. Lau. Beugungserscheinungen an doppelrastern. *Annalen der Physik*, 437(7-8):417–423, 1948.

[31] K. Patorski. The self imaging phenomenon and its application. *Progress in Optics E. Wolf editor*, 27:3–108, 1989.

[32] F. Gori. Lau effect and coherence theory. *Optics Communications*, 31(1):4–8, oct 1979.

[33] M. Arndt et al. Matter wave interferometry with composite quantum objects. In *Atom Interferometry*, number 188 in Proceedings of the international school of physics "Enrico Fermi", pages 89–142. SIF, 2014.

[34] S. Aghion et al. A moiré deflectometer for antimatter. *Nature Communications*, 5, jul 2014.

[35] E. Joos, H. D. Zeh, C. Kiefer, D. Giulini, J. Kupsch, and I. O. Stamatescu. *Decoherence and the appearance of a classical world in quantum theory*. Springer, 2003.

[36] S. Olivares. Superposition principle, spontaneous decoherence and c60 molecule interference. *J. Opt. B: Quantum Semiclass. Opt.*, 4:438–441, 2002.

[37] P.I. Villar and F.C. Lombardo. Decoherence in a two-slit diffraction experiment with massive particles. *Journal of Physics:Conference Series*, 67, 2007.

[38] B. McMorran, J. D. Perreault, T. A. Savas, and A. Cronin. Diffraction of 0.5 kev electrons from free-standing transmission gratings. *Ultramicroscopy*, 106:356–364, 2006.

[39] R. E. Grisenti et al. Determination of atom-surface van der waals potentials from transmission-grating diffraction intensities. *Phys. Rev. Lett.*, 83:1755–1758, 1999.

[40] E. M. Lifshitz. The theory of molecular attractive forces between solids. *Sov. Phys. JETP*, 2: 73–83, 1956.

[41] H. B. G. Casimir and D. Polder. The influence of retardation on the london-van der waals forces. *Phys. Rev.*, 73:360–372, Feb 1948.

[42] M. Marinescu, A. Dalgarno, and J. F. Babb. Retarded long-range potentials for the alkali-metal atoms and a perfectly conducting wall. *Phys. Rev. A*, 55:1530–1532, Feb 1997.

[43] A. D. Cronin and J. D. Perreault. Phasor analysis of atom diffraction from a rotated material grating. *Phys. Rev. A*, 70, 2004.

[44] R. Colella, A. W. Overhauser, and S. A. Werner. Observation of gravitationally induced quantum interference. *Phys. Rev. Lett.*, 34:1472–1474, Jun 1975.

[45] U. Bonse and M. Hart. An x-ray interferometer. *Applied Physics Letters*, 6(8):155–156, 1965.

[46] P. Storey and C. Cohen-Tannoudji. The feynman path integral approach to atomic interferometry. a tutorial. *J. Phys. II France*, 4(11):1999–2027, 1994.

[47] M. Kasevich and S. Chu. Atomic interferometry using stimulated raman transitions. *Phys. Rev. Lett.*, 67:181–184, Jul 1991.

[48] Müntinga et al. Interferometry with bose-einstein condensates in microgravity. *Phys. Rev. Lett.*, 110:093602, Feb 2013.

[49] S. Chu. *Atom Interferometry*, pages 317–370. Springer Berlin Heidelberg, Berlin, Heidelberg, 2001. ISBN 978-3-540-45338-3.

[50] C. J. Foot. *Atomic Physics (Oxford Master Series in Atomic, Optical and Laser Physics)*. Oxford University Press, 2005. ISBN 0198506961.

[51] URL `http://www.microglacoste.com/fg5x.php`. [Online; accessed 10-May-2018].

[52] K. W. Madison, Y. Wang, A. M. Rey, and K. Bongs. *Annual Review of Cold Atoms and Molecules: Volume 1*, volume 1 of *Annual Review of Cold Atoms and Molecules*. World Scientific, 2013.

[53] URL `https://web.stanford.edu/group/kasevich/cgi-bin/wordpress/?page_id=11`. Accessed: 9-5-2018.

[54] S. Dimopoulos, P. W. Graham, J. M. Hogan, and M. A. Kasevich. Testing general relativity with atom interferometry. *Phys. Rev. Lett.*, 98:111102, Mar 2007.

[55] M. de Angelis, A. Bertoldi, L. Cacciapuoti, A. Giorgini, G. Lamporesi, M. Prevedelli, G. Saccorotti, F. Sorrentino, and G. M. Tino. Precision gravimetry with atomic sensors. *Measurement Science and Technology*, 20(2):022001, 2009.

[56] F. W. Dyson, A. S. Eddington, and C. Davidson. A determination of the deflection of light by the sun's gravitational field, from observations made at the total eclipse of may 29, 1919. *Philosophical Transactions of the Royal Society of London A: Mathematical, Physical and Engineering Sciences*, 220(571-581):291–333, 1920.

[57] R. V. Pound and G. A. Rebka. Gravitational red-shift in nuclear resonance. *Phys. Rev. Lett.*, 3:439–441, Nov 1959.

[58] A. Einstein. Die Grundlage der allgemeinen Relativitätstheorie. *Annalen der Physik*, 354: 769–822, 1916.

[59] B. P. Abbott et al. Observation of gravitational waves from a binary black hole merger. *Phys. Rev. Lett.*, 116:061102, Feb 2016.

[60] P. A. R. Ade et al. Planck 2013 results. I. Overview of products and scientific results. *Astron. Astrophys.*, 571:A1, 2014.

[61] C. M. Will. *Theory and Experiment in Gravitational Physics, Revised Edition*. Cambridge University Press, 1993. ISBN 0521439736.

[62] A. Einstein. Die Feldgleichungen der Gravitation. *Sitzungsberichte der Königlich Preußischen Akademie der Wissenschaften (Berlin), Seite 844-847.*, 1915.

[63] C. Brans and R. H. Dicke. Mach's principle and a relativistic theory of gravitation. *Phys. Rev.*, 124:925–935, Nov 1961.

[64] M. D. C. Torri, S. Bertini, M. Giammarchi, and L. Miramonti. Lorentz invariance violation effects on uhecr propagation: A geometrized approach. *Journal of High Energy Astrophysics*, 18:5 – 14, 2018.

[65] R. Cowsik, T. Madziwa-Nussinov, S. Nussinov, and U. Sarkar. Testing violations of lorentz invariance with cosmic rays. *Phys. Rev. D*, 86:045024, Aug 2012.

[66] V. A. Kostelecký, editor. *Proceedings of the Seventh Meeting on CPT and Lorentz Symmetry*, 2016. Indiana University, Bloomington, World Scientific.

[67] P. Wolf and L. Blanchet. Analysis of sun/moon gravitational redshift tests with the ste-quest space mission. *Classical and Quantum Gravity*, 33(3):035012, 2016.

[68] S. Schlamminger, K.-Y. Choi, T. A. Wagner, J. H. Gundlach, and E. G. Adelberger. Test of the equivalence principle using a rotating torsion balance. *Phys. Rev. Lett.*, 100:041101, Jan 2008.

[69] J. G. Williams, S. G. Turyshev, and D. H. Boggs. Lunar laser ranging tests of the equivalence principle. *Classical and Quantum Gravity*, 29(18):184004, 2012.

[70] Steven Chu, Achim Peters, and Keng Yeow Chung. *Nature*, 400(6747):849–852, aug 1999.

[71] M. G. Tarallo, T. Mazzoni, N. Poli, D. V. Sutyrin, X. Zhang, and G. M. Tino. Test of einstein equivalence principle for 0-spin and half-integer-spin atoms: Search for spin-gravity

coupling effects. *Phys. Rev. Lett.*, 113:023005, Jul 2014.

[72] M Doser, C Amsler, A Belov, G Bonomi, P Bräunig, J Bremer, R Brusa, G Burkhart, L Cabaret, C Canali, et al. Exploring the wep with a pulsed cold beam of antihydrogen. *Classical and Quantum Gravity*, 29(18):184009, 2012.

[73] G.M. Tino et al. Precision gravity tests with atom interferometry in space. *Nuclear Physics B - Proceedings Supplements*, 243-244:203 – 217, 2013. Proceedings of the IV International Conference on Particle and Fundamental Physics in Space.

[74] A. M. Nobili and A. Anselmi. Relevance of the weak equivalence principle and experiments to test it: Lessons from the past and improvements expected in space. *Physics Letters A*, 2017. ISSN 0375-9601.

[75] G. B. Andresen et al. Confinement of antihydrogen for 1000 seconds. *Nature Physics*, 7(7): 558–564, jun 2011.

[76] M. Ahmadi et al. Observation of the 1S-2S transition in trapped antihydrogen. *Nature*, 541: 506–510, 2016.

[77] M. M. Nieto and T. Goldman. The arguments against “antigravity” and the gravitational acceleration of antimatter. *Physics Reports*, 205(5):221 – 281, 1991.

[78] M. Villata. Cpt symmetry and antimatter gravity in general relativity. *EPL (Europhysics Letters)*, 94(2):20001, 2011.

[79] D. J. Cross. Response to “CPT symmetry and antimatter gravity in general relativity”. *ArXiv:1108.5117*, 2011.

[80] A. Benoit-Lévy and G. Chardin. Introducing the dirac-milne universe. *Astronomy & Astrophysics*, 537:A78, jan 2012.

[81] A.P. Mills and M. Leventhal. Can we measure the gravitational free fall of cold rydberg state positronium? *Nuclear Instruments and Methods in Physics Research Section B: Beam Interactions with Materials and Atoms*, 192(1):102 – 106, 2002.

[82] D. B. Cassidy and S. D. Hogan. Atom control and gravity measurements using rydberg positronium. *Int. J. Mod. Phys.: Conference Series*, 30:1460259, 2014.

[83] T. Juffmann et al. Experimental methods of molecular matter-wave optics. *Rep. Prog. Phys.*, 76(8):086402, 2013.

[84] S. Weinberg. *The Quantum Theory of Fields, Volume 1: Foundations*. Cambridge University Press, 2005. ISBN 0521670535.

[85] K. A. Olive et al. Review of Particle Physics. *Chin. Phys.*, C38:090001, 2014.

[86] G. Gronniger, B. Barwick, and H. Batelaan. A three-grating electron interferometer. *New Journal of Physics*, 8(10):224, 2006.

[87] C. Fabre, M. Gross, J. Raimond, and S. Haroche. Measuring atomic dimensions by transmission of rydberg atoms through micrometre size slits. *J. Phys. B: At. Mol. Phys.*, 16:L671–L677, 1983.

[88] Maxwell D. G., I. Hromada, W. F. Holmgren, R. Trubko, and A. D. Cronin. Measurements of the ground-state polarizabilities of cs, rb, and k using atom interferometry. *Phys. Rev. A*, 92: 052513, Nov 2015.

[89] H. Uys, J. D. Perreault, and A. D. Cronin. Matter-wave decoherence due to a gas environment in an atom interferometer. *Phys. Rev. Lett.*, 95:150403, Oct 2005.

[90] R. Ferragut et al. Positronium formation in porous materials for antihydrogen production. *Journal of Physics: Conference Series*, 225(1):012007, 2010.

[91] S. Aghion et al. Characterization of a transmission positron/positronium converter for antihydrogen production. *Nuclear Instruments and Methods in Physics Research Section B: Beam Interactions with Materials and Atoms*, 407:55 – 66, 2017.

[92] S. L. Andersen et al. Positronium emission and cooling in reflection and transmission from thin meso-structured silica films. *Journal of Physics B: Atomic, Molecular and Optical Physics*, 48(20):204003, 2015.

[93] S. L. Andersen et al. Positronium emission and cooling in reflection and transmission from thin meso-structured silica films. *J. Phys. B: At. Mol. Opt. Phys.*, 48(20):204003, 2015.

[94] R. Ferragut C. Evans, S. Aghion et al. (In preparation).

[95] S. Cialdi et al. Efficient two-step positronium laser excitation to rydberg levels. *Nuclear Instruments and Methods in Physics Research Section B: Beam Interactions with Materials and Atoms*, 269(13):1527 – 1533, 2011.

[96] D. B. Cassidy, T. H. Hisakado, H. W. K. Tom, and A. P. Mills. Efficient production of rydberg positronium. *Phys. Rev. Lett.*, 108:043401, Jan 2012.

[97] T. F. Gallagher. *Rydberg Atoms (Cambridge Monographs on Atomic, Molecular and Chemical Physics)*. Cambridge University Press, 2005. ISBN 0521021669.

[98] F. Castelli, I. Boscolo, S. Cialdi, M. G. Giammarchi, and D. Comparat. Efficient positronium laser excitation for antihydrogen production in a magnetic field. *Phys. Rev. A*, 78:052512, Nov 2008.

[99] C. H. Cheng, C. Y. Lee, and T. F. Gallagher. Production of circular rydberg states with circularly polarized microwave fields. *Phys. Rev. Lett.*, 73:3078–3081, Dec 1994.

[100] R. Lutwak et al. Circular states of atomic hydrogen. *Phys. Rev. A*, 56:1443–1452, Aug 1997.

[101] E. Vliegen and F. Merkt. Stark deceleration of hydrogen atoms. *J. Phys. B: At., Mol. Opt. Phys.*, 39(11):L241–L247, 2006.

[102] A. Bermúdez, D. Gómez, and P. Salgado. *Electrostatics with MaxFEM*, pages 267–298. Springer International Publishing, Cham, 2014. ISBN 978-3-319-02949-8.

[103] S. D. Hogan. Rydberg-stark deceleration of atoms and molecules. *EPJ Techniques and Instrumentation*, 3(2), 2016.

[104] T. E. Wall, A. M. Alonso, B. S. Cooper, A. Deller, S. D. Hogan, and D. B. Cassidy. Selective production of rydberg-stark states of positronium. *Phys. Rev. Lett.*, 114:173001, Apr 2015.

[105] S. Nimmrichter and K. Hornberger. Theory of near-field matter-wave interference beyond the eikonal approximation. *Phys. Rev. A*, 78:023612, 2008.

[106] P. L. Kapitza and P. A. M. Dirac. *Proc. Cam. Philos. Soc.*, 29, 1933.

[107] H. Batelaan. The kapitza-dirac effect. *Contemporary Physics*, 41(6), 2000.

[108] D. L. Freimund, K. Aflatooni, and H. Batelaan. Observation of the kapitza-dirac effect. *Nature*, 413, 2001.

[109] S. Gerlich et al. A kapitza-dirac-talbot-lau interferometer for highly polarizable molecules. *Nature Physics*, 3, 2007.

[110] C. Hugenschmidt et al. The upgrade of the neutron induced positron source nepomuc. *Journal of Physics: Conference Series*, 443(1):012079, 2013.

[111] V. W. Hughes, D. W. McColm, K. Ziock, and R. Prepost. Formation of muonium and observation of its larmor precession. *Phys. Rev. Lett.*, 5:63–65, Jul 1960.

[112] K. Kirch et al. Testing antimatter gravity with muonium. *Int. J. Mod. Phys: Conference Series*, 30:1460258, 2014.

[113] A. C. L. Jones et al. Focusing of a rydberg positronium beam with an ellipsoidal electrostatic mirror. *Phys. Rev. Lett.*, 119:053201, Aug 2017.

[114] H. W. Lee. Theory and application of the quantum phase-space distribution functions. *Phys. Rep.*, 259(3):147 – 211, 1995.

[115] H. Batelaan et al. Classical and quantum atom fringes. In P. R. Berman, editor, *Atom Interferometry*, pages 85 – 120. Academic Press, San Diego, 1997. ISBN 978-0-12-092460-8.

[116] J. F. Schaff, T. Langen, and J. Schmeidmayer. Interferometry with atoms. In *Atom Interferometry*, number 188 in Proceedings of the international school of physics "Enrico Fermi", pages 1–87. SIF, 2014.

[117] M. K. Oberthaler. Inertial sensing with classical atomic beams. *Phys. Rev. A*, 54(4):3165–3172, 1996.

[118] M. Arndt B. Brezger and A. Zeilinger. Concepts for near-field interferometers with large molecules. *J. Opt. B: Quantum Semiclass. Opt.*, 5(2):S82, 2003.

[119] M. Born and E. Wolf. *Principles of Optics: Electromagnetic Theory of Propagation, Interference and Diffraction of Light*. Cambridge University Press, 1999. ISBN 0521642221.

[120] J. Jahns and A. W. Lohmann. The lau effect (a diffraction experiment with incoherent illu-

mination). *Opt. Commun.*, 28(3):263 – 267, 1979.

[121] W. B. Case. Wigner functions and weyl transforms for pedestrians. *Am. J. Phys*, 76(10): 937–946, 2008.

[122] J. D. Perreault, T. A. Savas, and A. Cronin. Using atomic diffraction of na from material gratings to measure atom-surface interactions. *Phys. Rev. A*, 71:053612, 2005.

[123] T. A. Savas, M. L. Schattenburg, J. M. Carter, and Henry I. Smith. Large-area achromatic interferometric lithography for 100 nm period gratings and grids. *J. Vac. Sci. Technol. B, Microelectron. Nanometer. Struct. Process. Meas. Phenom.*, 14(6):4167–4170, 1996.

[124] J. F. Clauser and S. Li. Talbot-vonlau atom interferometry with cold slow potassium. *Phys. Rev. A*, 49:R2213–R2216, 1994.

[125] M. K. Oberthaler. Anti-matter wave interferometry with positronium. *Nucl. Instr. and Meth. in Phys. Res. B*, 192:129–134, 2002.

[126] M. Giammarchi. Quantum interferometry and gravity with positronium. Talk given at the IUCSS Workshop on Signals for Nonminimal Lorentz and CPT Violation, Indiana University, Bloomington (IN), 2015. URL `http://pcgiammarchi.mi.infn.it/giammarchi/Giammarchi_QUPLAS_LVS2015.pdf`.

[127] F. Gori. Mode propagation of the field generated by collett-wolf schell-model sources. *Opt. Commun.*, 46:149, 1983.

[128] F. Zernike. The concept of degree of coherence and its application to optical problems. *Physica*, 5(8):785 – 795, 1938.

[129] A. T. Friberg and R. J. Sudol. Propagation parameters of gaussian schell-model beams. *Optics Communications*, 41(6):383 – 387, 1982.

[130] B. McMorran. *Electron Diffraction and Interferometry Using Nanostructures*. PhD thesis, The University of Arizona, 2009. URL `http://hdl.handle.net/10150/194029`.

[131] B. McMorran and A. Cronin. Gaussian Schell Source as Model for Slit-Collimated Atomic and Molecular Beams. *arXiv:0804.1162*, 2008.

[132] A. D. Cronin and B. McMorran. Electron interferometry with nanogratings. *Phys. Rev. A*, 74, 2006.

[133] B. Crosignani, B. Daino, and P. Di Porto. Light scattering by a rotating disk. *Journal of Applied Physics*, 42(1):399–403, 1971. doi: 10.1063/1.1659609.

[134] `http://www.radiant-dyes.com/index.php`. [Online; accessed 12-April-2018].

[135] `http://www.micronixusa.com/motion/index.cfm`. [Online; accessed 12-April-2018].

[136] `https://www.thorlabs.com/index.cfm`. [Online; accessed 12-April-2018].

[137] `https://ecatalog.mitutoyo.com/Linear-Scales-ABS-AT715-Series-539-Slim-Spar-Type-C1281.aspx`. [Online; accessed 2-July-2018].

[138] `http://www.lumarray.com/`. [Online; accessed 16-January-2018].

[139] G. Bradski. The OpenCV Library. *Dr. Dobb's Journal of Software Tools*, 2000.

[140] C. Amsler et al. A new application of emulsions to measure the gravitational force on antihydrogen. *J. Instrum.*, 8(02):P02015, 2013.

[141] A Ereditato. The study of neutrino oscillations with emulsion detectors. *Adv. High Energy Phys.*, 2013:1, 2013.

[142] V. J. Ghosh, D. O. Welch, and K. G. Lynn. Monte carlo studies of positron implantation in elemental metallic and multilayer systems. *AIP Conference Proceedings*, 303(1):37–47, 1994.

[143] G.C. Aers, P.A. Marshall, T.C. Leung, and R.D. Goldberg. Defect profiling in multilayered systems using mean depth scaling. *Applied Surface Science*, 85:196 – 209, 1995. Proceedings of the Sixth International Workshop on Slow-Positron Beam Techniques for Solids and Surfaces.

[144] J. Baró, J. Sempau, J.M. Fernández-Varea, and F. Salvat. Penelope: An algorithm for monte carlo simulation of the penetration and energy loss of electrons and positrons in matter. *Nucl. Instr. Meth. Phys. Res. Sec. B: Beam Interactions with Materials and Atoms*, 100(1):31 – 46, 1995.

[145] `http://pypenelope.sourceforge.net/`. [Online; accessed 16-January-2018].

[146] M. K. Mardia. *Statistics of directional data*. Academic Press, New York, 1972.

[147] R. Brun and F. Rademakers. ROOT: An object oriented data analysis framework. *Nucl. Instrum. Meth.*, A389:81–86, 1997.

[148] O. Tange. Gnu parallel - the command-line power tool. *;login: The USENIX Magazine*, 36(1): 42–47, Feb 2011. URL `http://www.gnu.org/s/parallel`.

[149] M. Kimura et al. Development of nuclear emulsions with $1\,\mu m$ spatial resolution for the aegis experiment. *Nucl. Instr. Meth. Phys. Res. Sec. A: Accelerators, Spectrometers, Detectors and Associated Equipment*, 732:325 – 329, 2013. Vienna Conference on Instrumentation 2013.

[150] D. A. Fischer, K. G. Lynn, and D. W. Gidley. High-resolution angle-resolved positron reemission spectra from metal surfaces. *Phys. Rev. B*, 33:4479–4492, Apr 1986.

[151] A. Aydin. Monte carlo calculations of low energy positrons in silicon. *NUKLEONIKA*, 50: 37–42, 2005.

[152] Koji Michishio et al. Observation of a shape resonance of the positronium negative ion. *Nature Communications*, 7:11060, mar 2016. doi: 10.1038/ncomms11060.

[153] P. Schmelcher. Regularity and irregularity in the centre of mass motion of the positronium atom in a magnetic field. *J. Phys. B: At., Mol. Opt. Phys.*, 25(11):2697, 1992.

[154] E. Vliegen and F. Merkt. On the electrostatic deceleration of argon atoms in high rydberg states by time-dependent inhomogeneous electric fields. *J. Phys. B: At., Mol. Opt. Phys.*, 38 (11):1623–1636, 2005.

[155] E. A. Solov'ev. Adiabatic invariants and the problem of quasiclassical quantization of many-dimensional systems. *Soviet Journal of Experimental and Theoretical Physics*, 48:635, October 1978.

[156] J.R. Dormand and P.J. Prince. A family of embedded runge-kutta formulae. *Journal of Computational and Applied Mathematics*, 6(1):19 – 26, 1980.

[157] E. Fehlberg. Klassische runge-kutta-formeln vierter und niedrigerer ordnung mit schrittweiten-kontrolle und ihre anwendung auf wärmeleitungsprobleme. *Computing*, 6(1): 61–71, Mar 1970.

[158] K. Ahnert and M. Mulansky. Odeint – solving ordinary differential equations in c++. *AIP Conference Proceedings*, 1389(1):1586–1589, 2011.

[159] M. Walt. *Introduction to Geomagnetically Trapped Radiation (Cambridge Atmospheric and Space Science Series)*. Cambridge University Press, 2005. ISBN 0521616115.

[160] R. E. Miles. On random rotations in $\mathbb{R}^3$. *Biometrika*, 52(3/4):636–639, 1965.

[161] H. A. Bethe and E. E. Salpeter. *Quantum Mechanics of One- And Two-Electron Atoms*. Martino Fine Books, 2014. ISBN 1614276226.

[162] R.F. Stebbings and F.B. Dunning. *Rydberg States of Atoms and Molecules*. Essays in nuclear astrophysics. Cambridge University Press, 1983. ISBN 9780521248235.

[163] M. H. Rice and R. H. Good. Stark effect in hydrogen$*$. *J. Opt. Soc. Am.*, 52(3):239–246, Mar 1962.

[164] R. J. Damburg and V. V. Kolosov. A hydrogen atom in a uniform electric field. *Journal of Physics B: Atomic and Molecular Physics*, 9(18):3149, 1976.

[165] D. Farrelly and W. P. Reinhardt. Uniform semiclassical and accurate quantum calculations of complex energy eigenvalues for the hydrogen atom in a uniform electric field. *Journal of Physics B: Atomic and Molecular Physics*, 16(12):2103, 1983.

[166] J. A. C. Gallas, H. Walther, and E. Werner. Simple formula for the ionization rate of rydberg states in static electric fields. *Phys. Rev. Lett.*, 49:867–870, Sep 1982.

[167] L. Fernández-Menchero and H. P. Summers. Stark effect in neutral hydrogen by direct integration of the hamiltonian in parabolic coordinates. *Phys. Rev. A*, 88:022509, Aug 2013. doi: 10.1103/PhysRevA.88.022509.

Acknowledgments

If my memory serves me well, this project started from a pile of hand-written notes that my supervisor Marco G. handed me as I began my Master's thesis. I will always be grateful to him for giving me the opportunity to turn those ideas into a real experiment. This task would not have been possible without the involvement of Ciro and Rafael, who put all their efforts into the eventual success of this measurement[1]. In the last four years we strove to do something that nobody ever did before. There will always be people who will use a different wording and state that we wasted four years of our lives to prove something everybody expected. Nonetheless I believe that to take the laws of Nature for granted is the ultimate act of arrogance.

Besides the core QUPLAS-0 team, there were many people who played a role in the activities described here or, most importantly, in my training as a physicist. I would like to thank my favourite quantum opticians, Stefano O., Fabrizio and Simone. Giancarlo and Massimiliano, whose laboratory we polluted with not-exactly-state-of-the-art equipment[2]. The L-NESS team, Marco L., Stefano A., Erasmo, Craig, Mario, Monica. The Bern group, Aki, Paola, Antonio. Special thanks also go to Tim Savas for his genuine interest in our research.

I thank Germano and Anna for reviewing my (rather verbose) thesis. I also thank, in advance, Matteo, Ciro and Giovanni, members of the final examination committee for their attention during my (equally verbose) presentation.

I am grateful to the very supportive group of friends, rather than colleagues, living at the 3$^{\text{rd}}$ floor of the LITA building: Andrea, Lorenzo, Giacomo, Silvia, Marco, Marcello. Of all the escape rooms we have been through, I think this PhD one earns a solid second place in my difficulty ranking, although the setting could have been better.

Many thanks go my family and friends for their support and understanding throughout this endeavour. Being a PhD student has been a fulfilling experience, however the time has come for me to move on and I still do not know what the future holds for me.

The only thing I know for sure is that I want you, Irene, to be a part of my life. A life that we are just starting to build together.

---

[1] Efforts also included putting their lives at risk by exchanging suspicious-looking refrigerated packages along the highway, in broad daylight. (Disclaimer: some nuclear emulsions were harmed in the process.)

[2] Which, nonetheless, allowed us to answer (in the affirmative) one of the most pressing open questions in modern physics: *can an electron plasma be noisier than old-school Norwegian black metal?*